DISS. ETH NO. 29567

Exploring
Dissipative and Coherent Spin Dynamics with Superradiant Quantum Gases

A thesis submitted to attain the degree of
DOCTOR OF SCIENCES
(Dr. sc. ETH Zurich)

presented by
RODRIGO FELIPE ROSA-MEDINA PIMENTEL
M. Sc., University of Heidelberg, Germany
born on 09.03.1994
citizen of Peru and Germany

accepted on the recommendation of
Prof. Dr. Tilman Esslinger, examiner
Prof. Dr. Oded Zilberberg, co-examiner

2023

Para mis padres, José Luis y Gisela.

Abstract

Experiments integrating ultracold quantum gases and optical cavities provide a versatile platform for exploring emergent collective phenomena, ranging from symmetry-breaking phase transitions to out-of-equilibrium many-body dynamics. In this thesis, we report on a series of experiments employing a ^{87}Rb Bose-Einstein condensate (BEC) coupled to a high-finesse optical cavity, with the goal of investigating photon-mediated dissipative and coherent spin dynamics. In the dispersive regime of atom-light interactions, we engineer cavity-assisted Raman transitions that couple specific internal and external modes of a degenerate quantum gas. This gives rise to superradiant Raman scattering of cavity photons, a process that is collectively enhanced by the number of participating atoms.

In a first project, we couple two internal and external modes to realize an extended Dicke model with tunable coherent and dissipative interactions. The system undergoes a superradiant phase transition featuring spin-changing self-organization of the atoms. We experimentally access a dissipation-stabilized phase and a discontinuous superradiant transition in an extended region of phase bistability. The underlying mechanism is a collective decay of the hybrid light-matter excitations, which we resolve in real time by probing the cavity spectrum.

In a second set of experiments, we engineer dynamical tunneling in a synthetic lattice in momentum space. Collective hopping between discrete momentum modes of a two-component BEC is implemented via superradiant Raman scattering, resulting in directional lattice dynamics due to the inherent cavity losses. By performing frequency-resolved measurements of the leaking cavity field, we resolve the individual tunneling events both in real time and non-destructively. We further extend our observations to a regime exhibiting mutually stimulating hopping cascades.

In a third project, we demonstrate a mechanism for generating correlated atom pairs in well-defined spin and momentum modes. The pairs are created within tens of microseconds following the exchange of virtual cavity photons. We report on the first observation of coherent pair oscillations involving momentum modes, and achieve independent optical control of unitary pair processes and competing dissipative superradiant scattering. By characterizing the pair statistics and momentum-space correlations, we reveal beyond mean-field features and show their correlated nature.

Our results demonstrate a comprehensive approach for studying photon-mediated magnetic phenomena in quantum gases. Extending the implemented cavity-assisted spin interactions to Hubbard systems can facilitate experimental access to strongly correlated magnetic phases, as proposed and theoretically investigated in a dedicated project. Finally, the observed pair mechanism paves the way for quantum-enhanced matter-wave interferometry and quantum simulation experiments beyond conventional solid-state systems.

Zusammenfassung

Experimente, die ultrakalte Quantengase und optische Resonatoren integrieren, sind eine vielseitige Plattform zur Erforschung emergenter kollektiver Phänomene, die von Symmetrie-brechenden Phasenübergängen bis hin zur Vielteilchendynamik außerhalb des Gleichgewichts reichen. In dieser Arbeit berichten wir über eine Reihe von Experimenten, bei denen ein ^{87}Rb-Bose-Einstein-Kondensat (BEC) an einen optischen Hochfinesse-Resonator gekoppelt wird, um Photonen-vermittelte dissipative und kohärente Spindynamik zu untersuchen. Im dispersiven Regime der Atom-Licht Wechselwirkungen erzeugen wir Resonator-vermittelte Raman-Übergängen, die spezifische interne und externe Moden eines entarteten Quantengases koppeln. Dies führt zu superradianter Raman-Streuung von Resonator-Photonen, ein Prozess, der kollektiv durch die Anzahl der beteiligten Atome verstärkt wird.

In einem ersten Projekt koppeln wir zwei spezifische interne und externe Moden, um ein erweitertes Dicke-Modell mit einstellbaren kohärenten und dissipativen Wechselwirkungen zu realisieren. Das System durchläuft einen superradianten Phasenübergang, der eine Spin-verändernde Selbstorganisation der Atome aufweist. Wir beobachten eine dissipationsstabilisierte Phase und einen diskontinuierlichen superradianten Übergang in einem ausgedehnten Bereich der Phasen-Bistabilität. Der zugrunde liegende Mechanismus ist ein kollektiver Zerfall der hybriden Licht-Materie-Anregungen, den wir in Echtzeit durch die Untersuchung des Resonator-Spektrums messen.

In einem zweiten Satz von Experimenten erzeugen wir dynamisches Tunneln in einem synthetischen Gitter im Impulsraum. Kollektives Tunneln zwischen diskreten Impulsmoden eines zweikomponentigen BEC wird durch superradiante Raman-Streuung implementiert, was zu gerichteter Gitterdynamik aufgrund der inhärenten Resonatorverluste führt. Durch frequenzaufgelöste Messungen des austretenden Resonatorfeldes lösen wir die einzelnen Tunnelereignisse, sowohl in Echtzeit als auch auf eine nicht-destruktive Weise, auf. Wir erweitern unsere Beobachtungen auf ein Regime, das gegenseitig stimulierende Tunnelkaskaden aufweist.

In einem dritten Projekt demonstrieren wir einen Mechanismus zur Erzeugung korrelierter Atompaare in wohldefinierten Spin- und Impulsmoden. Die Paare werden innerhalb von wenigen Mikrosekunden durch den Austausch virtueller Resonatorphotonen erzeugt. Wir berichten über die ersten Beobachtungen kohärenter Paaroszillationen, die Impulsmoden einbeziehen, und erreichen eine unabhängige optische Kontrolle über konkurrierende unitäre Paarprozesse und dissipative superradiante Streuung. Durch die Charakterisierung der Paarstatistik und der Impulsraumkorrelationen zeigen wir über das Mean-Field hinausgehende Effekte auf und demonstrieren ihre korrelierte Natur.

Unsere Ergebnisse zeigen eine umfassende Herangehensweise zur Untersuchung von Photonen-vermittelte magnetischen Phänomenen in Quantengasen. Die Erweite-

rung der implementierten Resonator-vermittelten Spin-Wechselwirkungen auf Hubbard Systeme kann experimentellen Zugang zu stark korrelierten magnetischen Phasen erleichtern, wie es in einem zusätzlichen Projekt vorgeschlagen und theoretisch untersucht wird. Schließlich ebnet der beobachtete Paarmechanismus den Weg für quantenverstärkte Interferometrie mit Materiewellen und Quantensimulationsexperimente, die über konventionelle Festkörpersysteme hinausgehen.

Contents

1 Introduction **1**

2 Dispersive light-matter interactions and superradiant Raman scattering **9**
- 2.1 Light-matter interactions in the dispersive regime 10
  - 2.1.1 From resonant to dispersive atom-light interactions 10
  - 2.1.2 Scalar and vectorial polarizability for $F = 1$ ^{87}Rb atoms . . . 13
  - 2.1.3 Cavity QED with dispersive atom-light interactions 14
  - 2.1.4 Many-body description and the Tavis-Cummings Hamiltonian 16
- 2.2 Superradiant Raman scattering 19
  - 2.2.1 Equations of motion of the open quantum system 20
  - 2.2.2 Diagnosing superradiant Raman scattering 21
  - 2.2.3 Exact solutions for small systems 23
  - 2.2.4 The role of real and virtual cavity photons 25

3 Experimental setup and upgrades **29**
- 3.1 Experimental apparatus 29
  - 3.1.1 Route to Bose-Einstein condensation 29
  - 3.1.2 High-finesse optical cavity 31
- 3.2 Preparation and detection techniques 33
  - 3.2.1 Heterodyne detection of the cavity field 33
  - 3.2.2 High-intensity absorption imaging 36
  - 3.2.3 Improved spin-selective preparation 38
- 3.3 Laser setup for driving cavity-assisted Raman transitions 39
  - 3.3.1 New laser setup 39
  - 3.3.2 Control over the spatial phase of the drives 41

4 Dissipative phases and transitions in a superradiant quantum gas **45**
- 4.1 Coupling scheme and theoretical description 47
  - 4.1.1 Coupling configuration and qualitative description 47
  - 4.1.2 Mapping to a generalized Dicke model 48
  - 4.1.3 Equations of motion and solutions of the open system 51
  - 4.1.4 Calculating the energy spectrum of the system 53
- 4.2 Realizing spin-changing self-organization 54
  - 4.2.1 A superradiant phase transition inducing spin-changing self-organization 54
  - 4.2.2 Observing the superradiant phase transition 57
- 4.3 Phase diagram of superradiant quantum gas with tunable decay . . . 61
  - 4.3.1 An extended Dicke model with tunable collective decay . . . 62
  - 4.3.2 Measuring the phase diagram of the open system 63

4.4 Bistability and hysteretic phase transitions 66
4.4.1 Bistability through dissipation 66
4.4.2 Observing a dissipation-induced hysteretic phase transition . 66
4.5 Probing the microscopic polariton excitations 68
4.5.1 Implementing cavity-assisted Raman spectroscopy 68
4.5.2 Measuring the lifetime of the excitations through real-time spectroscopy 69
4.6 Discussion and outlook 72

5 Dynamical tunneling in a momentum-space lattice 75
5.1 Theoretical description 78
5.1.1 Coupling configuration 78
5.1.2 Tight-binding Hamiltonian in momentum space 80
5.1.3 Superradiant scattering and non-Hermitian lattice dynamics . 83
5.1.4 Few-mode expansion and open system simulations 84
5.2 Observing cavity-mediated tunneling in a momentum-space lattice . 85
5.2.1 Experimental protocol 85
5.2.2 Real-time probing of dynamical tunneling 86
5.2.3 Multiple hopping events and lifetime in the momentum lattice 88
5.3 Characterization of collective tunneling 89
5.3.1 Collective hopping via superradiant Raman scattering 89
5.3.2 The properties of dynamical tunneling in our system 90
5.4 Observing hopping cascades in a momentum lattice 92
5.5 Discussion and outlook 94

6 Spin- and momentum-correlated atom pairs mediated by photon exchange 97
6.1 Theoretical description 99
6.1.1 Coupling scheme 99
6.1.2 Derivation of the effective Hamiltonian 101
6.1.3 Parametric amplification of pair production 103
6.1.4 Open system dynamics and truncated Wigner simulations . . 107
6.2 Observing coherent pair dynamics 109
6.2.1 Experimental protocol and first observations 109
6.2.2 Probing coherent pair oscillations 110
6.3 Parametric amplification of pair production of atom pairs in well-defined modes 112
6.3.1 Collectively enhanced pair production via superradiant photon exchange 113
6.3.2 Relevant time scales of the system 114
6.4 Controlling coherent and dissipative pair dynamics 115
6.4.1 Motivation and experimental protocol 115
6.4.2 Investigating the interplay between coherent and dissipative dynamics 116
6.5 Characterizing the pair quantum statistics 118
6.5.1 Measuring the pair statistics 119
6.5.2 The role of thermal and quantum fluctuations 120

6.6 Probing momentum-space correlations 121
  6.6.1 Extracting momentum-space correlation maps 122
  6.6.2 Correlated generation of spin and momentum pairs 122
6.7 Discussion and outlook 124
  6.7.1 Towards the detection of quantum correlations 125

7 Antiferromagnetic phases in a Bose-Hubbard model with cavity-mediated interactions 129
7.1 Coupling scheme and mapping to an extended Hubbard model . . . 131
  7.1.1 Coupling scheme 132
  7.1.2 Mapping to an extended Bose-Hubbard Hamiltonian 134
7.2 Ground state phase diagram 136
  7.2.1 Gutzwiller ansatz and order parameters 136
  7.2.2 Phase diagram at unity filling 138
7.3 Excitations above the antiferromagnetic Mott insulator 140
  7.3.1 Excitation branches in the zero-tunneling limit 141
  7.3.2 Spectrum at finite tunneling rates 142
7.4 Experimental feasibility and challenges 143
  7.4.1 Experimental parameters and observables 143
  7.4.2 Experimental challenges and future directions 145
7.5 Discussion and outlook 148

8 Conclusions and future directions 151
8.1 Extended Hubbard models with cavity-assisted Raman transitions . 152
8.2 Cavity-based detection schemes 154
8.3 Quantum simulation using photon-mediated atom pairs 157
  8.3.1 Implementing random spin models in momentum space . . . 158
  8.3.2 Engineering and observing spin-exchange processes 161
  8.3.3 Further directions 164

A Complementary theoretical calculations for momentum-space lattices 165
A.1 Equations of motion of the open system 165
A.2 Role of contact interactions in momentum-space lattices 166
A.3 Gross-Pitaevskii equation simulations 167
  A.3.1 Equations of motion and numerical simulations 168
  A.3.2 Dynamics due to harmonic confinement and contact interactions 168
  A.3.3 Cascaded hopping in the momentum lattice 171

Bibliography 173

Acknowledgments 201

List of publications 203

Curriculum Vitae 205

1 Introduction

Nature is complex. While the fundamental physical laws governing the microscopic properties of individual particles and their interactions are–to a great extent–well understood [1], they cannot be easily extrapolated to explain and predict the plethora of phenomena appearing at macroscopic scales. In his seminal essay *“More is different”* [2], Philip W. Anderson challenged the reductionist approach in natural sciences and emphasized the importance of *emergent behavior* for understanding interacting many-body systems: the collective properties of a large number of interacting particles are qualitatively different from the behavior of the individual constituents [3]. Indeed, a central focus of modern condensed matter physics is the study of emergent self-organization, revealing itself through phenomena like spontaneous symmetry breaking and phase transitions [4]. Notable examples include the formation of crystalline structures out of spatially homogeneous fluids [5], the emergence of spontaneous magnetization associated to quantum critical behavior [6], and the phenomena of superfluidity and superconductivity due to the condensation of bound electron pairs [7].

Upon preparing many-body systems in *out-of-equilibrium* conditions, emergent phenomena can extend far beyond static self-ordering and become inherently dynamical. This can be achieved by exposing the system of interest to external driving forces or coupling the relevant degrees of freedom to a thermal bath [8]. For example, subjecting paraelectric materials to short infrared laser pulses gives rise to metastable ferroelectricity [9, 10]. Similarly, transient superconductivity at high temperatures can be induced by illuminating materials with strong optical drives [11, 12]. The collective properties of these dynamical systems are typically inferred through measurements of bulk electric currents or spectroscopic probes [13]. Yet, tracing the observed phenomenology in naturally occurring materials back to the underlying microscopic processes remains a formidable task, mainly due to the lack of identical samples, the limited control over inter-particle interactions, and the difficulty in accessing microscopic observables. Thus, by these criteria, nature often appears exceedingly complex.

A complementary approach is provided by *synthetic many-body quantum systems*, which are meticulously designed and assembled under controlled laboratory conditions. These systems are intrinsically linked to the concept of *quantum simulators*, a notion originally introduced by Richard P. Feynman in 1982 [14]. Quantum simulators can be grouped into two broad categories, namely digital and analog [15]. Digital simulators aim to execute a series of gate operations on a discrete set of qubits (two-level quantum mechanical systems) to initialize, evolve and measure the dynamics of the associated many-body quantum system. Some notable experimental platforms in this category include superconducting qubits [16], trapped ion arrays [17] and individually addressable Rydberg atoms [18]. Analog simulators, conversely, aim to directly implement model Hamiltonians (or Lindbladians) that encapsulate the essential properties of relevant (open) many-body quantum systems. In this context, two of the most developed platforms are photonic systems [19, 20] and experiments with ultracold atoms [21, 22]. Digital simulators are currently limited by scalability constraints, as they inherently require error-free control over individual qubits [23]. Conversely, analog simulators exploit bulk properties of the underlying physical system, thereby enabling robust exploration of emergent collective phenomena in systems consisting of thousands to millions of interacting particles.

Photonic systems are among the most diverse platforms, ranging from coupled waveguide arrays, to quantum dots and integrated photonic circuits [19, 20]. Their key strengths lie in the high degree of addressability and mobility: the system of interest can be encoded in various degrees of freedom of individual photons, such as their spatial mode or polarization, which can be readily manipulated and detected. Furthermore, photons can be propagated with ease using waveguides or free-space optics, facilitating nonlocal couplings and interactions. However, unlike massive particles, photons do not naturally interact with each other in free space, which complicates direct investigations of strongly correlated many-body phenomena. To circumvent this limitation, photons are often coupled to matter degrees of freedom to engineer effective nonlinear dynamics: parametric processes in optically pumped nonlinear crystals give rise to entangled photon pairs [24], while quantum walks of correlated photons have been implemented using optical waveguide arrays [25]. By coupling a semiconductor quantum well to an optical microcavity [20, 26], the matter and light modes hybridize to form exciton-polariton quasiparticles that exhibit strong nonlinear optical properties [27]. They are well-suited for investigating collective phenomena such as exciton-polariton Bose-Einstein condensation [28] and emergent hydrodynamics [29]. Extending these systems to polariton lattices has proven to be a fruitful approach for studying a variety of tight-binding models [30] and topological photonics [31]. Photonic platforms are inherently *open quantum systems*, as photons are injected into the system of interest using external drives and irreversibly dissipate towards the environment. Recently, there has been an increased interest in fostering controlled dissipation channels to engineer non-equilibrium scenarios, with prime examples being the observation of exceptional points [32] and dissipative Mott insulators [33].

Experiments with *ultracold quantum gases* also constitute a highly flexible platform for exploring many-body quantum systems. They benefit from pristine control over the potential landscapes and inter-particle interactions experienced by the atoms, along with an effective isolation from the environment [21]. By cooling the atoms to their quantum-mechanical ground state, these experiments also offer the possibility to encode the dynamics in a discrete set of addressable modes, such as the sites of an optical lattice [22] or the different magnetic sublevels (spin states) of the electronic ground state manifold [34, 35]. Additionally, the microscopic dynamics can be reconstructed using spatially resolved measurements of the atomic density distribution [36, 37], both in real and momentum space, enabling the examination of correlation properties to discern collective behavior [38]. Ever since the observation of the superfluid-Mott insulator transition [39], cold-atom experiments have successfully simulated a variety of emergent phenomena. Key experimental observations include the crossover between a molecular Bose-Einstein condensate (BEC) and Bardeen-Cooper-Schrieffer pairing [40, 41], the emergence of quantum magnetism in two-component degenerate Fermi gases [42, 43] and the Berezinskii–Kosterlitz–Thouless quasi long-range order in a two-dimensional Bose gas [44]. Going beyond equilibrium configurations, cold-atom experiments have also been recently employed to study quantum transport between mesoscopic reservoirs [45, 46] and the onset of universal self-similar dynamics after quenching the inter-particle interactions [47–49]. However, unlike electrons in solid-state systems that interact via long-range Coulomb repulsion and fully delocalized photons in optical devices, neutral atoms typically interact through short-range van der Waals forces. In cold-atom experiments, the associated potentials can be accurately modeled as isotropic contact interactions [50]. Systems conventionally used to incorporate long-range interactions include dipolar gases, ultracold heteronuclear molecules and Rydberg atoms [51–56]. Although these systems have shed light on a variety of emergent phenomena, quantum simulation experiments can sometimes be limited by comparatively weak long-range interactions, low particle number densities, and short lifetimes, respectively.

Integrating atomic and photonic systems into hybrid platforms creates unique opportunities to bolster their strengths and overcome their limitations. Concretely, experiments combining *ultracold quantum gases* and *high-finesse optical cavities* constitute a versatile system to explore collective phenomena, leveraging the strong and tunable atom-light interactions [57, 58]. The mere presence of an optical cavity modifies the structure of the electromagnetic vacuum, significantly enhancing the coupling between the atoms and specific quantized cavity modes. In the dispersive regime of light-matter interactions, the atoms behave as a polarizable medium and can scatter photons from external laser drives into the cavity. This yields dynamical optical potentials that can mediate nonlocal interactions between the atoms.

In a hallmark quantum-simulation experiment, the Dicke superradiant phase transition [59–61] was realized and observed in our laboratory [62]: two specific motional states of a quantum degenerate BEC are coupled via cavity-assisted Bragg scattering, inducing normal mode softening [63]. Above a critical coupling strength, the system undergoes a symmetry-breaking phase transition [64] and the BEC spontaneously self-organizes into a crystalline checkerboard structure favored by the interference potential between the external drive and the emergent cavity field. Since this optical potential, in turn, self-consistently depends on the atomic density distribution, it effectively mediates global-range interactions between the atoms. The observation of the Dicke phase transition has sparked a very active research field [58]: successful extensions have implemented extended Bose-Hubbard models with competing short-range and global-range interactions [65–67], a supersolid breaking a continuous translation symmetry [68], tunable-range interactions interfering near-degenerate cavity modes [69] and, very recently, density-wave order in non-interacting [70] and unitary Fermi gases [71]. In all these experiments, the different phases can be non-destructively detected by monitoring the light field leaking from the cavity mirrors. As a result, these experiments realize driven-dissipative systems where the inherent cavity losses not only modify the critical exponent of the Dicke transition [72], but also induce rich out-of-equilibrium dynamics [73–75].

Recently, there has been increased interest in addressing the internal *spin degrees of freedom* of atoms to explore collective magnetic phenomena induced by cavity-mediated spin interactions [76]. This can be achieved experimentally by exploiting the vectorial polarizability of the atoms [77] and coupling different magnetic sublevels through cavity-assisted two-photon transitions, i.e., *Raman transitions*. Two prominent examples include the observation of emergent global magnetic ordering induced by spin-dependent [78] and spin-changing self-organization [79] in two-component BECs. In the former, the interplay between coherent atom-light interactions and cavity dissipation can be further controlled to engineer persistent limit cycles between spin- and density-ordered phases [73]. In a parallel route, experiments coupling thermal atomic ensembles to optical cavities have also successfully implemented photon-mediated spin-exchange interactions between the atoms [80–83], and recently demonstrated spatial control over nonlocal spin-mixing dynamics [84]. In these experiments, the atomic ensemble is deeply confined in a superimposed intracavity lattice to optimize the overlap between the atoms and the cavity mode. Effective spin models can be derived by performing weighted averages over multiple thermally occupied external modes [85], yet quantitative comparison with theory can sometimes be challenging. With a handful of remarkable exceptions [86, 87], these experiments often focus on implementing asymptotically unitary Hamiltonian dynamics, rather than harnessing the rich interplay between coherent and dissipative processes that are intrinsic to optical cavities.

Scope, objectives and projects

In this thesis, we present a comprehensive approach for engineering and experimentally investigating emergent dissipative and coherent spin dynamics in degenerate quantum gases. In our experiments, we employ a ^{87}Rb BEC dispersively coupled to a high-finesse optical cavity. We harness strong vectorial atom-light interactions to induce cavity-assisted Raman transitions between different Zeeman sublevels of the hyperfine ground state manifold of the BEC. The fundamental building blocks of the dynamics studied here are *superradiant Raman scattering* processes: the indistinguishable atoms undergo a dissipative population inversion between two or more well-defined modes, while collectively scattering photons from external drives into the cavity. This mechanism yields nonlocal cavity-mediated spin interactions in our system and closely resembles collective spontaneous emission, also known as Dicke superradiance [88]. The central objectives of this work are:

- To develop suitable experimental schemes to couple specific internal and external modes of a BEC, and a single mode of an optical cavity.
- To achieve experimental control over collective dissipative and coherent processes, and probe the emergent dynamics in an inherently driven-dissipative setting. Our investigations aim to broaden the scope of our experiment beyond extensions of the Dicke model and atomic self-organization.
- To understand the observed phenomena at a microscopic level, complementing extensive theoretical modeling with newly developed experimental protocols and observables.

Within this thesis, these goals are pursued through three experimental and one complementary theoretical project.

In a first project [89], we build upon prior findings on atomic self-organization and realize a superradiant phase transition with tunable coherent and dissipative channels. The atoms are illuminated by two standing-wave transverse drives, inducing cavity-assisted Raman transitions, and coupling two spin and motional states of the BEC. Above a critical coupling, the system undergoes a superradiant phase transition accompanied by spontaneous spin-changing self-organization. By independently controlling the co- and counter-rotating light-matter interactions, we observe a dissipation-stabilized normal phase and a discontinuous superradiant transition, which we probe via hysteresis measurements. The mechanism underlying these dissipative phenomena is a collective decay channel of the hybrid light-matter excitations (polaritons), closely related to superradiant Raman scattering. We develop a cavity-enhanced Raman spectroscopy technique to monitor the excitation dynamics in real time: beyond observing the normal mode softening, we also measure increasingly shorter polariton lifetimes when unbalancing the co- and counter-rotating couplings, which we connect to the observed dissipative phases.

In a second set of experiments [90], we move beyond extended Dicke models and engineer dynamical tunneling processes in a synthetic lattice in momentum space. Using two phase-shifted transverse laser drives, we independently control superradiant Raman scattering between discrete momentum states of two spin manifolds. Within a tight-binding description, we interpret these scattering events as cavity-assisted hopping in a momentum-space lattice. In this regime, the inherent cavity losses render the emergent lattice dynamics directional. By employing frequency-resolved measurements of the leaking cavity field, we resolve individual tunneling events in real time. We experimentally verify that superradiant Raman scattering is indeed the underlying mechanism and examine the properties of collective hopping in our system. By adjusting the energy offset between the two spin manifolds, we extend our results to a regime exhibiting mutually stimulating tunneling cascades. These two projects illustrate how the cavity field spectrum is a well suited observable for probing both excitation and out-of-equilibrium dynamics, in real time and in a non-destructive fashion.

In a final experimental project [91], we engineer and directly observe the formation of nonlocal spin- and momentum-correlated atom pairs. For this purpose, we initialize a zero-momentum BEC in the central magnetic sublevel ($m = 0$) of the $F = 1$ hyperfine ground-state manifold, and drive cavity-assisted Raman transitions using a strong running-wave transverse drive. Correlated atom pairs in $m = +1$ and $m = -1$ with opposite net momenta along the drive direction are created via coherent exchange of virtual cavity photons. Owing to the strong light-matter interactions, we observe the formation of pairs within tens of microseconds. We report on the first observation of coherent pair oscillations involving well-defined momentum modes. While the system remains open due to spurious cavity leakage, we demonstrate independent control over the coherent pair dynamics and competing dissipative superradiant scattering. The pair production mechanism resembles parametric amplification in nonlinear optics, which we confirm by examining the scaling of the dynamics with the initial atom number. Our observations are in quantitative agreement with truncated Wigner simulations taking the vacuum fluctuations of our system into account. We characterize the pair quantum statistics and demonstrate their correlated nature by probing noise correlations in momentum space. Our results pave the way for a fast generation of entangled matter-wave pairs.

A natural extension of our experiments is to combine cavity-mediated spin interactions and Hubbard physics in optical lattices to explore emergent magnetic phenomena in strongly correlated regimes. In a dedicated theory project [92], we propose and theoretically investigate an extended Bose-Hubbard model. We consider a feasible experimental scheme wherein a balanced spin mixture is confined in an optical lattice and illuminated by a transverse drive with tunable polarization [78]. This configuration results in photon-mediated interactions favoring either global density or spin ordering of the atoms. We calculate the mean-field phase diagram and identify emergent density- and spin-ordered phases both in superfluid and insulating regimes. Notably, an antiferromagnetic insulator is favored for arbitrarily small atom-cavity couplings, and stabilized through the interplay of short- and global-range interactions. Furthermore, we examine the low-energy spectrum and discover a spin-exchange excitation branch with a tunable gap. To facilitate experimental implementation, we address potential challenges related to the immiscibility of the two spin components and the inhomogeneous density distributions in the experiment, while also discussing experimental parameters and observables.

Our results illustrate a comprehensive approach for engineering, controlling, and detecting emergent many-body spin dynamics in driven-dissipative settings. In particular, our pair production scheme offers a flexible mechanism to establish nonlocal correlations between specific modes of a degenerate quantum gas. As discussed in the outlook of this thesis, two concrete future directions in the context of quantum simulation include the realization of random spin models in momentum space and photon-mediated Cooper pairing in bosonic systems.

Outline of this thesis

- In *chapter 2*, we introduce the relevant theoretical framework to model the experiments discussed in this thesis. We review dispersive light-matter interactions in cavity systems, and introduce the concepts of the scalar and vectorial polarizability. The latter gives rise to cavity-assisted Raman transitions and superradiant Raman scattering in spinor BECs, which we theoretically examine using complementary analytical and numerical methods. To obtain a microscopic picture, we discuss the role of real and virtual cavity photons mediating dissipative and coherent processes in our system, respectively.

- *Chapter 3* focuses on our experimental setup and the relevant upgrades performed during the course of this thesis. We concisely review the experimental sequence, summarize the central properties of our high-finesse optical cavity, and discuss the different preparation and detection techniques. The analysis methods employed to evaluate the cavity field spectra are also discussed in detail. Moreover, we characterize the new laser setup, installed for driving cavity-assisted Raman transitions.

- In *chapter 4*, we investigate an extended Dicke model with tunable coherent and dissipative couplings. We examine the associated superradiant phase transition leading to emergent spin-changing self-organization. Experimentally, we access a dissipation-stabilized normal phase and a first order superradiant transition using hysteresis measurements. To gain a microscopic understanding, we characterize the evolution of the collective light-matter excitations (polaritons) using a newly developed cavity spectroscopy technique.

- In the experiments discussed in *chapter 5*, we engineer and experimentally observe dynamical tunneling in a synthetic momentum-space lattice. We discuss the coupling scheme, theoretical model and experimental protocol. By probing the cavity field spectra, we locally resolve the lattice dynamics. Furthermore, we experimentally verify that superradiant Raman scattering is indeed the underlying mechanism and extend our observations to a regime showcasing mutually stimulating hopping cascades.

- The experiments discussed in *chapter 6* demonstrate the generation of spin- and momentum-correlated atom pairs, mediated by the exchange of virtual cavity photons. After theoretically modeling the system, we present our observations of coherent pair oscillations and study the scaling of the pair dynamics with the atom number. Moreover, we demonstrate independent experimental control over competing coherent and dissipative processes. We investigate the pair quantum statistics and momentum-space correlations to gain additional insights into the pair dynamics. Finally, we address the challenges associated with observing quantum correlations in our system.

- In *chapter 7*, we theoretically investigate an extended Bose-Hubbard model incorporating cavity-mediated spin-dependent interactions. After presenting the coupling scheme, we map the system to a two-component lattice model. Using a Gutzwiller ansatz, we calculate the mean-field phase diagram and identify spin- and density-ordered superradiant phases, both in superfluid and insulating regimes. Additionally, we characterize the low-lying excitations using a perturbative approach. Finally, we discuss potential observables and parameters, and address experimental challenges.

- Finally, in *chapter 8*, we summarize our findings and outline future directions for our experiment. We discuss four concrete proposals ranging from Hubbard models incorporating cavity-assisted Raman transitions, to cavity-based detection techniques, and quantum simulation experiments leveraging the observed pair mechanism.

The work presented in this thesis has been carried out together with Fabian Finger, Francesco Ferri, Nicola Reiter, Panagiotis Christodoulou, Nishant Dogra, Katrin Kroeger, Jacob Fricke, Matteo Soriente, Oded Zilberberg, Rui Lin, R. Chitra, Leon Carl, Sebastian D. Huber, Tena Dubcek, Tobias Donner, and Tilman Esslinger.

2 Dispersive light-matter interactions and superradiant Raman scattering

Understanding and controlling atom-light interactions is essential for advancing the field of ultracold atomic gases. Laser cooling and trapping techniques, such as magneto-optical [93] and optical dipole traps [94], are nowadays routinely employed in hundreds of experiments to produce and manipulate quantum degenerate atomic gases. These techniques share the common feature that the incident laser beams can be approximated as classical fields that do not experience appreciable back-action from the atomic ensemble [95]. However, the situation is vastly different when the light fields are confined inside the small mode volume of a high-finesse optical cavity. The cavity alters the structure of the electromagnetic vacuum and significantly enhances the electric field of a discrete set of cavity eigenmodes. There, strong and tunable atom-light interactions can inherently be harnessed, involving quantized light fields comprising few photons [57].

The field of *cavity quantum electrodynamics* (cavity QED) has greatly evolved ever since the first observations of cavity-enhanced spontaneous decay by Purcell in 1946 [96], when probing radio-frequency magnetic transitions. Pioneering experiments using single Rydberg atoms interacting with microwave cavities have facilitated the observation of coherent Rabi oscillations [97] and quantum jumps [98] mediated by single photons, demonstrating the quantized nature of light. Similar cavity QED experiments have been conducted with resonant atom-light interactions in the optical regime, enabling the observation of normal mode splitting induced by the electromagnetic vacuum (vacuum Rabi splitting) using single atoms [99, 100], and more recently employing quantum degenerate bosonic [101] and fermionic gases [102].

In recent years, there have been significant advancements in the field of many-body cavity QED, particularly in the context of quantum simulation [57, 58]. A key focus of these developments is the engineering of strong and tunable light-matter interactions in the dispersive regime, when the incident light fields are detuned far from the relevant atomic resonances [95]. By combining dispersive interactions with optical cavities, the resulting optical dipole potentials become dynamical and mediate effective long-range interactions between the atoms. In a seminal experiment, the Dicke superradiant phase transition [59] was realized by exploiting the self-organization of a Bose-Einstein condensate in the dynamical potential of an optical cavity [62]. Extensions thereof have successfully demonstrated Hubbard models featuring competing short- and long-range interactions [65–67], and supersolids breaking continuous translation symmetries [68].

Recently, there has been a growing interest in utilizing cavity-assisted Raman transitions to address the atomic spin degrees of freedom and explore long-range magnetic phenomena with ultracold atoms. Remarkably, experiments have observed Dicke transitions that involve both spin-dependent interactions [78] and spin-changing self-ordering processes [79]. These advancements open up new possibilities for studying dynamical gauge fields, exotic magnetic phases and emergent spin dynamics in quantum gases coupled to optical cavities [76].

Outline of the chapter

In this chapter, we review dispersive atom-light interactions in a cavity QED system, with a specific focus on spin-changing processes induced by cavity-assisted Raman transitions in Bose-Einstein condensates (BECs). In section 2.1, we derive an effective description of dispersive atom-light interactions relying on the scalar and vectorial polarizability. For dominant vectorial interactions, we map the many-body BEC system to a Tavis-Cummings model featuring two well-defined atomic modes. In section 2.2, we discuss the role of cavity dissipation, and simulate the emergent dynamics using complementary numerical and analytic approaches. We identify a regime exhibiting collectively enhanced population inversion and scattering of cavity photons, referred to as *superradiant Raman scattering.* This phenomenon is the building block for the different experiments studied in this thesis. Finally, we discuss the role of real and virtual cavity photons mediating nonlocal dissipative and unitary spin-exchange dynamics in our system.

2.1 Light-matter interactions in the dispersive regime

Here, we review the theoretical framework of atom-light interactions in the dispersive regime. In section 2.1.1, we start by deriving an effective description for multi-level atoms based on the scalar and vectorial polarizability. In section 2.1.2, we further discuss the polarizability for the experimentally relevant case of ^{87}Rb atoms in the $F = 1$ ground state manifold. We extend our theoretical framework to describe dispersive atom-light interactions with the quantized field of an optical cavity in section 2.1.3. Finally, in section 2.1.4, we derive the many-body Hamiltonian for a two-component Bose-Einstein condensate interacting with a transverse drive and a single cavity mode, and map it to the paradigmatic Tavis-Cummings model.

2.1.1 From resonant to dispersive atom-light interactions

We consider the interactions between a single multi-level atom and an incident optical field. In its most general form, the Hamiltonian is given by

$$\hat{H}_{\mathrm{SP}} = \hat{H}_{\mathrm{at}} + \hat{H}_{\mathrm{light}} + \hat{H}_{\mathrm{int}}. \tag{2.1}$$

The first term describes the bare energy of a multi-level atom

$$\hat{H}_{\mathrm{at}} = \frac{\hat{p}^2}{2M} + \sum_{\mathrm{e}} \hbar\omega_{\mathrm{e}} \left|\mathrm{e}\right\rangle\!\left\langle\mathrm{e}\right| , \tag{2.2}$$

and contains both kinetic and internal energy contributions. The operator $\hat{p}$ describes the momentum of an atom with mass M. The different excited states $\left|\mathrm{e}\right\rangle$

have an internal energy of $\hbar\omega_{\mathrm{e}}$ above the ground-state manifold $|\mathrm{g}\rangle$, which we assume to be degenerate for clarity. The light field can contain both classical and quantized modes, with the bare energy of the latter given by

$$\hat{H}_{\text{light}} = \sum_j \hbar\omega_j \hat{a}_j^\dagger \hat{a}_j. \tag{2.3}$$

The operator $\hat{a}_j^\dagger$ creates a photon of energy $\hbar\omega_j$ in the quantized mode j.

As the size of electronic orbitals ($\sim 0.1\,\mathrm{nm}$) is significantly smaller than the typical optical wavelengths ($\lambda_{\mathrm{d}} \approx 800\,\mathrm{nm}$), we can perform the dipolar approximation [103], and write atom-light interactions as

$$\hat{H}_{\text{int}} = -\hat{\mathbf{d}} \cdot \hat{\mathbf{E}}, \tag{2.4}$$

with $\hat{\mathbf{E}}$ being the light's electric field operator. When driving the atom at a frequency ω_{d}, the associated electric dipole operator $\hat{\mathbf{d}}$ can be expanded in terms of the ground- and excited-state manifolds

$$\hat{\mathbf{d}} = \sum_{\mathrm{e,g}} \langle \mathrm{e}|\hat{\mathbf{d}}|\mathrm{g}\rangle \, |\mathrm{e}\rangle\langle \mathrm{g}| \, e^{-i\omega_{\mathrm{d}}t} + \text{h.c.}, \tag{2.5}$$

where $\langle \mathrm{e}|\hat{\mathbf{d}}|\mathrm{g}\rangle$ are the corresponding dipole matrix elements. We consider a semi-classical description of light, comprising a classical drive and multiple quantized light modes

$$\hat{\mathbf{E}} = \hat{\mathbf{E}}^{(-)} + \hat{\mathbf{E}}^{(+)} = \left(\frac{E_{\mathrm{d}}}{2} f(\mathbf{r}) \mathbf{e}_{\mathrm{d}} + \sum_j E_{0,j} g_j(\mathbf{r}) \hat{a}_j^\dagger \mathbf{e}_j \right) e^{-i\omega_{\mathrm{d}}t} + \text{h.c.}\ . \tag{2.6}$$

The classical drive has an electric field amplitude E_{d}, polarization $\mathbf{e}_{\mathrm{d}}$ and spatial mode structure $f(\mathbf{r})$. Accordingly, the variables $E_{0,j}$, $\mathbf{e}_j$ and $g_{\mathrm{k}}(\mathbf{r})$ define the vacuum electric field, polarization direction and spatial mode of the j-th quantized light mode. The negative $\hat{\mathbf{E}}^{(-)}$ and positive part $\hat{\mathbf{E}}^{(+)}$ of the electric field will account for co- and counter-rotating interactions, respectively.

The Rabi couplings between the different ground- and excited states are defined as $\Omega_{\mathrm{eg}} = -\langle \mathrm{e}|\hat{\mathbf{d}}|\mathrm{g}\rangle \, \hat{\mathbf{E}}^{(+)}/\hbar$. We perform a unitary transformation to a rotating frame at the drive frequency ω_{d} using the generator $\hat{H}_{\text{rot}} = \hbar\omega_{\mathrm{d}} \left(\sum_{\mathrm{e}} |\mathrm{e}\rangle\langle\mathrm{e}| + \sum_{\mathrm{j}} \hat{a}_{\mathrm{j}}^\dagger \hat{a}_{\mathrm{j}} \right)$. As the frequency of the optical drive ($\omega_{\mathrm{d}} \approx 2\pi \times 400\,\mathrm{THz}$) exceeds by orders of magnitude the achievable Rabi couplings ($|\Omega_{\mathrm{eg}}| \approx 2\pi \times 1\,\mathrm{kHz} - \mathrm{MHz}$), we can apply the rotating-wave approximation [104] and neglect rapidly oscillating terms $\propto e^{\pm 2i\omega_{\mathrm{d}}t}$. Thereby, we obtain a time-independent Hamiltonian

$$\hat{H}_{\text{SP}} = \frac{\hat{p}^2}{2M} - \sum_{\mathrm{e}} \hbar\delta_{\mathrm{e}} \, |\mathrm{e}\rangle \, \langle\mathrm{e}| - \sum_j \hbar\delta_j \hat{a}_j^\dagger \hat{a}_j + \sum_{\mathrm{e,g}} \hbar\Omega_{\mathrm{eg}} \, |\mathrm{e}\rangle\langle\mathrm{g}| + \hbar\Omega_{\mathrm{eg}}^* \, |\mathrm{g}\rangle\langle\mathrm{e}| \, . \tag{2.7}$$

In this rotating frame, both the energy of the excited internal states and the quantized light modes are determined by their detunings with respect to the drive field, i.e., $\delta_\mathrm{e} = \omega_\mathrm{d} - \omega_\mathrm{e}$ and $\delta_\mathrm{j} = \omega_\mathrm{d} - \omega_\mathrm{j}$, respectively. The interaction term in Eq. (2.7) coherently couples the ground $|\mathrm{g}\rangle$ and excited states $|\mathrm{e}\rangle$ at a rate $|\Omega_\mathrm{eg}|$.

In the *resonant regime* of atom-light interactions, the atomic detunings are small in comparison to the respective couplings ($|\delta_\mathrm{e}| \lesssim \Omega_\mathrm{eg}$), yielding coherent Rabi oscillations between the ground- and excited-state manifolds. In this thesis, we will consider light-matter interactions in the *dispersive regime*. There, the detuning between the driving field and the excited state greatly exceeds the Rabi frequency ($|\delta_\mathrm{e}| \gg \Omega_\mathrm{eg}$) and the excited-state linewidth ($|\delta_\mathrm{e}| \gg \gamma_\mathrm{e}$). The excited electronic states of the atom $|\mathrm{e}\rangle$ can be adiabatically eliminated, as their occupation probabilities are negligible [103]. In this off-resonant limit, the atom-light interactions can then be approximately written as

$$\hat{H}_\mathrm{int} = \sum_{j,k} \hat{\mathbf{E}}_j^{(-)} \hat{\alpha}_{j,k} \hat{\mathbf{E}}_k^{(+)}. \tag{2.8}$$

The polarizability tensor $\hat{\alpha}_{j,k} = \hat{\alpha}_s + \hat{\alpha}_v + \hat{\alpha}_t$ is a matrix (rank-2 tensor), which can be decomposed in scalar $\hat{\alpha}_s$, vectorial $\hat{\alpha}_v$ and tensorial contributions $\hat{\alpha}_t$ [77]. These are given by

$$\hat{\alpha}_s = \alpha_s \delta_{j,k} \hat{I}, \tag{2.9}$$

$$\hat{\alpha}_v = -i\frac{\alpha_v}{2F} \epsilon_{jkl} \hat{F}_l \tag{2.10}$$

$$\hat{\alpha}_t = \alpha_t \frac{3(\hat{F}_j\hat{F}_k + \hat{F}_k\hat{F}_j) - 2F^2\hat{I}\delta_{j,k}}{2F(2F-1)}, \tag{2.11}$$

with $\delta_{j,k}$ and ϵ_{jkl} being the Kronecker delta and Levi-Civita symbols, respectively. We describe the $2F+1$ different levels of the ground-state manifold $|\mathrm{g}\rangle$ with the angular momentum operator $\hat{\mathbf{F}}$ of length F. The *scalar* (α_s), *vectorial* (α_v) and *tensorial polarizabilities* (α_t) are fully determined by the internal structure of the atom and the frequency of the incident light field $\omega_\mathrm{d} = 2\pi c/\lambda_\mathrm{d}$, with λ_d being the corresponding wavelength, as discussed in the next section. The tensorial polarizability is negligible ($\alpha_t \approx 0$) for ^{87}Rb atoms in the electronic ground-state manifold and a laser drive at the typical experimental wavelength $\lambda_\mathrm{d} \approx 785 - 790$ nm [78].

In this limit, we can write the complete single-particle Hamiltonian as

$$\hat{H}_\mathrm{SP} = \frac{\hat{p}^2}{2M} - \sum_j \hbar\delta_j \hat{a}_j^\dagger \hat{a}_j + \alpha_s \hat{\mathbf{E}}^{(+)} \cdot \hat{\mathbf{E}}^{(-)} - i\frac{\alpha_v}{2F}\left(\hat{\mathbf{E}}^{(+)} \times \hat{\mathbf{E}}^{(-)}\right) \cdot \hat{\mathbf{F}}. \tag{2.12}$$

The Hamiltonian in Eq. (2.12) describes dispersive light-matter interactions in the ground-state manifold of a spin-F atom. This Hamiltonian encompasses two distinct types of interactions:

- Scalar processes ($\propto \alpha_s$) are independent of the atom's spin state and lead to an AC Stark shift of the ground-state manifold. The shift is proportional to the intensity of the incident light field ($\propto |\hat{\mathbf{E}}|^2$). In the presence of spatial modulation of the intensity, scalar light-matter interactions can be employed to confine atoms in optical dipole traps [95] and optical lattices [21].

- Vectorial processes ($\propto \alpha_v$) depend on the spin state of the atom $\hat{\mathbf{F}}$. They can be interpreted as a synthetic magnetic field $\hat{\mathbf{B}} = i\alpha_v(\hat{\mathbf{E}}^{(+)} \times \hat{\mathbf{E}}^{(-)})/(2F\mu_\mathrm{M})$ [105] determined by the electric fields at the position of the atom, with μ_M being the atomic magnetic moment. For a quantization axis along the z direction, these processes can give rise to either spin-dependent potentials ($\propto \hat{F}_z$) [78, 106] or to two-photon Raman processes ($\propto \hat{F}_{x,y}$) inducing coherent couplings between the different spin levels [107].

A detailed derivation of atom-light interactions in the dispersive regime can be also found in the PhD thesis of Nishant Dogra [108].

2.1.2 Scalar and vectorial polarizability for $F = 1$ ^{87}Rb atoms

In our experiments, we prepare a ^{87}Rb Bose-Einstein condensate in the $F = 1$ hyperfine manifold of the electronic ground state $5^2S_{1/2}$, and explore atom-light interactions in the dispersive regime employing the D-line doublet. We consider large atomic detunings δ_e that are much greater than the hyperfine splitting of the ground state ($\Delta_\mathrm{HFS} \approx 2\pi \times 6.834\,\mathrm{GHz}$) as well as the splittings of the two relevant excited states $5^2P_{1/2}$ ($\Delta_\mathrm{HFS} = 2\pi \times 816.7\,\mathrm{MHz}$) and $5^2P_{3/2}$ excited states ($\Delta_\mathrm{HFS} < 2\pi \times 266.7\,\mathrm{MHz}$) [109]. The transitions $5^2P_{1/2} \rightarrow 5^2P_{1/2}$ and $5^2P_{1/2} \rightarrow 5^2P_{3/2}$ are referred to as the D_1 and D_2 lines of ^{87}Rb, respectively. In this limit, the scalar and vectorial polarizabilities can be written as

$$\begin{aligned}
\alpha_s &= \frac{d_0^2}{3\hbar}\left(\frac{2}{\delta_2} + \frac{1}{\delta_1}\right), \\
\alpha_v &= -\frac{d_0^2}{3\hbar}\left(\frac{1}{\delta_2} - \frac{1}{\delta_1}\right),
\end{aligned} \tag{2.13}$$

with $d_0 = 2.538 \times 10^{-29}\,\mathrm{C\,m}$ being the dipole transition matrix element of the D_1 line [77, 95]. The atomic detunings between the laser drive and the D_1 and D_2 lines are given by $\delta_1 = \omega_\mathrm{d} - \omega_{\mathrm{D}_1}$ and $\delta_2 = \omega_\mathrm{d} - \omega_{\mathrm{D}_2}$, respectively. In Fig. 2.1(a), we plot the scalar (α_s) and vectorial (α_v) polarizabilities for different drive wavelengths $\lambda_\mathrm{d} = 2\pi c/\omega_\mathrm{d}$. Both α_s and α_v diverge in the vicinity of the D_2 ($\lambda_{\mathrm{D}_2} = 780.247$ nm) and D_1 lines ($\lambda_{\mathrm{D}_1} = 794.979$ nm), where the dispersive treatment of light-matter interactions becomes invalid. When the detunings are much larger than the fine-structure splitting between the D_2 and D_1 lines, $|\delta_{1,2}| \gg (\omega_{\mathrm{D2}} - \omega_{\mathrm{D1}}) = \Delta_\mathrm{FS}$, the scalar polarizability simplifies to the expression for a two-level system, given by $\alpha_s \approx d_0^2/(\hbar\delta)$, where $\delta = \delta_2 \approx \delta_1$. In this case, the vectorial polarizability becomes negligible ($\alpha_v \approx 0$). Conversely, the laser drive should resolve the fine-structure splitting, in order to induce appreciable vectorial light-matter interactions. This is indeed the case for the two drive wavelengths employed in our experiments

As shown in Fig. 2.1(a) and Tab. 2.1, the scalar polarizability vanishes at $\lambda_\mathrm{TO} = 790.01858$ nm [110], the *tune-out wavelength* of ^{87}Rb in the $F = 1$ manifold. This is due to a complete compensation of the AC Stark shifts arising from the D_2 (red) and D_1 lines (blue detuned drive). Since α_v retains a finite value at λ_TO, we can induce cavity-mediated vectorial interactions while minimizing potentially detrimental effects arising from the scalar polarizability, such as optical dipole traps and

λ_d(nm)	784.700	790.019
α_s $(\mathrm{CV^{-1}m^2})$	-2.298×10^{-37}	0
$\alpha_v/2(\mathrm{CV^{-1}m^2})$	1.066×10^{-37}	1.025×10^{-37}

Table 2.1: Scalar (α_s) and vectorial polarizabilities (α_v) for $\lambda_\mathrm{d} = 784.700$ nm (chapters 4 and 5) and $\lambda_\mathrm{d} = 790.019$ nm (chapter 6).

cavity-induced atomic self-organization [62]. This is especially important for the experiments outlined in chapter 6, as the drive is operated at large laser powers.

2.1.3 Cavity QED with dispersive atom-light interactions

In the experiments discussed in this thesis, we couple a ^{87}Rb BEC in the $F = 1$ ground-state manifold to the fundamental mode of high-finesse optical cavity. The technical details of the experimental sequence and optical cavity setup can be found in sections 3.1.1 and 3.1.2, respectively.

In the simplest configuration, the atoms are illuminated by a single far-detuned transverse laser drive with frequency ω_d. The drive propagates in the z direction, has linear polarization along the y axis, and an electric field amplitude E_d, as depicted in Fig. 2.1(b). The atoms are coupled to the fundamental mode of an optical cavity that extends along the x axis and consists of two orthogonal linear polarizations, z and y. The negative component of the total electric field can be expressed as

$$\hat{\mathbf{E}}^{(-)} = \frac{E_\mathrm{d}}{2} f(z) e^{-i\omega_d t} \mathbf{e}_y + E_0 g(x) \hat{a}_z \mathbf{e}_z + E_0 g(x) \hat{a}_y \mathbf{e}_y, \tag{2.14}$$

with $g(x) = \cos(kx)$ and E_0 defining the standing-wave cavity mode and the electric field per cavity photon. The bosonic operators $\hat{a}_z$ and $\hat{a}_y$ annihilate photons in the corresponding modes. We assume a common wavenumber for the cavity and transverse drive modes $k = \omega_\mathrm{d}/c$, as the drive frequency and the cavity resonance only differ by $\sim 2\pi \times 10\,\mathrm{MHz}$. The transverse drive mode structure is kept as a variable $f(z)$, as the drive can be employed both in a running-wave $f(z) = e^{ikz}$ and standing-wave configuration $f(z) = \cos(kz)$, see section 3.3.2.

We consider a magnetic field B oriented along the z direction, which defines the quantization axis. Using Eq. (2.12), we derive the Hamiltonian for a single atom dispersively coupled to an optical cavity

$$\begin{aligned}
\hat{H}_{\mathrm{SP}} &= \hat{H}_0 + \hat{H}_s + \hat{H}_v \quad \text{with,} \\
\hat{H}_0 &= \frac{\hat{p}^2}{2M} + \hbar\omega_z \hat{F}_z + \hbar q \hat{F}_z^2 - \hbar\delta_c \sum_{j=\{z,y\}} \hat{a}_j^\dagger \hat{a}_j, \\
\hat{H}_s &= \alpha_s \hat{\mathbf{E}}^{(+)} \cdot \hat{\mathbf{E}}^{(-)} \\
&= \alpha_s \frac{E_{\mathrm{d}}^2}{4} |f(z)|^2 + \alpha_s E_0^2 g^2(x) \left(\hat{a}_z^\dagger \hat{a}_z + \hat{a}_y^\dagger \hat{a}_y \right) + \alpha_s \frac{E_{\mathrm{d}} E_0}{2} g(x) \left[f(z) \hat{a}_y^\dagger + f(z)^* \hat{a}_y \right], \\
\hat{H}_v &= -i \frac{\alpha_v}{2F} \left(\hat{\mathbf{E}}^{(+)} \times \hat{\mathbf{E}}^{(-)} \right) \cdot \hat{\mathbf{F}} \\
&= i\alpha_v \frac{E_{\mathrm{d}} E_0}{4} g(x) \left[f(z) \hat{a}_z^\dagger - f(z)^* \hat{a}_z \right] \hat{F}_x + i\alpha_v \frac{E_0^2}{2} g^2(x) \left(\hat{a}_z^\dagger \hat{a}_y - \hat{a}_y^\dagger \hat{a}_z \right) \hat{F}_x.
\end{aligned} \tag{2.15}$$

In consists of three different contributions:

- The Hamiltonian $\hat{H}_0$ describes the bare energy of atom and cavity field. The linear and quadratic Zeeman splittings are given by $\omega_z/B = -2\pi \times 700\,\mathrm{kHz/G}$ and $q/B^2 = 2\pi \times 72\,\mathrm{Hz/G}^2$ [34], respectively, with $\hat{\mathbf{F}} = (\hat{F}_x, \hat{F}_y, \hat{F}_z)^T$ being the spin operator for the $F = 1$ manifold. We consider the system in a rotating frame at ω_{d}, such that the energy of the two cavity modes[1] is determined by their detuning with respect to the drive $\delta_{\mathrm{c}} = \omega_{\mathrm{d}} - \omega_{\mathrm{c}}$.

- The Hamiltonian $\hat{H}_s$ captures atom-light interactions mediated by the scalar polarizability. Its first contribution describes the AC stark shift induced by the transverse drive. For a standing-wave configuration, $|f(z)|^2 = \cos^2(kz)$, this gives rise to an optical lattice at the position of the atom with lattice depth $V_{\mathrm{d}} = -\alpha_s E_{\mathrm{d}}^2/4$. The second contribution yields a dynamical intra-cavity optical lattice $[g^2(x) = \cos^2(kx)]$ with a lattice depth proportional to the number of cavity photons. This term can also be interpreted as a *dispersive shift* of the corresponding cavity resonances [108], which is modulated in space and has a maximal value of $U_0 = \alpha_s E_0^2/\hbar$. The third term in $\hat{H}_s$ describes the interference potential between drive and the y-polarized cavity mode. For a standing-wave drive, $f(x) = \cos(kz)$, this term gives rise to a dynamical checkerboard potential $\propto (\hat{a}_y + \hat{a}_y^\dagger)\cos(kx)\cos(kz)$ coupling to the real quadrature of the y-polarized cavity field. Such scalar light-matter interactions have been successfully employed to realize the Dicke superradiant phase transition in our experiment [62].

- Finally, the Hamiltonian $\hat{H}_v$ captures the vectorial light-matter interactions. The first term describes *cavity-assisted Raman transitions* that change the internal spin state of the atom ($\propto \hat{F}_x$) while scattering a photon from the drive into the z-polarized cavity mode ($\hat{a}_z^\dagger$) or vice versa ($\hat{a}_z$). During such two-photon transitions, the atom acquires recoil momenta in both the drive and

---

[1] For clarity, we neglect here the birefringence between the z-and y- polarized cavity modes, which is on the order of $2\pi \times 2.2$ MHz and consider a common resonance frequency ω_{c}.

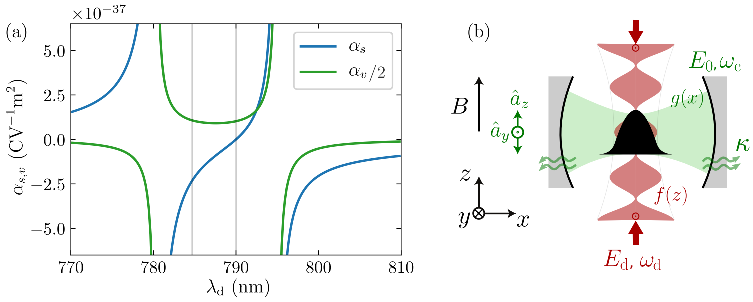

Figure 2.1: Dispersive atom-light interactions in an optical cavity. **(a)** Scalar (α_s) and vectorial polarizabilities (α_v) for ^{87} Rb atoms in the $F = 1$ hyperfine manifold as function of the drive wavelength λ_d. Our experiments are performed either at 784.700 nm or 790.019 nm, as indicated by the gray lines. For the exact numerical values, see Tab. 2.1. **(a)** Schematic representation of the experimental setup, depicting a quantum gas (black shape) coupled to the fundamental mode of a high-finesse optical cavity with a spatial mode profile $g(x)$ and two orthogonal linear polarizations (photon annihilation operators $\hat{a}_{y,z}$). The cavity has a resonance frequency of ω_c and an electric field per photon of E_0. The atoms are illuminated by a y-polarized transverse drive, with frequency ω_d and electric field amplitude E_d. The drive propagates along z and has a mode profile of $f(z)$. A magnetic field along z defines the quantization axis.

cavity directions, reflecting the spatial structure of the underlying interference potential $g(x)f(z)$. Cavity-assisted Raman transitions play a crucial role in this work and form the basis for the experiments discussed in the following chapters. The second term in $\hat{H}_v$ accounts for Raman transitions induced by scattering photons between the y- and z-polarized cavity modes. In our experiment, these contributions can be neglected since $E_\mathrm{d} \gg E_0$ and $|\delta_\mathrm{c}| \neq |\omega_z|$ [108].

2.1.4 Many-body description and the Tavis-Cummings Hamiltonian

This section presents the derivation of the effective many-body Hamiltonian of a spinor Bose-Einstein condensate dispersively coupled to an optical cavity by a transverse laser drive. We neglect scalar atom-light interactions ($\alpha_s = 0$), which can be experimentally achieved by operating the drive at the tune-out wavelength λ_TO. Thereby, we simplify the single-particle Hamiltonian in Eq. (2.15) to

$$\hat{H}_\mathrm{SP} = -\hbar\delta_\mathrm{c}\hat{a}^\dagger\hat{a} + \frac{\hat{p}^2}{2M} + \hbar\omega_z\hat{F}_z + \hbar q\hat{F}_z^2 + i\alpha_v\frac{E_\mathrm{d}E_0}{4}\cos(kx)\cos(kz)[\hat{a}^\dagger - \hat{a}]\hat{F}_x. \tag{2.16}$$

For clarity, we assume standing-wave mode profiles both for the cavity and transverse drive fields, with $g(x) = \cos(kx)$ and $f(z) = \cos(kz)$, respectively. In Eq. (2.16), we disregard the y-polarized cavity mode as it can be only occupied by the scalar processes ($\alpha_s = 0$), and introduce the shorthand notation $\hat{a} := \hat{a}_z$.

We extend our analysis to a many-body system, considering a spinor Bose-Einstein condensate consisiting of indistinguishable atoms, dispersively coupled to the cavity.

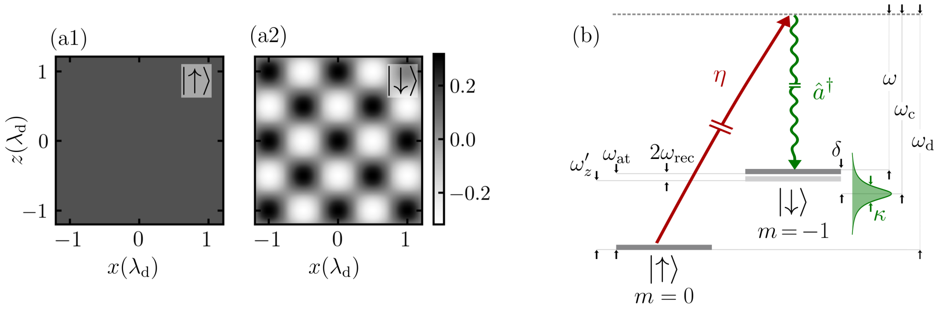

Figure 2.2: Mapping of the Tavis-Cummings model. **(a)** Spatial profile of the relevant modes. The mode $|\uparrow\rangle$ is captured by the homogeneous single-particle wave function $\psi_0 \propto 1$ in the $m = 0$ Zeeman sublevel (a1), whereas the mode $|\downarrow\rangle$ in $m = -1$ is spatially modulated, i.e., $\psi_{-1} \propto \cos(kx)\cos(kz)$ with $k = 2\pi/\lambda_{\mathrm{d}}$ (a2). **(b)** Level scheme. In the lab frame, the separation between the two modes ω_{at} arises from the effective Zeeman splitting $\omega_z' = -\omega_z + q$ and the photon recoil frequency ω_{rec}. In a suitable rotating frame at ω_{at}, the system is described by the Tavis-Cummings Hamiltonian, cf. Eq. (2.19), which is fully parameterized by the Raman coupling η and the two-photon detuning δ between a resonant cavity-assisted Raman transition (ω) and the cavity resonance (ω_c). The drive frequency and the decay rate of the cavity field are ω_{d} and κ, respectively.

We perform a two-mode expansion of the underlying spin-1 atomic field operator

$$\hat{\Psi}(\mathbf{x}) = \Big(\hat{\Psi}_{+1}(\mathbf{x}),\, \hat{\Psi}_0(\mathbf{x}),\, \hat{\Psi}_{-1}(\mathbf{x})\Big)^T = \Big(0,\;\psi_0(x,z)\hat{c}_\uparrow,\;\psi_{-1}(x,z)\hat{c}_\downarrow\Big)^T, \qquad (2.17)$$

fulfilling the commutation relations for indistinguishable bosons $[\hat{\Psi}_j(\mathbf{x}), \hat{\Psi}_k^\dagger(\mathbf{x}')] = \delta_{jk}\delta(\mathbf{x}-\mathbf{x}')$ with $j, k = \{+1, 0, -1\}$. For conciseness, we operate at sufficiently large second-order Zeeman splitting $\hbar q \gg \alpha_v E_{\mathrm{d}} E_0$ [89] and neglect the occupation of the $m = +1$ Zeeman sublevel, i.e., $\hat{\Psi}_{+1}(\mathbf{x}) = 0$. As such, we can effectively reduce the system to an effective spin-1/2 system occupying two well-defined modes, $|\downarrow\rangle$ and $|\uparrow\rangle$, in the remaining Zeeman sublevels $m = -1$ and $m = 0$. The operators $\hat{c}_\downarrow$ and $\hat{c}_\uparrow$ annihilate atoms in the modes $|\downarrow\rangle$ and $|\uparrow\rangle$, respectively.

Within our two-mode expansion, we consider a scenario where the BEC is initially prepared in the $m = 0$ Zeeman sublevel. The BEC is a quantum degenerate gas, where all the atoms occupy to very good approximation a zero-momentum single-particle state [111], which we label as $|\uparrow\rangle$ and describe by the homogeneous wave function $\psi_0(x, z) = \frac{k}{2\pi}$ in the xz-plane. The $m = -1$ Zeeman sublevel can only be populated via cavity-assisted Raman transitions from the $m = 0$ state. During these processes, the atoms acquire symmetrically photon recoil momentum $\pm\hbar k$ along the drive (k_z) and cavity (k_x) directions. As a result, the atoms exhibit a spatial modulation associated with the interference potential of the two light fields in real space, proportional to $g(x)f(z) = \cos(kx)\cos(kz)$. This motivates the definition of the single-particle wave function $\psi_{-1}(x, z) = \frac{k}{\pi}\cos(kx)\cos(kz)$ for atoms in the $m = -1$ Zeeman sublevel, which we refer to as mode $|\downarrow\rangle$. These wave functions are normalized within a unit cell of size $\mathcal{R} = [-\pi/k, \pi/k)^2$, and are plotted in Fig. 2.2(a). In momentum space, the two wave functions can be written as $\psi_0(k_x, k_z) = |k_x = 0, k_z = 0\rangle$

and $\psi_{-1}(k_x, k_z) = 1/2(|{+k}, {+k}\rangle + |{-k}, {+k}\rangle + |{+k}, {-k}\rangle + |{-k}, {-k}\rangle)$. The latter describes a symmetric superposition of $\pm\hbar k$-momentum states along the drive and cavity direction, and inherits its spatial symmetry directly from the drive-cavity interference potential $g(x)f(z) = \cos(kx)\cos(kz)$.

Resorting to second quantization [112], we derive the many-body Hamiltonian

$$\begin{aligned}\hat{H}_{\mathrm{MB}} = &-\hbar\delta_{\mathrm{c}}\hat{a}^\dagger\hat{a}\\ &+\int_{\mathcal{R}}\hat{\Psi}^\dagger(\mathbf{x})\left[\frac{\hat{p}^2}{2M}+\hbar\omega_z\hat{F}_z+\hbar q\hat{F}_z^2+i\frac{\alpha_v E_{\mathrm{d}}E_0}{4}\cos(kx)\cos(kz)(\hat{a}^\dagger-\hat{a})\hat{F}_x\right]\hat{\Psi}(\mathbf{x})d\mathbf{x},\\ &= -\hbar\delta_{\mathrm{c}}\hat{a}^\dagger\hat{a}+\hbar(-\omega_z+q+2\omega_{\mathrm{rec}})\hat{c}_\downarrow^\dagger\hat{c}_\downarrow+i\hbar\eta(\hat{a}^\dagger-\hat{a})(\hat{c}_\downarrow^\dagger\hat{c}_\uparrow+\hat{c}_\uparrow^\dagger\hat{c}_\downarrow),\\ &= -\hbar\delta_{\mathrm{c}}\hat{a}^\dagger\hat{a}-\hbar\omega_{\mathrm{at}}\hat{J}_z+\hbar\eta(\hat{a}^\dagger+\hat{a})(\hat{J}_-+\hat{J}_+).\end{aligned} \tag{2.18}$$

The state in $m = -1$ with density modulation has a higher energy compared to its $m = 0$ counterpart, primarily due to the negative linear Zeeman splitting $\omega_z < 0$. Furthermore, the total energy splitting between the two modes $-\hbar\omega_{\mathrm{at}} = \hbar(-\omega_z + q + 2\omega_{\mathrm{rec}})$ includes the kinetic energy resulting from the photon recoil momenta imparted on the atoms by the Raman process, as sketched in Fig. 2.2(b). The corresponding photon recoil frequency is given by $\omega_{\mathrm{rec}} = \hbar k^2/(2M)$. We define the Raman coupling strength as $\eta = \sqrt{2}\alpha_v E_{\mathrm{d}} E_0/8$. In the last line of Eq. (2.18), we introduce the pseudo spin-$N/2$ algebra $\hat{\mathbf{J}}$, with $\hat{J}_z = (\hat{c}_\uparrow^\dagger\hat{c}_\uparrow - \hat{c}_\downarrow^\dagger\hat{c}_\downarrow)/2$, $\hat{J}_- = \hat{c}_\downarrow^\dagger\hat{c}_\uparrow$ and $\hat{J}_+ = \hat{c}_\uparrow^\dagger\hat{c}_\downarrow$. These operators satisfy the canonical commutation relations for angular momentum operators, e.g., $[\hat{J}_z, \hat{J}_+] = \hat{J}_+$. Additionally, we consider a global phase rotation of the cavity field $\hat{a} \to \hat{a}e^{i\pi/2}$ and a shift of the zero-point energy of the system by $\hbar\omega_{\mathrm{at}}(\hat{c}_\downarrow^\dagger\hat{c}_\downarrow + \hat{c}_\uparrow^\dagger\hat{c}_\uparrow)/2$.

For our experimental parameters, the bare mode splittings $\omega_{\mathrm{at}} \approx \omega_z = -2\pi \times 10 - 50\mathrm{MHz}$ are orders of magnitude larger than the achievable Raman couplings $\eta \lesssim 2\pi \times 1\,\mathrm{kHz}$. As a result, two-photon transitions mediated by a cavity field at the frequency of the transverse drive ω_{d} are effectively suppressed. However, due to the finite linewidth of the cavity mode, the cavity field is not restricted to a single frequency and can accommodate multiple spectral components. To address this, we shift the cavity field close to resonance with the expected two-photon process. We introduce a rotating frame transformation induced by the generator $\hat{H}_{\mathrm{rot}} = -\hbar\omega_{\mathrm{at}}(\hat{a}^\dagger\hat{a} + \hat{J}_z)$, and derive the many-body Hamiltonian

$$\hat{H}_{\mathrm{MB}} = -\hbar\delta\hat{a}^\dagger\hat{a} + \hbar\eta\left(\hat{a}^\dagger\hat{J}_- + \hat{a}\hat{J}_+\right), \tag{2.19}$$

after performing the rotating-wave approximation. In this rotating frame, the two atomic modes become degenerate and the many-body Hamiltonian is fully parameterized by the Raman coupling η and the effective two-photon detuning $\delta := \delta_{\mathrm{c}} + \omega_{\mathrm{at}} = (\omega_{\mathrm{d}} + \omega_{\mathrm{at}}) - \omega_{\mathrm{c}}$. As illustrated in Fig. 2.2(b), the variable δ quantifies the detuning between cavity resonance ω_c and the frequency of the cavity field required to drive resonant two-photon transitions

$$\omega = \omega_{\mathrm{d}} + \omega_{\mathrm{at}}. \tag{2.20}$$

Crucially, the cavity field becomes stationary (time independent) at this frequency and carries an excess energy of ω_{at} in comparison to the drive field ω_{d}. This ensures total energy conservation in the light-matter system, as the energy of the atoms changes by $-\omega_{\mathrm{at}}$ when undergoing a cavity assisted Raman transition between the modes $|\uparrow\rangle \rightarrow |\downarrow\rangle$. The many-body Hamiltonian derived in Eq. (2.19) constitutes a dispersive implementation of the paradigmatic Tavis-Cummings model [113], which describes an ensemble of N indistinguishable two-level atoms interacting with a quantized mode of the electromagnetic field.

2.2 Superradiant Raman scattering

Our considerations so far have treated light-matter interactions as purely unitary processes generated by suitable Hamiltonians. However, an ensemble of atoms coupled to an optical cavity is inherently a many-body open quantum system. This is because the associated cavity field leaks from mirrors at a rate κ. Additionally, atomic dissipation can occur in the form of excited-state decay with a rate Γ.

The Tavis-Cummings model introduced in Eq. (2.19) can operate in two relevant limits.

- In the *strong-coupling limit*, the collective atom-light interactions exceed all relevant dissipation scales, $\sqrt{N}\eta \gg \kappa, \Gamma$, and quantum mechanical effects become pronounced. Experiments operating in this regime have resolved the vacuum Rabi splitting for single atoms [100] and degenerate quantum gases [101, 102].

- In the *bad cavity limit*, the decay rate of the cavity field significantly exceeds the strength of atom-light interactions and atomic dissipation, i.e., $\kappa \gg \sqrt{N}\eta$ and $\kappa \gg \Gamma$. Experiments operating in this regime are particularly interesting in the context of cavity-assisted cooling [114] and superradiant lasers [86].

In this thesis, we consider cavity-assisted Raman transitions within the dispersive regime, with our experiment operating in the bad cavity limit. In this regime, the cavity decay rate $\kappa = 2\pi \times 1.25\,\mathrm{MHz}$ greatly exceeds the collectively enhanced atom-light interactions, $\sqrt{N}\eta \lesssim 2\pi \times 0.3\,\mathrm{MHz}$, for typical atom numbers $N \lesssim 90000$ and two-photon coupling rates $\eta \lesssim 2\pi \times 0.001\,\mathrm{MHz}$. Additionally, spontaneous decay between the different Zeeman sublevels of the electronic ground-state manifold is negligible ($\Gamma = 0$), guaranteeing $\kappa \gg \Gamma$. It is worth noting that our experiment can also operate in the strong-coupling limit for individual atoms when considering resonant light-matter interactions [115]. In that regime, the large atom-light coupling rates, $g_0 \approx 2\pi \times 10.3\,\mathrm{MHz}$, dominate over κ and $\Gamma = 2\pi \times 6.1\,\mathrm{MHz}$ [109], facilitating the observation of the experimental observation of vacuum Rabi splitting [101].

In this section, we investigate the dynamics of an open Tavis Cummings system operating in the bad cavity limit. In section 2.2.1, we derive equations of motion for the open system. We observe superradiant Raman scattering accompanied by a collective spin decay, which we diagnose by analytically solving the mean-field equations of motion in Eq. (2.2.2). To further validate our results, we present exact solutions for small system sizes in section 2.2.3. Finally, in section 2.2.4, we discuss the role of real and virtual cavity photons mediating dissipative and coherent nonlocal dynamics in our system.

2.2.1 Equations of motion of the open quantum system

Due to photons leaking out of the cavity, our light-matter system is inherently coupled to the environment. We assume Markovian dissipation [2], and can describe the system by means of a Lindblad master equation [116, 117] starting from the Tavis-Cummings Hamiltonian in Eq. (2.19). We obtain

$$\frac{d\hat{\rho}}{dt} = -\frac{i}{\hbar}\left[\hat{H}_{\mathrm{MB}}, \hat{\rho}\right] + \mathcal{L}[\hat{\rho}, \hat{a}] = -\frac{i}{\hbar}\left[\hat{H}_{\mathrm{MB}}, \hat{\rho}\right] + \kappa[2\hat{a}\hat{\rho}\hat{a}^{\dagger} - \{\hat{a}^{\dagger}\hat{a}, \hat{\rho}\}], \tag{2.21}$$

with $\hat{\rho}$ being the density matrix of the atom-cavity system [118], and $[\hat{A}, \hat{B}] = \hat{A}\hat{B} - \hat{B}\hat{A}$ ($\{\hat{A}, \hat{B}\} = \hat{A}\hat{B} + \hat{B}\hat{A}$) defining the quantum-mechanical commutator (anticommutator) for arbitrary operators $\hat{A}$ and $\hat{B}$. The Lindblad operator $\mathcal{L}[\hat{\rho}, \hat{a}]$ describes the dissipative contributions to the dynamics associated with a cavity field decay rate κ. We do not consider direct atomic decay between the modes $\hat{c}_{\uparrow}$ and $\hat{c}_{\downarrow}$, as spontaneous emission between Zeeman sublevels of the same hyperfine manifold is negligible. In order to model the evolution of relevant observables, we derive Heisenberg equations of motion (EOMs) for the photonic and atomic operators of the open system

$$\begin{aligned}
\frac{d\hat{a}}{dt} &= \frac{i}{\hbar}[\hat{H}_{\mathrm{MB}}, \hat{a}] + \mathcal{L}[\hat{a}, \hat{a}] = (i\delta - \kappa)\hat{a} - i\eta(\hat{J}_x - i\hat{J}_y), \\
\frac{d\hat{J}_x}{dt} &= \frac{i}{\hbar}[\hat{H}_{\mathrm{MB}}, \hat{J}_x] = i\eta(\hat{a} - \hat{a}^{\dagger})\hat{J}_z, \\
\frac{d\hat{J}_y}{dt} &= \frac{i}{\hbar}[\hat{H}_{\mathrm{MB}}, \hat{J}_y] = -\eta(\hat{a} + \hat{a}^{\dagger})\hat{J}_z, \\
\frac{d\hat{J}_z}{dt} &= \frac{i}{\hbar}[\hat{H}_{\mathrm{MB}}, \hat{J}_z] = \eta(\hat{a} + \hat{a}^{\dagger})\hat{J}_y - i\eta(\hat{a} - \hat{a}^{\dagger})\hat{J}_x,
\end{aligned} \tag{2.22}$$

where $\hat{J}_x = (\hat{J}_+ + \hat{J}_-)/2$ and $\hat{J}_y = i(\hat{J}_- - \hat{J}_+)/2$ define the x- and y-projection of the pseudo-spin operator $\hat{\mathbf{J}}$.

We introduce normalized expectation values for the cavity field $\alpha = \langle\hat{a}\rangle/\sqrt{N}$ and the different projections of the spin operators $j_l = \langle\hat{J}_l\rangle/N$, where N is the total atom number and $l \in \{x, y, z\}$. In the limit of large particle numbers $N \to \infty$, we assume a decoupling between the different operators[3] $\langle\hat{A}\hat{B}\rangle \approx \langle\hat{A}\rangle\langle\hat{B}\rangle$. In this limit, we derive mean-field equations of motion for the open Tavis-Cummings model

---

[2] In Markovian processes, the effect of the environment on the system depends only its current state, and not on its history [116]. This is the case when the characteristic correlation time of the environment is much smaller than the typical timescales of the system's evolution.

[3] This mean-field approximation disregards fluctuations of all operators, such as $\mathrm{std}(\hat{A})/N \to 0$, which we generally expected to vanish in the limit $N \to \infty$. For finite N, the fluctuation dynamics can be quantitatively captured by considering higher-order cumulant expansion [119].

$$\begin{aligned}\frac{d\alpha}{dt} &= (i\delta-\kappa)\alpha - i\sqrt{N}\eta(j_x - ij_y),\\ \frac{dj_x}{dt} &= i\sqrt{N}\eta(\alpha-\alpha^*)j_z,\\ \frac{dj_y}{dt} &= -\sqrt{N}\eta(\alpha+\alpha^*)j_z,\\ \frac{dj_z}{dt} &= \sqrt{N}\eta(\alpha+\alpha^*)j_y - i\sqrt{N}\eta(\alpha-\alpha^*)j_x.\end{aligned} \tag{2.23}$$

The collective nature of light-matter interactions in the Tavis-Cummings model is already visible in Eq. (2.23), as the interaction strength scales with atom number ($\sqrt{N}\eta$), while the normalized expectation values of the spin operator remain of order $\mathcal{O}(1)$ due to $j_x^2 + j_y^2 + j_z^2 = 1/4$. This $\sqrt{N}$-scaling of the light-matter interactions is at the heart of collective phenomena, such as Dicke superradiance [88, 120] as discussed in detail in the next section.

Numerical simulations of equations of motion

We numerically evolve the mean-field equations of motion using the MATLAB built-in 'ode45' solver which is based on a Runge-Kutta (4,5) method [121]. It employs variable time step sizes and the error tolerance in each step is constrained to 10^{-8}. To sample the fluctuations on top of the mean-field observables, we assume an initially small photon field of the form $\alpha(t=0) = [\mathrm{randn}(0,0.5) + i\cdot\mathrm{randn}(0,0.5)]/\sqrt{N}$ with pseudo-random numbers $\mathrm{randn}(0,0.5)$ sampled from a normal distribution with (μ,σ)=(0,0.5). This assumption is compatible with an initial coherent vacuum state for the cavity field, as $\left\langle\sqrt{N}(\alpha+\alpha^*)/2\right\rangle = 0$ and $\mathrm{var}_S\left(\sqrt{N}(\alpha+\alpha^*)/2\right) = 1/4$, where $\langle\rangle_S$ and var_S denote the average and variance over a sufficiently large number of samples $S \gtrsim 200$.

2.2.2 Diagnosing superradiant Raman scattering

In this section, we discuss the solutions of the mean-field EOMs in our system. When initialized in the unstable mode $|\uparrow\rangle$, the system exhibits a collectively enhanced population inversion. We investigate the evolution of the associated superradiant cavity pulses for different atom numbers, and compare them to an analytic estimate. The results obtained in this section provide the theoretical foundations to assess superradiant Raman scattering in our system.

We numerically solve the mean-field equations of motion (EOMs) in Eq. (2.23) for typical experimental parameters: $\kappa = 2\pi\times 1.25\,\mathrm{MHz}$, $\eta = 2\pi\times 1\,\mathrm{kHz}$, and an initial state with $N = 50,000$ atoms prepared in the $|\uparrow\rangle$ state. We choose to operate at cavity resonance, $\delta = 0$. In this parameter regime, the system is deep in the bad cavity limit with $\kappa \gg \sqrt{N}\eta$. In Fig. 2.3(a), we show the time evolution of the normalized spin imbalance $j_z(t)$ and the mean number of cavity photons $n_{\mathrm{ph}}(t) = \langle\hat{a}^\dagger\hat{a}\rangle \approx N\alpha^*\alpha$. We observe a complete population inversion from $|\uparrow\rangle$ to $|\downarrow\rangle$ ($j_z = 1/2 \to -1/2$) within few milliseconds, accompanied by a transient pulse

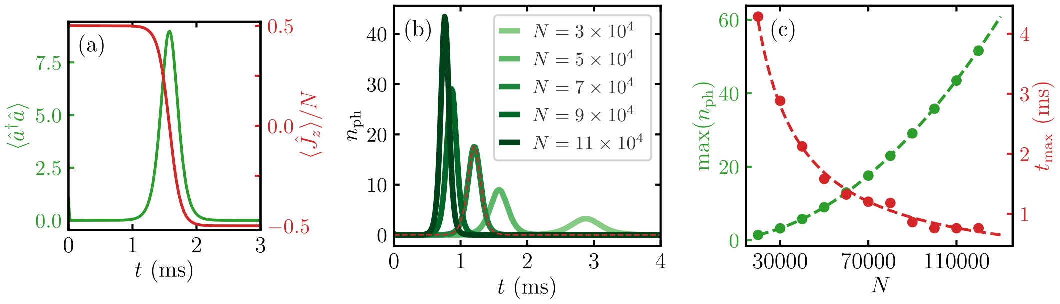

Figure 2.3: Superradiant Raman scattering in the open Tavis-Cummings model. **(a)** Mean-field simulations of the average photon number $n_{\rm ph} = \langle \hat{a}^\dagger \hat{a} \rangle$ (green) and the mode imbalance $\langle \hat{J}_z \rangle / N$ (red curve) for $N = 5 \times 10^4$, showcasing a complete population inversion ($|{\uparrow}\rangle \to |{\downarrow}\rangle$) accompanied by a transient cavity pulse. **(b)** Simulated photon pulses $n_{\rm ph}$ for different atom numbers N. The red dashed curve is an analytic estimate [Eq. (2.26)], and quantitatively agrees with the simulations. **(c)** Extracted peak photon number $\max(n_{\rm ph})$ (green) and associated delay $t_{\rm max}$ (red circles) for different N. The analytic estimates (dashed lines) confirm the scaling $\max(n_{\rm ph}) \propto N^2$ and $t_{\rm max} \propto 1/N$, which is the hallmark of superradiant photon scattering [120]. We use the typical experimental parameters $\delta = 0$, $\kappa = 2\pi \times 1.25\,\text{MHz}$ and $\eta = 2\pi \times 1\,\text{kHz}$.

of the cavity field. The photon pulse vanishes ($n_{\rm ph} \to 0$) once all the atoms occupy the steady state $|{\downarrow}\rangle$ ($j_z = -1/2$).

We further investigate the nature of this cavity-mediated spin decay, by numerically simulating the dynamics for different atom numbers N, and otherwise identical parameters. In Fig. 2.3(b), we show representative $n_{\rm ph}(t)$ curves for $N = 30000 - 110000$ atoms. For increasingly larger N, we observe stronger photon pulses occurring earlier in time. We systematically study this behavior by extracting the peak photon number $\max(n_{\rm ph})$ and its associated time delay $t_{\rm max}$ for different N, cf. Fig. 2.3(c). Remarkably, we find that the peak photon number scales super-linearly with N, specifically as $\max(n_{\rm ph}) \propto N^2$, while the delay time monotonically decays as $t_{\rm max} \propto 1/N$.

To elucidate this scaling behavior and the collective nature of the observed dynamics, we derive analytic estimates for the different observables. We adiabatically eliminate the cavity field [122]; this is a valid approximation as the cavity decay rate significantly exceeds the atomic energy scales, i.e., $\kappa \gg \omega_{\rm rec}$ and $\kappa > \sqrt{N}\eta$. From Eq. (2.23), we obtain

$$\frac{d}{dt}\alpha = 0 \Rightarrow \alpha = -\frac{i\sqrt{N}\eta}{\delta^2 + \kappa^2}(i\delta + \kappa)(j_x - i j_y). \tag{2.24}$$

This equation implies that the cavity field is always in a steady state ($\frac{d\alpha}{dt} = 0$) and instantaneously follows the dynamics of the atomic state. In particular, a non-vanishing cavity field ($\alpha \neq 0$) is associated with finite coherences ($j_{x,y} \neq 0$) between the two relevant atomic modes $|{\downarrow}\rangle$ and $|{\uparrow}\rangle$. This is compatible with our simulations in Fig. 2.3(a), as the photon pulse $n_{\rm ph}(t)$ vanishes in the steady state with $j_z = -1/2$ and $j_{x,y} = 0$. We insert Eq. (2.24) in the mean-field EOMs in Eq. (2.23) and obtain an ordinary differential equation for the spin imbalance

$$\frac{d}{dt}j_z = -2N\gamma(j_x^2 + j_y^2) = -2N\gamma\left(\frac{1}{4} - j_z^2\right), \tag{2.25}$$

where we introduce the effective single-particle dissipative coupling $\gamma = \eta^2\kappa/(\kappa^2+\delta^2)$ and use the total spin conservation $j_x^2 + j_y^2 + j_z^2 = 1/4$ in the last step. We consider an initial state in the vicinity of $|\uparrow\rangle$, $\mathbf{j}(t=0) = [\epsilon\cos\theta, \epsilon\sin\theta, \sqrt{1-\epsilon^2}]^T/2$, with $\epsilon \ll 1$ and $\theta \in [0, 2\pi)$. For this initial condition, we derive analytic solutions for $j_z(t)$ and $n_{\mathrm{ph}}(t)$

$$\begin{aligned} j_z(t) &= -\frac{1}{2}\tanh\left(\frac{t - t_{\max}}{\tau}\right), \\ n_{\mathrm{ph}}(t) &= N\alpha^*\alpha = \frac{N^2\gamma}{\kappa}\left(\frac{1}{4} - j_z^2(t)\right) = \max(n_{\mathrm{ph}})\cdot\operatorname{sech}^2\left(\frac{t - t_{\max}}{\tau}\right), \end{aligned} \tag{2.26}$$

where we introduce the photon pulse width $\tau = 1/(N\gamma)$ and delay time $t_{\max} = \ln\bigl(4/\epsilon^2\bigr)/(2N\gamma)$ associated with the photon pulse maximum $\max(n_{\mathrm{ph}}) = N^2\gamma/(4\kappa)$. In Figs. 2.3(b,c), we also compare the analytic solutions from Eq. (2.26) with the numerical simulations of the mean-field EOMs. The analytical estimates are in quantitative agreement with our simulations, both at the level of individual photon traces [red dashed curve in Fig. 2.3(b)], and the scaling $\max(n_{\mathrm{ph}})$ [green] and $t_{\max}$ [red dashed curve in Fig. 2.3(c)].

These results demonstrate the main features of *superradiant Raman scattering* in our system. As evident from our analytic calculation, the cavity-assisted population inversion observed in the open Tavis-Cummings model ($|\uparrow\rangle \to |\downarrow\rangle$) is collectively enhanced by the number of participating atoms N, resulting in monotonically falling delay times $t_{\max} \propto 1/N$ and a super-linear scaling of the peak photon number $\max(n_{\mathrm{ph}}) \propto N^2$. This behavior is in direct contrast to spontaneous emission of light, where an ensemble of N independent two-level atoms decays towards the ground state while emitting into free-space modes of the electromagnetic vacuum. In that case, the delay time $t_{\max} = 1/\Gamma_{\mathrm{SE}}$ depends only on the excited-state linewidth Γ_{SE} and is independent of N, whereas the peak amplitude $\max(n_{\mathrm{ph}}) \propto N$ exhibits a linear scaling with atom number. This can be directly derived from the corresponding optical Bloch equations [24].

2.2.3 Exact solutions for small systems

The results discussed so far were obtained using mean-field methods to simulate the dynamics of the open Tavis-Cummings model. This semi-classical approximation is expected to be valid for the large particle numbers in our experiments ($N > 10000$), and neglects the role of quantum fluctuations. In this section, we briefly discuss exact solutions of the master equation for small particle numbers ($N \leq 40$) and recover the phenomenology discussed in the previous section. These results serve as a validation of the mean-field techniques discussed in the previous section.

To numerically solve the full master equation in Eq. (2.21), we employ the built-in Lindblad solver of the QuTiP Python library [123]. The method expands the density

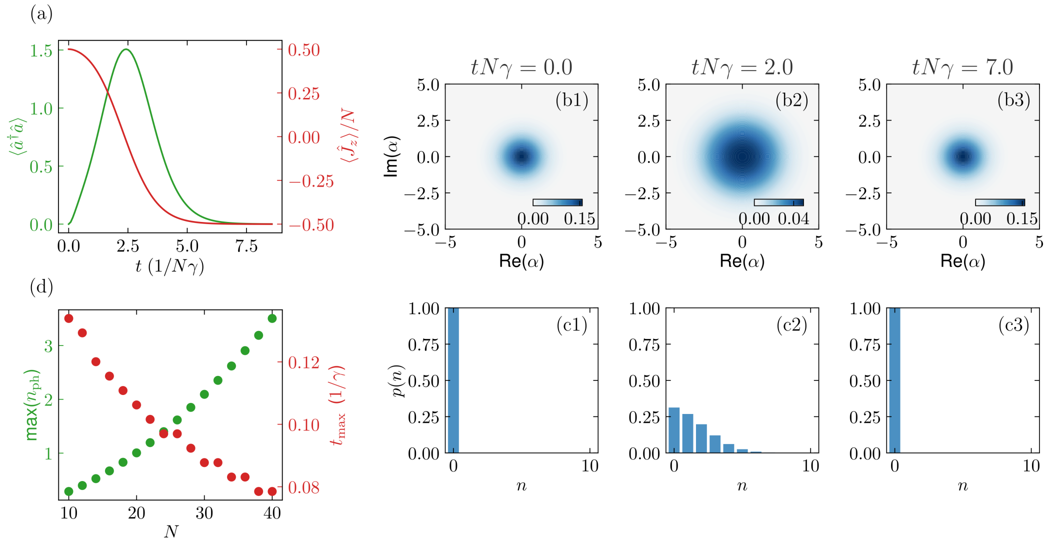

Figure 2.4: Superradiant scattering from exact solutions of the master equation. **(a)** Time evolution of the average photon number $\langle \hat{a}^\dagger \hat{a} \rangle$ (green) and the mode imbalance $\langle \hat{J}_z \rangle / N$ (red curve) for $N = 20$, $\delta = 0$ and $\eta/\kappa = 0.06$. Similar to the mean-field case, the simulations show a complete population inversion $|\uparrow\rangle \rightarrow |\downarrow\rangle$ accompanied by a transient cavity pulse. **(b)** Husimi distribution $Q(\alpha)$ and **(c)** Fock state occupation $p(n)$ of the transient cavity field at three representative times. The former illustrating the overlap of cavity field with an infinite set of coherent states $|\alpha\rangle$. While both the initial (b1,c1) and steady-state cavity field (b3,c3) are compatible with a coherent vacuum state with $p(n) = 1$, close to the photon peak maximum at $t = 2/N\gamma$ (b2,c2) the cavity field shows a broader distribution characterized by the transient occupation of multiple Fock states. **(d)** Scaling of the peak photon number $\max(n_{\mathrm{ph}}) \propto N^2$ and $t_{\max}$ its delay with atom number for $N \leq 40$, demonstrating superradiant scattering for small systems.

matrix in a basis of Fock states for the cavity field $|n\rangle$ and the two atomic modes $|N_\downarrow, N_\uparrow\rangle$, with $\{n,\ N_\downarrow,\ N_\uparrow\} \in \mathbb{N}$ and $N = N_\downarrow + N_\uparrow$. The photonic Hilbert space is truncated to $n \leq N$. As the dimension of the density matrix rapidly increases with atom number ($\mathcal{O}(N^2)$), this method is technically limited to small systems on the order of $N \approx 40$ atoms in conventional desktop computers[4].

In Fig. 2.4(a), we plot the expectation values of the photon number $\langle \hat{a}^\dagger \hat{a} \rangle$ and the normalized population imbalance and $\langle \hat{J}_z \rangle / N$ obtained by solving the master equation for $N = 20$ atoms initialized in $|N_\downarrow = 0, N_\uparrow = N\rangle \otimes |n = 0\rangle$. In direct resemblance to the mean-field dynamics in Fig. 2.3, we observe a complete population inversion of the system towards the mode $|\downarrow\rangle$ ($\langle \hat{J}_z \rangle = -N/2$), accompanied by a transient cavity pulse with the characteristic hyperbolic secants shape.

We further examine the state of the photon field at different instances of the evolution by evaluating the Husimi Q-function $Q(\alpha) = \langle \alpha | \hat{\rho}_{\mathrm{ph}} | \alpha \rangle / \pi$ [Fig. 2.4(b1-3)] and the occupation $p(n)$ of the different Fock states $|n\rangle$ [Fig. 2.4(c1-3)]. The Q-function of the reduced density matrix $\hat{\rho}_{\text{ph}}$ quantifies the overlap of a given state of the photon field with a continuous set of coherent states $|\alpha\rangle$. As expected, both the initial and long-time steady state of the photon field are compatible with coherent vacuum states with $p(0) = 1$ and a narrow Q-function centered around $\alpha = 0$, cf. Fig. 2.4(b1,c1) and (b3,c3), respectively. During the dynamics, the photon field transiently occupies multiple Fock states and displays a broader Husimi function centered around $\alpha = 0$, as shown in Figs. 2.4(b2, c2). The occupation of Fock states exhibits qualitative similarities to a Bose-Einstein distribution, which describes the population of discrete energy levels by indistinguishable bosonic particles in thermal equilibrium. The exact functional form of this distribution is defined in section 6.1.3. This observation suggests that in the bad cavity limit ($\kappa \gg \sqrt{N}\eta$), the transient cavity field evolves in thermal equilibrium with the environment. A more comprehensive study of the evolving photon distributions during superradiant decay behavior is beyond the scope of this thesis.

---

[4] In our theory work in Ref. [124], we exactly solve the master equation of the Tavis-Cummings model for up to $N \approx 200$ atoms by performing the calculations in a computer cluster.

Finally, we investigate the peak photon number $\max(n_{\text{ph}})$ and its associated delay $t_{\max}$ by solving the master equation for up to $N = 40$ atoms, see Fig. 2.4(d). While the small system size precludes a quantitative scaling analysis of $t_{\max}$, we observe a clear super-linear increase in pulse amplitude with atom number $\max(n_{\text{ph}}) \propto N^2$. This agrees with the mean-field results discussed in Fig. 2.3(c), further supporting the occurrence of superradiant Raman scattering in our system. Due to the large atom numbers in our experiments ($N \approx 10^4 - 10^5$), we rely on mean-field methods as the basis of our theoretical modeling for the various experiments discussed in chapters 4, 5, and 6.

2.2.4 The role of real and virtual cavity photons

In the final section of this chapter, we provide a microscopic picture for the dissipative and coherent processes in the open Tavis-Cummings model For this purpose, we introduce the concepts of real and virtual cavity photons.

Real cavity photons

To further interpret the dissipative dynamics, we adiabatically eliminate the cavity field in the master equation in Eq. (2.21) at an operator level

$$\frac{d\hat{a}}{dt} = 0 \Rightarrow \hat{a} = -\frac{i\eta}{\delta^2 + \kappa^2}(i\delta + \kappa)\hat{J}_-. \tag{2.27}$$

and obtain an effective atom-only Lindblad operator

$$\mathcal{L}_{\text{eff}}[\hat{\rho}_{\text{at}}] = \gamma[2\hat{J}_-\hat{\rho}_{\text{at}}\hat{J}_+^\dagger - \{\hat{J}_+\hat{J}_-, \hat{\rho}_{\text{at}}\}]. \tag{2.28}$$

Here, ρ_{at} denotes the reduced density matrix of the atomic system, with effective single-particle dissipative coupling $\gamma = \eta^2\kappa/(\delta^2 + \kappa^2)$ [89, 124]. The Lindbladian in Eq. (2.28) is generated by the collective jump operator $\hat{L} = \hat{J}_- \propto \hat{a}$, where $\hat{a}$ is the cavity photon annihilation operator. From the point of view of the atomic system, cavity decay acts as a *nonlocal dissipation channel*: every photon leaked from the cavity ($\propto \hat{a}$) is associated with the inversion of a single spin ($|\uparrow\rangle \rightarrow |\downarrow\rangle$), which is delocalized throughout the atomic ensemble ($\propto \hat{J}_-$).

This dissipative channel gives rise to superradiant Raman scattering and population inversion of the atomic ensemble towards $|\downarrow\rangle$ with collectively enhanced rates $N\gamma$, as schematically shown in Fig. 2.5(a). As discussed in the previous section, this process yields a transient cavity field leaking from the cavity mirrors. We refer to these photons as *real cavity photons* as they can be directly measured outside of the cavity, using single-photon counting modules [101] or heterodyne detection schemes [89]. Superradiant scattering is at the heart of so-called superradiant lasers [125, 126], which were first experimentally realized employing Raman transitions in cold thermal ensembles [86, 127] and more recently exploiting the clock transition in earth-alkaline atoms [128, 129].

Virtual cavity photons

To facilitate the interpretation of the relevant unitary dynamics, we use Eq. (2.27) to eliminate the cavity field in the Tavis-Cummings Hamiltonian. Thereby, we obtain an effective atom-only description

$$\hat{H}_{\text{eff}} \approx \hbar\chi \hat{J}_+ \hat{J}_- = \hbar\chi \left(\frac{N^2}{4} - \hat{J}_z^2 \right), \tag{2.29}$$

with the effective single-particle coherent coupling strength $\chi = \eta^2\delta/(\delta^2 + \kappa^2)$. Here, we employ the relation $\hat{J}_+\hat{J}_- = \hat{J}^2 - \hat{J}_z^2 - \hat{J}_z$ for the spin operators and transform to a suitable rotating frame [124] to eliminate linear terms $\propto \hat{J}_z$. At a fundamental level, the Hamiltonian in Eq. (2.29) acts on a pairs of atoms (A, B) and induces a correlated spin-exchange process, i.e., $\hat{J}_+\hat{J}_- |\downarrow\rangle_A \otimes |\uparrow\rangle_B = |\uparrow\rangle_A \otimes |\downarrow\rangle_B$ and $\hat{J}_+\hat{J}_- |\uparrow\rangle_A \otimes |\downarrow\rangle_B = |\downarrow\rangle_A \otimes |\uparrow\rangle_B$.

In our system, these coherent interactions are mediated by a higher-order four-photon scattering process: a first Raman transition changes the spin state of an atom ($|\uparrow\rangle \rightarrow |\downarrow\rangle$) while creating a cavity photon ($\hat{a}^\dagger$), which can be rescattered into the drive by a second atom ($\hat{a}$) inducing the opposite spin flip ($|\downarrow\rangle \rightarrow |\uparrow\rangle$), see schematic representation in Fig. 2.5(b). We refer to these photons as *virtual cavity photons* [130], as they cannot be directly detected outside the cavity. Yet, they mediate *nonlocal spin-exchange interactions* with collectively enhanced rates $N\chi$. Such interactions have been recently employed to experimentally realize many-body dynamical phases in cold thermal atomic ensembles [83], and proposed as a mechanism for synthesizing photon-induced Cooper pairs in degenerate Fermi gases [131, 132]. Additionally, the effective Hamiltonian in Eq. (2.29) is also a one-axis twisting Hamiltonian ($\propto \hat{J}_z^2$), which has been successfully implemented in cavity QED experiments with thermal atoms to generate spin squeezing [133, 134].

We emphasize that the relative rate of coherent and dissipative processes $\chi/\gamma = \delta/\kappa$ can be controlled by adjusting the two-photon detuning δ, facilitating the experimental access to primarily dissipative ($|\chi/\gamma| \lesssim 1$) and unitary regimes ($|\chi/\gamma| \gg 1$) in our system. Both limits are of central relevance for this thesis. In chapter 5, we experimentally demonstrate dynamical tunneling in a synthetic lattice in momentum space induced by real cavity photons. In chapter 6, we observe spin- and

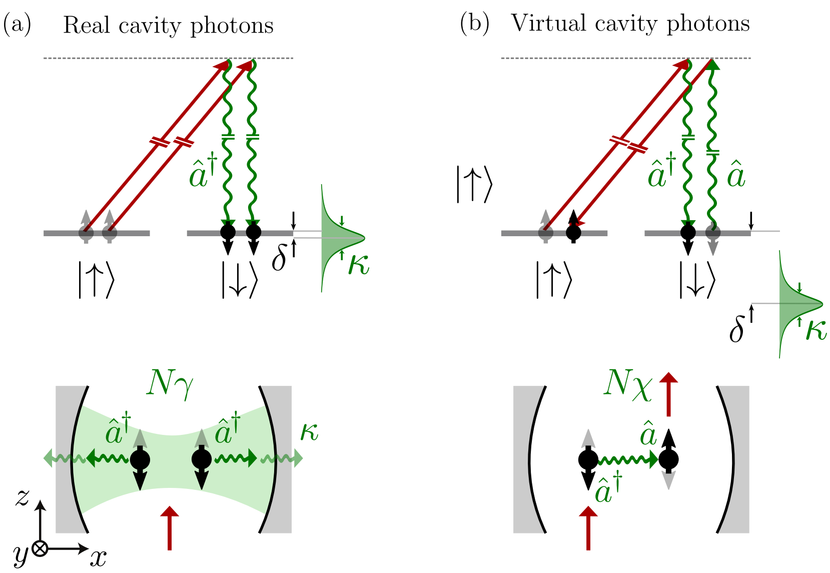
(a) Real cavity photons
(b) Virtual cavity photons
$\hat{a}^\dagger$
$\hat{a}$
$|\uparrow\rangle$
$|\downarrow\rangle$
δ
κ
$N\gamma$
$N\chi$
z
y
x

Figure 2.5: Real and virtual cavity photons mediating nonlocal dissipative and coherent interactions. **(a)** Real cavity photons arise from dissipation of the underlying light field near the two-photon resonance ($|\delta| \lesssim \kappa$). This results in a superradiant population inversion ($|\uparrow\rangle \to |\downarrow\rangle$) with a collectively enhanced rate $N\gamma$, as illustrated in the level scheme (upper) and the cavity schematics (lower panel). **(b)** Virtual cavity photons arise from unitary Hamiltonian contributions, and dominate the dynamics away from the two-photon resonance ($|\delta| \gg \kappa$). These virtual photons are transiently created ($\hat{a}^\dagger$) by an atom undergoing a Raman transition ($|\uparrow\rangle \to |\downarrow\rangle$) and are subsequently absorbed ($\hat{a}$) by a second atom in $|\downarrow\rangle$ undergoing the opposite process ($|\downarrow\rangle \to |\uparrow\rangle$). They mediate nonlocal spin-exchange interactions between atom pairs with a collective rate $N\chi$.

momentum-correlated atom pairs in a spin-1 BEC mediated by the exchange of virtual cavity photons.

3 Experimental setup and upgrades

All the experiments presented in this thesis were conducted in the *Cavity Experiment* at ETH Zurich. The experimental apparatus was constructed between 2002 and 2005 for studying phenomena at the intersection between many-body physics and cavity Quantum Electrodynamics [57, 58]. The original design of experimental setup can be found in the PhD theses of Anton Öttl [135] and Stephan Ritter [136]. Throughout the years, the experimental setup has undergone constant upgrades to meet the increasing demands of the experiments.

In this chapter, we provide a concise overview of the experimental setup, followed by a detailed discussion of recent upgrades. We begin with an introduction to the experimental setup in section 3.1, covering the preparation of a Bose-Einstein condensate and highlighting the central features of our high-finesse optical cavity. In section 3.2, we discuss relevant preparation and detection techniques, focusing on frequency-resolved heterodyne measurements of the cavity field and high-intensity absorption imaging of the atoms. Finally, in section 3.3, we provide a comprehensive characterization of the newly installed laser setup for driving cavity-assisted Raman transitions, which is central to the experiments discussed in this thesis.

3.1 Experimental apparatus

The experimental apparatus is set up on two optical tables. The first one (*laser table*) houses the optical setup to generate and control the laser fields used for cooling, confining, probing, and detecting the atoms. The laser beams are then transmitted through optical fibers to a second table, referred to as the *science table*, where additional optical elements adjust their polarization and precise beam shape. The science table houses the vacuum system, which consists of two nested chambers, see Fig. 3.1(a): the high-vacuum *prechamber* (10^{-9}mbar) is built inside the ultra-high vacuum *main chamber* (10^{-11}mbar). The two chambers are connected to independent ion pumps, with a differential pumping tube maintaining the high pressure gradient. In the vacuum chamber, there are several coils used to produce both offset magnetic fields and gradients required for manipulating the atoms [137].

In section 3.1.1, we provide an overview of the experimental sequence employed to produce a Bose-Einstein condensate inside the optical cavity. Furthermore, we discuss the central properties of our high-finesse optical cavity in section 3.1.2.

3.1.1 Route to Bose-Einstein condensation

The experimental sequence starts in the prechamber, where a magneto-optical trap (MOT) [93] is loaded from the background pressure of ^{87}Rb atoms released from a dispenser source, see Fig. 3.1(a). The MOT cooler laser is detuned by $\Delta_{\mathrm{MOT}} \approx -4\Gamma$

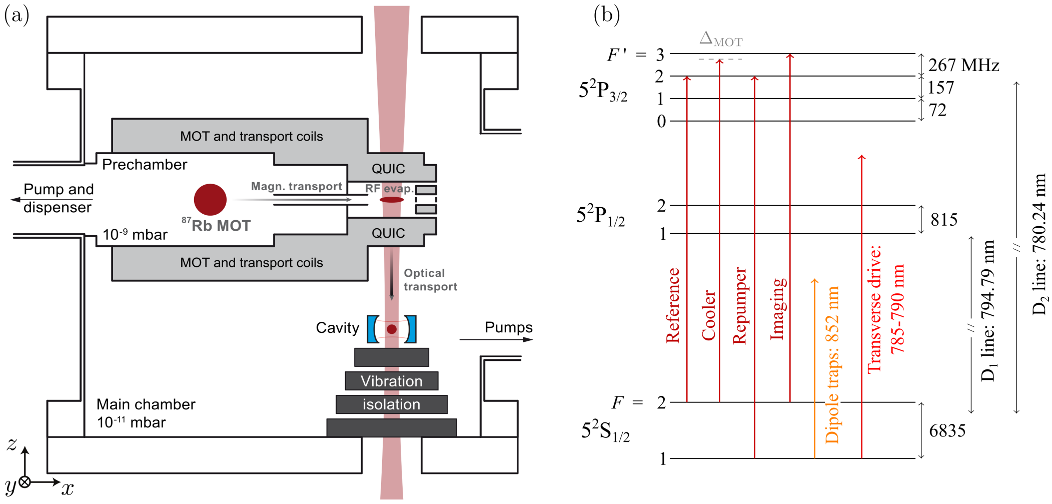
(a)
MOT and transport coils
Prechamber
QUIC
Pump and dispenser
Magn. transport
RF evap.
^{87}Rb MOT
10^{-9} mbar
QUIC
MOT and transport coils
Optical transport
Cavity
Pumps
Vibration isolation
Main chamber
10^{-11} mbar
z
y
x
(b)
Δ_{MOT}
$F' = 3$
2
1
0
$5^2P_{3/2}$
267 MHz
157
72
2
1
$5^2P_{1/2}$
815
Reference
Cooler
Repumper
Imaging
Dipole traps: 852 nm
Transverse drive: 785-790 nm
D_1 line: 794.79 nm
D_2 line: 780.24 nm
$F = 2$
$5^2S_{1/2}$
1
6835

Figure 3.1: Experimental setup. **(a)** BEC preparation in an optical cavity. The ^{87}Rb atoms are first loaded into a magneto-optical trap (MOT) in the prechamber. Following a molasses stage and optical pumping to $|F = 1, m = 0\rangle$, they are magnetically transported to the main chamber (10^{-11} mbar). Here, the atoms are confined in a magnetic QUIC trap and further cooled via radio frequency-assisted evaporation. After being optically transported into the cavity, the atoms are confined by a crossed dipole trap and undergo optical evaporation to form a BEC. Adapted from Ref. [138]. **(b)** ^{87}Rb atoms' level scheme and laser setup overview. The total angular momentum of the ground (excited) electronic states is denoted by F (F'). The MOT cooler laser addresses the $F = 2 \rightarrow F' = 3$ transition and is supplemented by a repumper laser addressing on the $F = 1 \rightarrow F' = 3$ transition. These lasers are stabilized with respect to a reference laser locked on $F = 2 \rightarrow F' = 2$ [108], which is can be adjusted in frequency to image the atoms on the $F = 2 \rightarrow F' = 3$ transition. Additionally, the far-detuned dipole laser (852 nm) and transverse drive (785-790 nm) are used to optically confine and probe the atoms, respectively. The subfigures (a) and (b) have been adapted from Refs. [139] and [108], respectively.

from the $F = 2 \rightarrow F' = 3$ transition, with $\Gamma = 2\pi \times 6.07\,\mathrm{MHz}$ referring to the natural linewidth of the $F' = 3$ manifold. Here, F (F') indicates the total angular momentum quantum number of the electronic ground state $5^2S_{1/2}$ (excited state $5^2P_{3/2}$) of ^{87}Rb, as shown in the ^{87}Rb level scheme in Fig. 3.1(b). Additionally, we employ a repumper laser addressing the $F = 1 \rightarrow F' = 3$ transition to suppress accumulation of atoms in the $F = 1$ manifold, as the MOT cooling transition is not closed [109]. Thereby, we cool $\sim 10^9$ atoms from room temperature to hundreds of µK within 8 to 10 s. The atomic cloud is further cooled to sub-Doppler temperatures (few µK) via a 20 ms-long optical molasses stage [140].

Next, the atoms are optically pumped to the low-field seeking state $|F{=}1, m{=}-1\rangle$, with m indicating the magnetic (Zeeman) sublevel. The atoms are magnetically trapped and transported [141] within 1.2 s over $\sim$ 82 mm to the main chamber. There, they are loaded into a quadrupole-Ioffe-configuration (Quic) trap [142], and undergo radio frequency-assisted evaporative cooling to obtain a thermal cloud of $\sim 10^6$ atoms close to quantum degeneracy. This step is the longest in the sequence, lasting for 18 to 24 s due to the slow thermalization of the remaining ^{87}Rb atoms.

The atoms are confined by a standing-wave optical potential generated by interfering two counter-propagating beams along the z-direction (transport beams), cf. Fig. 3.1(a). The transport beams operate at 852 nm and are far red-detuned from the ^{87}Rb transitions [Fig. 3.1(b)]. By adjusting the relative frequency between the two beams, the standing-wave potential progressively moves along the $-z$ direction [115]. This optical conveyor belt transports the atoms by $\sim$ 36 mm into the optical cavity, where crossed dipole trap formed by one of the transport beams and an additional orthogonal beam propagating in y direction. After a last step of optical evaporation ($\sim$ 1 s), we obtain an almost pure Bose-Einstein condensate (BEC) formed by 2×10^4 to 10^5 quantum-degenerate ^{87}Rb atoms ($\gtrsim 0.9$ condensate fraction).

We proceed with the actual experiments, and probe the BEC for variable times ranging from tens of microseconds to hundreds of milliseconds. To achieve this, we illuminate the atoms with far detuned transverse drive lasers (see section 3.3) that induce cavity-assisted two-photon transitions, mediating global-range interactions between the atoms. The photon field leaking from the cavity is continuously recorded in a non-destructive fashion using a frequency-resolved heterodyne setup, see section 3.2.1. Finally, we perform a destructive measurement of the atoms' momentum-space distribution through absorption imaging after free time-of-flight expansion (see section 3.2.2). Each experimental cycle has a duration of 30 to 35 seconds.

To ensure the successful implementation of the experimental sequence, we require precise addressing and control of multiple electronic and optical devices and synchronization of the data acquisition. To accomplish this, a central runner computer generates the necessary analog and digital signals using custom experimental control software written by Thilo Stoeferle [143]. These signals are then distributed amongst various devices, such as arbitrary-wave generators, optical shutters, or power supplies for the different coils. After each experimental sequence, the data from the absorption images and the heterodyne detection are stored and processed on dedicated computers. A detailed description of the optimized experimental sequence can be found in the thesis of Lorentz Hruby [138]. Additionally, Nishant Dogra's thesis [108] provides a comprehensive overview of the current laser system and coil layout.

3.1.2 High-finesse optical cavity

In our experiment, we prepare a Bose-Einstein condensate inside a high-finesse optical cavity to engineer strong and tunable light-matter interactions. In this section, we provide a concise summary of the main properties of our optical cavity that are relevant for the experiments discussed in this thesis. A detailed description of its design and characterization can be found in Ref. [137].

The optical cavity consists of two highly reflective mirrors spaced by $l = 176\,\mu\text{m}$ and coated for 780 ± 40 nm. The mirrors have a large radius of curvature ($R = 75\,\text{mm} \gg l$), forming a quasi-planar symmetric Fabry-Perot resonator. In the chosen frame of reference, the cavity mirrors are aligned along the x direction, as shown in

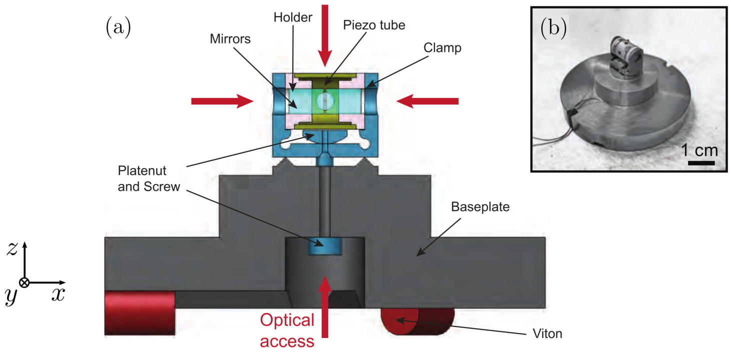

Figure 3.2: High-finesse optical cavity. **(a)** Schematic representation. Two highly-reflective mirrors spaced by $l = 176\,\mu\text{m}$ are attached to a piezo tube, facilitating adjustment of l. Two pairs of holes in the piezo tube provide optical access along the y and z directions. The cavity setup is mounted on a vibration isolation stage. **(b)** Photograph of the assembled optical cavity setup. Adapted from Ref. [137].

Fig. 3.2(a). The finesse of the optical cavity is given by

$$\mathcal{F} = \frac{2\pi}{2\mathcal{T} + 2\mathcal{L}} = 3.4 \times 10^5, \tag{3.1}$$

where $\mathcal{T} = 2.3\,\text{ppm}$ and $\mathcal{L} = 6.9\,\text{ppm}$ are the transmission and losses of the mirrors, respectively. The cavity's free spectral range is

$$f_{\text{FSR}} = \frac{c}{2l} = 852\,\text{GHz}, \tag{3.2}$$

with c being the speed of light. From Eqs. (3.1) and (3.2), we derive the decay rate of the cavity field around 780 nm as

$$\kappa = \frac{\pi f_{\text{FSR}}}{\mathcal{F}} = 2\pi \times 1.25\,\text{MHz}. \tag{3.3}$$

In the experiments discussed in this thesis, we exclusively couple the atoms to the lowest order transverse electromagnetic mode (TEM_{00}), while the contribution from higher-order modes is negligible. This is due to the large transverse mode splitting of 18.5 GHz [115]. The TEM_{00} has a waist of $w_0 = 25.3\,\mu\text{m}$ yielding a mode volume of $V_0 = 8.8 \times 10^4\,\mu\text{m}^3$. The corresponding vacuum electric field amplitude is $E_0 = \sqrt{\hbar\omega_c/(2\epsilon_0 V_0)}$, with ω_c and ϵ_0 being the resonance frequency of the cavity and the vacuum permitivity. For the typical values of $\omega_c = 2\pi \times 382.047\,\text{THz}$ (chapters 4 and 5) and $\omega_c = 2\pi \times 379.477\,\text{THz}$ (chapter 6), we obtain $E_0 = 403\,\text{V/m}$ and $E_0 = 402\,\text{V/m}$, respectively. The TEM_{00} mode is split into two orthogonal linearly polarized eigenmodes, which are tilted by 22° with respect to the y- and z-axes, respectively. Due to the birefringence of the cavity mirrors, the resonance frequency of the predominantly y-polarized mode is shifted by $\delta_B = 2\pi \times 2.2\,\text{MHz}$.

The cavity mirrors are attached to a piezoceramic tube, which allows for precise adjustment of the cavity length l and consequently the resonance frequency $\omega_c/2\pi$ by $\lesssim 0.5 f_{\text{FSR}}$ (see Fig. 3.2(a)). The latter is actively stabilized by feedbacking on the reflection of a weak intra-cavity field at 830 nm and acting on the piezo tube.

Simultaneously, the frequency of this field is stabilized with respect to the transverse drive frequency (ω_d) using a transfer cavity locking scheme. This ensures that the fluctuations of ω_c and ω_d become commensurate, and that the cavity detuning $\Delta_c = \omega_\mathrm{c} - \omega_\mathrm{d}$ remains a fixed quantity. The field at 830 nm creates an intra-cavity standing-wave potential with a lattice depth of $0.01 E_\mathrm{rec}$, which has negligible influence on the dynamics of the BEC. A detailed overview of the current locking scheme can be found in the thesis of Lorenz Hruby [138].

3.2 Preparation and detection techniques

Here, we present the different preparation and detection techniques relevant for our experiments. In section 3.2.1, we discuss the detection of the cavity field: After reviewing the fundamentals of balanced heterodyne detection and providing an overview of our setup, we discuss how to extract frequency-resolved observables from our measurements. In sections 3.2.2 and 3.2.3, we provide an overview of our absorption imaging setup and discuss the improved preparation of atoms in the $m = 0$ Zeeman sublevel, respectively.

3.2.1 Heterodyne detection of the cavity field

Fundamentals of heterodyne detection

In our experiment, we perform a balanced heterodyne detection [144] of the photon field leaking out of the cavity, $E_\mathrm{s} = E_\mathrm{s} e^{i(\omega_\mathrm{s} t + \phi_\mathrm{s})}$, with electric field amplitude E_s, frequency ω_s and phase ϕ_s. The cavity field is overlapped with a strong local oscillator (LO) field, $E_\mathrm{LO} = E_\mathrm{LO} e^{i(\omega_\mathrm{LO} t + \phi_\mathrm{LO})}$, on a 50:50 beamsplitter, as illustrated in Fig. 3.3(a). At the two outputs of the beamsplitter, we obtain the following intensity beat notes

$$I_\pm = \frac{1}{2}\left(|E_\mathrm{s}|^2 + |E_\mathrm{LO}|^2\right) \pm E_\mathrm{LO} E_\mathrm{s} \cos(\delta t + \phi), \tag{3.4}$$

which are detected on identical photodiodes. Here, $\delta = \omega_\mathrm{s} - \omega_\mathrm{LO}$ and $\phi = \phi_\mathrm{s} - \phi_\mathrm{LO}$ are the relative frequency and phase between the cavity signal and the LO.

In balanced heterodyne detection schemes, the two beat notes $I_\pm$ are subtracted from each other to obtain the output signal

$$S(t) = I_+ - I_- = 2 E_\mathrm{LO} E_\mathrm{s} \cos(\delta t + \phi), \tag{3.5}$$

which contains both the frequency, phase and amplitude information of the cavity field. A central advantage of this detection technique is that the cavity output frequency is down-mixed from the optical domain ($\omega_\mathrm{s} \approx 2\pi \times 400\,\mathrm{THz}$) to the radio frequency (RF) domain ($\delta \approx 2\pi \times 50\,\mathrm{MHz}$). This facilitates detection using commercially available photo detectors and RF electronics. Additionally, the large LO field amplitude ($E_\mathrm{LO} \gg E_\mathrm{s}$) amplifies the output signal $S(t)$ above technical noise levels, allowing operation in a regime where photon shot noise becomes dominant [145]. A

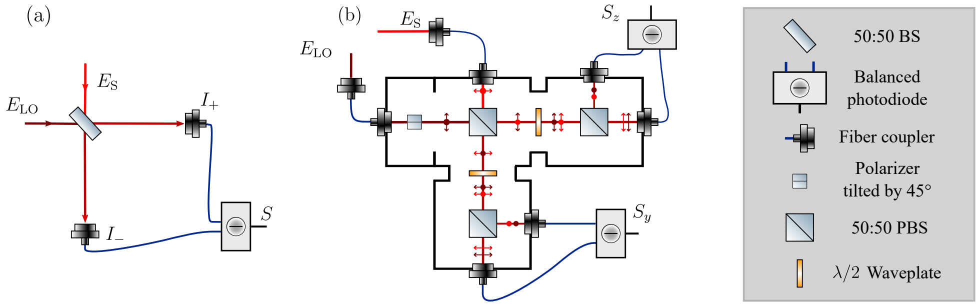

Figure 3.3: Balanced heterodyne detection. **(a)** Working principle. The signal E_S and local oscillator (LO) E_{LO} fields are overlapped on a beamsplitter (BS) and sent to the two inputs of a balanced photodiode. The measured intensities I_+ and I_- are subtracted from each other to obtain the heterodyne output S. **(b)** Optical path of the new heterodyne setup. The signal and LO fields are fiber coupled into a rigid multicube interferometer comprising multiple polarizing beamsplitters (PBS), which can be used to perform heterodyne measurements of the y- and z-polarized cavity modes, S_y and S_z. Adapted from [147].

quantum-mechanical derivation of balanced heterodyne detection can be found in Ref. [146].

New heterodyne setup

In previous experiments, the heterodyne output $S(t)$ was electronically split and demodulated from $\delta \approx 2\pi \times 50\,\text{MHz}$ to $2\pi \times 47\,\text{kHz}$ to extract the relevant quadratures of the light field. The bandwidth of this *old heterodyne setup* was limited to $B_{\text{old}} = 2\pi \times 250\,\text{kHz}$ due to the RF electronics used. A detailed description of this setup can be found in the theses of Renate Landig [145] and Nishant Dogra [108].

In the experiments discussed in this thesis, we employ the *new heterodyne setup* developed by former master student Joshua Maas [147]. In this setup, the cavity output signal and the local oscillator field are fiber-coupled into a rigid multicube interferometer, as illustrated in Figure 3.3(b). There, the z- and y-polarized cavity modes are optically separated and measured using independent balanced photodiodes. The corresponding output signals $S_z(t)$ and $S_y(t)$ are sampled by analog-to-digital converters at a rate of 250 MS/s, yielding a large detection bandwidth of $B_{\text{new}} = 2\pi \times 125\,\text{MHz}$. To store and process these signals, we employ a custom Python-based software architecture [147].

One of the central advantages of the new heterodyne setup is its large detection bandwidth B_{new}, which facilitates the simultaneous detection of cavity-assisted Raman processes and intra-spin self-organization of the atoms [64]. When operating in a single drive configuration at frequency ω_{d}, we typically set the local oscillator frequency to $\omega_{\text{LO}} - \omega_{\text{d}} = 2\pi \times 59.55\,\text{MHz}$ and operate at large Zeeman splittings of $\omega_z \approx -2\pi \times 50\,\text{MHz}$. As discussed in section 2.1.3, cavity-assisted Raman transitions between the Zeeman sublevels $m \to m \pm 1$ are associated with a transient cavity field at $\omega_{\text{s},1} \approx \omega_{\text{d}} \mp \omega_z$, while self-organization results in a steady-state field at $\omega_{\text{s},2} = \omega_{\text{d}}$ [64]. Due to the large detection bandwidth of $B_{\text{new}} = 2\pi \times 125\,\text{MHz}$, we can discern the cavity signals associated with Raman processes ($\omega_{\mathrm{LO}} - \omega_{\mathrm{s},1} < B_{\mathrm{new}}$) and self-organization ($\omega_{\mathrm{LO}} - \omega_{\mathrm{s},2} < B_{\mathrm{new}}$) without requiring hardware modifications.

In the experiments presented in this thesis, we utilize a polarizing beamsplitter at the cavity output and measure the z- and y-polarized cavity modes using the new and old heterodyne setups, respectively. Recently, we have removed the old heterodyne setup for improved experimental access, and the new heterodyne is being used to monitor both polarizations.

Frequency-resolved evaluation of light-field measurements

In every experimental realization, we use the new heterodyne setup to record the output $S(t)$ during the probing stage of the experiment, cf. Eq. (3.5). We digitally demodulate the output signal at the target frequency ω_{T} to obtain

$$\begin{aligned} X(t) &= S(t)\cos(\omega_{\mathrm{T}} - \omega_{\mathrm{LO}}) = 2E_{\mathrm{s}}E_{\mathrm{LO}}\left[\cos(\delta_{\mathrm{T}}t + \phi) + \cos(\Omega_{\mathrm{T}}t + \phi)\right], \\ Y(t) &= -S(t)\sin(\omega_{\mathrm{T}} - \omega_{\mathrm{LO}}) = 2E_{\mathrm{s}}E_{\mathrm{LO}}\left[\sin(\delta_{\mathrm{T}}t + \phi) - \cos(\Omega_{\mathrm{T}}t + \phi)\right]. \end{aligned} \tag{3.6}$$

The quantities $X(t)$ and $Y(t)$ consist of both low and high frequency components at $\delta_{\mathrm{T}} = \omega_{\mathrm{s}} - \omega_{\mathrm{T}}$ and $\Omega_{\mathrm{T}} = \omega_{\mathrm{s}} + \omega_{\mathrm{d}} - 2\omega_{\mathrm{LO}}$, respectively. The fast oscillations can be suppressed using a suitable digital low-pass filter. We identify $X(t)$ and $Y(t)$ as the two orthogonal quadratures of the cavity field, with a phase shift of $\pi/2$, in an effective rotating frame defined by the target frequency ω_{T}. We compute the complex cavity field amplitude as

$$\alpha(t) = X(t) + iY(t), \tag{3.7}$$

which contains the complete amplitude and frequency information of the cavity field. To evaluate the different spectral components, we calculate the discrete fast Fourier transform (FFT) of $\alpha(t)$ as

$$\mathrm{FFT}(\alpha)(\omega) = \frac{\mathrm{d}t}{\sqrt{\tilde{N}}} \sum_j \alpha^*(t_j) e^{-i\omega t_j}, \tag{3.8}$$

where t_j is the time of the j^{th} step, $\mathrm{d}t = t_{j+1} - t_j$ and $\tilde{N} = T/dt$ is the total number of steps in the integration window T [73]. We compute the power spectral density (PSD) as $\mathrm{PSD}(\omega)=|\mathrm{FFT}(\alpha)|^2(\omega)$, and construct *photon number spectrograms* of the cavity field

$$\tilde{n}_{\mathrm{ph}}(t, \omega - \omega_{\mathrm{T}}) = \frac{\mathrm{PSD}(\omega)}{T}, \tag{3.9}$$

by dividing the traces into $n = t_{\mathrm{ac}}/T$ time intervals, each of which overlaps with the previous one by 50%. Here, t_{ac} indicates the total acquisition time during the probing state.

The photon number spectrogram derived in Eq. (3.9) is extensively used in thesis to obtain time- and frequency-resolved measurements of the cavity field. Its time resolution $\delta t_{\mathrm{R}} = T/2$ is set by the integration time T of the FFTs, which is typically set to $T = 150 - 300\,\mu\mathrm{s}$. Conversely, the frequency resolution is Fourier limited

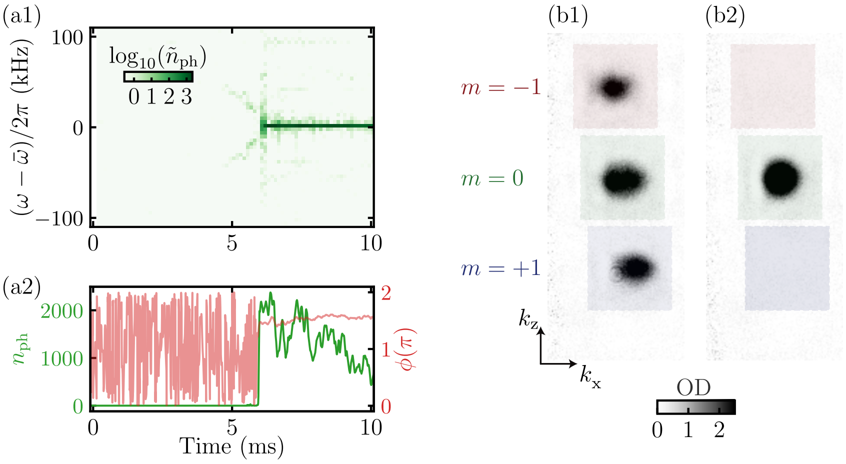

Figure 3.4: Evaluation of photonic and atomic observables. **(a)** Intra-cavity photon field associated with spin-changing self-organization. (a1) Photon number spectrograms $\tilde{n}_{\rm ph}$ at the target frequency $\omega_{\rm T} = \bar{\omega}$ obtained for an integration time $T = 250\,\mu$s. (a2) Average photon number $n_{\rm ph}$ and phase ϕ of the cavity field at $\bar{\omega}$. See section 4.2.1 for details on experimental protocol. **(b)** Representative spin-resolved momentum distributions in the Zeeman sublevels (m) of $F = 1$, obtained after Stern-Gerlach separation and $t_{\rm TOF} = 8$ ms time-of-flight expansion. The absorption image in (b1) shows the atomic distribution after a $\pi/2$ radio frequency rotation starting from $m = -1$, while (b2) shows a $m = 0$ preparation with an additional cleaning gradient.

to $\delta f_{\rm R} = 1/T \approx 6.6 - 3.3\,$kHz. The sensitivity of photon number spectrograms is experimentally calibrated to $\delta\tilde{n}_{\rm ph} \approx 0.22$ at $T = 250\,\mu$s. Using Eq. (3.9), we can extract the average number of photons in a specific frequency interval $\omega - \omega_{\rm T} \in \Omega$ as $n_{\rm ph}(t) = \sum_\Omega \tilde{n}_{\rm ph}(t, \omega - \omega_{\rm T})$. Additionally, the relative phase between the cavity field and the local oscillator at $\omega = \omega_{\rm T}$ can be determined by evaluating the argument of the complex-valued field $\phi(t) = \arg[\alpha(t)]$ [64].

In Fig. 3.4(a), we present an exemplary evaluation of the z-polarized cavity field associated with spin-changing self-organization of the atoms. As discussed in section 4.2, a BEC is illuminated by a two-frequency transverse drive $(\omega_{b,r})$. A superradiant phase transition is signaled by a macroscopic cavity field at $\bar{\omega} = (\omega_b + \omega_r)/2$. This is shown by the representative photon number spectrogram in Fig. 3.4(a1), where we choose the target frequency $\omega_{\rm T} = \bar{\omega}$. For completeness, we present the average photon number $n_{\rm ph}$ integrated over a region $\Omega = 2\pi \times [-15, 15]$kHz and the phase of the cavity field ϕ in Fig. 3.4(a2).

3.2.2 High-intensity absorption imaging

At the end of every experimental cycle, we destructively measure the momentum-space distribution of the atoms by performing high-intensity absorption imaging after free time-of-flight (TOF) expansion [148]: after the probing stage, all confining potentials are switched off and the atoms expand for $t_{\rm TOF} = 5 - 8$ ms, effectively mapping the initial momentum-space distribution into real space. As our experiments take place in the $F = 1$ ground state manifold, the atoms are first transferred to $F = 2$ using the repumper laser and the imaged on the nearly closed transition $F = 2 \rightarrow F' = 3$, see Fig. 3.1(b).

We image the atoms through the cavity slit along the y-direction[1]. The attenuation of imaging beam is determined by the Beer–Lambert law

$$\frac{d}{dy} I(x, y, z) = -n(x, y, z)\sigma(I)I(x, y, z), \tag{3.10}$$

with $n(x, y, z)$ and $\sigma(I) = \sigma_0/[1 + I/I_{\mathrm{sat}}]$ being the density distribution of the atoms and the resonant absorption cross section, respectively. The latter depends on the saturation intensity of the imaging transition I_{sat} and on the low-intensity absorption cross section σ_0 [148]. By integrating the Beer-Lambert law, we obtain the integrated density distribution in the xz plane

$$n(x, z) = \int_{y_0}^{y_\mathrm{f}} n(x, y, z)dy = -\frac{1}{\sigma_0}\left[\ln\left(\frac{I(y_\mathrm{f})}{y_0}\right) - \frac{I(y_\mathrm{f}) - I(y_0)}{I_{\mathrm{sat}}}\right], \tag{3.11}$$

with $I(y_0)$ $[I(y_\mathrm{f})]$ being the intensity of the imaging beam before [after] passing through the atomic cloud. Experimentally, we record first an image with atoms (I_A), a subsequent bright image without atoms (I_B) and a final dark image (I_D). The corresponding intensities are estimated as $I(y_\mathrm{f}) = I_\mathrm{A} - I_\mathrm{D}$ and $I(y_0) = I_\mathrm{B} - I_\mathrm{D}$, respectively.

Additionally, during the time-of-flight (TOF) expansion, we apply a strong magnetic field gradient along the z direction to perform a Stern-Gerlach experiment. This gradient spatially separates the atoms occupying different magnetic sublevels m of the $F = 1$ manifold, allowing us to obtain spin- and momentum-resolved atomic distributions. An exemplary absorption image demonstrating this separation is shown in Fig. 3.4(b1). The magnification of the y-imaging setup is calibrated to 5.08(3) using Kapitza-Dirac diffraction [149], while its spatial resolution is limited to $\sim 9\,\mu\mathrm{m}$ due to the narrow separation between the cavity mirrors. For a detailed characterization of the current imaging setup, refer to the thesis of Lorenz Hruby [138].

To obtain the correct atomic density from Eq. (3.11), we need to accurately calibrate both I_{sat} and σ_0. Both quantities depend on the polarization of the imaging beam [109], which is challenging to estimate a priori at the position of the atoms. For the experiments discussed in chapters 4 and 5, we calibrate I_{sat} closely following the procedure discussed in Ref. [145]. We image the BEC at different intensities I and optimize the free fit parameter I_{sat} to obtain constant total atom numbers $N(I) = \sum_{x,z} n(x, z)$ irrespective of I. However, the imaging intensity I can fluctuate over an order of magnitude at the position of the atoms due to fringes originating from light scattering at the edges of the cavity mirrors. For the experiments discussed in chapter 6, we account explicitly for short-scale spatial variations of the imaging-beam intensity following Ref. [150]. The cross section σ_0 enters as a global proportionality factor in Eq. (3.11) and is calibrated by comparing the measured atom numbers $N(I)$ to the results inferred from the dispersive shift of the cavity resonance in the presence of atoms [108]; this results in a systematic uncertainty of $\sim 15\%$ for the total number of atoms. By recording hundreds of images without atoms, we calibrate the technical detection noise to $\sigma_{\mathrm{det}} = 190(20)$ atoms in the regions of interest typically occupied by the BEC. Additionally, we verify that there are no significant spin-dependent effects affecting the atom counting: we prepare a polarized BEC in $m = -1$ Zeeman sublevel of the $F = 1$ hyperfine manifold, drive three-level Rabi oscillations and observe a constant total atom number while the populations in the three m states change.

---

[1] We can also perform simultaneous absorption imaging along z direction, see Ref. [108], which is currently employed solely for alignment purposes.

3.2.3 Improved spin-selective preparation

To generate photon-mediated atom pairs in chapter 6, it was essential to improve the initial state preparation of the atoms in the $|F = 1, m = 0\rangle$ Zeeman sublevel. In previous experiments [78], BECs in different magnetic sublevels m were prepared using Landau-Zener sweeps starting from $|F = 1, m = -1\rangle$ while optically transporting the atoms into the cavity. However, this approach results in large shot-to-shot fluctuations, with $\Delta N_0/N_0 = 0.14(1)$ for the atom number in $|1, 0\rangle$ compared to $\Delta N_{-1}/N_{-1} = 0.039(2)$ for the initial BEC in $|1, -1\rangle$. Here, N_m and ΔN_m are the mean and standard deviation of the atom number in the different Zeeman sublevels m obtained from ~ 50 experimental realizations. These significant fluctuations are attributed to temporal variations in the bias magnetic field experienced by the atoms during the Landau-Zener sweeps, as well as shot-to-shot fluctuations in the optical transport speed.

To improve atom number stability in $|1, 0\rangle$, we resort to radio frequency (RF)-assisted preparation in the optical cavity. Ideally, we would perform RF rotations of the atomic spin at high bias fields where the quadratic Zeeman splitting q is much larger than the RF Rabi frequency Ω_{RF}. This would allow us to exclusively drive RF transitions between the magnetic sublevels $|1, -1\rangle$ and $|1, 0\rangle$. However, the electrodes of piezo electric tube surrounding the cavity [Fig. 3.2(a)] shield the atoms from signals in the radio frequency range $\omega_{\mathrm{RF}} \gtrsim 2\pi \times 1\,\mathrm{MHz}$ [108].

Therefore, we reduce the bias magnetic field to $B = 0.64\,\mathrm{G}$, which corresponds to a small linear Zeeman splitting $\omega_z = -2\pi \times 0.45\,\mathrm{MHz}$, and drive resonant RF transitions. After $t = 25\,\mu\mathrm{s}$ ($\pi/2$-pulse), we transfer the atoms to the single-particle state $|\phi\rangle = (|1, -1\rangle + \sqrt{2}\,|1, 0\rangle + |1, +1\rangle)/2$. This state is chosen to maximize the $|1, 0\rangle$ fraction when performing a RF rotation starting from $|1, -1\rangle$, assuming a negligible second-order Zeeman splitting ($q \ll \Omega_{\mathrm{RF}}$). In Fig. 3.4(b1), we show a typical absorption image after RF preparation and Stern-Gerlach separation during TOF expansion. To obtain a pure BEC in the $|1, 0\rangle$ Zeeman sublevel we apply a strong magnetic field gradient in the xy plane, effectively removing the magnetically sensitive atoms in $|1, -1\rangle$ and $|1, +1\rangle$, as shown in Fig. 3.4(b2).

By employing this RF-assisted preparation technique, we successfully obtained a Bose-Einstein condensate (BEC) in the $|1, 0\rangle$ Zeeman sublevel with significantly reduced shot-to-shot fluctuations of $\Delta N_0/N_0 = 0.045(2)$. The improved stability of the initial state preparation is crucial for observing the coherent pair oscillations discussed in section 6.2. When preparing atoms in $|1, 0\rangle$ using Landau-Zener sweeps,

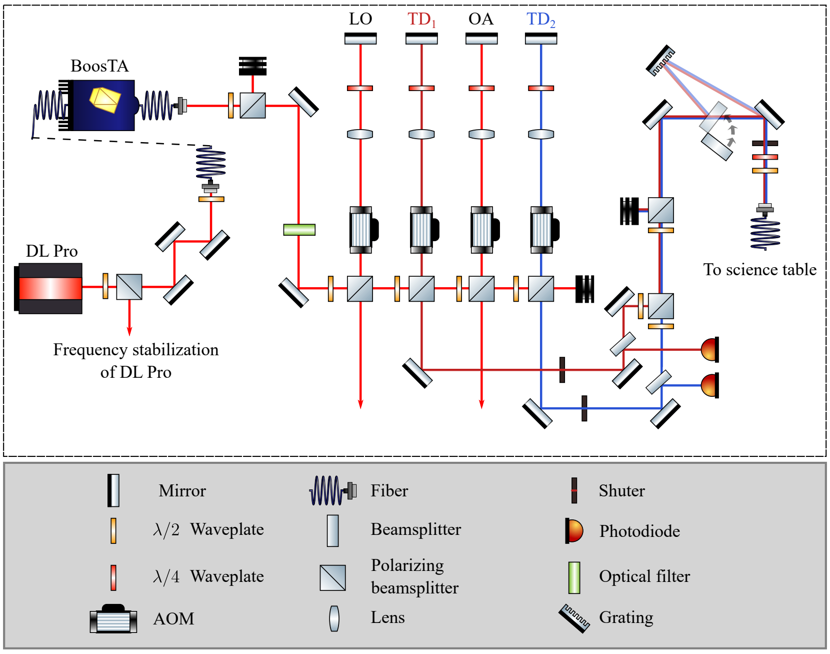
LO
TD1
OA
TD2
BoosTA
DL Pro
Frequency stabilization of DL Pro
To science table
Mirror
Fiber
Shuter
λ/2 Waveplate
Beamsplitter
Photodiode
λ/4 Waveplate
Polarizing beamsplitter
Optical filter
AOM
Lens
Grating

Figure 3.5: Optical path of transverse drive lasers (laser table). The transverse drives are derived from a frequency stabilized Toptica DL pro laser, which seeds the BoosTA tapered amplifier (TA). Its output is split into four paths: local oscillator (LO), cavity on axis (OA), and two independent transverse drive beams (TD_1 in dark red and TD_2 in blue). The frequencies of these beams are adjusted using double-pass acousto-optical modulators (AOMs). After sending a small fraction of the TDs to photodiodes for intensity stabilization, they are combined on a polarizing beamsplitter, with a second one used for polarization matching. Prior to fiber coupling the TDs into the science table, they can pass through a reflection grating to narrow the broad TA spectrum (see main text).

the oscillations were fully averaged out by the large shot-to-shot fluctuations.

3.3 Laser setup for driving cavity-assisted Raman transitions

During the course of this thesis, we upgraded the laser setup used to generate the transverse drive beams inducing cavity-assisted Raman transitions. The upgrade was motivated by two main factors: increasing the available laser power and obtaining two independently tunable drive beams. In section 3.3.1, we present and characterize the new laser setup. Furthermore, in section 3.3.2, we discuss the various configurations employed for the transverse drives and demonstrate experimental control over their relative spatial phase.

3.3.1 New laser setup

The transverse drive is derived from a Toptica DL pro laser located in the laser table, providing $\sim 50\,\mathrm{mW}$ of laser power at $\lambda_{\mathrm{d}} = 785 - 790$ nm. To increase the available power, we installed a Toptica BoosTA tapered amplifier (TA), as schemat-

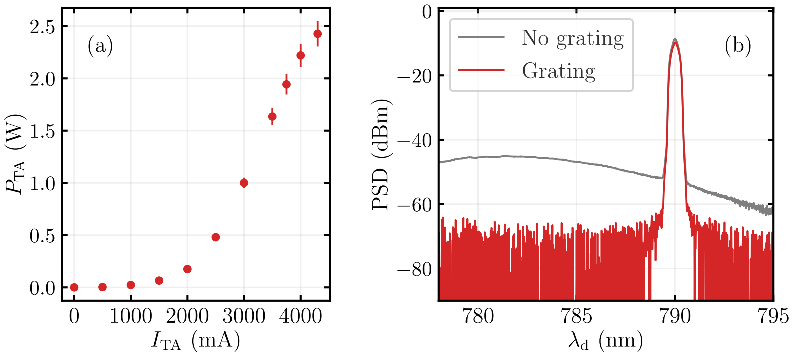

Figure 3.6: Characterizing the tapered amplifier (TA) of the transverse drive setup. **(a)** TA output power P_{TA} as a function of the applied chip current I_{TA} at $\lambda_{\mathrm{d}} = 784.7\,\mathrm{nm}$. In our experiments, we typically operate at $I_{\mathrm{TA}} \approx 3500\,\mathrm{mA}$. **(b)** Power spectral density (PSD) of the TA measured in the science table for a $\lambda_{\mathrm{d}} = 790.02\,\mathrm{nm}$ seed. The PSD exhibits a broad background spectrum (gray curve) due to amplified spontaneous emission and includes significant resonant light components. To suppress these contributions (red curve), we install a reflection grating in the experimental table, spatially separating different spectral components, and preventing fiber coupling of the TA background spectrum. The spectra are recorded using the Yokogawa AQ6370C optical spectrum analyzer.

ically shown in Fig. 3.5. The TA is seeded by $\sim 45\,\mathrm{mW}$ of laser light from the DL pro and is fiber coupled both at the input and output. We characterize the laser power in the TA output P_{TA} as a function of the current applied to the TA chip I_{TA}, see Fig. 3.6(a). For $I_{\mathrm{TA}} > 1000$ mA, the tapered amplifier starts lasing, and the output power monotonically increases until it saturates at $P_{\mathrm{TA}} = 2.5$ W for $I_{\mathrm{TA}} = 4500$ mA. To increase the TA lifetime, we typically operate it at intermediate currents $I_{\mathrm{TA}} = 3500$ mA, obtaining $P_{\mathrm{TA}} = 1.5$ W of coherent laser light.

To obtain two independently adjustable transverse drives (TD_1 and TD_2), we split the TA output using successive polarizing beamsplitters (PBS), see Fig. 3.5. We adjust the frequencies of the individual drives using acousto-optical modulators (AOMs) operated in a double-pass configuration. Two additional AOM paths are used to adjust the frequency of the local oscillator (LO) for the heterodyne detection and the on-axis (OA) beam to probe the cavity resonance. After passing through the AOMs, a small power fraction (5 %) of each transverse is split and sent to a photodiode used for intensity stabilization[2]. The two transverse drives are then combined in a PBS, with a second one used to match their polarization. Finally, they are sent through a 15 m-long fiber to the science table.

We characterize the spectral composition of the BooTA output. In Fig. 3.6(b), we measure the TA power spectral density (PSD) when seeding it at $\lambda_{\mathrm{d}} = 790.02\,\mathrm{nm}$

---

[2] In chapter 4, a different intensity stabilization scheme is employed for the experiments. The two TDs with frequencies $\omega_{r,b}$ are overlapped with the local oscillator (LO) at ω_{LO} on a fast photodiode close to the vacuum chamber in the science table. The beat notes at $\omega_r - \omega_{\mathrm{LO}}$ and $\omega_b - \omega_{\mathrm{LO}}$ are electronically separated to stabilize each TD independently. However, it was observed that the drifts of the TD-LO overlap on the science table were significantly larger than the temporal variations of the TD fiber coupling. As a result, this scheme was abandoned for later projects.

(gray curve). We observe a strong peak at λ_d, accompanied by broad spectral distribution centered around $\lambda_\mathrm{d} = 780\,\mathrm{nm}$. The latter is attributed to amplified spontaneous emission in the TA chip. This broad spectral distribution is particularly detrimental for our experiments, as it contains non-negligible fractions of light resonant with the D_2 ($\lambda_{\mathrm{D2}} = 780.02\,\mathrm{nm}$) and D_1 lines ($\lambda_{\mathrm{D1}} = 797.98\,\mathrm{nm}$) of $^{87}\mathrm{Rb}$ [109], which give rise to enhanced heating and atom loss [95].

To suppress resonant light, we spectrally filter the TA output. When operating at $\lambda_\mathrm{d} = 784.7\,\mathrm{nm}$ (chapters 4 and 5), we employ a combination of two optical band-pass filters (Iridian-785nm and Semrock LL01-785-12) to suppress the spectral components outside a $\lambda_\mathrm{d} \pm 2$ nm transmission window. In chapter 6, we operate the transverse drive at $\lambda_\mathrm{d} = 790.02\,\mathrm{nm}$, which lies outside the bandwidth of the above listed optical filters. Instead, we employ a reflection grating (Edmund optics, 18000 Grooves/mm) to spatially separate the desired spectral component at λ_d from the broad background in the experimental table, preventing the latter to be fiber coupled to the science table. The grating is installed $\sim 25\,\mathrm{cm}$ away from the optical fiber and reflects about $\sim 60\%$ of the total laser power in its first order. In Fig. 3.6(b), we also show the PSD in the science table when including the reflection grating (red curve). As expected, we observe a suppression of the TA background to noise levels (PSD $\lesssim 80\,\mathrm{dBm}$).

When operating the system in a single drive configuration, we produce up to $P_\mathrm{d} = 150\,\mathrm{mW}$ of frequency and intensity stabilized laser light in the science table. In the two-drive configuration, we typically obtain up to $P_\mathrm{d} = 40\,\mathrm{mW}$ per TD beam. The factor of two reduction in power in the latter case is due to the last polarizing beamsplitter (PBS) used before the fiber to match the polarization of the two transverse drives. For comparison, before the TA installation, the available TD laser power in the science table was more than an order of magnitude smaller ($P_\mathrm{d} < 10\,\mathrm{mW}$) and insufficient to induce cavity-assisted Raman transitions.

3.3.2 Control over the spatial phase of the drives

In this section, we discuss the experimental control over spatial profile and relative phase of the transverse drives at the position of the atoms. After being fiber coupled to the science table, the transverse drive (TD) beams pass through beam shaping optics and a pair of motorized $\lambda/2$- and $\lambda/4$-waveplates to adjust their polarization. The TDs enter the vacuum chamber along the vertical (z) direction, propagate through the cavity and exit the chamber again. The thesis of Kristian Baumann [151] provides a complete overview of the TD optical setup in the science chamber, whereas the TD polarization is characterized in the thesis of Katrin Kroeger [152]. We calibrate the lattice depths associated with the transverse drives using Kapitza-Dirac diffraction [149], with the exact calibration procedure being detailed in Ref. [108].

For the experiments discussed in chapters 4 and 5, we operate the TDs in a standing-wave configuration. In a new optical breadboard placed above the vacuum chamber [152], we install the required optical elements to retro-reflect the transverse drives onto the atoms, see illustration in Fig. 3.7. Depending on the desired spatial phase between the two transverse drives, we employ two different motorized retro-reflecting mirror R_1 and R_2, which are placed at a distance of z_1 and z_2 from the

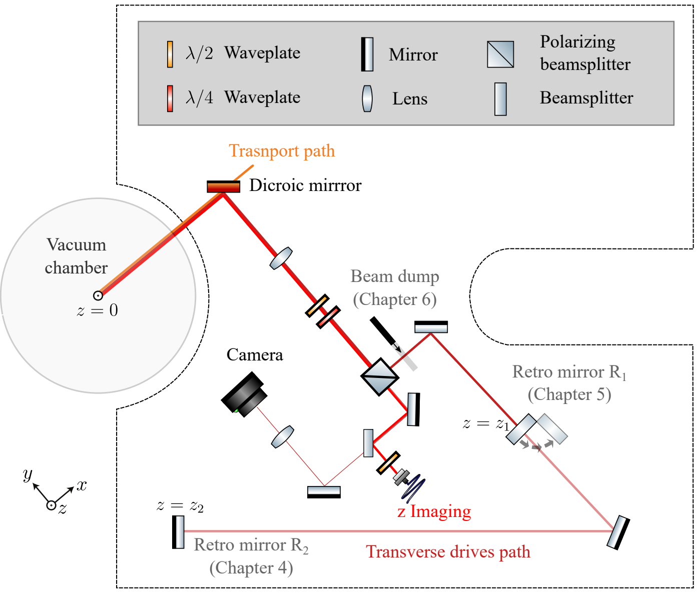
λ/2 Waveplate
λ/4 Waveplate
Mirror
Lens
Polarizing beamsplitter
Beamsplitter
Trasnport path
Dicroic mirrror
Vacuum chamber
z = 0
Beam dump (Chapter 6)
Camera
Retro mirror R1 (Chapter 5)
z = z1
y
x
z
z = z2
z Imaging
Retro mirror R2 (Chapter 4)
Transverse drives path

Figure 3.7: Optical path of transverse drive (TD) retro reflection (science table). After exiting the vacuum chamber along z direction, the two TD beams (dark red lines) can be retro-reflected by the motorized mirrors R_2 and R_1 which are placed at a distance z_2 and z_1 from the BEC, respectively. The combined standing-wave modulations are either in or out of phase at the position of the atoms, respectively. The polarization of the retro-reflecting path is adjusted using a pair of motorized waveplates. To obtain running-wave drive, we can block the retro-reflection using a beam dump. Adapted from Ref. [152].

BEC, respectively.

To model the combined standing-wave potential at the position of the atoms, we consider two classical y-polarized fields propagating along z-direction. The negative part of the total electric field $\mathbf{E}^{(-)}$ is

$$\mathbf{E}^{(-)} = \frac{E_r}{2}\cos(k_r z)\mathbf{e}_y e^{-i\omega_r t} + \frac{E_b}{2}\cos(k_b z)\mathbf{e}_y e^{-i\omega_b t}, \tag{3.12}$$

with $E_{r,b}$, $\omega_{r,b}$ and $k_{r,b} = \omega_{r,b}/c$ being the amplitudes, frequencies and wavenumbers of the two drives. The phase reference for both fields is determined by the position of the retro-reflecting mirror at $z = 0$. When considering a quantization axis along the $-z$ direction and dispersive atom-light interactions [see Eq. (2.12)], this linearly polarized electric field gives rise to an optical lattice potential

$$\begin{aligned} V_{\text{tot}}(z) = \alpha_s \hat{\mathbf{E}}^{(+)} \cdot \hat{\mathbf{E}}^{(-)} &= \frac{\alpha_s}{4}\left[E_r^2\cos^2\left(\frac{\omega_r}{c}z\right) + E_b^2\cos^2\left(\frac{\omega_b}{c}z\right)\right] \\ &= \underbrace{V\cos\left(\frac{\omega_b - \omega_r}{c}z\right)}_{V_{\text{env}}}\cos\left(\frac{2\bar{\omega}}{c}z\right) + V, \end{aligned} \tag{3.13}$$

where α_s is the scalar polarizability, $\bar{\omega} = (\omega_b + \omega_r)/2$ and $V = -\alpha_s E^2/4$ is the maximal lattice depth per drive in a balanced configuration, i.e., $E = E_r = E_b$. The expression in Eq. (3.13) comprises a rapidly varying $\lambda/2$-periodic lattice potential, with $\lambda = 2\pi c/\bar{\omega}$, and a slowly changing envelope V_{env}. In Fig. 3.8(a1), we plot the envelope potential as a function of the distance z between the retro-reflecting mirror and the BEC and the frequency difference between the drives $\omega_b - \omega_r$. For the relevant frequency differences $\omega_b - \omega_r \approx 2\pi \cdot 100\,\mathrm{MHz}$, the envelope function V_{env} periodically oscillates in space over a distance of $z \approx 1.5\,\mathrm{m}$.

For the experiments discussed in chapter 4, we employ the retro-reflecting mirror R_2 at a distance of $z_2 = 1.562\,\mathrm{m}$ from the BEC, see Fig. 3.7. For the considered frequency difference of $\omega_b - \omega_r = 2\pi \times 96\,\mathrm{MHz}$, the envelope function $V_{\mathrm{env}}(z_2) = V$ becomes maximal as the two optical lattices are in phase at the position of the atoms, see Fig. 3.8(a2). The resulting in-phase optical lattice motivates the introduction of identical spatial mode profiles for the transverse drives $f_{r,b} \propto \cos(kz)$, with $k = (k_r + k_b)/2$, when operating in this configuration. They are used to derive the extended Dicke model considered in chapter 4, see Eq. (4.1).

For the experiments presented in chapter 5, we also operate the drives at $\omega_b - \omega_r = 2\pi \times 96\,\mathrm{MHz}$ and place the second retro-reflecting mirror R_1 at a distance $z_1 = 0.781\,\mathrm{m}$ from the BEC, see Fig. 3.7. The two transverse drives are then fully out of phase at the position of the atoms yielding a vanishing envelope function $V_{\mathrm{env}}(z_1) = 0$, see Fig. 3.8(a2). Due to the suppressed combined standing-wave modulation, we refer to this setting as the *erased lattice configuration*. Since variations of V_{env} are negligible within the extent of the atomic cloud ($\sim 10\,\mu\mathrm{m}$), we introduce spatial mode profiles for the two drives $f_r(\mathbf{x}) = \cos(kz)$ and $f_b(\mathbf{x}) = \sin(kz)$. These mode profiles are used to derive the Hamiltonian inducing cavity-assisted tunneling in a momentum lattice in chapter 5.

To experimentally assess the quality of the erased lattice configuration, we place the mirror R1 at $z_1 = 0.781(5)$m and increase the combined lattice to $V = 24.2(1)$Erec within 20 ms. We vary the imbalance between the two drives at a fixed V and measure the population in the lattice momentum peaks $k_z = \pm 2k$ after time-of-flight expansion (see insets in Fig. 3.8(b)). By performing complementary measurements with a single drive, we can convert the measured populations in $k_z = \pm 2k$ into equivalent lattice depths. In Fig. 3.8, we show the inferred equivalent lattice depth for different nominal imbalances. For optimally balanced drives with a small imbalance of 0.5(4) Erec, we measure a small residual lattice depth of 0.8(4) Erec, which indicates a suppression of the total lattice modulation by a factor > 30 compared to the single-drive case.

Finally, for the experiments discussed in chapter 6, we simplify the transverse drive setup. We illumine the atoms with a single drive (TD_1) at frequency ω_{d} and block the retro-reflection with a removable beam dump, see Fig. 3.7. Hence, the drive is operated in a running-wave configuration with a spatial profile given by $f(z) = e^{ikz}$, with wavenumber $k = \omega_{\mathrm{d}}/c$.

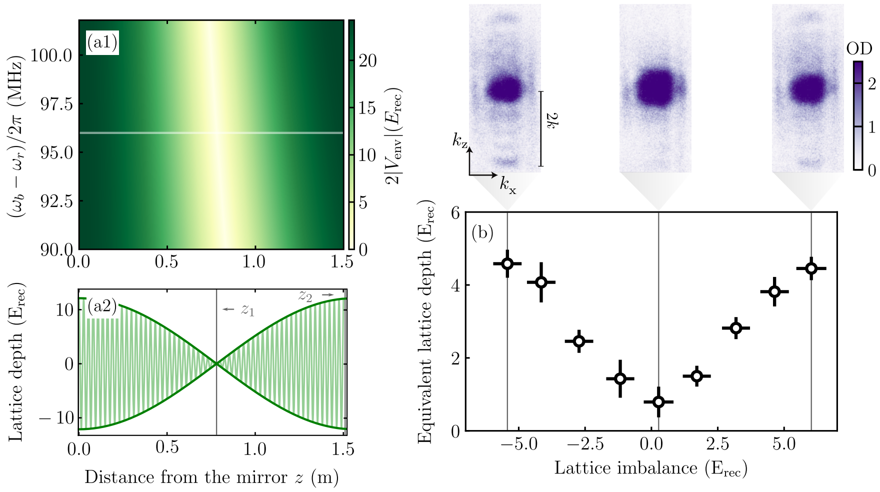

Figure 3.8: Controlling the relative spatial phase of the transverse drives. (a1) Lattice envelope V_{env} generated by the transverse drives as a function of their frequency difference $\omega_b - \omega_r$ and the distance z between the retro-reflecting mirror and the BEC. **(a2)** Combined standing-wave potential $V_{\text{Tot}}(z)$ (light green) and lattice envelope (dark green) for the experimentally relevant difference $\omega_b - \omega_r = 2\pi \cdot 96\,\text{MHz}$ [white line in (a1)]. For $z_1 = 0.781\,\text{m}$ ($z_2 = 2z_1$), the envelope vanishes (is maximal) as the two standing-wave modulations are out of phase (in phase) at the position of the BEC. Here, we set $V = 12\ E_{\text{rec}}$ and undersample $V_{\text{Tot}}(z)$ for better visibility. **(b)** Experimental verification of the erased lattice configuration for $z = z_1$. We infer the equivalent lattice depth as a function of drive imbalance for large combined lattices $V = 24.2(1)\,\text{E}_{\text{rec}}$ (see main text). A suppression of the lattice depth by a factor of > 30 is observed when the two drives are balanced drives. Insets: momentum-space distributions in $m = -1$, showing occupation of lattice momentum peaks at $k_z = \pm 2k$ for finite lattice imbalances, with k being the photon recoil momentum. Adapted from Ref. [90].

4 Dissipative phases and transitions in a superradiant quantum gas

Open many-body systems can challenge the fundamental laws governing the physics of systems in thermal equilibrium. In the idealized case of an ensemble of particles, isolated from the environment and at zero temperature, the ground state phases are solely determined by energy minimization [153, 154]. However, in open systems, the interplay between coherent dynamics within the system and its interaction with the environment yields much richer phenomenology [26, 155–159]. Such interaction is not only unavoidable but can be exploited via the engineering of external drives and coupling to specific baths [160–163].

Historically, cold-atoms experiments have aimed to isolate interacting many-body systems from the environment for performing analog quantum simulation [164, 165], see Fig. 4.1(a1). Close to zero temperature, the ground state properties of these systems are determined by the competition of different energy scales, such as the kinetic and internal energies of the atoms, and their effective interaction strength $\bar{\eta}$ [153]. When the interactions are increased above a critical value, $\bar{\eta} > \eta_c$, the system can undergo a quantum phase transition to a spatially ordered configuration, as depicted Fig. 4.1(a2). Such phases are characterized by a mean-field order parameter assuming non-zero values, $\Theta \neq 0$, each indicating a different symmetry-broken configuration. Experiments simulating many-body phase transitions with ultracold atoms are diverse, and include the superfluid-Mott insulator transition [39], the formation of the Fermi-Hubbard antiferromagnet [42, 43] and the superfluid-supersolid phase transitions [68, 166]. However, these 'closed systems' are only in good approximation fully isolated from the environment; they are indeed affected by spurious dissipative processes, such as atom loss and heating which can prove detrimental to the accessible phases and dynamics [21].

In recent years, the experimental access provided by ultracold atoms has sparked a revival of interest in many-body systems interacting with their environment [167, 168]. Observations arising from the system's openness include the emergence of multistable phases [169–172], the stabilization of insulators [33, 173] and the appearance of dissipation-induced limit cycles [73–75]. Besides their fundamental interest, non-equilibrium phenomena bear the prospect of becoming versatile tools for engineering new materials ranging from exciton condensates to light-induced superconductors [174–178]. The properties of these phases emerge from tuning the elementary excitations by hybridization with the incident light field [179, 180], providing a natural coupling to the environment in presence of optical drives and losses [181, 182]. To gain further insight into this phenomenology, it is essential to achieve experimental control over coherent and dissipative channels and at the same time to gain access to the microscopic processes underlying the observed macroscopic phases [183].

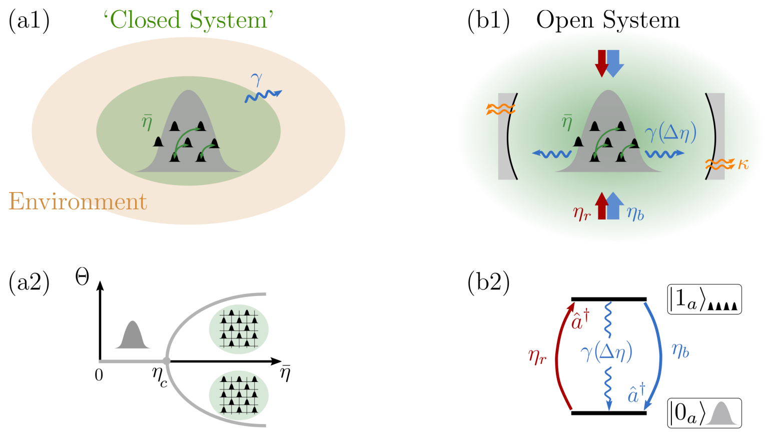

Figure 4.1: Engineered coherent and dissipative coupling in a quantum gas. **(a)** Closed system implementations. (a1) Conventional cold-atom experiments aim to isolate an interacting quantum gas, with typical interaction rate $\bar{\eta}$, from the environment. (a2) Mean-field ground states. For sufficiently strong interactions $\bar{\eta} > \eta_c$, the system may undergo a symmetry-breaking transition to an ordered phase characterized by the macroscopic order parameter $\Theta \neq 0$. However, all feasible experimental implementations are only approximately fully isolated many-body systems, as they are subject to spurious dissipative processes (with rate γ). **(b)** Engineered many-body open system. (b1) Coupling a degenerate quantum gas to an optical cavity via two external drives ($\eta_{b,r}$) inherently realizes an open system due to cavity losses at rate κ. (b2) Schematic coupling mechanism. The drives implement co- and counter-rotating light-matter interactions, hybridizing two well-defined atomic modes ($|0_a\rangle, |1_a\rangle$) with the cavity field (operator $\hat{a}^\dagger$). At the same time, the decay rate $\gamma(\Delta\eta)$ of the underlying light-matter excitations can be controlled via the drive imbalance $\Delta\eta = (\eta_b - \eta_r)/2$. In such systems, the interplay between controlled coherent and dissipative processes results in a rich phenomenology.

In this chapter, we engineer an open many-body system with photon-mediated interactions that is subject to tunable coherent and dissipative couplings by preparing a degenerate quantum gas in a high-finesse optical cavity, see Fig. 4.1. The atomic system can be accurately captured by two well-defined modes $|0\rangle_a$ and $|1\rangle_a$, which incorporate not only two differing internal levels but also homogeneous ($|0\rangle_a$) and density-modulated external states ($|1\rangle_a$), as illustrated in Fig. 4.1(b2). We employ two laser drives to independently control the strength of co- and counter-rotating light-matter interactions, η_r and η_b. As we increase the average coherent interactions $\eta = (\eta_r + \eta_b)/2$, the atomic modes hybridize with the cavity field $\hat{a}$ to form polariton modes, giving rise to a superradiant phase transition above a critical coupling, $\bar{\eta} > \eta_c$. The openness of the system arises from cavity losses at a rate κ and gives rise a collective decay of the excited polariton modes, $\gamma(\Delta\eta)$, which we control by adjusting the relative strength of the two drives $\Delta\eta = (\eta_b - \eta_r)/2$. For dominant dissipative couplings, this results in significant qualitative changes of the phase diagram. Specifically, we observe the appearance of a dissipation-stabilized phase and a discontinuous phase transition in a bistable region, as pointed out in previous theoretical works in Refs. [159, 184]. To provide a microscopic description of our system, we connect our observations to the properties of the underlying polariton excitations which we characterize experimentally and theoretically.

Outline of this chapter

In section 4.1, we map cavity-assisted Raman scattering in our system to an extended Dicke model with tunable co- and counter-rotating light-matter couplings and discuss the theoretical framework to analyze the open system dynamics. In section 4.2, we focus on the case of balanced couplings where our system is mapped to a spinor Dicke model. We present a direct experimental observation of the corresponding superradiant phase (SP) transition and discuss the associated technical challenges. In section 4.3, we investigate the interplay between coherent and dissipative dynamics by controlling the strength of the co- and counter-rotating couplings, and demonstrate the emergence of a dissipation-stabilized normal phase (DSNP). In section 4.4, we show how this interplay further influences the system's dynamical behavior, resulting in DSNP-SP bistability and a discontinuous phase transition. In section 4.5, we present a new protocol for probing of the underlying light-matter excitation dynamics in real time. By characterizing the excitation dynamics, we establish a relation between the observed macroscopic phases and the elementary microscopic processes in our system. Finally, in section 4.6, we summarize our findings and provide perspectives for future experiments.

Parts of this chapter have been published in Ref. [90]:

> F. Ferri*, R. Rosa-Medina*, F. Finger, N. Dogra, M. Soriente, O. Zilberberg, T. Donner and T. Esslinger. *Emerging Dissipative Phases in a Superradiant Quantum Gas with Tunable Decay.* Physical Review X **11**, 041046 (2021)
> * These authors contributed equally to this work

4.1 Coupling scheme and theoretical description

In this section, we discuss the theoretical framework of our experiments. After a qualitative discussion of the coupling scheme in section 4.1.1, we map our system to a generalized Dicke model featuring tunable co- and counter-rotating couplings in section 4.1.2. We derive the equations of motion and steady-state solutions for the open system in section 4.1.3. Finally, in section 4.1.4, we discuss the framework for analyzing the excitation spectrum of our system.

4.1.1 Coupling configuration and qualitative description

In our experiments, we trap a ^{87}Rb Bose-Einstein condensate (BEC) inside our optical cavity and illuminate it with a two-frequency optical standing-wave drive perpendicular to the cavity axis, cf. Fig. 4.2(a). The BEC is formed by $N \approx 10^5$ atoms initialized in the $m = -1$ Zeeman sublevel of the $F = 1$ manifold. A strong magnetic field $B = 68.3\,\mathrm{G}$ along the $-z$-direction defines the quantization axis and yields a linear Zeeman splitting $\omega_z = -2\pi \times 48$ MHz between the $m = -1$ and $m = 0$ sublevels. The two driving fields at $\lambda_\mathrm{d} = 784.7\,\mathrm{nm}$ operate in the dispersive regime, with their frequencies ω_b and ω_r being set on opposite sides of the cavity resonance ω_c and $\omega_b - \omega_r \approx 2|\omega_z|$, cf. Fig. 4.2(b). Their standing-wave modulations are in phase at the position of the atoms, forming a one-dimensional $\lambda_\mathrm{d}/2$-periodic lattice potential. For technical details on the experimental implementation, see section 3.3.2.

Each transverse drive realizes cavity-assisted Raman transitions between the $m = -1$ and $m = 0$ levels, as depicted in Fig. 4.2(b). The resulting system can be described by considering two atomic states comprising well-defined spin and motional modes: the initial ground state of the trapped BEC in $m = -1$ [state $|0_a\rangle$] and an excited-momentum state in the neighboring Zeeman sublevel $m = 0$ [state $|1_a\rangle \propto \cos(kx)\cos(kz)\hat{F}_+ |0_a\rangle$], with $\hat{F}_+$ and $k = 2\pi/\lambda_\mathrm{d}$ being the $F = 1$ raising operator and the photon recoil momentum, respectively. The two Raman drives implement tunable co- and counter-rotating light-matter interactions, with rates η_r and η_b, respectively. When balanced ($\eta_r = \eta_b$), the many-body system reduces to a dispersive implementation of the Dicke Hamiltonian [61] exhibiting superradiant phase transition above a critical coupling strength. This phase is characterized by a steady-state cavity field at the intermediate frequency between the drives $\bar{\omega} = (\omega_b + \omega_r)/2$ and by an emergent λ_d-periodic checkerboard modulation of the atomic transverse magnetization [79].

Our experiment inherently realizes an open quantum system, as the cavity field decays at a rate κ. Close to the Dicke limit, cavity losses only result in a small shift of the critical coupling. However, by adjusting the imbalance between the co- and counter-rotating couplings, $\Delta\eta = (\eta_b - \eta_r)/2$, we can modify the decay rate $\gamma \propto \Delta\eta$ of the associated light-matter excitations (polaritons). The underlying microscopic process is superradiant Raman scattering of photons induced by each laser drive and the dissipatively-broadened density of states of the cavity. As we experimentally demonstrate in the following sections, this tunable dissipation channel significantly alters the superradiant phase transition, introducing dissipation-stabilized normal phases and hysteretic transitions.

4.1.2 Mapping to a generalized Dicke model

We consider two y-polarized transverse drive fields propagating along the z-direction (with frequencies $\omega_{r,b}$ and amplitudes $E_{r,b}$) and the quantized field of the cavity. The negative part $\hat{\mathbf{E}}^{(-)}$ of the total electric field is

$$\hat{\mathbf{E}}^{(-)} = \frac{E_r}{2} f_r(\hat{\mathbf{x}})\mathbf{e}_y e^{-i\omega_r t} + \frac{E_b}{2} f_b(\hat{\mathbf{x}})\mathbf{e}_y e^{-i\omega_b t} + E_0 g(\hat{\mathbf{x}})\hat{a}\mathbf{e}_z. \tag{4.1}$$

The operator $\hat{a}$ annihilates z-polarized photons in the TEM$_{00}$ cavity mode with vacuum electric field amplitude E_0. Given their small frequency difference $\omega_b - \omega_r = 2\pi \times 96$ MHz, we consider a common wavenumber $k = \bar{\omega}/c$ for the standing-wave drives, with $\bar{\omega} = (\omega_b + \omega_r)/2$. We account for finite-size effects, by considering the finite transverse extension of the spatial modes $f_{r,b}(\hat{\mathbf{x}}) = f(\hat{\mathbf{x}}) = \exp\left[-2x^2/w_x^2 - 2y^2/w_y^2\right]\cos(kz)$. Furthermore, the cavity mode profile is given by $g(\hat{\mathbf{x}}) = \exp\left[-2(y^2 + z^2)/w_c^2\right]\cos(kx)$. The corresponding waist sizes are $[w_x, w_y, w_c] = [24, 27, 25]$ µm [145].

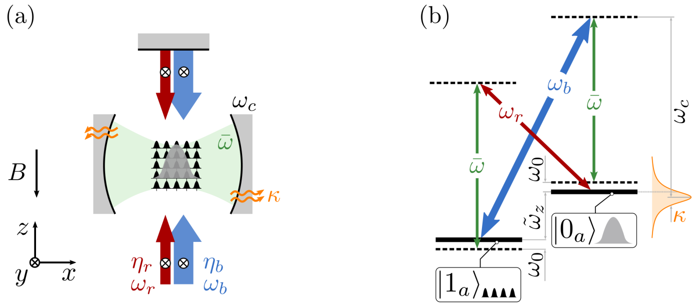

Figure 4.2: Experimental setup. **(a)** Schematics of the experimental setup. A BEC inside a high-finesse cavity (with resonant frequency ω_c and field decay rate κ) is illuminated by two y-polarized transverse drives with Raman couplings $\eta_{b,r}$ and frequencies $\omega_{b,r}$. The two standing-wave drives are in phase at the position of the BEC, see section 3.3.2. A magnetic field B along $-z$-direction defines the quantization axis. **(b)** Simplified level scheme. The BEC in the $m = -1$ Zeeman sublevel (mode $|0_a\rangle$) is coupled to a spatially modulated state in $m = 0$ ($|1_a\rangle$), separated by an energy offset $\hbar\tilde{\omega}_z$. In the superradiant phase, a coherent z-polarized cavity field builds up at the intermediate frequency $\bar{\omega} = (\omega_b + \omega_r)/2$ (green arrows). The corresponding two-photon transitions at $\bar{\omega}$ are detuned from the bare atomic states $|0_a\rangle$, $|1_a\rangle$ by $\mp\omega_0$ [dashed lines in (b)], requiring softening of the underlying excitations.

We consider dispersive atom-light interaction, as derived in the general Hamiltonian of Eq. (2.12). We derive the single-particle Hamiltonian

$$\hat{H}_{\mathrm{SP}} = \hat{H}_{\mathrm{at}} + \hat{H}_{\mathrm{cav}} + \hat{H}_{\mathrm{s}} + \hat{H}_{\mathrm{v}}, \tag{4.2}$$

in a rotating frame induced by the generator $\hat{H}_{\mathrm{rot}} = \hbar\bar{\omega}\hat{a}^\dagger\hat{a} - \hbar\omega_z'\hat{F}_z$, with $\omega_z' = (\omega_b - \omega_r)/2$. In this rotating frame, a cavity field oscillating at $\bar{\omega} = (\omega_b + \omega_r)/2$ becomes time independent. The bare atomic Hamiltonian

$$\hat{H}_{\mathrm{at}} = \frac{\hat{p}^2}{2M} + V_{\mathrm{ext}}(\hat{\mathbf{x}}) + \hbar\delta_z\hat{F}_z + \hbar q\hat{F}_z^2, \tag{4.3}$$

can be written in terms of the $F = 1$ spin operator $\hat{\mathbf{F}} = (\hat{F}_x, \hat{F}_y, \hat{F}_z)^T$. The external trapping potential $V_{\mathrm{ext}}(\hat{\mathbf{x}})$ is kept fixed during the experiments. In this rotating frame, the energy difference between the Zeeman sublevels is determined by the effective linear shift $\delta_z = \omega_z + \omega_z'$ and the quadratic Zeeman splitting $\hbar q > 0$. The Hamiltonian of the bare cavity mode reads

$$\hat{H}_{\mathrm{cav}} = -\hbar\Delta_c\hat{a}^\dagger\hat{a}, \tag{4.4}$$

with $\Delta_c = \bar{\omega} - \omega_c$ defining the detuning with respect to the cavity resonance ω_c.

The atom-light interactions comprise scalar and vectorial contributions

$$\begin{aligned}\hat{H}_{\mathrm{s}} &= \frac{\alpha_s}{4}(E_b^2 + E_r^2)f(\hat{\mathbf{x}})^2 + \alpha_s E_0^2\hat{a}^\dagger\hat{a}g(\hat{\mathbf{x}})^2,\\ \hat{H}_{\mathrm{v}} &= \frac{\alpha_v}{8}E_0\left[(E_b + E_r)\left(\hat{a} + \hat{a}^\dagger\right)\hat{F}_x + (E_b - E_r)\,i\left(\hat{a} - \hat{a}^\dagger\right)\hat{F}_y\right]f(\hat{\mathbf{x}})g(\hat{\mathbf{x}}),\end{aligned} \tag{4.5}$$

where we apply a global rotation of the cavity field $\hat{a} \to \hat{a}e^{i\pi/2}$. The first term of $\hat{H}_s$ describes a one-dimensional lattice potential created by the drives (z-direction), with maximal lattice depth $V_\mathrm{d} = -\alpha_s(E_b^2 + E_r^2)/4$. The second term in $\hat{H}_s$ is responsible for the dispersive shift of the cavity resonance due to a weak dynamical lattice along x, with maximal dispersive shift per atom $U_0 = \alpha_s E_0^2/\hbar$. The vectorial interactions, $\hat{H}_v$, induce cavity-assisted Raman transition between the Zeeman sublevels of the $F = 1$ manifold. Here, the spin-changing terms $\hat{F}_x$ and $\hat{F}_y$ are mediated by orthogonal quadratures of the cavity field, and can be independently controlled by the amplitude sum and difference of the two drives $E_{r,b}$, respectively.

Many-body Hamiltonian in a two-mode approximation

We derive the many-body Hamiltonian for a spinor BEC using the formalism of second quantization

$$\hat{H} = \hat{H}_\mathrm{cav} + \int \hat{\Psi}^\dagger(\mathbf{x}) \left(\hat{H}_\mathrm{at} + \hat{H}_\mathrm{s} + \hat{H}_\mathrm{v}\right) \hat{\Psi}(\mathbf{x}) d\mathbf{x}, \tag{4.6}$$

where $\hat{\Psi}(\mathbf{x}) = \left(\hat{\Psi}_{+1}(\mathbf{x}),\, \hat{\Psi}_0(\mathbf{x}),\, \hat{\Psi}_{-1}(\mathbf{x})\right)^T$ is a spin-1 atomic field operator. At this level, we neglect collisional interactions for sufficiently low densities. At the large magnetic field we operate, $B = 68.3\,\mathrm{G}$, cavity-assisted Raman transitions to $m = +1$ are detuned by $\Delta_{+1} \approx 2q = 2\pi \times 0.7$ MHz, which determines the fastest timescale of the atomic evolution. This allows us to adiabatically eliminate the atomic operator $\hat{\Psi}_{+1}$, and restrict the dynamics to the Zeeman sublevels $m = -1$ and $m = 0$.

We map our system to a generalized Dicke model by further restricting the Hilbert space to two well-defined spin and momentum modes. In the normal phase, the $m = -1$ BEC occupies the ground state of the total trapping potential arising from the external trap V_ext and the attractive lattice potential of the drives V_d, cf. Eq (4.5). We label this ground state as $|0_a\rangle$, with corresponding wave function $\Phi_{0_a}(\mathbf{x})$. Cavity-assisted Raman transitions couple $|0_a\rangle$ to a density-modulated state in $m = 0$, which we refer to as $|1_a\rangle$. The correspoding single-particle wave function is given by $\Phi_{1_a}(\mathbf{x}) = \mathcal{N}\Phi_{0_a}(\mathbf{x})\cos(kx)\cos(kz)$, with $\mathcal{N}$ being a suitable normalization factor. When increasing the driving strength, the ground state $|0_a\rangle$ evolves from a harmonically confined BEC to a stack of pancake-shaped BECs trapped in the maxima of the standing-wave drives. Within this two-mode description, the spinor field operator takes the form $\hat{\Psi}(\mathbf{x}) = (0,\, \Phi_{1_a}(\mathbf{x})\hat{c}_{1_a},\, \Phi_{0_a}(\mathbf{x})\hat{c}_{0_a})^T$, where $\hat{c}_{0_a}$ and $\hat{c}_{1_a}$ are bosonic annihilation operators for the respective modes.

Within this two-mode approximation, the many-body Hamiltonian is given by

$$\begin{aligned}\hat{H} = &-\hbar\left[\Delta_c - N\mathcal{I}(V_\mathrm{d})U_0\right]\hat{a}^\dagger\hat{a} + \hbar\omega_0(V_\mathrm{d})\hat{J}_z \\ &+ \frac{\alpha_v}{4\sqrt{2}}\mathcal{M}(V_\mathrm{d})E_0\left[(E_b + E_r)(\hat{a} + \hat{a}^\dagger)\hat{J}_x + i(E_b - E_r)(\hat{a} - \hat{a}^\dagger)\hat{J}_y\right],\end{aligned} \tag{4.7}$$

where we introduce pseudo-spin-$N/2$ operators $\hat{J}_x = (\hat{c}_{1_a}^\dagger\hat{c}_{0_a} + \hat{c}_{0_a}^\dagger\hat{c}_{1_a})/2$, $\hat{J}_y = (\hat{c}_{1_a}^\dagger\hat{c}_{0_a} - \hat{c}_{0_a}^\dagger\hat{c}_{1_a})/2i$ and $\hat{J}_z = (\hat{c}_{1_a}^\dagger\hat{c}_{1_a} - \hat{c}_{0_a}^\dagger\hat{c}_{0_a})/2$. We indicate with $\hbar\omega_0(V_\mathrm{d})$ the energy difference between the bare atomic modes. The different overlap integrals are defined as $\mathcal{I}(V_\mathrm{d}) = \langle 0_a| g(\mathbf{x})^2 |0_a\rangle /N$ and $\mathcal{M}(V_\mathrm{d}) = \langle 0_a| f(\mathbf{x})g(\mathbf{x}) |1_a\rangle /N$. A detailed discussion of their scaling can be found in the PhD thesis of Nishant Dogra [108].

In the limit of small lattice depths, the many-body Hamiltonian can be simplified to

$$\hat{H} = -\hbar\Delta_c \hat{a}^\dagger \hat{a} + \hbar\omega_0 \hat{J}_z + 2\hbar\bar{\eta}(\hat{a} + \hat{a}^\dagger)\hat{J}_x + 2i\hbar\Delta\eta(\hat{a} - \hat{a}^\dagger)\hat{J}_y, \tag{4.8}$$

where we substitute $[\Delta_c - N\mathcal{I}(V_\mathrm{d})U_0] \rightarrow \Delta_c$, and define $\eta_{b,r} = \frac{\alpha_v}{4\sqrt{2}}\mathcal{M}(V_\mathrm{d})E_0 E_{b,r}$ and $\hbar\omega_0 = \hbar(\omega_z' - \omega_z + 2\omega_\mathrm{rec})$ for $V_\mathrm{d} \rightarrow 0$. Additionally, we introduce the average Raman coupling $\bar{\eta} = (\eta_b + \eta_r)/2$ associated with both drives and the coupling imbalance $\Delta\eta = (\eta_b - \eta_r)/2$. A slight rearrangement of terms gives

$$\hat{H} = -\hbar\Delta_c \hat{a}^\dagger \hat{a} + \hbar\omega_0 \hat{J}_z + \hbar\eta_b(\hat{a}\hat{J}_+ + \hat{a}^\dagger \hat{J}_-) + \hbar\eta_r(\hat{a}^\dagger \hat{J}_+ + \hat{a}\hat{J}_-), \tag{4.9}$$

with $\hat{J}_\pm = \hat{J}_x \pm i\hat{J}_y$. Here, it becomes apparent that the couplings η_b and η_r control the strength of the co- and counter-rotating light-matter interactions, respectively. This enhanced level of experimental control over atom-light interactions in our system stems from coupling two specific spin and momentum modes using two independently tunable Raman drives, and is not present in conventional cold-atom implementations of the Dicke model solely relying on external atomic modes [62].

The model introduced in Eq. (4.8) is a *generalized Dicke Hamiltonian* [159, 184–187], also referred to as *interpolating Dicke Tavis-Cummings model* [159, 184]. In the limit of balanced drives, $\Delta\eta = 0$, it reduces to of the paradigmatic Dicke model [61, 62], coupling the real quadrature cavity field to the coherence between the two atomic modes $\hat{J}_x$. Increasing $\Delta\eta > 0$ induces a concurrent coupling to the orthogonal atomic coherence $\hat{J}_y$ mediated by the imaginary quadrature of the cavity field. In the limit of large imbalances, $\Delta\eta = \bar{\eta}$ $(\eta_r = 0)$, the Hamiltonian in Eqs. (4.8) and (4.9) converges to the Tavis-Cummings model [113], which we theoretically discuss in the previous chapter.

The generalized Dicke Hamiltonian in Eq. (4.8) has a $\mathbb{Z}_2 \times \mathbb{Z}_2$ symmetry [159]. This symmetry is associated with a simultaneous transformation of the real or imaginary quadratures of the cavity field together with the corresponding spin operators, i.e., $[(\hat{a} + \hat{a}^\dagger),\ \hat{J}_x] \rightarrow -[(\hat{a} + \hat{a}^\dagger),\ \hat{J}_x]$ and $[i(\hat{a} - \hat{a}^\dagger),\ \hat{J}_y] \rightarrow -[i(\hat{a} - \hat{a}^\dagger),\ \hat{J}_y]$. In the Tavis-Cummings limit, $\Delta\eta = \bar{\eta}$, the system possesses an enlarged $U(1)$ symmetry [159], as the Hamiltonian is invariant under the continuous phase transformation $[\hat{a},\ \hat{J}_-] \rightarrow [\hat{a},\ \hat{J}_-]e^{i\varphi}$, with $\varphi \in [0, 2\pi)$.

4.1.3 Equations of motion and solutions of the open system

Our experiment inherently realizes an open quantum system as the cavity field decays at a finite rate $\kappa = 2\pi \times 1.25\,\mathrm{MHz}$, and the associated dynamics cannot be fully captured by a many-body Hamiltonian. Starting from the Lindblad master equation discussed in Eq. (2.21), we derive mean-field equations of motion (EOMs)

$$\begin{aligned}
\frac{\mathrm{d}}{\mathrm{d}t}\alpha &= i\Delta_c\alpha - i2\sqrt{N}\bar{\eta}X - 2\sqrt{N}\Delta\eta Y - \kappa\alpha\,, \\
\frac{\mathrm{d}}{\mathrm{d}t}X &= -\omega_0 Y - 4\sqrt{N}\Delta\eta\alpha_{\mathrm{Im}}Z - \Gamma_\phi X\,, \\
\frac{\mathrm{d}}{\mathrm{d}t}Y &= \omega_0 X - 4\sqrt{N}\bar{\eta}\alpha_{\mathrm{Re}}Z - \Gamma_\phi Y\,, \\
\frac{\mathrm{d}}{\mathrm{d}t}Z &= 4\sqrt{N}\bar{\eta}\alpha_{\mathrm{Re}}Y + 4\sqrt{N}\Delta\eta\alpha_{\mathrm{Im}}X\,.
\end{aligned} \tag{4.10}$$

Here, we introduce normalized mean-field observables $\alpha = \langle\hat{a}\rangle/\sqrt{N}$ and $K = \langle\hat{J}_K\rangle/N$, with $K \in \{X, Y, Z\}$, and define $\alpha_{\mathrm{Re}} = \mathrm{Re}(\alpha)$ and $\alpha_{\mathrm{Im}} = \mathrm{Im}(\alpha)$. In the EOMs, we further include a phenomenological spin dephasing term with rate Γ_ϕ, which we attribute to the combined effect of atomic collisions and magnetic field fluctuations [72]. This term is compatible with a Lindblad term of the form $\mathcal{L}[\hat{J}_z] = \Gamma_\phi[2\hat{J}_z\hat{\rho}\hat{J}_z - \{\hat{J}_z\hat{J}_z, \hat{\rho}\}]$ [89].

We set the derivatives of the EOMs to zero, e.g., $\frac{\mathrm{d}}{\mathrm{d}t}X = 0$, and solve for the steady-state solutions of the system. We note that the *normal phase* with $\alpha = X = Y = 0$ and $Z = -1/2$ is always a trivial steady-state solution of the mean-field EOMs. This phase is characterized by a vanishing cavity field $\alpha = 0$ and by all atoms occupying the atomic ground state $|0_a\rangle$, i.e., $Z = -1/2$.

The system can also support a *superradiant phase* exhibiting a non-vanishing cavity field $\alpha \neq 0$. By imposing total spin conservation, $X^2 + Y^2 + Z^2 = 1/4$, we obtain the following set of nontrivial steady-state solutions

$$\begin{aligned}
\alpha_{\mathrm{Re}} &= \pm\sqrt{c}\sqrt{\frac{2a_2^2b_1 + a_2b_2^2 - 2a_2b_3(a_1+b_1) + 2a_1b_3^2 + \mathrm{sgn}[\Delta\eta_N - \bar{\eta}_N]a_2|b_2|\sqrt{b_2^2 - 4(a_1-b_1)(a_2-b_3)}}{2(a_2^2b_1^2 + a_1^2b_3^2 + a_1a_2(b_2^2 - 2b_1b_3))}}\,, \\
\alpha_{\mathrm{Im}} &= \frac{b_2^2 - \mathrm{sgn}[\Delta\eta_N - \bar{\eta}_N]|b_2|\sqrt{4(b_1-a_1)(a_2-b_3) + b_2^2}}{2b_2(a_2-b_3)}\alpha_{\mathrm{Re}}\,, \\
X &= -\frac{\Delta_c\alpha_{\mathrm{Re}} + \kappa\alpha_{\mathrm{Im}}}{2\bar{\eta}_N}\,, \qquad Y = \frac{\Delta_c\alpha_{\mathrm{Im}} - \kappa\alpha_{\mathrm{Re}}}{2\Delta\eta_N}\,, \\
Z &= -\frac{\left(\bar{\eta}_N^2 + \Delta\eta_N^2\right)\Delta_c - \sqrt{\left(\bar{\eta}_N^2 - \Delta\eta_N^2\right)^2\Delta_c^2 - 4\kappa^2\bar{\eta}_N^2\Delta\eta_N^2}}{16\bar{\eta}_N^2\Delta\eta_N^2}\omega_0 = \mathcal{A}\omega_0\,,
\end{aligned} \tag{4.11}$$

where we introduce the normalized couplings $\bar{\eta}_N = \sqrt{N}\bar{\eta}\,, \Delta\eta_N = \sqrt{N}\Delta\eta$, and

$$\begin{aligned}
&a_1 = 16\mathcal{A}^2\bar{\eta}_N^2\,, \quad a_2 = 16\mathcal{A}^2\Delta\eta_N^2\,, \quad b_1 = \left(\kappa^2/\Delta\eta_N^2 + \Delta_c^2/\bar{\eta}_N^2\right)/4\,, \\
&b_2 = \kappa\Delta_c\left(1/\bar{\eta}_N^2 - 1/\Delta\eta_N^2\right)/2\,, \quad b_3 = \left(\kappa^2/\bar{\eta}_N^2 + \Delta_c^2/\Delta\eta_N^2\right)/4\,, \quad c = 1/4 - \mathcal{A}^2\omega_0^2\,.
\end{aligned} \tag{4.12}$$

The superradiant phase is characterized by the system occupying a superposition between the ground $|0_a\rangle$ and excited state $|1_a\rangle$, as signaled by the non-vanishing atomic coherences $X \neq 0$ and $Y \neq 0$. For sufficiently large cavity detunings $|\Delta_c| > \kappa$, these coherences are primarily associated with the real (α_{Re}) and imaginary quadratures of the cavity field (α_{Im}), respectively. For $\Delta_c < 0$, the system features four different superradiant solutions with (α_{Re}, X), ($-\alpha_{\mathrm{Re}}$, $-X$), (α_{Im}, Y) and ($-\alpha_{\mathrm{Im}}$,

$-Y$) which is a direct consequence of the underlying $\mathbb{Z}^2 \times \mathbb{Z}^2$ symmetry of the generalized Dicke Hamiltonian, as discussed in the previous section. A detailed derivation of these steady-state solutions can be found in the PhD thesis of Matteo Soriente in Ref. [188].

4.1.4 Calculating the energy spectrum of the system

To examine the stability behavior of the steady-state solutions and characterize the energy spectrum of the open system, we expand the order parameters as $\alpha = \alpha_0 + \delta\alpha, X = X_0 + \delta X, Y = Y_0 + \delta Y, Z = Z_0 + \delta Z$ around the steady-state solutions $(\alpha_0, X_0, Y_0, Z_0)$, chosen to be either the normal or the superradiant phase. A similar treatment has been used in Refs. [159, 189]. We start from the mean-field EOMs in Eq. (4.10), consider only linear contribution of the fluctuations $(\delta\alpha, \delta X, \delta Y, \delta Z)$, and obtain

$$\frac{\mathrm{d}}{\mathrm{d}t}\begin{pmatrix}\delta\alpha_{\mathrm{Re}}\\ \delta\alpha_{\mathrm{Im}}\\ \delta X\\ \delta Y\\ \delta Z\end{pmatrix} = \mathbf{M_0}\begin{pmatrix}\delta\alpha_{\mathrm{Re}}\\ \delta\alpha_{\mathrm{Im}}\\ \delta X\\ \delta Y\\ \delta Z\end{pmatrix}, \tag{4.13}$$

with the stability matrix

$$\mathbf{M_0} = \begin{pmatrix} -\kappa & -\Delta_c & 0 & -2\Delta\eta_N & 0 \\ \Delta_c & -\kappa & -2\bar{\eta}_N & 0 & 0 \\ 0 & -4\Delta\eta_N Z_0 & -\Gamma_\phi & -\omega_0 & -4\Delta\eta_N\alpha^0_{\mathrm{Im}} \\ -4\bar{\eta}_N Z_0 & 0 & \omega_0 & -\Gamma_\phi & -4\bar{\eta}_N\alpha^0_{\mathrm{Re}} \\ 4\bar{\eta}_N Y_0 & 4\Delta\eta_N X_0 & 4\Delta\eta_N\alpha^0_{\mathrm{Im}} & 4\bar{\eta}_N\alpha^0_{\mathrm{Re}} & 0 \end{pmatrix}. \tag{4.14}$$

By diagonalizing $\mathbf{M_0}$, we obtain both eigenfrequencies of the system and evaluate the stability of the different steady-state solutions [189]. Specifically, the imaginary part of the eigenvalues represents the energy cost associated with different excitation branches, while an eigenvalue with a positive real part indicates that the corresponding steady-state solution becomes unstable against small linear perturbations.

In our system, the underlying excitations are *polariton modes* [190, 191]. The collective light-matter excitations either hybridize the cavity field with the atomic components (photonic branches) or the atomic excitations with the light field of the cavity (atomic branches). Due to the large separation between the photonic and atomic energy scales in our experiment, $|\Delta_c| \gg \omega_0$, we can disregard the involvement of the photonic branches in the dynamics which are associated with eigenfrequencies $\omega^{\mathrm{ph}}_\pm \approx \pm i\Delta_c$ [191].

In the normal phase, we can derive an analytic expression for the eigenfrequecies off the atomic polaritons, after eliminating the cavity field in the limit $\kappa \gg \omega_0$ and neglecting spin dephasing $\Gamma_\phi = 0$. Diagonalizing the stability matrix yields

$$\omega_\pm = -N\frac{\kappa}{\kappa^2 + \Delta_c^2}(\eta_b^2 - \eta_r^2) \pm i\omega_0\sqrt{\left(1 - \frac{\bar{\eta}^2}{\eta_c^2}\right)\left(1 - \frac{\Delta\eta^2}{\eta_c^2}\right)}, \tag{4.15}$$

where we additionally introduce the critical coupling strength

$$\eta_c = \sqrt{\frac{-\omega_0(\Delta_c^2 + \kappa^2)}{4N\Delta_c}}. \tag{4.16}$$

In the following sections, we extensively rely on Eq. (4.15) to characterize the behavior of our system. In section 4.2.1, we analyze the Dicke limit ($\Delta\eta = 0$) and discuss how the softening of the atomic polaritons leads to a superradiant phase transition. In section 4.3.1, we investigate how a finite coupling imbalance, $\Delta\eta > 0$, introduces a tunable decay channel for the polariton excitations, significantly altering the phase diagram of the open system.

The results presented in this section can also be independently calculated using a Keldysh action formalism for open quantum systems [89] and taking the limit $\kappa \gg \omega_0$. Details on these calculations can be found in the PhD thesis of Matteo Soriente [188].

4.2 Realizing spin-changing self-organization

In this section, we investigate our system in the limit of balanced Raman couplings (Dicke limit). As discussed in section 4.2.1, the system undergoes a superradiant phase transition accompanied by an emergent modulation of the atomic transverse magnetization, which we refer to as spin-changing self-organization. In section 4.2.2, we present direct experimental observations of this phase transition, and further discuss the relevant experimental protocols and limitations.

4.2.1 A superradiant phase transition inducing spin-changing self-organization

We consider the limiting case of balanced Raman drives, $\eta_r = \eta_b = \bar{\eta}$, where the Hamiltonian in Eq. (4.8) takes the form of the Dicke model [59, 61]

$$\begin{aligned} \hat{H} &= -\hbar\Delta_c \hat{a}^\dagger \hat{a} + \hbar\omega_0 \hat{J}_z + 2\hbar\bar{\eta}(\hat{a} + \hat{a}^\dagger)\hat{J}_x \\ &= -\hbar\Delta_c \hat{a}^\dagger \hat{a} + \hbar\omega_0 \hat{J}_z + \hbar\eta_b \left(\hat{a}\hat{J}_+ + \hat{a}^\dagger \hat{J}_-\right) + \hbar\eta_r \left(\hat{a}^\dagger \hat{J}_+ + \hat{a}\hat{J}_-\right). \end{aligned} \tag{4.17}$$

The Dicke Hamiltonian describes an ensemble of N indistinguishable two-level atoms, $|0_a\rangle$ and $|1_a\rangle$, coupled to a single mode of a cavity field. The associated atom-light interactions effectively occur in the ultrastrong coupling regime where the strengths of co-rotating ($\propto \eta_b$) and counter-rotating ($\propto \eta_r$) interactions become equal [61]. In this regime, the system undergoes a second-order phase transition from a normal to a superradiant phase when the light-matter coupling $\bar{\eta}$ exceeds a critical value η_c.

The Dicke model and its associated superradiant phase transition were first realized in our experiment in Ref. [62]: that implementation relies on encoding the two atomic states in well-defined external modes of a BEC within the $m = -1$ Zeeman sublevel, and coupling them via cavity-assisted Bragg scattering. In particular, the superradiant phase is associated with a superposition of both atomic modes, resulting in a λ-periodic checkerboard modulation of the atomic density [64]. In our

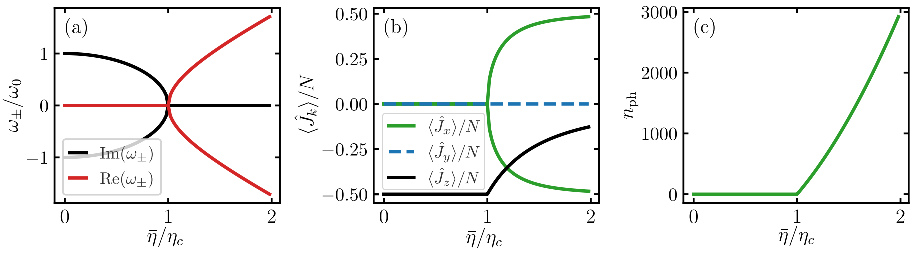

Figure 4.3: Superradiant phase transition in the Dicke model. **(a)** Eigenfrequencies of the excited atomic polariton $\omega_\pm$ in the normal phase as a function of the coupling strength $\bar{\eta}$. The imaginary part indicates the energy cost associated with creating $[\mathrm{Im}(\omega_+) > 0]$ and annihilating $[\mathrm{Im}(\omega_-) < 0]$ an excitation, which softens and vanishes at the critical coupling η_c. For $\bar{\eta} > \eta_c$, the positive real part $\mathrm{Re}(\omega_-) > 0$ indicates a dynamical instability and a second-order transition to the superradiant phase. **(b)** Expectation values of the atomic pseudo-spin operators $\langle \hat{J}_k \rangle$, with $k \in \{x, y, z\}$, and the cavity photon number n_{ph} **(c)**. For $\bar{\eta} < \eta_c$, the system is the normal phase, with all atoms occupying the ground-state mode $|0_a\rangle$ ($\langle \hat{J}_z \rangle /N = -1/2$) and $n_{\mathrm{ph}} = 0$. The superradiant phase at $\bar{\eta} > \eta_c$ is characterized by a macroscopic cavity field ($n_{\mathrm{ph}} \gg 0$) and the atoms occupying a superposition in the two modes ($|0_a\rangle$, $|1_a\rangle$) in one of two symmetry-broken configurations with $\langle \hat{J}_x \rangle > 0$ or $\langle \hat{J}_x \rangle < 0$.

implementation, the two atomic levels $|0_a\rangle$ and $|1_a\rangle$ are also associated with two different internal spin states, encoded in the Zeeman sublevels $m = -1$ and $m = 0$. This key difference results in qualitatively different real-space configurations in the superradiant phase [79].

To characterize the phases of the system, we begin by examining the behavior of the underlying excitation spectrum in the normal phase. In Fig. 4.3(a), we plot the imaginary $\mathrm{Im}(\omega_\pm)$ and real parts $\mathrm{Re}(\omega_\pm)$ of the eigenfrequencies $\omega_\pm$ associated with excited atomic polariton, cf Eq. (4.15). For vanishing light-matter coupling, $\bar{\eta} = 0$, the imaginary part (red curves) reflects the energy cost associated with creating $[\mathrm{Im}(\omega_+) = +\omega_0]$ or annihilating $[\mathrm{Im}(\omega_-) = -\omega_0]$ a single atom in the excited atomic state $|1_a\rangle$. When increasing $\bar{\eta}$, the eigenfrequencies soften due to hybridization of $|1_a\rangle$ with the cavity field. Above the critical coupling, $\bar{\eta} = \eta_c$, we obtain $\mathrm{Im}(\omega_\pm) = 0$ and an eigenvalue with a positive real part $\mathrm{Re}(\omega_-) > 0$ (black curve). This behavior signals a dynamical instability of the normal phase [189], and thereby *second-order phase transition* to a superradiant phase at $\bar{\eta} = \eta_c$.

The superradiant phase is characterized by a steady-state cavity field and by the atoms occupying a superposition in the two modes. We simplify Eqs. (4.11) for $\Delta\eta = 0$, and obtain the following expectation values

$$
\begin{aligned}
&X = \frac{\langle \hat{J}_x \rangle}{N} = \pm \frac{1}{2}\sqrt{1 - \left(\frac{\eta_c}{\bar{\eta}}\right)^4}, \quad Y = \frac{\langle \hat{J}_y \rangle}{N} = 0, \quad Z = \frac{\langle \hat{J}_z \rangle}{N} = -\frac{1}{2}\left(\frac{\eta_c}{\bar{\eta}}\right)^2, \\
&\alpha = \frac{\langle \hat{a} \rangle}{\sqrt{N}} = \frac{2\bar{\eta}}{\Delta_c - i\kappa} X.
\end{aligned}
\tag{4.18}
$$

in the superradiant phase, see also Ref. [61].

In Figs. 4.3(b,c) we plot the steady-state solutions of atomic [Fig. 4.3(b)] and photonic observables [Figs. 4.3(c)] for typical experimental parameters $N = 10 \times$

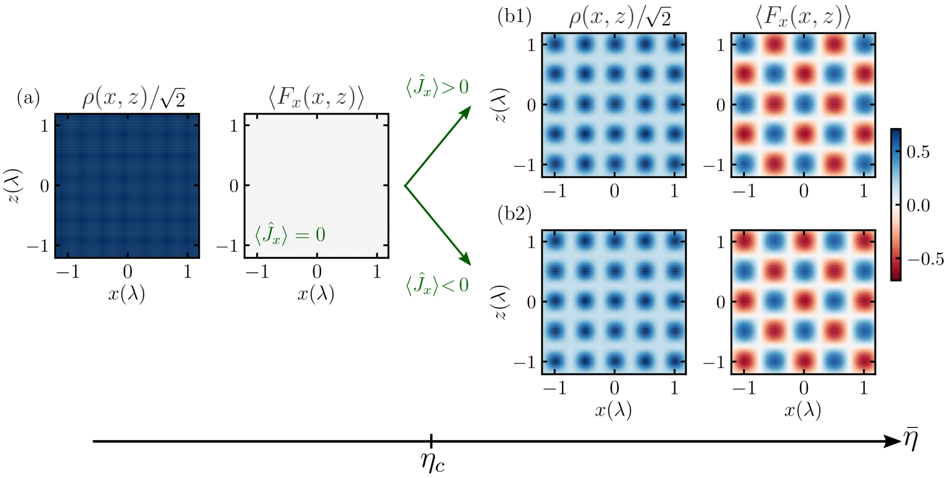

Figure 4.4: Spatial configurations of spin-changing self-organization. **(a)** Density distribution $\rho_0(x,z)$ (left) and transverse magnetization $\langle F_x(x,z)\rangle$ (right panel) of the underlying $F = 1$ system in the normal phase ($\bar{\eta} < \eta_c$). The homogeneous density distribution $\rho_0(x,z) = 1$ and vanishing magnetization $\langle F_x(x,z)\rangle = 0$ reflects all atoms occupying the mode $|0_a\rangle$. **(b)** Corresponding $\rho_0(x,z)$ and $\langle F_x(x,z)\rangle$ distributions in the superradiant phase for the two symmetry-broken configurations with $\langle \hat{J}_x\rangle > 0$ (b1) and $\langle \hat{J}_x\rangle < 0$ (b2) for $|\langle \hat{J}_x\rangle|/N = 1/4$. The density distributions exhibit a $\lambda/2$-periodic square modulation due to finite occupation of the excited state $|1_a\rangle$. The two symmetry-broken configurations are associated with λ-periodic checkerboard modulations of $\langle F_x(x,z)\rangle$, shifted by $\lambda/2$ with respect to each other.

10^4, $\omega_0 = 2\pi \times 50\,\text{kHz}$ and $\Delta_c = -2\pi \times 5\,\text{MHz}$. In the normal phase, $\bar{\eta} < \eta_c$, the system exclusively occupies the ground state mode $|0_a\rangle$, with $Z = \langle \hat{J}_z\rangle/N = -1/2$ and a vanishing mean number cavity photons $n_{\text{ph}} = N|\alpha|^2 = 0$. In contrast, the superradiant phase is characterized by a macroscopic cavity field $n_{\text{ph}} > 0$ and occupation of the excited atomic mode $|1_a\rangle$, i.e., $Z > -1/2$ and $X \neq 0$. Due to the underlying $\mathbb{Z}_2$-symmetry of the Dicke Hamiltonian, the system allows for two distinct symmetry-broken configurations with $X > 0$ and $X < 0$, together with a self-consistent cavity field $\alpha \propto X$.

We emphasize that both the Dicke model in Eq. (4.17) and the underlying single-particle Hamiltonian in Eq. (4.2) are derived in a rotating frame, where the cavity field oscillates at the intermediate frequency of the two Raman drives, i.e., $\bar{\omega} = (\omega_b + \omega_r)/2$. Hence, the stationary steady-state cavity field in the superradiant phase [cf. Fig. 4.3(c)] oscillates at the well-defined frequency $\bar{\omega}$, as schematically depicted in Fig. 4.2(b). In the next section, we rely on frequency resolved measurements of the cavity field to directly demonstrate this superradiant phase transition.

Furthermore, we visualize the real-space configuration of the atoms in the different phases. In the thermodynamic limit $N \to \infty$ [61], we can neglect correlations between the different modes and approximate the many-body state $|\psi\rangle_{\text{MB}} = |\psi\rangle^{\otimes N}$ as a product state. The single-particle wave functions $\psi_m(x,z)$ in the different

Zeeman sublevels $m \in \{+1, 0, -1\}$ read

$$\begin{aligned}|\psi\rangle &= (\psi_{+1}(x,z),\ \psi_0(x,z),\ \psi_{-1}(x,z))^T \\ &= (0, \operatorname{sign}(X)\sqrt{|X|}\Phi_{1_a}(x,z), \sqrt{1-|X|}\Phi_{0_a}(x,z))^T. \end{aligned} \tag{4.19}$$

We compute the associated atomic density distribution and transverse magnetization as $\rho(x,z) = |\langle\psi|\psi\rangle|^2 = |\psi_{-1}|^2 + |\psi_0|^2$ and $\langle F_x(x,z)\rangle = \langle\psi|\hat{F}_x|\psi\rangle$, respectively. Here, $\hat{F}_x$ is the corresponding $F = 1$ spin operator. For illustrative purposes, we consider the limiting case of small transverse drive lattice depths, $V_d \to 0$, with $\Phi_{0_a}(x,z) = \mathcal{N}$ and $\Phi_{1_a}(x,z) = \mathcal{N}\cos(kx)\cos(kz)$. Loading the atoms in deep transverse lattices $V_\mathrm{d} \neq 0$ does not significantly modify this microscopic picture, as the atomic density solely acquires a global modulation along the drive direction, i.e., $\rho(x,z) \propto \cos^2(kz)$.

In Fig. 4.4, we visualize the density distribution and transverse magnetization both for the normal [Fig. 4.4(a)] and superradiant phases [Fig. 4.4(b,c)]. The former is characterized by an homogenous density distribution $\rho(x,z) = 1$ and a vanishing transverse magnetization, as all atoms occupy the single-particle wavefunction $\Phi_{0_a}(x,z)$. In the superradiant phase, the system exhibits a squared $\lambda/2$-periodic density modulation in the xz-plane[1] due to concurrent occupation of $\Phi_{1_a}(x,z)$. The superradiant phase is associated with a staggered λ-periodic checkerboard modulation of the transverse magnetization $\langle F_x(x,z)\rangle$. Specifically, the two symmetry-broken configurations $X > 0$ [Fig. 4.4(b)] and $X < 0$ [Fig. 4.4(c)] are associated with $\lambda/2$-shifted spin textures with $\langle F_x(0,0)\rangle > 0$ and $\langle F_x(0,0)\rangle < 0$, respectively.

Due to the emergent ordering of the atomic magnetization and the cavity-assisted Raman processes that drive the superradiant phase transition, we refer to this phenomenon as *spin-changing self-organization* of the atomic system.

4.2.2 Observing the superradiant phase transition

Experimental protocol and observables

We prepare a BEC of $N \approx 9 \times 10^4$ atoms in the Zeeman sublevel $m = -1$, i.e., in the ground state $|0_a\rangle$. A magnetic field along the $-z$-direction defines the quantization axis, generating a linear Zeeman splitting of $\omega_z \approx 2\pi \times 48$ MHz. To obtain two standing-wave drives in phase at the position of the atoms, we set their frequency difference to $\omega_b - \omega_r = 2\pi \times 96\,\mathrm{MHz}$ and place the retro-reflecting mirror at a distance $z_1 = 1.562\,\mathrm{m}$ from the BEC, see section 3.3.2 for technical details. We increase the associated Raman couplings strengths via smooth s-shape ramps

$$\eta_{r,b}(t) = \eta_{r,b}^{\max}\left[3\left(\frac{t}{t_\mathrm{ramp}}\right)^2 - 2\left(\frac{t}{t_\mathrm{ramp}}\right)^3\right], \tag{4.20}$$

with $\eta_{r,b}^{\max}$ and t_ramp being the maximal coupling strength and the ramp duration, respectively. From the many-body Hamiltonian in Eq. (4.7), we can calibrate the corresponding Raman couplings as

---

[1] It is worth noting that the two relevant atomic modes are encoded in different Zeeman sublevels, hindering interference terms of the form $\psi^*_{-1}(x,z)\psi_0(x,z)$ which would otherwise give rise to a checkerboard modulation of the atomic density [62].

$$\eta_{r,b} = \frac{\mathcal{M}(V_\mathrm{d})}{2\sqrt{2}} \frac{\alpha_v}{\mathrm{sgn}[\alpha_s] \cdot \alpha_s} \sqrt{-\frac{U_0 V_{r,b}}{\hbar}}, \tag{4.21}$$

with $V_{r,b}$ being the lattice depths of the drive at $\omega_{r,b}$ and U_0 being the dispersive shift at $\lambda_\mathrm{d} = 784.7\,\mathrm{nm}$.

The BEC is confined in the combined potential of the harmonic trap $V_\mathrm{ext}(\mathbf{x})$, with trapping frequencies $[\omega_{hx}, \omega_{hy}, \omega_{hz}] = 2\pi \times [220(3), 24.6(8), 170.1(3)]$ Hz, and the transverse drive standing-wave potential $V_\mathrm{d}(\mathbf{x}) = -(V_r + V_b) f(\mathbf{x})^2 = -V_\mathrm{d} f(\mathbf{x})^2$, see Eq. (4.2). To calculate the single-particle wavefunction Φ_{0_a}, we consider s-wave scattering and employ a Thomas-Fermi approximation for the interacting BEC [111]. We further consider the transverse drive potential as a succession of independent harmonic traps; this is well justified since the superradiant phase transition occurs at large lattice depths $V_\mathrm{d} \gtrsim 25\ \hbar\omega_\mathrm{rec}$. We find numerically that the overlap integral $\mathcal{M}(V_\mathrm{d})$ converges to $\mathcal{M}_\mathrm{max} = 0.68$ for $V_\mathrm{d} \to \infty$, and employ this value when evaluating Eq. (4.21).

From our heterodyne measurements of the z-polarized cavity field, we construct photon number spectrograms $\tilde{n}_\mathrm{ph}(\omega, t)$, as described in section 3.2.1. Additionally, we integrate the spectrograms within a narrow frequency range of $\pm 2\pi \times 2.5$ kHz around $\bar{\omega}$ to obtain the photon traces $n_\mathrm{ph}(t)$ corresponding to the cavity field at the frequency $\bar{\omega} = (\omega_b + \omega_r)/2$, which is associated with spin-changing self-organization. The drive at ω_r is red-detuned from cavity resonance ω_c and may induce spurious intra-spin self-organization accompanied by the build-up of a y-polarized cavity field [62, 78]. During our measurements, we continuously monitor such cavity field with an auxiliary heterodyne setup; we never observe any signal above noise levels.

Measurements

In Fig. 4.5(a), we present a representative experimental realization for a cavity detuning $\Delta_c = -2\pi \times 4.0(2)\,\mathrm{MHz}$ and excited-state splitting $\omega_0 = 2\pi \times 44(2)\,\mathrm{kHz}$. We increase the average Raman coupling $\bar{\eta}$ (solid) within $t_\mathrm{ramp} = 10\,\mathrm{ms}$ at a negligible imbalance $\Delta\eta \approx 0$ (dashed black curve), see Fig. 4.5(a1). Once the coupling strength reaches a critical value around $\bar{\eta} \gtrsim 2\pi \times 0.4\,\mathrm{kHz}$ for $t \gtrsim 5\,\mathrm{ms}$, we observe an abrupt increase of the average number of cavity photons $n_\mathrm{ph}(t)$ (green curve) signaling the onset of a superradiant phase transition. In Fig. 4.5(a2), we present the corresponding photon number spectrogram $\tilde{n}_\mathrm{ph}(\omega, t)$. Above the critical coupling, we observe a strong cavity field comprising thousands of photons at the intermediate frequency of the two drives, $\bar{\omega}$. In the vicinity of the transition, we observe a broad frequency distribution spreading around $(\omega - \bar{\omega}) = [-20, 15]$kHz; we attribute this to the occupation of excited polariton branches due to spurious non-adiabatic effects induced by the coupling ramps.

We accumulate multiple experimental realizations for different cavity detunings Δ_c, and map out the experimental phase diagram of the system. In Fig. 4.5(b), we plot the measured photon number n_ph in the ($\bar{\eta}$,Δ_c) parameter space. For negative detunings, $\Delta_c < 0$, we observe a sharp boundary between the normal ($n_\mathrm{ph} = 0$) and superradiant phases ($n_\mathrm{ph} > 0$) which progressively shifts to larger couplings with

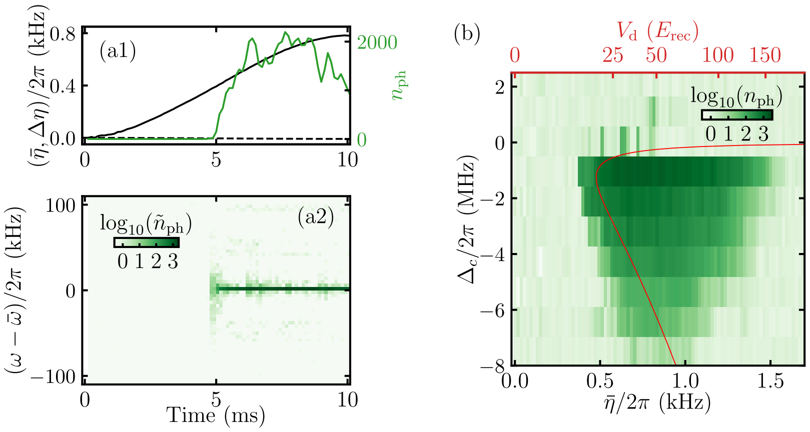

Figure 4.5: Observing spin-changing self-organization. **(a)** Experimental protocol and observations. (a1) We increase the average coupling $\bar{\eta}$ (solid) at negligible imbalances $\Delta\eta$ (dashed line). The superradiant transition is signaled by a macroscopic intra-cavity field with average photon number $n_{\mathrm{ph}} > 0$ (green curve). (a2) Corresponding photon number spectrogram $\tilde{n}_{\mathrm{ph}}(t, \omega)$, showing that the cavity field locks at the intermediate frequency between the two drives $\omega = \bar{\omega}$. The integration time is set to $T = 150\,\mu\mathrm{s}$. **(b)** Phase diagram of the system, showing n_{ph} in the $(\bar{\eta}, \Delta_c)$ parameter space. We observe a superradiant transition for negative cavity detunings $\Delta_c < 0$ in agreement with the theoretical phase boundary (red curve). At large couplings, the system departs from the superradiant phase, likely due to heating and atom loss arising from the large transverse drive lattice depths V_{d}.

increasing negative detunings. This is due to the larger energy cost associated with occupying the cavity field at large Δ_c [see Eq. (4.17)], and is in reasonable agreement with the theoretical expectations for the critical coupling (red line) obtained from Eq. (4.16). At positive detunings, $\Delta_c > 0$, the cavity field remains unoccupied apart from small photon spikes $n_{\mathrm{ph}} \lesssim 20$. We attribute them to residual oscillations between the normal and superradiant phases induced by dynamical variations of the dispersive shift [62].

Our frequency resolved measurements of an emergent z-polarized cavity field at the well-defined frequency $\bar{\omega} = (\omega_r + \omega_b)/2$, together with the experimental phase diagram, demonstrate that our system undergoes a superradiant phase transition via cavity-assisted Raman processes. The first experimental observation of spin-changing self-organization in a BEC has been reported in Ref. [79].

Technical limitations

The phase diagram in Fig. 4.5(c) shows a clear reduction of n_{ph} at large coupling strengths, until the system eventually exits the superradiant phase. These observations extend beyond an elementary Dicke model description and are related to the large transverse lattice depths V_{d} required to access the superradiant phase in our system, reaching $V_{\mathrm{d}} \approx 200 E_{\mathrm{rec}}$ for $\bar{\eta} = 2\pi \times 1.7\,\mathrm{kHz}$ [cf. Fig. 4.5(c)]. Such deep lattices can induce significant heating and atom loss [95], thereby limiting the extent of the superradiant phase.

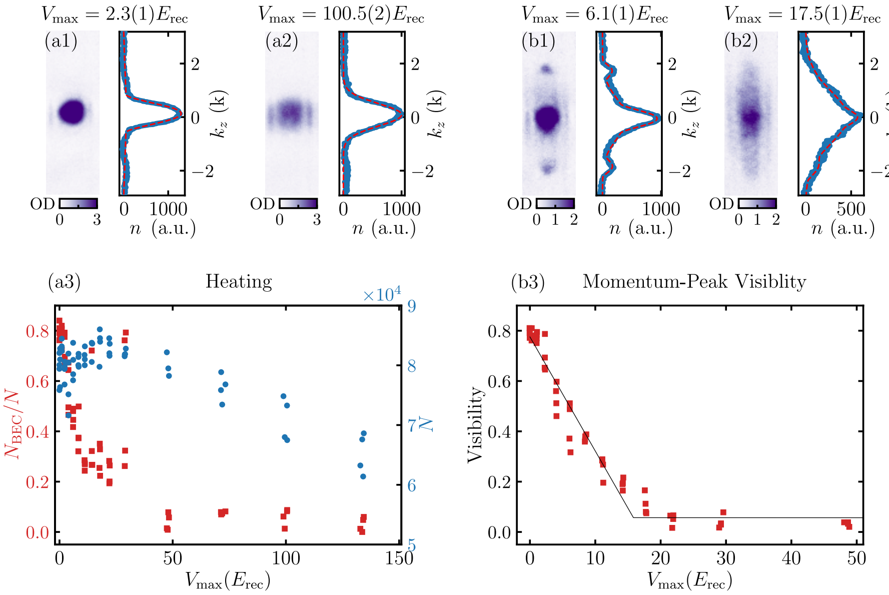

Figure 4.6: Heating and coherence in deep optical lattices. **(a)** Measuring heating and atom loss. (a1,a2) Typical time-of-flight images in $m = -1$ (right panel) after adiabatically ramping up the transverse lattice to $V_{\max}$ within $t_{\mathrm{ramp}} = 15\,\mathrm{ms}$ and down to zero in t_{ramp}. The distributions are integrated along the cavity axis (left panel) and fitted with a bimodal distribution (red curve). (a3) BEC fraction N_{BEC}/N and total atom number N as a function of $V_{\max}$, showing significant heating and atom loss with increasing maximal lattice depths. The atomic ensemble becomes thermal ($N_{\mathrm{BEC}}/N \approx 0$) for $V_{\max} \gtrsim 50E_{\mathrm{rec}}$. **(b)** Probing phase coherence in the system. (b1,b2) Typical momentum-space distributions after increasing the lattice to $V_{\max}$ within t_{ramp} and suddenly switching off all confining potentials. The integrated density distributions are fitted with a bimodal fit complemented by two Thomas-Fermi profiles centered at the lattice momenta $k_z = \pm 2k$. (b3) The momentum-peak visibility as a function of $V_{\max}$ quantifies the degree of phase coherence in the lattice. We observe transition to an incoherent phase around $V_{\mathrm{d}}^{\mathrm{SF}} = 16.6(3)\ E_{\mathrm{rec}}$, which is determined by a double linear fit (line).

To investigate this experimentally, we prepare a BEC in $m = -1$ and increase the transverse lattice depths to $V_{\max}$ within $t_{\mathrm{ramp}} = 15\,\mathrm{ms}$, while keeping Δ_c sufficiently large to suppress cavity-assisted Raman transitions. To assess the influence of heating and atom loss, we adiabatically ramp down the lattice within t_{ramp} and image the atoms after free time-of-flight expansion. In Figs. 4.6(a1) and (a2), we show exemplary realizations for $V_{\max} = 2.3(1)E_{\mathrm{rec}}$ and $V_{\max} = 100.5(2)E_{\mathrm{rec}}$ (left panels). We integrate the absorption images along the x direction (right panels) and perform a bimodal fit [108] to quantify heating and atom loss (red curves): the first component captures the atoms in the condensate with a Thomas-Fermi profile, while the second component is a Gaussian distribution encompassing thermal atoms. We evaluate the condensate fraction as N_{BEC}/N, with N_{BEC} being the total number of atoms in the condensate. In Fig. 4.6(a3), we plot both N_{BEC}/N and the total number of atoms N as a function of $V_{\max}$. The condensate fraction monotonically decreases and reaches $N_{\mathrm{BEC}}/N = 0$ for $V_{\max} \approx 50\ E_{\mathrm{rec}}$, indicating significant heating at large lattice depths and the system becoming a thermal gas. Furthermore, we observe significant atom loss at large $V_{\max}$, due to spurious spontaneous emission [95] and enhanced three-body losses [192] in deep optical lattices.

Hence, we attribute the deviation of the observed phase diagram from the theoretical expectations at large lattice depths to the combined influence of atom loss and heating. Specifically, the critical coupling increases with decreasing atom number as $\eta_c \propto 1/\sqrt{N}$ [Eq. (4.16)], whereas the effective atom-light interactions of a thermal atomic cloud might be reduced due to spurious inhomogeneous broadening [193, 194].

The presence of deep optical lattices can also significantly alter the phase coherence of the BEC wavefunction [195]. To assess this, we suddenly switch off all confining potentials after ramping the lattice depth to $V_{\max}$ within t_{ramp}, and image the atoms after free time-of-flight expansion. We present the corresponding results in Fig. 4.6(b). At small lattice depths $V_{\max} = 6.1(1)E_{\mathrm{rec}}$ [Fig. 4.6(b1)], we observe a Thomas-Fermi profile centered around $k_z = 0$ and two coherent interference peaks at $k_z = \pm 2k$ associated with the recoil momenta imparted by the underlying lattice $V_{\mathrm{d}} = V_{\max}\cos^2(kz)$. Already at intermediate lattice depths $V_{\max} = 17.5(1)E_{\mathrm{rec}}$ [Fig. 4.6(b2)], these interference peaks are already entirely washed out, and the system exhibits a broad momentum distribution. To evaluate these measurements, we extend our bimodal fit with additional Thomas-Fermi profiles centered around $k_z = \pm 2k$ [red curves in Figs. 4.6(b1,b2)]. Closely following Ref. [65], we quantify the degree of phase coherence in our system via the visibility of the different momentum peaks $(N_{\mathrm{BEC}} + N_{+2k} + N_{-2k})/N$, with $N_{\pm 2k}$ being the fitted atom number around the $k_z = \pm 2k$ peaks. In Fig. 4.6(b3), we plot the visibility as a function of $V_{\max}$. For small lattice depths, we observe large superfluid fractions that rapidly decrease with increasing lattice depths and eventually vanish at intermediate values. A double linear fit yields $V_{\mathrm{d}}^{\mathrm{SF}} = 16.6(3)\ E_{\mathrm{rec}}$ (solid line), indicating a transition from a phase-coherent superfluid to an incoherent phase in the optical lattice [195, 196].

In our system, the critical coupling $\eta_c \gtrsim 2\pi \times 0.4\,\mathrm{kHz}$ of the superradiant transition is associated with large lattice depths around $V_{\mathrm{d}}^{c} \gtrsim 20E_{\mathrm{rec}}$. Since $V_{\mathrm{d}}^{c} > V_{\mathrm{d}}^{\mathrm{SF}}$, the atoms occupy a phase-incoherent state in the transverse drive lattice when undergoing spin-changing self-organization. Therefore, we refrain from presenting time-of-flight images in the superradiant phase in this chapter, as they resemble Fig. 4.6(b2) and do not provide direct insights into the real-space configuration of the atoms[2].

4.3 Phase diagram of superradiant quantum gas with tunable decay

We investigate the phase diagram of our system with imbalanced co- and counter-rotating couplings. In section 4.3.1, we identify two superradiant Raman scattering

---

[2] The observed critical lattice depths V_{d}^{c} are considerably larger than the typical values for intra-spin self-organization in our experiment $V_{\mathrm{d}}^{c} \approx 5\,\mathrm{E}_{\mathrm{rec}}$ [78]. This discrepancy is due to intra-spin self-organization being induced by scalar light-matter interactions, with $|\alpha_s| > |\alpha_v|$ for $\lambda_{\mathrm{d}} = 784.7\,\mathrm{nm}$.

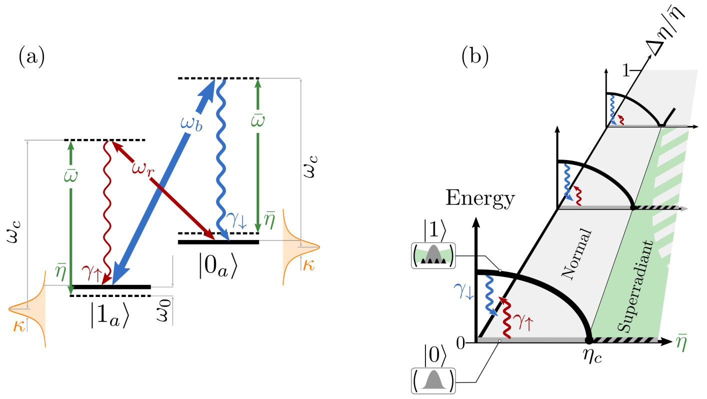

Figure 4.7: Tunable coherent and dissipative couplings in a superradiant quantum gas. **(a)** Detailed coupling scheme. The BEC ($|0_a\rangle$) couples to a spatially modulated state $|1_a\rangle$. In the superradiant phase, a coherent intra-cavity field builds up at the intermediate frequency $\bar{\omega}$ (green) of the two transverse drives at ω_r (red) and ω_b (blue arrow). Cavity losses induce additional superradiant Raman scattering (blue and red wiggly arrows) with rates $\gamma_{\downarrow,\uparrow}$ depending on the density of states of the cavity (orange curve). **(b)** Controlling the polariton decay. The atom-light interactions give rise to two low-energy polaritons $|0\rangle$ and $|1\rangle$, corresponding to decoupled and coupled light-matter modes, respectively. Increasing the average coupling $\bar{\eta}$ softens the energy of $|1\rangle$ (black line). Concurrently, superradiant Raman scattering induces dissipative decay ($\gamma_\downarrow$) and amplification ($\gamma_\uparrow$) of the excited polariton $|1\rangle$. For small coupling imbalances $\Delta\eta/\bar{\eta}$, the rates are balanced and mode softening is accompanied by a phase transition from a normal (gray) to a superradiant phase (green) for $\bar{\eta} > \eta_c$. By increasing $\Delta\eta/\bar{\eta}$, the growing polariton decay $\gamma_\downarrow$ leads first to bistability (green-gray hashed) and then to the suppression of the superradiant transition.

channels as the microscopic processes responsible for polariton decay in our system. This tunable decay channel significantly modifies the phase diagram of the open system. In section 4.3.2, we experimentally measure the phase diagram and identify the presence of a dissipation-stabilized normal phase for arbitrarily large light-matter couplings.

4.3.1 An extended Dicke model with tunable collective decay

In the previous section, we presented our observations of a superradiant Dicke phase transition in the limit of balanced Raman couplings $\Delta\eta = 0$. This second-order phase transition arises from softening of the excited atomic polariton, as shown in Fig. 4.3(a). Building upon these results, we now examine scenarios involving imbalanced co- and counter-rotating Raman couplings with $\Delta\eta \neq 0$ ($\eta_b \neq \eta_r$), adding a new layer of complexity to the system. In this regime, the role of cavity dissipation becomes more prominent.

For imbalanced couplings, the excited atomic polariton acquires a non-vanishing real part in the normal phase. From the corresponding eigenvalues in Eq. (4.15), we obtain

$$\begin{aligned}\gamma = \mathrm{Re}(\omega_\pm) &= -N\frac{\kappa}{\kappa^2+\Delta_c^2}(\eta_b^2-\eta_r^2) = -N\frac{\kappa}{4(\kappa^2+\Delta_c^2)}\bar{\eta}\Delta\eta \\ &= -(\gamma_\downarrow - \gamma_\uparrow). \end{aligned} \tag{4.22}$$

This expression implies that for an open system ($\kappa > 0$) and arbitrarily small positive coupling imbalances ($\Delta\eta > 0$), the excited polariton decays at a rate of $\gamma < 0$ in the normal phase. The individual contributions can be re-written as

$$\gamma_{\downarrow,\uparrow} = N\eta_{b,r}^2\rho(\bar{\omega}), \tag{4.23}$$

where we identify $\rho(\bar{\omega}) = \kappa/[(\bar{\omega}-\omega_c)^2+\kappa^2]$ as the *density of states of the cavity* around the frequency $\bar{\omega}$ [189]. This expression indicates that the underlying mechanism for the damping (amplification) $\gamma_\downarrow$ ($\gamma_\uparrow$) of the polariton arises from *superradiant Raman scattering* of photons from a single drive at ω_b (ω_r) into the bath of vacuum modes provided by the cavity. As illustrated in Fig. 4.7(a), the nonlocal dissipative channels $\gamma_\downarrow$ (blue) and $\gamma_\uparrow$ (red wiggly arrow) are controlled by the strength of the corresponding Raman drives η_b and η_r, respectively, and induce collectively enhanced population inversion between the modes $|1_a\rangle \to |0_a\rangle$ ($|0_a\rangle \to |1_a\rangle$), accompanied by the leakage of real cavity photons. For an in-depth theoretical discussion on superradiant Raman scattering, refer to sections 2.2.2 and 2.2.4 in chapter 2.

The interplay between coherent and dissipative processes significantly impacts the superradiant phase transition in our system, resulting in the emergence of new dissipative phases and extended regions of phase bistability, as schematically illustrated in Fig. 4.7(b). Close to the Dicke limit ($\Delta\eta/\bar{\eta} = 0$), the coherent light-matter interactions dominate, inducing a complete softening of the excited state polariton ($|1\rangle$) and a second-order transition from the normal (gray) to the superradiant phase (green area) above a critical coupling η_c. By increasing the imbalance $\Delta\eta/\bar{\eta}$, we enhance the collective decay of excited polariton $\gamma_\downarrow$, resulting in an extended region of phase bistability (green-gray hashed region) and eventually in the dissipative suppression of the superradiant transition. In the following sections, we experimentally explore the rich phase diagram of this open system by leveraging our experimental control over coherent and dissipative couplings.

4.3.2 Measuring the phase diagram of the open system

We investigate the phase diagram of our system in the ($\bar{\eta}$, $\Delta\eta$) parameter space. We restrict the experiments to $0 \leq \Delta\eta \leq \bar{\eta}$, as the properties of the system are specular for $0 \leq \bar{\eta} \leq \Delta\eta$, cf. Eq. (4.8). We prepare a BEC of $N = 1.28(8) \times 10^5$ in the mode $|0_a\rangle$ at $\omega_0 = 2\pi \times 44(2)$ kHz, and map out the phase diagram by increasing the Raman couplings within $t_{\mathrm{ramp}} = 10\,\mathrm{ms}$ while keeping the ratio $\Delta\eta/\bar{\eta}$ fixed. The onset of a superradiant phase is signaled by the build-up of a coherent cavity field at frequency $\bar{\omega}$ with average photon number $n_{\mathrm{ph}} > 0$, see the inset in Fig. 4.8. Additional details regarding the experimental protocol and data processing can be found in section 4.2.2.

In Fig. 4.8, we present experimental phase diagrams for three different cavity detunings: $\Delta_c/2\pi = -2\pi \times 5.0(2)\,\mathrm{MHz}$ (a), $\Delta_c/2\pi = -4.0(2)\,\mathrm{MHz}$ (b), and

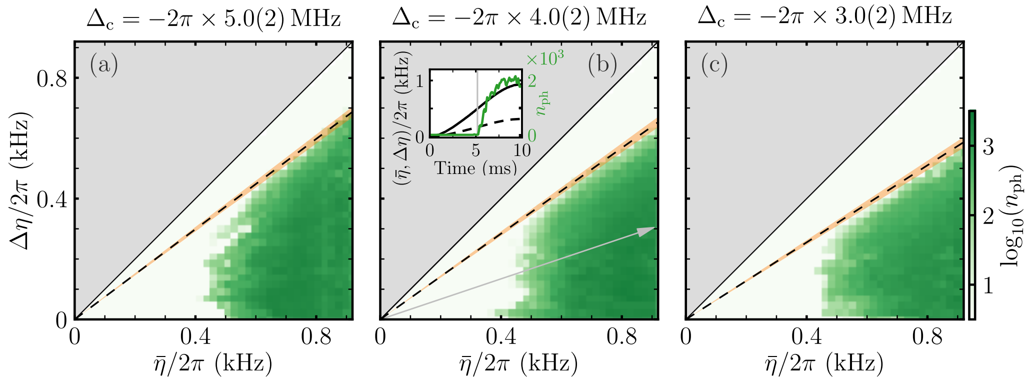

Figure 4.8: Experimental phase diagrams of the extended Dicke model. Average photon number n_{ph} in the $(\bar{\eta}, \Delta\eta)$ parameter space for different cavity detunings $\Delta_c/2\pi = -5.0(2)$ MHz **(a)**, $-4.0(2)$ MHz **(b)** and $-3.0(2)$ MHz **(c)**. The inset shows the experimental protocol: we increase the couplings $\bar{\eta}$ (solid) and $\Delta\eta$ (dashed black line) while keeping the ratio $\Delta\eta/\bar{\eta}$ constant [gray arrow in (b)]; the superradiant transition is signaled by the buildup of a strong cavity field with $n_{\mathrm{ph}} > 0$ (green curve). For large imbalances $\Delta\eta/\bar{\eta} \gg 0$, the superradiant phase is suppressed at large couplings. The dashed line indicates a fit to determine this phase boundary.

$\Delta_c/2\pi = -3.0(2)$ MHz (c). The phase diagrams are obtained by combining measurements for 51 different ratios $\Delta\eta/\bar{\eta}$, with 5 realizations each. At small imbalances ($\Delta\eta \ll \bar{\eta}$), the system exhibits the phenomenology of the Dicke model. We observe a superradiant phase transition ($n_{\mathrm{ph}} > 0$) when the average coupling $\bar{\eta}$ surpasses a critical value, which is only weakly dependent on $\Delta\eta$. In contrast, at larger ratios $\Delta\eta/\bar{\eta}$, the superradiant phase transition is suppressed, and the system remains in the normal phase at large couplings $\bar{\eta}$. We fit the slope of the observed phase boundary $(\Delta\eta/\bar{\eta})_{\mathrm{DSNP}}$ (dashed line), with the orange area indicating the fitting error. Remarkably, we observe that the region where the superradiant phase transition is suppressed clearly increases at smaller cavity detunings $\Delta_c \to 0$.

To interpret our observations, we compare the measured phase diagram at $\Delta_c/2\pi = -4.0(2)$ MHz with the expectations obtained from complementary theoretical methods. The phase diagrams in Figs. 4.9(a) and (b) are obtained from the analytic solutions in Eq. (4.18) and from numerical simulations of the mean-field equations of motion in Eq. (4.10), respectively. The analytic phase diagram in Fig. 4.9(a) allows us to identify three distinct mean-field phases: in addition to the normal phase (NP) and the superradiant phase (SP), the open system features a *dissipation-stabilized normal phase* (DSNP). The existence of a DSNP near the line $\Delta\eta/\bar{\eta} = 1$ is a direct consequence of the open character of our system. Remarkably, the system remains in a normal phase even when the coupling strengths greatly exceed the critical value η_c (blue line), leading to a population inversion scenario, as previously pointed out in Refs. [159, 184]. At a microscopic level, the DSNP is stabilized against a superradiant transition by the dominant decay of the underlying polariton excitations, see Eq. (4.22). In section 4.5, we provide a comprehensive experimental characterization of these polariton excitations, further elucidating this relationship.

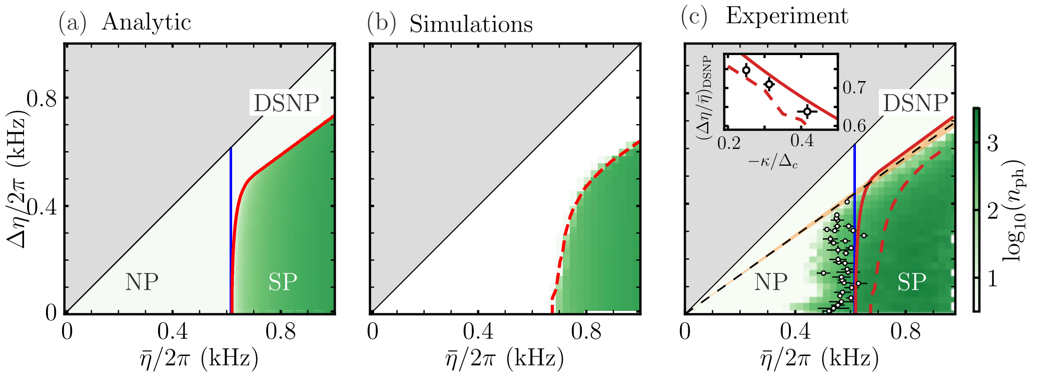

Figure 4.9: Comparison of theoretical and experimental phase diagrams. Theoretical phase diagrams obtained from analytic **(a)** and numerical mean-field simulations **(b)** for the parameters in Fig. 4.8(b). The different ground-state configurations of the system are the normal phase (NP), superradiant phase (SP) and the dissipation-stabilized normal phase (DSNP). The critical coupling for the closed system η_c is marked by a blue line. **(c)** Experimental phase diagram for $\Delta_c = -2\pi \times 4.0(2)$ MHz [Fig. 4.8(b)]. The dots indicate the average critical couplings extracted from a data subset at constant $\Delta\eta/\bar{\eta}$. We mark the boundary of the SP obtained from the analytic (solid red) and numerical calculations (dashed red curve). Inset: critical slope $(\Delta\eta/\bar{\eta})_{\mathrm{DSNP}}$ against $-\kappa/\Delta_c$, showing the DSNP-SP boundary. As $|\Delta_c|$ nears κ, the slope decreases, indicating a larger DSNP region. Our results are captured by the analytical (solid) and numerical predictions (dashed line).

The different theoretical predictions are in reasonable agreement with the experimental phase diagram, which we plot in Fig. 4.9(c). We extract the critical coupling η_c (white data points) using piece-wise linear and power-law fits, and compare it to the analytic (solid red) and numerical phase boundaries (dashed red lines). The small deviation of the phase boundaries can be attributed to residual non-adiabatic effects arising from the finite duration of the coupling ramps. In the inset of Fig. 4.9(c), we plot the critical slopes of the DSNP $(\Delta\eta/\bar{\eta})_{\mathrm{DSNP}}$ as a function of $-\kappa/\Delta_c$ for the three phase diagrams presented in Fig. 4.8. The slope decreases with increasing $-\kappa/\Delta_c$ signaling a larger DSNP; this is due to the density of states of the cavity increasing for $\Delta_c \to 0$, cf. Eq. (4.23). Additionally, our observations agree well with the slope obtained from the analytic (solid) and numerical estimates (dashed line). The former can be directly obtained

$$(\Delta\eta/\bar{\eta})_{\mathrm{DSNP}} = \kappa/\Delta_c \left(1 - \sqrt{1 + \Delta_c^2/\kappa^2}\right), \tag{4.24}$$

by enforcing that the population imbalance Z in Eq. (4.18) is always real valued.

4.4 Bistability and hysteretic phase transitions

Here, we explore the phenomenon of phase bistability in our system. As discussed in section 4.4.1, we expect a discontinuous phase transition between the superradiant and the dissipation-stabilized normal phases. In section 4.4.2, we provide direct experimental evidence of bistability through comprehensive hysteresis measurements.

4.4.1 Bistability through dissipation

We further investigate the boundary between the superradiant phase (SP) and the dissipation-stabilized normal phase (DSNP) observed at large coupling imbalances $\Delta\eta/\bar{\eta}$. Previous theoretical works [159, 186] predict the existence of an intermediate region where both phases are stable. Accordingly, we anticipate a discontinuous first-order phase transition, in contrast to the conventional second-order transition induced by mode softening in the Dicke model [63].

The existence of bistability can be understood in terms of the competition between coherent and dissipative processes in our system, as discussed in previous sections. As the coupling imbalance $\Delta\eta/\bar{\eta}$ increases, the dissipative decay rate of the excited polariton γ enhances population in the ground-state polariton mode $|0\rangle$ and counteracts the coherent coupling $\bar{\eta}$ responsible for the superradiant phase transition. In the regime of comparable coherent and dissipative couplings, the phase to which the system converges depends on its initial preparation. If the BEC is initially prepared in the DSNP, it remains stable due to the dominant polariton decay. On the other hand, if the system is prepared in the SP, the dissipative decay is counteracted by the presence of a large coherent intra-cavity field, which contributes to keeping the excited polariton mode $|1\rangle$ significantly populated. In an intuitive picture, preparing the system in the symmetry-broken superradiant phase renders it more rigid against dissipative processes induced by cavity dissipation.

4.4.2 Observing a dissipation-induced hysteretic phase transition

To explore the DSNP-SP boundary, we modify our experimental protocol to include multiple coupling ramps, as illustrated in Fig. 4.10(a1). We initialize the system in the DSNP by increasing the coupling $\bar{\eta}$ above η_c within $t_{\mathrm{ramp}} = 6\,\mathrm{ms}$ at large imbalance $\Delta\eta/\bar{\eta} = 0.78$ (dotted black arrow). While keeping the average coupling $\bar{\eta}$ fixed, we perform subsequent forward (purple) and backward sweeps (orange arrow) of $\Delta\eta$, each within $t_{\mathrm{ramp}} = 3\,\mathrm{ms}$. We empirically optimize the duration of the ramps to mitigate atom loss ($< 0.15N$) and ensure an adiabatic evolution of the system ($t_{\mathrm{ramp}} \gg 1/\omega_0$). To obtain a theoretical estimate of bistability region, we assess the stability of the different phases using the dynamical matrix derived in Eq. (4.14). The reference phase diagrams in Figs. 4.10(a1,b1) highlight the regions where only the normal (white) or superradiant phases (dark green) are stable, together with an extended region of phase bistability (light green).

In Fig. 4.10(a2), we present a typical trace of the cavity photon number n_{ph} when crossing the boundaries between the DSNP→SP (purple curve) and SP→DSNP (orange curve) in a single experimental realization at $\bar{\eta} = 2\pi \times 0.61(1)\,\mathrm{kHz}$. We observe clear hysteresis behavior, as the system remains in the DSNP (SP) for significantly

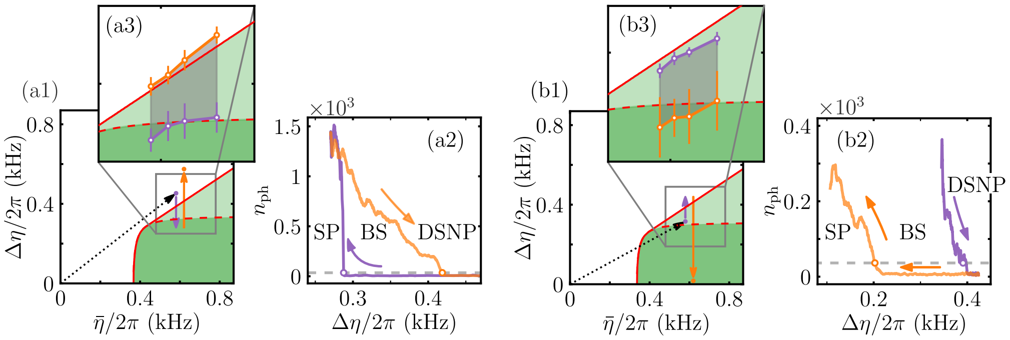

Figure 4.10: Probing hysteresis at the SP-DSNP boundary. **(a)** Observation of hysteresis. (a1) Experimental protocol in the $(\bar{\eta}, \Delta\eta)$ phase space, showing the preparation ramp in the DSNP (black), the forward (purple) and backward ramps (orange arrow) into the SP. (a2) Exemplary trace of the mean cavity photon number n_{ph}. At intermediate couplings $\Delta\eta$, we observe hysteresis signaling the region of phase bistability (BS). (a3) Mapping bistability BS region. The data points indicate the DSNP-SP boundary detected during the forward (purple) and backward (orange) path for different values $\bar{\eta}$. These boundaries are determined by setting a threshold of $n_{\mathrm{ph,th}} = 36$ photons [gray line in (a2)]. The reference phase diagrams (a1, a3) highlight the normal phase (white), the SP (dark green) and BS region (light green). **(b)** Complementary hysteresis measurements. (b1) Experimental protocol, showing an initial preparation in the SR phase. (b2) Typical photon trace and (b3) experimental mapping of the BS region. Here, we prepare $N = 1.10(8) \times 10^5$ at $\Delta_c = -2\pi \times 3.0(5)$ MHz and $\omega_0 = 2\pi \times 40(5)$ kHz.

smaller (larger) coupling imbalances $\Delta\eta$ when originally occupying the corresponding phases. This is in agreement with the expected discontinuous character of the transition [186] and demonstrates the existence of phase bistability (BS) in our system. By performing hysteresis measurements at different average couplings $\bar{\eta}$ in Fig. 4.10(a3), we map out an experimentally accessible region where both the SP and DSNP are stable (gray area). The data points are the mean values of 12 to 18 realizations and indicate the superradiant transition in the forward (purple points) and backward ramps (orange points). The observed region of phase bistability (shaded area) is quantitatively captured by our theoretical expectations (light green area).

Our hysteresis measurements are potentially affected by atom loss and heating during the experimental protocol. These processes affect the collective atom-cavity coupling, and consequently shift the stability boundaries of the different phases. To examine this potential limitation, we complement our results with hysteresis measurements in the opposite direction, see Fig. 4.10(b1). We initialize the system in the SP by increasing the coupling at moderate imbalances $\Delta\eta/\bar{\eta} = 0.54$ (dotted black arrow) and perform then analogous forward (purple) and backward sweeps (orange arrow) of $\Delta\eta$ at fixed $\bar{\eta}$. In Fig. 4.10(b2), we present a representative realization at $\bar{\eta} = 2\pi \times 0.61(1)\,\mathrm{kHz}$ where we also observe a clear hysteresis in the SP-DSNP boundary. For completeness, we map the extension of the observed bistability region in Fig. 4.10(a3) using this complementary protocol. We attribute the small shift of the phase boundaries towards smaller values of $\Delta\eta/\bar{\eta}$ to excess atom loss when initializing the system in the SP phase [89].

Our observations of hysteresis and phase bistability using two complementary protocols confirm that the effects of atom loss and heating are not significantly detrimental to our experiments. The observed first-order transition between the DSNP-SP phases is a result of the open nature of our system and is qualitatively different from the well-studied second-order transition between the NP-SP phases in the Dicke model [62, 63]. Previous experiments exploring extended Dicke models with tunable co- and counter-rotating terms have been conducted using thermal atomic clouds [193, 194]. While the DSNP has been observed in those experiments, our results constitute the first experimental observation of dissipation-induced bistability and hysteresis in a generalized Dicke system.

4.5 Probing the microscopic polariton excitations

The observations discussed thus far focus on the ground-state properties of our system, revealing dissipation-stabilized phases and hysteretic transitions. One of the key strengths of cold-atom experiments is the ability to directly access the underlying quasiparticle excitations of many-body systems, providing insights into the elementary microscopic processes responsible for the emergence of macroscopic phenomena. Since the first implementation of Bragg spectroscopy in Bose-Einstein condensates [197], spectroscopic techniques have found widespread use to study the excitation spectrum of strongly-correlated systems [198–200]. However, these techniques often require hundreds to thousands of experimental realizations under identical parameters to scan across narrow resonance features, making them sensitive to technical drifts and fluctuations. In our system, this limitation can be overcome by means of cavity-assisted Bragg spectroscopy [63, 201]. This method not only amplifies Bragg scattering, but also provides real-time access to excitations through the cavity field.

Here, we investigate the excitation dynamics of our system. In section 4.5.1, we present a new experimental technique facilitating real-time and non-destructive probing of the polariton excitations in single experimental realizations. In section 4.5.2, we examine the polariton excitations on top of the normal phase for various coupling imbalances and benchmark our findings through comprehensive numerical simulations. Notably, we measure polariton lifetimes varying over several orders of magnitude, which we relate to the observed macroscopic phases.

4.5.1 Implementing cavity-assisted Raman spectroscopy

To measure the evolution of the excitation spectra, we prepare a BEC in $|0_a\rangle$ and ramp up the coupling strengths $\eta_{r,b}(t)$. While increasing the couplings we inject a z-polarized excitation field through the cavity with $n_{\text{probe}} < 10$ photons for 1 ms, see Fig. 4.11(a). The excitation field is derived from the same laser as the transverse drives and the local oscillator for the heterodyne setup; its frequency is adjusted to be close to the bare excited polariton resonance $\bar{\omega} + \omega_0$. At the end of the excitation pulse ($t = 0$), the excited polariton mode evolves freely according to the dynamics of the open system. We monitor this free evolution in real time by measuring the spectrum of the cavity field. We refer to this technique as *cavity-assisted Raman* *spectroscopy*, as the polariton excitations involve also two different internal levels with $m = -1$ and $m = 0$.

Simulations of the experimental protocol

We validate our cavity-assisted Raman spectroscopy protocol by numerically simulating the associated mean-field equations of motion. The probe field is described by a classical z-polarized electric field propagating along the cavity axis

$$E_{\text{probe}}(t, x) = \tilde{E}_{\text{probe}} \sqrt{n_{\text{probe}}(t)} \cos(kx) \mathrm{e}^{-i\omega_{\text{probe}} t - i\phi_{\text{probe}}}, \tag{4.25}$$

with frequency $\omega_{\text{probe}} = \bar{\omega} + \omega_0 + \delta_{\text{probe}}$. Here, $n_{\text{probe}}(t)$, ϕ_{probe} and δ_{probe} are the average intra-cavity photon number, relative phase and detuning with respect to the cavity field associated with the polariton branch ω_+ at low couplings. Additionally, the probe electric field per photon is given by $\tilde{E}_{\text{probe}}$. Following an analogous approach to Eq. (4.8), we obtain a time-dependent many-body Hamiltonian describing the interactions of the light-matter system with probe field. In a rotating frame at $\bar{\omega}$, it reads

$$\hat{H}_{\text{exc}} = \hat{H}_{\text{MB}} + 4\sqrt{n_{\text{probe}}(t)} \left[\hbar\bar{\eta} \sin(\Phi(t)) \hat{J}_x + \hbar\Delta\eta \cos(\Phi(t)) \hat{J}_y \right], \tag{4.26}$$

with $\Phi(t) = (\omega_0 + \delta_{\text{probe}})t + \phi_{\text{probe}}$. The probe beam stimulates the atomic coherences $\hat{J}_x$ and $\hat{J}_y$ via phase-modulated amplitudes $\propto \sin(\Phi(t))$ and $\propto \cos(\Phi(t))$, respectively, similar to cavity-enhanced Bragg spectroscopy [63]. Hence, we expect to coherently transfer non-negligible atomic populations to the excited state if we approach the low coupling two-photon resonance $\delta_{\text{probe}} = 0$. Following the procedure outlined in section 4.1.3, we derive mean-field equations of motion from the Hamiltonian in Eq. (4.26), and numerically solve them to simulate our spectroscopy protocol. The relative phase ϕ_{probe} drifts between different experimental realizations due to slow changes in the optical paths, resulting in fluctuations of the total number of atoms transferred to the excited state. For typical experimental parameters, we excite between 8% and 12% of the atoms at the end of the probe pulse.

4.5.2 Measuring the lifetime of the excitations through real-time spectroscopy

We prepare $N = 9.6(4) \times 10^4$ atoms in $|0_a\rangle$ for $\omega_0 = 2\pi \times 48(4)$ kHz and $\Delta_c = -2\pi \times 5.8(1)$ MHz, and ramp up the coupling strengths $\eta_{r,b}(t)$ within $t_{\text{ramp}} = 9.1$ ms. Additionally, we inject a weak 1 ms-probe pulse through the cavity with $n_{\text{probe}} = 7.2(1)$ photons and $\delta_{\text{probe}} = 2\pi \times 2.0(4)$ kHz, cf. Fig. 4.11(a).

In Figs. 4.11(b), we present representative single-shot spectrograms of the cavity field $\tilde{n}_{\text{ph}}(\omega, t)$ showing the excitation pulse and the subsequent evolution of the system for increasingly larger values of $\Delta\eta/\bar{\eta}$. In the Dicke limit [$\Delta\eta/\bar{\eta} = 0$, Fig. 4.11(b1)], the main components of the spectrum start around $\bar{\omega} \pm \omega_0$ and evolve towards $\bar{\omega}$ as the coupling $\bar{\eta}$ is increased, reflecting the softening of the excited polariton. At the critical point $\bar{\eta} = \eta_c$, the energy gap between the ground and

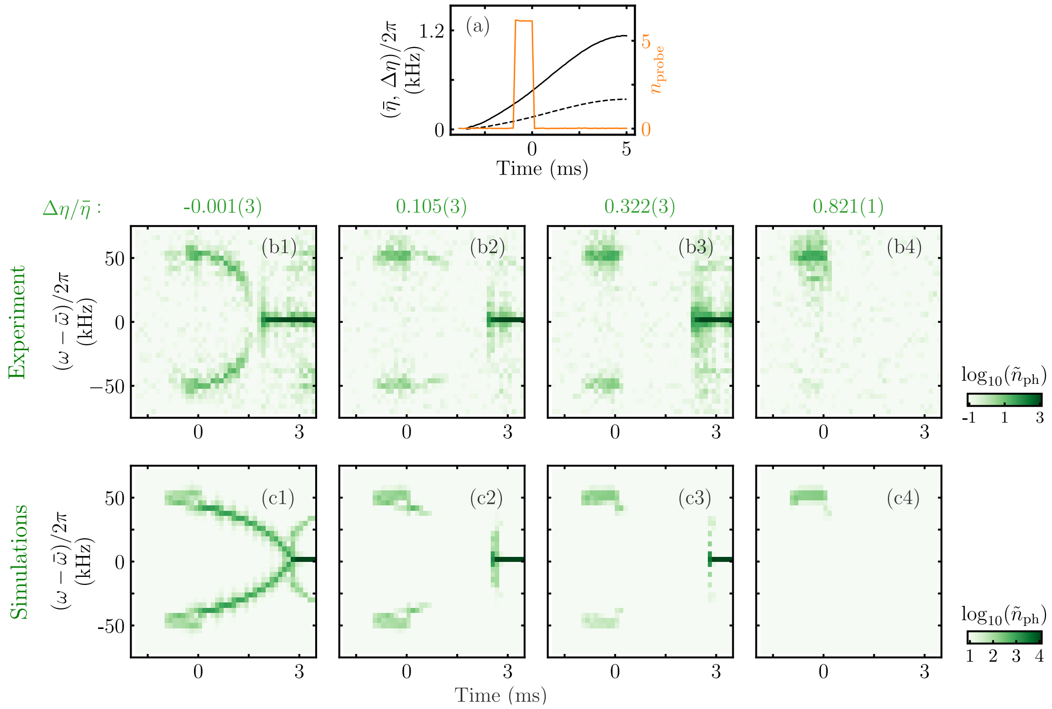

Figure 4.11: Real-time spectroscopy of the light-matter excitations. (a) Experimental protocol. While increasing $\bar{\eta}$ (solid black) and $\Delta\eta$ (dashed) at constant $\Delta\eta/\bar{\eta}$, we inject a weak probe pulse along the cavity axis (orange) to populate the excited polariton. **(b)** Representative experimental spectrograms, showing the number of photons $\tilde{n}_{\mathrm{ph}}$ as a function of time and frequency for different ratios $\Delta\eta/\bar{\eta}$. In the Dicke limit (b1), we observe a complete softening of the long-lived polariton excitations preceding the superradiant phase, indicated by a strong spectral component at $\omega = \bar{\omega}$. When increasing $\Delta\eta/\bar{\eta}$ (b2,b3), the polariton modes decay faster, until the superradiant phase is fully suppressed at large $\Delta\eta/\bar{\eta} = 0.82$ (b4). **(c)** Corresponding spectrograms obtained from numerical simulations, which accurately reproduce the observed polariton dynamics. We include spin dephasing with $\Gamma_\phi = 2\pi \times 0.1\,\mathrm{kHz}$.

excited-state polariton vanishes, and the superradiant phase transition occurs indicated by the build-up of a strong coherent field at frequency $\bar{\omega}$. As the relative imbalance $\Delta\eta/\bar{\eta}$ is increased [Figs. 4.11(b1,b2)], the mode softening is accompanied by a strong decay of the polariton excitations. At the same time, the superradiant phase transition occurs only at slightly later times until, for large enough $\Delta\eta/\bar{\eta}$, the transition is fully suppressed [Fig. 4.11(b3)].

In Figs. 4.11(c), we present the results obtained from numerical simulations using Eq. (4.26). The simulated spectrograms reproduce our experimental observations for different values of $\Delta\eta/\bar{\eta}$, showcasing both mode softening in the Dicke limit [Figs. 4.11(c1)] and the increasingly faster polariton decay with growing coupling imbalance [Figs. 4.11(c2-c4)]. When increasing $\Delta\eta/\bar{\eta}$, the spectrograms show a clear asymmetry, with the positive spectral component ($\omega_{-,\mathrm{S}} - \bar{\omega} > 0$) becoming more prominent than its negative counterpart ($\omega_{+,\mathrm{S}} - \bar{\omega} < 0$). We identify them with the elementary processes annihilating and creating an excited atomic polariton $|1\rangle$, with

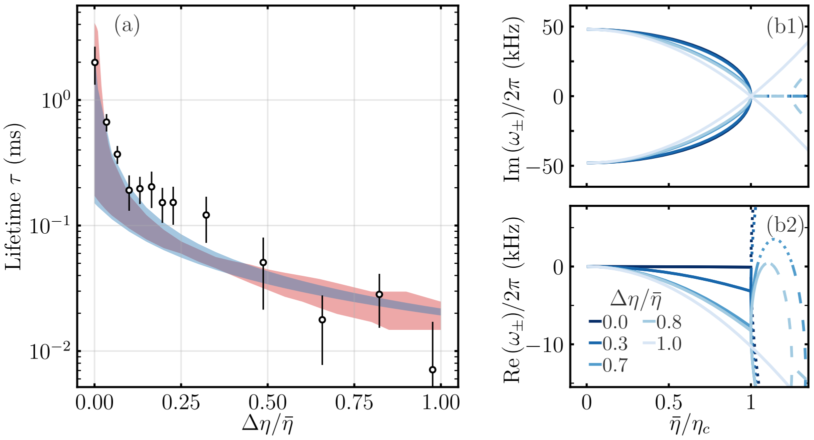

Figure 4.12: Probing the polariton lifetime. **(a)** Lifetime τ of the excitations in the normal phase as a function of the coupling imbalance $\Delta\eta/\bar{\eta}$. When increasing $\Delta\eta/\bar{\eta}$, the observed lifetime decreases over two orders of magnitude. This is captured by our analytic (blue) and numerical estimations (red shaded region), assuming a phenomenological spin dephasing between $\Gamma_\phi = 0$ (upper bound) and $\Gamma_\phi = 2\pi \times 0.5\,\mathrm{kHz}$ (lower bound). **(b)** Normal phase excitation spectrum as a function of average coupling $\bar{\eta}$. (b1) The imaginary part represents the energy cost associated with creating $[\mathrm{Im}(\omega_+) > 0]$ and annihilating $[\mathrm{Im}(\omega_-) < 0]$ a single polariton excitation. (b2) The real part of the spectrum remains negative at large coupling imbalances, $\mathrm{Re}(\omega_\pm) < 0$, indicating that polariton damping suppresses the superradiant transition and gives rise to a dissipation-stabilized normal phase. The different line shapes indicate stable normal phase (solid) superradiant phases (dotted) or phase bistability (dashed). Here, we set $\Gamma_\phi = 0$.

rates $\gamma_\downarrow$ and $\gamma_\uparrow$, respectively. Close to the Dicke limit [Figs. 4.11(b1,c1)] both process are balanced ($\gamma_\downarrow \approx \gamma_\uparrow$), whereas the annihilation of excited polaritons is strongly favored when increasing $\Delta\eta/\bar{\eta}$, $\gamma_\downarrow > \gamma_\uparrow$, giving rise to the observed asymmetry[3].

We experimentally determine the lifetime of the polariton excitations τ for different coupling imbalances $\Delta\eta/\bar{\eta}$. We acquire the photon number traces $n_{\mathrm{ph}}(t)$ with a time resolution of 10 µs by integrating the recorded photon number spectrograms $\tilde{n}_{\mathrm{ph}}(\omega, t)$ over a broad frequency region of $(\omega - \bar{\omega})/2\pi \in [-150, 150]$ kHz. Then, we numerically compute the cumulative signal $s(t) = \int_0^t n_{\mathrm{ph}}(t')dt'$, which takes the form $s(t) = s_{\max}(1 - e^{-t/\tau})$ when the photon number decays exponentially, i.e., $n_{\mathrm{ph}} \propto e^{-t/\tau}$. The lifetime τ is determined by the time at which $s(t)$ has reached a fraction $(1 - e^{-1})$ of its maximal value before entering the superradiant phase. We exclude experimental realizations where the atomic response during the excitation pulse falls below the noise level. Empirically, this method proves more robust in determining τ than relying on exponential fits of $n_{\mathrm{ph}}(t)$, particularly when evaluating weak spectrogram signals. As an exception, we extract τ from a fit of $s(t)$ for $\Delta\eta/\bar{\eta} = 0$.

---

[3] Notice, that we identify the positive spectral component at $\omega_{-,\mathrm{S}} - \bar{\omega} > 0$ with the annihilation of polaritons which is associated with a negative eingefrequency $\mathrm{Im}(\omega_-) \leq 0$, see Fig. 4.3(a). This is a direct consequence of total energy conservation in the system, as the positive spectral component of the cavity field at $\omega_{-,\mathrm{S}} > \bar{\omega}$ acquires the energy excess created by annihilating a polariton excitation.

In Fig. 4.12(a), we present the observed lifetimes τ of the polariton excitations as a function of $\Delta\eta/\bar{\eta}$. When modifying the coupling imbalance, the lifetimes change over orders of magnitude with $\tau \approx 2\,\mathrm{ms}$ in the Dicke limit ($\Delta\eta/\bar{\eta} = 0$) and $\tau \lesssim 0.01\,\mathrm{ms}$ in the Tavis-Cummings regime ($\Delta\eta/\bar{\eta} = 1$). We compare our findings to the lifetime of polariton excitations in the normal phase (blue shaded region), $\tau = -1/[2\mathrm{Re}(\omega_\pm)]$, which we obtain by diagonalizing the stability matrix in Eq. (4.14). Here, we consider constant coupling strengths at the end of the excitation pulses as the lifetime does not appreciably change within the duration of the probe pulse. For a closer comparison to the experiment, we perform numerical simulations for different values $\Delta\eta/\bar{\eta}$ and evaluate them identically to the experimental data (red shaded region). The systematic uncertainty of the theory estimations (extent of the shaded regions) is defined by considering variable spin dephasing rates Γ_ϕ within the range $2\pi \times [0, 0.5]$ kHz. This rate agrees with the estimated concessional dephasing rate in the total trapping potential, as derived in Ref. [72]. Both methods are in reasonable agreement with our observations, with the numerical simulations more accurately reflecting the experimental data for large coupling imbalances.

The direct connection between the decay of polariton excitations and the emergence of a dissipation-stabilized phase can be understood by analyzing the excitation spectrum of the open system, as shown in Fig. 4.12(b). The imaginary part of the spectrum reflects the energy cost associated with polariton excitations [Fig. 4.12(b1)], while the real part indicates damping (negative) or amplification (positive) [Fig. 4.12(b2)]. In particular, the superradiant transition occurs only when the real part $\mathrm{Re}[\omega_\pm]$ acquires positive contributions above the critical point η_c [189, 202, 203]. However, for sufficiently large coupling imbalances $\Delta\eta/\bar{\eta} \gtrsim 0.8$, the damping rate of the soft polariton mode $\gamma_\downarrow$ becomes dominant, counteracting the coherent build-up of the superradiant phase. This leads to the emergence of a dissipation-stabilized normal phase for arbitrarily large couplings $\bar{\eta} > \eta_c$.

Our new cavity-assisted Raman spectroscopy technique facilitates real-time access to the polariton dynamics in the normal phase. We observe a reduction of the polariton lifetime over orders of magnitude when increasing the coupling imbalance, indicating that collective polariton decay is the microscopic process underlying the observed dissipation-stabilized normal phase.

4.6 Discussion and outlook

In this chapter, we presented an experimental realization of an extended Dicke model, featuring independently tunable co- and counter-rotating light-matter interactions. Our implementation relies on inducing cavity-assisted Raman transitions between adjacent Zeeman sublevels of a degenerate Bose gas, and facilitates experimental access to emergent dissipative phases and transitions.

In the limit of balanced couplings, the system can be described by a Dicke Hamiltonian exhibiting a superradiant phase transition. This transition is characterized by spin-changing self-organization of the Bose-Einstein condensate (BEC), resulting in the formation of symmetry-broken checkerboard patterns of the transverse magnetization. We experimentally observed this superradiant transition using frequency-resolved measurements of the cavity field. Furthermore, we characterized the associated phase diagram. As a straightforward technical extension, we could benefit from operating the transverse drives at the tune-out wavelength of ^{87}Rb [110], $\lambda_{\mathrm{TO}} = 790.02\,\mathrm{nm}$, as done in chapter 6. This would allow us to suppress spurious optical lattice potentials ($V_{\mathrm{d}} = 0$) and induce spin-changing self-organization in a coherent superfluid regime. By employing time-of-flight images, we could directly observe and analyze the spatial structure of the emergent magnetic phases [79]. Operating at the tune-out wavelength has the added experimental advantage that it minimizes off-resonant spontaneous emission at any given Raman coupling rate [204], mitigating spurious heating and atom losses. Furthermore, it would be interesting to investigate the superradiant phases at low magnetic fields [193], where all the Zeeman sublevels of either the $F = 1$ or $F = 2$ manifolds become accessible giving rise to complex real-space magnetization patterns.

We demonstrated that by varying the imbalance of co- and counter-rotating light-matter interactions, we can induce a tunable competition between coherent and dissipative processes across the superradiant phase transition. This leads to the emergence of a dissipation-stabilized phase and a discontinuous phase transition, which we experimentally characterized. Through real-time measurements of the excitation dynamics, we identified the decay of the polariton modes as the microscopic mechanism underlying the observed macroscopic phenomena. In future experiments, we could investigate the regime of dominant counter-rotating couplings, $\Delta\eta/\bar{\eta} < 0$, where the system is expected to exhibit a plethora of non-equilibrium dynamics, ranging from limit cycles to spin flip instabilities and chaotic dynamics [186]. Extending our experiments to a regime with small atom or photon numbers could unveil beyond mean-field effects, such as quantum jumps in the bistability region as recently predicted in Refs. [205, 206]. Furthermore, combining our findings on prominent dissipative effects with cavity-mediated spin-orbit coupling [207, 208] could open up new avenues for studying such phenomena in a dissipative regime. Finally, squeezing of light fluctuations can be achieved over a wide parameter range at the NP-DSNP boundary. As shown in Fig. 4.12(b), the imaginary parts of the polariton eigenfrequencies merge while their real parts bifurcate, giving rise to excitation branches that either squeeze or broaden fluctuations. Characterizing the normal mode fluctuations in this regime can potentially shed light on the generation of light squeezing in the vicinity of exceptional points in non-Hermitian systems [209–211].

5 Dynamical tunneling in a momentum-space lattice

Experiments with ultracold quantum gases have successfully realized a wide variety of lattice models, facilitating the exploration of complex out-of-equilibrium phenomena in highly controlled settings [21, 168]. Lattice bonds which dynamically depend on the local particle configuration are ubiquitous in diverse fields of physics, ranging from lattice gauge theories in particle physics [212–214] to electron-phonon coupling in condensed-matter systems [215, 216]. Specifically, lattice experiments with ultracold atoms featuring density-dependent tunneling hold the potential to realize correlated many-body phenomena, such as pair superfluidity [217–219] and quantum scars [220, 221]. So far, density-dependent tunneling in optical lattices has been implemented via periodic driving [222–227] or dipolar interactions [228], yet solely inferred from spectroscopic measurements or by indirect comparison to theory. Additionally, in such real-space implementations it remains challenging to directly probe particle currents and evolving tunneling rates [229–231], which are essential to diagnose dynamical hopping.

In recent years, the study of ultracold atoms in *synthetic dimensions* has garnered significant interest for quantum simulation of artificial gauge fields and topological physics [35]. These schemes rely on encoding discrete lattice degrees of freedom in well-defined spin [232] and momentum modes [233] of degenerate quantum gases. In Fig. 5.1(a), we illustrate the central idea behind *momentum-space lattices*: a Bose-Einstein condensate (BEC) initialized in a zero-momentum state ($p = 0$) is illuminated by a pair of counter-propagating laser drives with wavevectors k and $-k$ [Fig. 5.1(a1)]. One of the lasers has a single frequency ω, whereas the other contains multiple frequency tones ω_j. In the dispersive regime, the BEC undergoes stimulated Bragg transitions [149] and scatters photons between the two counter-propagating drives, acquiring discrete recoil momenta in units of $\pm 2\hbar k$. As depicted in Figure 5.1(a2), Bragg scattering becomes resonant when the drive frequencies are tuned to match the parabolic free-space dispersion relation of the BEC. The discrete momentum states occupied by the atoms $p_j = 2j\hbar k$ ($j \in \mathbb{Z}$) can be interpreted as lattice sites in momentum space. In the resonant case, the dynamics can be described by a tight-binding Hamiltonian of the form

$$\hat{H} = \hbar \sum_j t_j \hat{c}_{j+1}^\dagger \hat{c}_j + \text{h.c.}, \tag{5.1}$$

as originally proposed in Ref. [233]. The operator $\hat{c}_j^\dagger$ creates an atom in the momentum state p_j (site j), and the complex tunneling rate $t_j = \eta_j \mathrm{e}^{i\phi_j}$ fully determined by the two-photon coupling η_j and the relative phase between the drives at ω and ω_j, see Fig. 5.1(a3). Experiments involving momentum-space lattices have provided a versatile platform for studying out-of-equilibrium dynamics in topological [234] and non-Hermitian systems [235], leveraging on their outstanding control over tunneling rates and site-resolved access through time-of-flight imaging.

Thus far, these experiments have primarily focused on single-particle physics. In this chapter, we demonstrate a complementary experimental platform for engineering dynamical tunneling events in a momentum-space lattice and directly measure them in real-time. We illustrate the central idea in Fig. 5.1(b): a BEC is coupled to a high-finesse optical cavity by a laser drive at frequency ω, giving rise to two-photon transitions that occupy the initially empty cavity mode ($\hat{a}^\dagger$), see schematics in Fig. 5.1(b1). Due to the large cavity linewidth $\hbar\kappa \gg E_{\mathrm{rec}}$, a single cavity mode can accommodate multiple spectral components ω_j and induce resonant two-photon transitions between the momentum states $p_j \to p_{j+1}$, as illustrated in the free-space dispersion in Fig. 5.1(b2). In a tight-binding representation, this can be interpreted as lattice model featuring dynamical tunneling rates, $t_j \propto \langle \hat{a}^\dagger(t) \exp(i\omega_j t)\rangle$, which evolve together with the emergent cavity field $\langle \hat{a}^\dagger(t)\rangle$ [Fig. 5.1(b3)]. In particular, we can locally resolve the hopping events through frequency-resolved measurements of the different frequency components of the leaking cavity field[1].

Our experimental implementation involves a spinor BEC coupled to the fundamental mode of our high-finesse optical cavity by a pair of far-detuned transverse laser drives. Cavity-assisted Raman scattering transfers atoms between two Zeeman sublevels, $m = -1$ and $m = 0$, while imparting momentum to the BEC in multiples of the photon recoil. This gives rise to spin and particle dynamics in a two-dimensional momentum grid, which we interpret as photon-assisted tunneling events in a synthetic lattice [233]. The individual hopping events are mediated by specific spectral components of the cavity field, which self-consistently evolve with the local configuration of the atoms. Unlike experiments employing classical drives to control single-particle hopping rates [236], in our setup, the tunneling rate dynamically depends on the formation of coherences between neighboring lattice sites. The underlying mechanism is superradiant Raman scattering [86, 127], which is facilitated by cavity losses and collectively enhanced by the number of participating atoms [237–240]. This makes our system non-Hermitian and renders the tunneling dynamics highly directional. At the same time, we can make use the cavity leakage to gain non-destructive, real-time access of the tunneling dynamics. By performing frequency-resolved measurements of the cavity field, we locally resolve the tunneling events in the momentum grid. A key feature of our implementation is that tunneling processes in opposite directions occur via different quantum paths and are independently controlled by the two Raman drives, respectively.

Our proof-of-principle implementation demonstrates a flexible platform for exploring non-equilibrium lattice physics, thanks to the possibility to optically engineer dynamical tunneling events and resolve them via the cavity field.

---

[1] Fig. 5.1(b) is intended solely as a schematic representation to emphasize the main differences compared to conventional momentum-space lattices shown in Fig. 5.1(a). The depicted coupling scheme in Fig. 5.1(b) would be technically unfeasible since an intra-cavity standing-wave drive with $V_{\mathrm{d}} \gtrsim 5\,\mathrm{E}_{\mathrm{rec}}$ would give rise to lattice quasimomentum states and significantly flatten the associated particle dispersion relation. This in turn would hinder our ability to locally identify different tunneling events through frequency-resolved measurements of the cavity field.

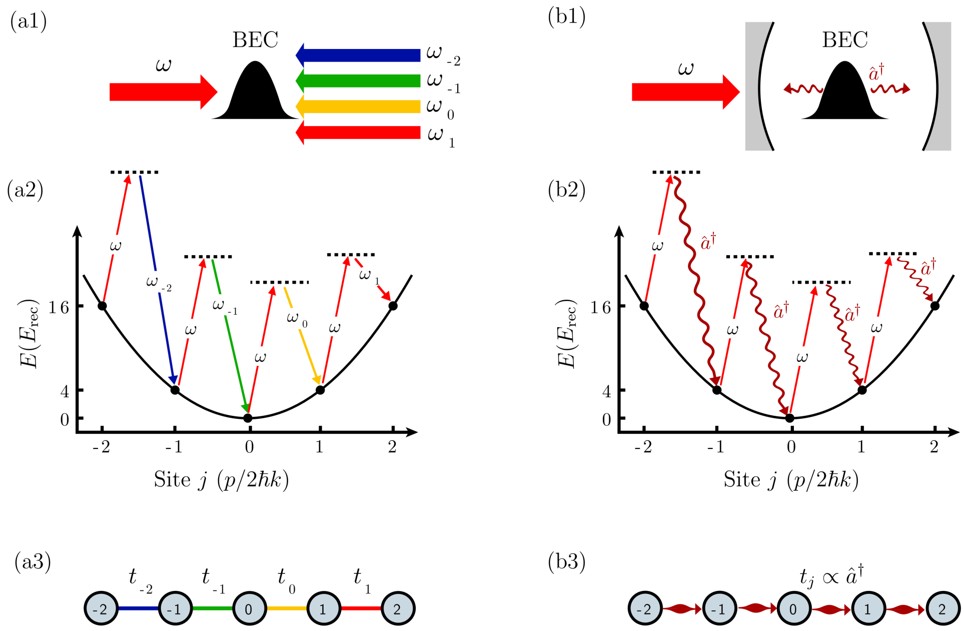

Figure 5.1: Implementing momentum-space lattices in a BEC. **(a)** Conventional momentum lattices. (a1) Experimental scheme showing a zero-momentum BEC ($p_0 = 0$) illuminated by two counter-propagating drives, containing a single (ω) and multiple frequency tones (ω_j), respectively. (a2) Free-particle dispersion relation. When the frequency difference of the two drives compensates the kinetic energy cost, the BEC undergoes resonant Bragg scattering and occupies a discrete set of momentum states $p_j = 2j\hbar k$, with $\hbar k$ being the photon recoil momentum. (a3) Momentum-space lattice. In a tight-binding picture, the discrete momentum states p_j are interpreted as lattice sites connected by photon-assisted tunneling with tunable rates t_j. **(b)** Dynamical momentum-space lattices in an optical cavity. (a1) Schematic experimental implementation, showing a BEC ($p = 0$) coupled to a single mode of an optical cavity (creation operator $\hat{a}^\dagger$) and illuminated by a laser drive with frequency ω. (b2) Free-particle dispersion, showing multiple cavity-assisted Bragg transitions. Within the cavity linewidth κ, the cavity mode can support multiple spectral components (wiggly arrows) and induce resonant two-photon transitions between the states $p_j \to p_{j+1}$. (b3) Cavity-assisted tunneling is inherently dynamical, $t_j \propto \hat{a}^\dagger$, as it is mediated by the emerging cavity field. This figure has been adapted from Refs. [233] and [241].

Outline of this chapter

In section 5.1, we discuss the coupling scheme and establish a tight-binding model in momentum space to describe cavity-assisted Raman scattering involving two phase-shifted transverse drives. After deriving the corresponding many-body Hamiltonian, we further discuss the open system dynamics associated with superradiant Raman scattering. In section 5.2, we present the experimental protocol and the first observations of dynamical tunneling in a momentum-space lattice. Specifically, we demonstrate non-destructive and real-time access to the tunneling dynamics via frequency-resolved measurements of the cavity field. In section 5.3, we investigate the collective nature of the tunneling dynamics due to the underlying superradiant

Raman scattering processes. Our experimental observations can be extended to a regime exhibiting a cascade of lattice currents, as discussed in section 5.4. Finally, in section 5.5, we summarize our findings and discuss potential extensions of our experiments.

Parts of this chapter have been published in Ref. [90]

> R. Rosa-Medina*, F. Ferri*, F. Finger, N. Dogra, K. Kroeger, R. Lin, R. Chitra, T. Donner and T. Esslinger. *Observing Dynamical Currents in a Non-Hermitian Momentum Lattice.* Physical Review Letters **128**, 143602 (2022)
> * These authors contributed equally to this work

5.1 Theoretical description

Here, we discuss the theoretical framework to model our experiments on dynamical tunneling in momentum-space lattices. After discussing the coupling scheme in section 5.1.1, we map our experimental system to a tight-binding Hamiltonian in momentum space featuring cavity-assisted hopping (section 5.1.2). We analyze the non-Hermitian lattice dynamics arising from superradiant Raman scattering in section 5.1.3, and derive an effective few-mode description in section 5.1.4 to numerically simulate the emergent dynamics.

5.1.1 Coupling configuration

Similar to the experiments discussed in chapter 4, we prepare a ^{87}Rb BEC of $N \approx 10^5$ atoms in the $m = -1$ Zeeman sublevel of the $F = 1$ hyperfine ground-state. A bias magnetic field along the $-z$-direction generates a Zeeman splitting of $\omega_z = 2\pi \times 48$ MHz and defines the quantization axis. The atomic cloud is illuminated by two retro-reflected laser fields propagating along the z direction with wavelength $\lambda_\mathrm{d} = 784.7$ nm and Raman couplings $\eta_{r,b}$, see Fig. 5.2(a). For our choice of quantization axis ($-z$), the relevant cavity mode is π polarized, while the two drives are in a superposition of the two drive fields can be decomposed into a balanced superposition of σ_+ and σ_- polarizations. Their exact frequencies $\omega_{r,b}$ lie on opposite sides of the effective cavity resonance ω_c, $\omega_r < \omega_c < \omega_b$, with $\omega_b - \omega_\mathrm{c} \approx \omega_z$ and $\omega_r - \omega_\mathrm{c} \approx -\omega_z$.

The key technical difference with respect to the experiments discussed in chapter 4 is that the standing-wave modulations of the two drives are shifted by $\lambda_\mathrm{d}/4$ at the position of the atoms. For balanced laser powers, the combined optical lattice potential is fully erased, as illustrated in Fig. 5.2(a). This configuration facilitates experimental access to coherent momentum-space atomic distributions using time-of-flight imaging, in contrast to the project discussed in the previous chapter [cf. Fig. 4.6(b)]. For technical details on the implementation of the out-of-phase standing-wave drives, refer to section 3.3.2.

The two incident laser drives induce cavity-assisted Raman transitions between the two adjacent Zeeman sublevels $m = -1$ and $m = 0$, which we refer to as $|0\rangle$ and $|1\rangle$, see coupling scheme Fig. 5.2(b). The initial BEC in $|0\rangle$ can be described by a

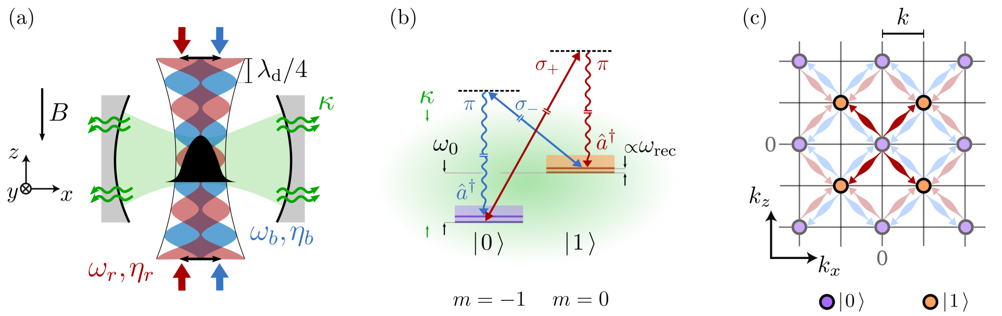

Figure 5.2: Setup and coupling scheme. **(a)** Experimental setup. A BEC coupled to an optical cavity with decay rate κ is illuminated by two x-polarized Raman drives with frequencies $\omega_{r,b}$ and coupling rates $\eta_{r,b}$. Their standing-wave modulations are shifted by $\lambda_\mathrm{d}/4$ with respect to each other at the position of the atoms. **(b)** Coupling scheme. Cavity-assisted Raman scattering involving two $\sigma_\pm$-polarized drives and the π-polarized cavity mode induces population transfer between specific momentum states of two different spin manifolds $|0\rangle$ ($m=-1$) and $|1\rangle$ ($m=0$); the two drives control the transitions $|0\rangle \to |1\rangle$ and $|1\rangle \to |0\rangle$, respectively. In a rotating frame at $(\omega_r+\omega_b)/2$, the different states are split by a tunable spin offset ω_0 and multiples of the recoil frequency ω_rec. **(c)** Momentum-space picture. A cavity-assisted Raman transition induced by the η_r drive (red arrow) transfers a BEC in $|0\rangle$ (central purple circle) to the spin state $|1\rangle$ (orange circles), imparting symmetric recoil momentum $\pm\hbar k$ on the atoms along the cavity (k_x) and drive (k_z) directions. Successive cavity-assisted Raman transitions (faint arrows) can be interpreted as photon-assisted tunneling in a two-dimensional momentum lattice.

zero-momentum state $|k_x=0,k_z=0\rangle$ along the drive (k_z) and cavity directions (k_x), see central purple circle in Fig. 5.2(c). When scattering σ_+-polarized photons from the Raman drive at ω_r into the cavity mode (red arrows), the atoms change their spin state to $|1\rangle$ (orange circles) and obtain symmetric photon recoil momentum $\pm\hbar k$ along k_x and k_z, occupying the well-defined momentum mode $|\pm k,\pm k\rangle$, see Figs. 5.2(a,b). The Raman drive at η_b can then scatter σ_--polarized photons into the cavity (blue arrows), and populate higher-order momentum states such as $|0,\pm 2k\rangle$ and $|\pm 2k,\pm 2k\rangle$ while changing their spin state back to $|0\rangle$ (purple circle). The splitting between the two spin manifolds $|0\rangle$ and $|1\rangle$ is given by ω_0 in a rotating frame at the intermediate frequency between the two drives $\bar{\omega}=(\omega_r+\omega_b)/2$.

When considering further sequential cavity-assisted Raman transitions, we can identify a discrete set of momentum states spaced by integer multiples of the photon recoil momentum $k=2\pi/\lambda_d$ along the drive (k_z) and cavity (k_x) directions, as schematically depicted in Fig. 5.2(c). In the next sections, we will map such processes to a two-dimensional tight-binding model in momentum space describing cavity-assisted dynamical tunneling. Importantly, the linewidth of the underlying cavity field ($\kappa = 2\pi\times 1.25\,\mathrm{MHz}$) is orders of magnitude larger than both the internal level splitting ($\omega_0 \approx 2\pi\times 50\,\mathrm{kHz}$) and the recoil frequency of ^{87}Rb atoms ($\omega_\mathrm{rec}=2\pi\times 3.73\,\mathrm{kHz}$). Hence, a single cavity mode can support multiple spectral components and induce resonant cavity-assisted Raman transitions in an extended momentum-space lattice. Notably, our implementation also comprises two spin sectors $|0\rangle$ and $|1\rangle$, resulting in a spin-textured momentum lattice.

5.1.2 Tight-binding Hamiltonian in momentum space

We derive the single-particle Hamiltonian of the system, adhering to the general framework outlined in section 2.1.3. The negative part $\hat{\mathbf{E}}^{(-)}$ of the total electric field is

$$\hat{\mathbf{E}}^{(-)} = \frac{E_r}{2} f_r(z)\mathbf{e}_y e^{-i\omega_r t} + \frac{E_b}{2} f_b(z)\mathbf{e}_y e^{-i\omega_b t} + E_0 g(x)\hat{a}\mathbf{e}_z. \tag{5.2}$$

The operator $\hat{a}$ annihilates z-polarized photons in the fundamental mode of the cavity with vacuum electric field amplitude $E_0 = 403$ V/m (see section 3.1.2). The two transverse drives are x polarized and propagate along the z direction. Their frequencies and electric field amplitudes are $\omega_{r,b}$ and $E_{r,b}$, respectively. Given their small frequency difference $\omega_b - \omega_r = 2\pi \times 96$ MHz, we consider a common wavenumber $k = \bar{\omega}/c$ for the two drives, with $\bar{\omega} = (\omega_b + \omega_r)/2$. We neglect the transverse Gaussian modulation of the electric fields, and assume mode profiles $f_r(z) = \cos(kz)$ and $f_b(z) = \sin(kz)$ for the two out-of-phase drives at ω_r and ω_b, respectively. The cavity mode profile is given by $g(x) = \cos(kx)$.

Analogous to section 4.1.2, we derive the single-particle Hamiltonian

$$\hat{H}_{\mathrm{SP}} = \hat{H}_{\mathrm{at}} + \hat{H}_{\mathrm{cav}} + \hat{H}_s + \hat{H}_v, \tag{5.3}$$

in a rotating frame induced by the generator $\hat{H}_{\mathrm{rot}} = \hbar\bar{\omega}\hat{a}^\dagger\hat{a} - \hbar\omega_z'\hat{F}_z$, with $\omega_z' = (\omega_b - \omega_r)/2$. In this rotating frame, a cavity field oscillating at $\bar{\omega} = (\omega_b + \omega_r)/2$ becomes time independent. The bare atomic and cavity Hamiltonians are respectively

$$\begin{aligned} \hat{H}_{\mathrm{at}} &= \frac{\hat{p}^2}{2M} + V_{\mathrm{ext}}(\hat{\mathbf{x}}) + \hbar\delta_z\hat{F}_z + \hbar q\hat{F}_z^2, \\ \hat{H}_{\mathrm{cav}} &= -\hbar\Delta_{\mathrm{c}}\hat{a}^\dagger\hat{a}, \end{aligned} \tag{5.4}$$

with $\hat{\mathbf{F}} = (\hat{F}_x, \hat{F}_y, \hat{F}_z)^T$ being the $F = 1$ spin operator. The internal energy of the atom is parameterized by the effective linear splitting $\delta_z = \omega_z + \omega_z'$ and the second order Zeeman shift q. The external trapping potential $V_{\mathrm{ext}}(\hat{\mathbf{x}})$ is kept fixed during the experiments. The detuning $\Delta_{\mathrm{c}} = \bar{\omega} - \omega_c$ determines the bare energy of the cavity photons, with ω_c being the cavity resonance.

As discussed in section 2.1, dispersive light-matter interactions can be decomposed into scalar and vectorial contributions. The scalar interactions are given by

$$\hat{H}_s = \frac{\alpha_s}{4}\left[E_b^2 f_b^2(z) + E_r^2 f_r^2(z)\right] + \alpha_s E_0^2 g^2(x)\hat{a}^\dagger\hat{a}. \tag{5.5}$$

In the limit of balanced drives, $E_r^2 = E_b^2$, the combined static lattice vanishes at the position of the atoms due to $f_r^2(z) + f_b^2(z) = 1$. In the experiments discussed in this chapter we opt to use x-polarized transverse drives to suppress contributions of the y-polarized cavity mode ($\hat{a}_y$), see Eq. (2.15). Such contributions could otherwise induce a competing superradiant phase transition associated with atomic self-organization [62].

The vectorial light-matter interactions are central for our considerations and read

$$\begin{aligned} \hat{H}_v &= -\frac{\alpha_v E_r E_0}{8} g(x) f_r(z)\left[\hat{a}\hat{F}_- + \hat{a}^\dagger\hat{F}_+\right] + \frac{\alpha_v E_b E_0}{8} g(x) f_b(\mathbf{x})\left[\hat{a}\hat{F}_+ + \hat{a}^\dagger\hat{F}_-\right] \\ &= -\hbar\eta_r\cos(kx)\cos(kz)\left[\hat{a}\hat{F}_- + \hat{a}^\dagger\hat{F}_+\right] + \hbar\eta_b\cos(kx)\sin(kz)\left[\hat{a}\hat{F}_+ + \hat{a}^\dagger\hat{F}_-\right], \end{aligned} \tag{5.6}$$

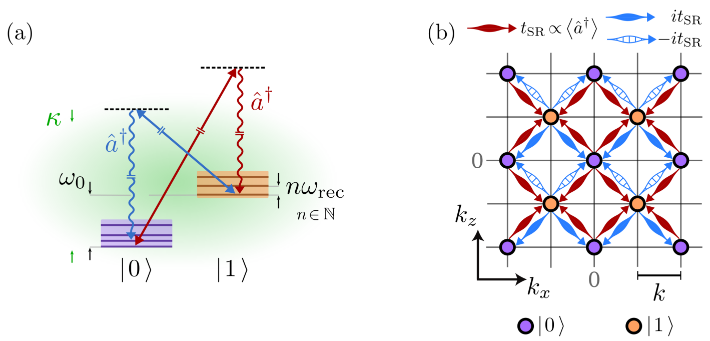

Figure 5.3: Realizing dynamical tunneling in a momentum-space lattice. **(a)** Coupling scheme. Raman scattering, involving absorption from two independent drives η_r (solid red) and η_b (solid blue arrow), and net emission of photons in the cavity mode (wiggly arrows, creation operator $\hat{a}^\dagger$), induces population transfer between specific momentum states of two different spin manifolds $|0\rangle$ (purple) and $|1\rangle$ (orange lines). In a rotating frame at $\bar{\omega}$, these states are offset by the two-photon detuning ω_0 and by multiples of the recoil frequency ω_{rec}, with $\omega_{\mathrm{rec}} \leq \omega_0 \ll \kappa$. **(b)** Tunneling dynamics in a momentum lattice. Cavity-assisted Raman scattering couples discrete momentum states of $|0\rangle$ (purple) and $|1\rangle$ (orange circles) differing by $\pm k$ (recoil momentum) in x and z directions. The two drives at ω_r (red) and ω_b (blue arrows) control different tunneling paths; the hopping rate dynamically depends on the emergent cavity field, with $t_{\mathrm{SR}} \propto \langle\hat{a}^\dagger\rangle$.

where we introduce the Raman couplings $\eta_{r,b} = \alpha_v E_{r,b} E_0/(8\hbar)$. The light-matter interactions in Eq. (5.6) closely resemble the Hamiltonian from the previous chapter, see Eq. (4.5), with one small yet critical difference. The co- and counter-rotating contributions of light-matter interactions are associated to different spatial mode profiles, due to the two standing-wave drives being out-of-phase at the position of the atoms, with $f_b(\mathbf{x}) = \sin(kz)$ and $f_r(\mathbf{x}) = \cos(kz)$, respectively. This subtle difference has a significant impact on the dynamics, as the system can no longer be mapped to a conventional two-mode Dicke model.

Tight-binding description in momentum space

We now map the system to a tight-binding Hamiltonian in momentum space. We consider a discrete set of two-dimensional atomic plane waves in the xz plane

$$\psi^{\sigma}_{(l_x,l_z)}(\hat{\mathbf{x}}) = \frac{k}{2\pi} e^{ik(l_x x + l_z z)} \otimes |\sigma = m+1\rangle\,. \tag{5.7}$$

Their wavenumbers are multiples ($l_{x,z} \in \mathbb{Z}$) of the photon recoil momentum $k = \bar{\omega}/c = 2\pi/\lambda_{\mathrm{d}}$, and the index $|\sigma\rangle$ refers to the spin state $\sigma \in \{0,1\}$ associated with the Zeeman sublevel $m \in \{-1,0\}$. The states are normalized within a unit cell of size $\mathcal{R} = [-\pi/k, \pi/k)^2$. We refer to the corresponding single-particle states as $|l_x, l_z\rangle_\sigma$. As in the previous chapter, we neglect cavity-assisted Raman transitions to the $m = +1$ Zeeman sublevel as they are detuned by $\delta_{+1} \approx 2q = 2\pi \times 0.7$ MHz at the large bias magnetic fields $B \approx 68.3$ G we operate.

To obtain a many-body description, we exploit the fact that the initial BEC in $m = -1$ can be described by a zero-momentum mode with $|0,0\rangle_0$, and that each cavity-assisted Raman process simultaneously changes the spin (σ) and momentum states of the atoms (l_x, l_z) by ±1. We expand the atomic field operator as

$$\hat{\Psi}(\hat{\mathbf{x}}) = \sum_{\{j_x,j_z\}\in\mathbb{Z}} \psi^0_{(2j_x,2j_z)}(\hat{\mathbf{x}})\hat{c}^0_{(2j_x,2j_z)} + \psi^1_{(2j_x+1,2j_z+1)}(\hat{\mathbf{x}})\hat{c}^1_{(2j_x+1,2j_z+1)}, \tag{5.8}$$

with the operators $\hat{c}^\sigma_{(2j_x+\sigma,2j_z+\sigma)}$ annihilating particles in the mode $|2j_x+\sigma, 2j_z+\sigma\rangle_\sigma$. In second quantization [112], we derive the corresponding as many-body Hamiltonian

$$\hat{H} = \hat{H}_0 + \hat{H}_\mathrm{t}. \tag{5.9}$$

The diagonal term is given by

$$\begin{aligned}\hat{H}_0 &= \hat{H}_\mathrm{cav} + \int_{\mathcal{R}} \hat{\Psi}^\dagger(\hat{\mathbf{x}})\left[\hat{H}_s + \hat{H}_\mathrm{at}\right]\hat{\Psi}(\hat{\mathbf{x}})d\mathbf{x}\\ &= -\hbar\tilde{\Delta}_\mathrm{c}\hat{a}^\dagger\hat{a} + \sum_{\substack{\{j_x,j_z\}\in\mathbb{Z}\\ \sigma\in\{0,1\}}} \hbar[\sigma\omega_0 + \omega^\mathrm{kin}(2j_x+\sigma, 2j_z+\sigma)]\hat{c}^{\sigma\dagger}_{(2j_x+\sigma,2j_z+\sigma)}\hat{c}^\sigma_{(2j_x+\sigma,2j_z+\sigma)},\end{aligned} \tag{5.10}$$

with $\tilde{\Delta}_\mathrm{c} = \Delta_\mathrm{c} - NU_0/2$ being the dispersively shifted cavity detuning. As illustrated in Fig. 5.3(a), the energy offset between the different atomic modes arises from a kinetic energy contribution $\omega^\mathrm{kin}_{(2j_x+\sigma,2j_z+\sigma)} = [(2j_x+\sigma)^2 + (2j_z+\sigma)^2]\omega_\mathrm{rec}$ and a tunable splitting between the two spin manifolds $\omega_0 = (\omega_b - \omega_r)/2 + \omega_z - q$.

For balanced Raman couplings, $\eta_b \approx \eta_r$, we can neglect scalar interactions as they result in an erased lattice configuration, see Eq. (5.6). Furthermore, the small dynamical intra-cavity lattice $V_\mathrm{c} = -\hbar\alpha_s E_0^2\langle\hat{a}^\dagger\hat{a}\rangle \lesssim 0.3\hbar\omega_\mathrm{rec}$ has negligible influence on the observed dynamics for typical cavity photon numbers ($\langle\hat{a}^\dagger\hat{a}\rangle \lesssim 20$). The vectorial light-matter interactions couple the different atomic modes and yield

$$\begin{aligned}\hat{H}_\mathrm{t} &= \int\hat{\Psi}^\dagger(\hat{\mathbf{x}})\hat{H}_v\hat{\Psi}(\hat{\mathbf{x}})d\mathbf{x}\\ &= -\sum_{\substack{\{j_x,j_z\}\in\mathbb{Z}\\ s_{1,2}=\pm1}}\left[\frac{\hbar\eta_r\hat{a}^\dagger}{\sqrt{8}}\hat{c}^{1\dagger}_{(2j_x+s_1,2j_z+s_2)}\hat{c}^0_{(2j_x,2j_z)} - is_2\frac{\hbar\eta_b\hat{a}^\dagger}{\sqrt{8}}\hat{c}^{0\dagger}_{(2j_x,2j_z)}\hat{c}^1_{(2j_x+s_1,2j_z+s_2)}\right] + \text{h.c.}.\end{aligned} \tag{5.11}$$

This Hamiltonian describes cavity-assisted tunneling between neighboring states in a two-dimensional momentum grid, where even (odd) sites are exclusively populated by atoms in the spin state $|0\rangle$ ($|1\rangle$), as illustrated in Fig. 5.3(b). Crucially, each tunneling process changes the spin state of the atoms and is associated with the creation ($\propto \hat{a}^\dagger$) or annihilation of cavity photons ($\propto \hat{a}$).

In the limit of balanced Raman couplings $\eta := \eta_r = \eta_b$, we introduce a *dynamical tunneling rate*

$$t_\mathrm{SR}(t) = -\frac{\eta\langle\hat{a}^\dagger(t)\rangle}{\sqrt{8}}. \tag{5.12}$$

This hopping rate is not solely determined by the external laser drives ($\propto \eta$), but also self-consistently evolves with the expectation value of the emergent cavity field ($\propto \langle \hat{a}^\dagger(t) \rangle$). This is in direct contrast to conventional synthetic lattices engineered with ultracold atoms [233], where tunneling rates are fully determined by the incident classical laser drives. As evident from Eq. (5.11), the two laser drives η_r and η_b independently control tunneling between the spin manifolds $|0\rangle \to |1\rangle$ [red] and $|1\rangle \to |0\rangle$ [blue arrows in Fig. 5.3(b)], respectively. In the latter case, we obtain sign-changing hopping rates $\mp it_{\mathrm{SR}}$ for tunneling events towards lattice sites with additional $\pm k$ momentum in z-direction; this is a direct consequence of the phase-shifted spatial modulation of the corresponding drive, i.e., $f_b(z) = \sin(kx) = i(e^{-ikz} - e^{ikz})/2$. The presence of tunneling terms with opposite signs results in observable destructive interference between different tunneling paths, as discussed in section 5.2.

5.1.3 Superradiant scattering and non-Hermitian lattice dynamics

In our experiments, photon loss at the cavity mirrors makes our system inherently open and significantly alters the dynamics, leading to a non-Hermitian evolution within the momentum lattice. The tunneling Hamiltonian H_{t} in Eq. (5.11) constitutes a multi-level version of the Tavis-Cummings model discussed in chapter 2, see Eq. (2.19): a single cavity mode ($\hat{a}$) mediates transitions involving multiple momentum modes ($|l_x, l_z\rangle_\sigma$) of the two spin levels $|0\rangle$ and $|1\rangle$. The associated collective coupling rates are given by $\eta_{r,b}\sqrt{N/8}$. Since our experiment operates in the bad cavity regime (overdamped regime), with $\kappa \gg \eta_{r,b}\sqrt{N/8}$, we expect the lattice dynamics to be strongly dissipative and facilitated by superradiant Raman scattering.

In an illustrative picture, the evolution of the system is primarily determined by Raman processes that create cavity photons ($\propto \hat{a}^\dagger$), as the opposite process of absorbing photons ($\propto \hat{a}$) is hindered by cavity losses. Consequently, the non-Hermitian dynamics in the momentum lattice becomes directional, with preferred tunneling directions illustrated by the red and blue arrows in Fig. 5.2(c). Furthermore, we expect that the individual tunneling events are mediated by superradiant Raman scattering processes, which are collectively enhanced by the number of participating atoms, as derived in section 2.2.2 of chapter 2. This gives rise to tunneling rates that evolve self-consistently with the coherences between the sites involved in each hopping process.

This behavior is fundamentally different from the spin-changing self-organization phase transition discussed in section 4.2 of the previous chapter. In that case, the system can be mapped to an extended Dicke model with tunable co- and counter-rotating interactions due to the matching spatial phase of the two Raman drives. As also observed in Ref. [79], in that case a low-momentum stable superradiant phase is created above a critical driving strength.

Frequency characteristics of superradiant photon pulses

In our experiment, the large cavity decay rate $\kappa = 2\pi \times 1.25\,\mathrm{MHz}$ leads to a broad Lorentzian density of states [189] for the cavity field associated with superradiant scattering

$$\rho(\omega) = \frac{\kappa}{(\omega - \omega_c)^2 + \kappa^2}, \tag{5.13}$$

where $\kappa \gg \omega_0$ and $\kappa \gg \omega_{\text{rec}}$. As a result, a single cavity mode can accommodate multiple spectral components and enable tunneling in an extended momentum lattice via superradiant Raman scattering.

As discussed in section 2.1.4 for a two-mode Tavis-Cummings model, energy conservation is expected to hold for the complete system of photons and atoms during superradiant Raman scattering [120]. We extend this notion to the relevant case of a multi-level Tavis-Cummings system and obtain the frequency of the cavity fields associated with superradiant Raman scattering events. These frequencies have to overcome both the internal and kinetic energy cost to populate different sites in the momentum lattice

$$\begin{aligned}
\omega^r_{(f_x,f_z,i_x,i_z)} &= \bar{\omega} - \omega_0 - [\omega^{\text{kin}}_{(f_x,f_z)} - \omega^{\text{kin}}_{(i_x,i_z)}],\\
\omega^b_{(f_x,f_z,i_x,i_z)} &= \bar{\omega} + \omega_0 - [\omega^{\text{kin}}_{(f_x,f_z)} - \omega^{\text{kin}}_{(i_x,i_z)}].
\end{aligned} \tag{5.14}$$

The spectral components of the cavity field at the frequencies $\omega^r(f_x, f_z, i_x, i_z)$ and $\omega^b(f_x, f_z, i_x, i_z)$ induce Raman scattering between the spin levels $|0\rangle \to |1\rangle$ and $|1\rangle \to |0\rangle$, respectively. In our experiment, these scattering events are selectively induced by the transverse drives at frequencies ω_r and ω_b. The global splitting between the spin levels causes these two transitions to shift in opposite directions, $\mp\omega_0$, facilitating the identification of the corresponding tunneling processes. The indices (i_x, i_z) and (f_x, f_z) denote the initial and final lattice sites of a given tunneling process, respectively.

5.1.4 Few-mode expansion and open system simulations

As discussed in previous sections, we expect the tunneling dynamics to be determined by the interplay between the tunneling Hamiltonian in Eq. (5.11) and cavity field decay. To efficiently simulate the dynamics of the first few superradiant processes and obtain a minimal theoretical description, we consider appropriate superpositions of different lattice sites. Specifically, we identify four low-energy atomic modes

$$\begin{aligned}
\hat{\psi}_0 &= \hat{c}^0_{(0,0)},\\
\hat{\psi}_1 &= \left(\hat{c}^1_{(1,1)} + \hat{c}^1_{(1,-1)} + \hat{c}^1_{(-1,1)} + \hat{c}^1_{(-1,-1)}\right)/2,\\
\hat{\psi}_2 &= i\left(\hat{c}^1_{(1,-1)} + \hat{c}^1_{(-1,-1)} - \hat{c}^1_{(1,1)} - \hat{c}^1_{(-1,1)}\right)/2,\\
\hat{\psi}_3 &= i\left(\hat{c}^0_{(0,-2)} - \hat{c}^0_{(0,2)}\right)/\sqrt{2},
\end{aligned} \tag{5.15}$$

which are coupled to each other via the Hamiltonian in Eq. (5.11). In real space, the corresponding single-particle wave functions of these orthonormal modes are $\psi_0 \propto 1$, $\psi_1 \propto \cos(kx)\cos(kz)$, $\psi_2 \propto \cos(kx)\sin(kz)$ and $\psi_3 \propto \sin(2kz)$. In momentum space, the operator $\hat{\psi}_0$ is associated with the central lattice site $|0,0\rangle_0$, cf. Eq. (5.15), whereas the remaining modes can be expressed as superpositions of specific lattice sites

$$\begin{aligned}
\hat{\psi}_1 : \quad & |\pm 1, \pm 1\rangle_1 = \frac{1}{2}\left(|1,-1\rangle_1 + |-1,-1\rangle_1 + |-1,1\rangle_1 + |1,1\rangle_1\right), \\
\hat{\psi}_2 : \quad & |\pm 1, \mp 1\rangle_1 = \frac{i}{2}\left(-|1,-1\rangle_1 + |-1,-1\rangle_1 - |-1,1\rangle_1 + |1,1\rangle_1\right), \\
\hat{\psi}_3 : \quad & |0, \mp 2\rangle_0 = \frac{i}{\sqrt{2}}\left(|0,-2\rangle_0 - |0,2\rangle_0\right). \qquad (5.16)
\end{aligned}$$

Within this momentum-space truncation, the Hamiltonian in Eq. (5.9) can be simplified to

$$\begin{aligned}
\hat{H}_{\text{cut}} = & -\hbar\tilde{\Delta}_{\text{c}}\hat{a}^\dagger\hat{a} + \hbar(\omega_0 + 2\omega_{\text{rec}})(\hat{\psi}_1^\dagger\hat{\psi}_1 + \hat{\psi}_2^\dagger\hat{\psi}_2) + 4\hbar\omega_{\text{rec}}\hat{\psi}_3^\dagger\hat{\psi}_3 \\
& - \frac{\hbar\eta}{\sqrt{2}}\hat{a}^\dagger\left[\hat{\psi}_1^\dagger\hat{\psi}_0 - \frac{1}{\sqrt{2}}\hat{\psi}_3^\dagger\hat{\psi}_1 + \frac{1}{\sqrt{2}}\hat{\psi}_2^\dagger\hat{\psi}_3 - \hat{\psi}_0^\dagger\hat{\psi}_2\right] + \text{ h.c. }. \qquad (5.17)
\end{aligned}$$

To efficiently simulate the open system dynamics, we derive mean-field equations of motion for the expectation values of the cavity field $\alpha = \langle\hat{a}\rangle/\sqrt{N}$, atomic populations $\rho_{jj} = \left\langle\hat{\psi}_j^\dagger\hat{\psi}_j\right\rangle/N$, and coherences $\rho_{jk} = \left\langle\hat{\psi}_j^\dagger\hat{\psi}_k\right\rangle/N$, with $\{j,k\} \in \{0,1,2,3\}$. This approach allows us to include a phenomenological spin dephasing rate of approximately $\Gamma_\phi = 2\pi \times 0.2\,\text{kHz}$ between the two different spin manifolds $|0\rangle$ and $|1\rangle$, which damps the corresponding atomic coherences. This dephasing is attributed to the combined effect of atomic collisions and magnetic field fluctuations [89]. The exact equations of motion are presented in Eqs. (A.2) of appendix A.1.

5.2 Observing cavity-mediated tunneling in a momentum-space lattice

In this section, we report on the first experimental observations of dynamical tunneling in a momentum-space lattice. In section 5.2.1, we present the details of the experimental protocol. In section 5.2.2, we discuss our experimental observations and demonstrate how frequency resolved measurements of the cavity leakage can be employed to perform non-destructive real-time measurements of the tunneling dynamics. Finally, in section 5.2.3, we access an experimental regime showcasing multiple tunneling events in an extended momentum grid and discuss the experimental factors limiting the lifetime of the momentum lattice.

5.2.1 Experimental protocol

Our experiments start with a zero-momentum Bose-Einstein condensate initialized in the $m = -1$ Zeeman sublevel (state $|0\rangle$), i.e., in the central lattice site $|0,0\rangle_0$. We increase the lattice depth of the two standing-wave drives via smooth s-shape ramps

$$V_{r,b}(t) = V_{r,b}^{\max}\left[3\left(\frac{t}{t_{\text{ramp}}}\right)^2 - 2\left(\frac{t}{t_{\text{ramp}}}\right)^3\right], \qquad (5.18)$$

with $V_{r,b}^{\max}(t)$ being the corresponding peak lattice depth and t_{ramp} being the duration of the ramp. As detailed in section 3.3.1, we independently stabilize the intensity of the two Raman drives. The s-shape ramps have been empirically optimized to mitigate spurious heating and atom loss during loading in the transverse drive potentials [108]. In each experimental run, we maintain fixed values for the cavity detuning $\tilde{\Delta}_{\text{c}}$ and the offset between the two spin manifolds ω_0. These parameters can be adjusted independently by varying the cavity resonance frequency ω_{c} and the first-order Zeeman splitting ω_z, respectively. While ramping up the transverse drives, we employ our frequency-resolved heterodyne detection to record the z-polarized cavity field, see section 3.2.1 for technical details. Additionally, we perform destructive measurements of the spin and momentum distributions of the atoms using time-of-flight absorption imaging, as described in section 3.2.2.

5.2.2 Real-time probing of dynamical tunneling

In a first set of experiments, we prepare $N = 1.06(2) \times 10^5$ atoms in the site $|0, 0\rangle_0$. We operate at $\omega_0 = 2\pi \times 72.5(5)\,\text{kHz}$ and $\tilde{\Delta}_{\text{c}} = -2\pi \times 0.7(2)\,\text{MHz}$. To initialize the lattice dynamics, we ramp the two Raman drives together to $\eta_{r,b} = 2\pi \times 0.62(2)\,\text{kHz}$ within $t_{\text{ramp}} = 1.5\,\text{ms}$, as plotted in Fig. 5.4(a).

In Fig. 5.4(b), we present a representative photon number spectrogram $\tilde{n}_{\text{ph}}(t, \omega)$ of the leaking cavity field, see section 3.2.1 for technical details. The spectrogram reveals three distinct photon pulses at different frequencies, which we attribute to specific tunneling events in the momentum lattice: $|0, 0\rangle_0 \to |\pm1, \pm1\rangle_1 \to |0, \mp2\rangle_0 \to |\pm1, \mp1\rangle_1$. We directly confirm the involvement of these states by measuring the spin and momentum distribution of the atoms at different stages of the evolution, as shown in Figs. 5.4(c). The initial atomic distribution in Fig. 5.4(c1) is consistent with the system populating the site $|0, 0\rangle_0$, while the atomic distributions after the first [Fig. 5.4(c2)] and second superradiant pulses [Fig. 5.4(c3)] indicate the occupation of the modes $|\pm1, \pm1\rangle_1$ and $|0, \mp2\rangle_0$, respectively. The observed population imbalance between sites with $k_z > 0$ and $k_z < 0$ is attributed to spurious optical losses in the retro-reflected path of the standing-wave drives in the $-z$ direction.

We compare the emission frequencies of the three photon pulses with the expectations from total energy conservation (Eq. (5.14)). The gray lines in Fig. 5.4(b) indicate the corresponding frequencies $\omega^r_{(\pm1,\pm1,0,0)}$, $\omega^b_{(\pm2,\pm2,\pm1,\pm1)}$, and $\omega^r_{(\pm1,\pm1,\pm2,\pm2)}$, which are in reasonable agreement with our observations. Additionally, we perform ab initio few-mode numerical simulations following Eqs. (A.2) and plot the obtained spectrogram in Fig. 5.4(d), which accurately reproduces our experimental observations. The presence of tunneling terms with opposite signs $\pm i t_{\text{SR}}$ can give rise to *destructive path interference* when the atoms tunnel towards inner sites in z-direction, see Hamiltonian in Eq. (5.11). In our experiments, this effect manifests in the suppressed hopping $|\pm1, \pm1\rangle_1 \not\to |0, 0\rangle_0$ after the first tunneling event, as directly shown by the atomic distributions in Fig. 5.4(c3).

The strength of the emerging cavity field and the overall tunneling rate depends, in principle, on the sum of all two-site coherences connected by Raman scattering, as described by Eq. (5.11). Nonetheless, tunneling events between specific lattice

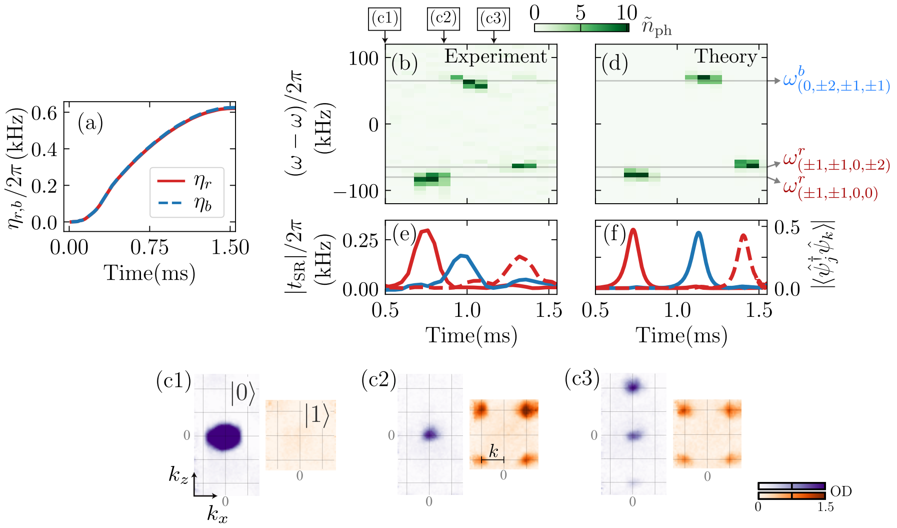

Figure 5.4: Real-time observation of dynamical tunneling. **(a)** Experimental protocol, showing a typical ramp of the two independent Raman couplings η_r and η_b. **(b)** Representative photon number spectrogram $\tilde{n}(t,\omega)$ displaying three time- and frequency-resolved superradiant pulses. We choose $T = 150\,\mu\mathrm{s}$ as the integration time. **(c)** Spin-resolved momentum distributions of the atoms at different stages of the evolution [see square labels in (b)]. **(d)** Spectrogram obtained from mean-field simulations. The horizontal lines in (b) and (d) indicate the pulse frequencies expected total energy conservation in Eq. (5.14). **(e)** Experimental tunneling amplitudes $|t_{\mathrm{SR}}|$, integrated in a $\delta\omega = 2\pi \times 5$ kHz window around the first (solid red), second (solid blue) and third photon peak (dashed red line) of the spectrogram in (b), respectively. **(f)** Simulated two-mode coherences $|\langle\hat{\psi}_1^\dagger\hat{\psi}_0\rangle|$, $|\langle\hat{\psi}_3^\dagger\hat{\psi}_1\rangle|$ and $|\langle\hat{\psi}_2^\dagger\hat{\psi}_3\rangle|$. Our observations are in quantitative agreement with the theoretical expectations, demonstrating that we can employ frequency-resolved measurements of the cavity field to resolve the tunneling events in the momentum lattice in real time.

sites are associated with well-defined cavity spectral components that satisfy total energy conservation. These spectral components selectively stimulate the formation of coherences between adjacent sites, provided they are not empty. Importantly, off-resonant stimulation of further lattice bonds is negligible when the tunneling rates are sufficiently small, i.e., $|t_{\mathrm{SR}}| \ll \omega_0$ and $|t_{\mathrm{SR}}| \ll \omega_{\mathrm{rec}}$. This results in *local dynamical tunneling* that depends on local occupations, similar to density-dependent hopping in real-space optical lattices [242]. This behavior is reflected by the simulated evolution of the coherences between adjacent lattice sites, as shown in Fig. 5.4(f). Therefore, we can associate each cavity pulse with a specific tunneling event in the momentum lattice and use Eq. (5.12) to infer the corresponding tunneling amplitudes $|t_{\mathrm{SR}}|$, as plotted in Fig. 5.4(e).

While the representative atom number distributions in Figs. 5.4(c) are obtained through multiple destructive measurements under identical experimental conditions, the cavity field spectrogram in Fig. 5.4(b) is acquired within a single experimental realization. Hence, our observations in this section demonstrate that we can reliably utilize frequency-resolved measurements of the leaking cavity field to locally resolve tunneling events in real time. Beyond our few-mode simulations, our experimental results are further validated by independent Gross-Pitaevskii equation simulations conducted by Rui Lin, as detailed in the Supplemental Material of Ref. [90] and summarized in appendix A.3.

5.2.3 Multiple hopping events and lifetime in the momentum lattice

In the previous section, we conducted proof-of-principle experiments demonstrating cavity-assisted tunneling in a momentum-space lattice. However, our observations were limited to few tunneling events involving small lattices. To explore tunneling dynamics in larger lattices, we increase the Raman coupling rates to significantly larger values, $\eta_{r,b} = 2\pi \times 1.44(3)\,\text{kHz}$, within $t_{\text{ramp}} = 3.6\,\text{ms}$, as plotted in Fig. 5.5(a). Experimentally, these Raman couplings correspond to the maximally available laser powers in a two-drive configuration, see section 3.3.1.

In Fig. 5.5(b), we present a representative cavity field spectrogram showcasing up to seven well-separated photon pulses. We identify the involved lattice sites by analyzing the frequency of the cavity field and comparing it to the expectation from Eq. (5.14) (gray lines). Thereby, we identify cavity pulses mediating tunneling events involving external lattice sites, such as $|2,2\rangle_0$. In Fig. 5.5(c), we provide a schematic representation of the inferred tunneling events. We emphasize that the tunneling events are not restricted to the processes depicted in Fig. 5.5(c), as they arise from multiple competing quantum paths. We speculate that even more lattice sites can be occupied by performing faster coupling ramps. However, this is technically challenging due to the limited bandwidth of the transverse drive intensity stabilization setup.

We identify the following experimental limitations to the maximum number of accessible tunneling events in our system:

- First, the momentum states move out of the grid nodes due to oscillatory motion in the harmonic trap [236]. For non-interacting systems, this rate is solely determined by the trap frequencies ($\omega_h \approx 2\pi \times 200$ Hz) yielding lifetimes around $T_{\text{LT}} \approx 0.5\,\text{ms}$ for the corresponding momentum states after each photon pulse. To evaluate the influence of the external confinement and contact interactions on the lattice dynamics, we perform supplementary Gross-Pitaevskii (GP) simulations as a benchmark, see appendix A.3. Our simulations indicate that the repulsive contact interactions in ^{87}Rb atoms effectively increase the lifetime in the momentum lattice to $T_{\text{LT}} \gtrsim 1.0\,\text{ms}$ after each tunneling event, see Fig. A.1 in the appendix A.3 for a detailed discussion. Indeed, this timescale approximately corresponds to the observed time delay between the final two photon pulses in Fig. 5.5(b).

- Second, heating of the BEC from off-resonant spontaneous emission progressively melts the momentum lattice when approaching the recoil temperature, which is around $T_{\text{rec}} = \hbar\omega_{\text{rec}}/k_{\text{B}} \approx 180$ nK, with k_{B} being the Boltzmann constant. However, as the recoil temperature greatly exceeds the initial temperature of our BEC $T \approx 90\,\text{nK}$ [108], this effect is negligible within the

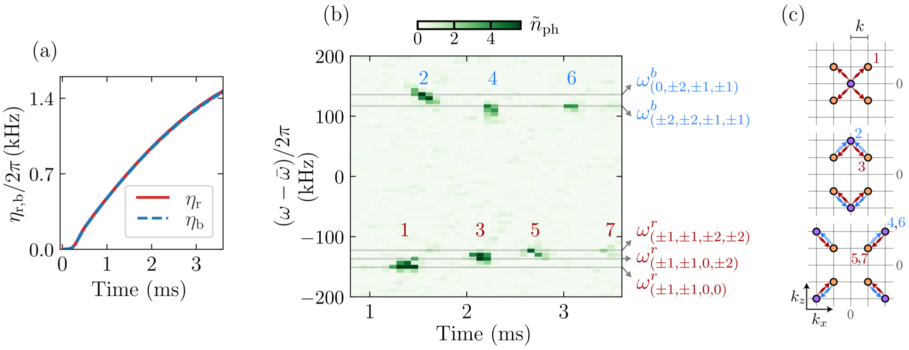

Figure 5.5: Identifying multiple hopping events in the momentum lattice. **(a)** Ramp protocol, illustrating a ramp of the Raman couplings $\eta_{r,b}$ to the value associated with the maximum available laser power. **(b)** Photon number spectrogram displaying multiple cavity pulses, and **(c)** schematic representation of the inferred tunneling (1-7) in the momentum lattice. The horizontal lines in (b) indicate the pulse frequencies expected from total energy conservation, see Eq. (5.14), and allow us to locally resolve multiple tunneling events in a single experimental realization. We operate at $\omega_0 = 2\pi \times 142(3)\,\mathrm{kHz}$ and $\tilde{\Delta}_{\mathrm{c}} = -2\pi \times 1.2(2)\,\mathrm{MHz}$.

duration of our experiments.

5.3 Characterization of collective tunneling

In this section, we further characterize the dynamical nature of cavity-assisted tunneling in our system. In section 5.3.1, we experimentally demonstrate that the observed cavity pulses arise from superradiant Raman scattering and are collectively enhanced by the number of participating atoms. Moreover, in section 5.3.2, we leverage on this collective behavior to further elucidate the dynamical character of tunneling in our system.

5.3.1 Collective hopping via superradiant Raman scattering

We systematically characterize the first tunneling event $|0,0\rangle_0 \to |\pm1,\pm1\rangle_1$, which gives rise to occupation of a symmetric superposition of nearest-neighboring sites $|\pm1,\pm1\rangle_1 = 1/2\sum_{l,m=\pm1}|l,m\rangle_1$, see Eq. (5.16). We prepare a variable number of atoms N in the central lattice site $|0,0\rangle_0$, and slowly increase the coupling to $\eta_{r,b} = 2\pi \times 0.40(1)$ kHz within $t_{\mathrm{ramp}} = 14\,\mathrm{ms}$. In this regime we always observe a single cavity pulse, effectively isolating the first tunneling event.

In Fig. 5.6(a), we plot the corresponding coupling ramp together with representative traces of the cavity photon number $n_{\mathrm{ph}}(t)$ for different initial atom numbers N. When increasing N, we observe stronger photon pulses occurring earlier in time. Following theoretical analysis of superradiant Raman scattering in section 2.2.2, we rely on Eq. (2.26) and fit the observed photon pulses with a hyperbolic function

$$n_{\mathrm{ph}}(t) = \max(n_{\mathrm{ph}}) \cdot \operatorname{sech}^2\left(\frac{t-t_{\max}}{\tau}\right), \tag{5.19}$$

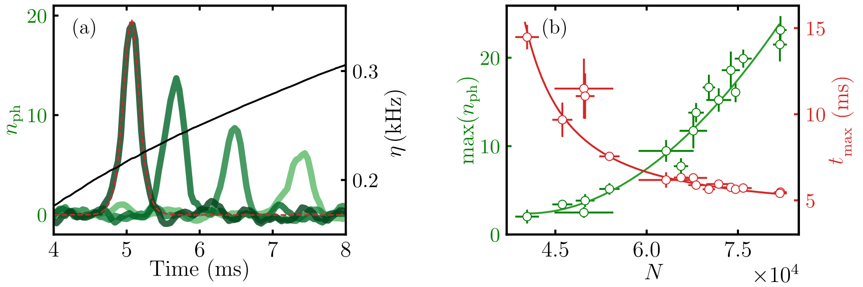

Figure 5.6: Collective hopping via superradiant Raman scattering. **(a)** Representative cavity pulses for different initial atom numbers $N = (8.1, 6.6, 4.9, 2.9) \times 10^4$ (darker to lighter green curves), together with a typical fit (dashed red) and coupling ramp $\eta := \eta_r = \eta_b$ (solid black line). **(b)** Photon pulse amplitude $\max(n_{\mathrm{ph}})$ and time delay $t_{\max}$ versus N, with a power-law fits (solid curves) yielding exponents of $p = 1.8(3)$ and $p = -1.3(3)$, respectively. The super-linear scaling of $\max(n_{\mathrm{ph}})$ with the number of atoms indicates that the system undergoes superradiant Raman scattering, and that the associated tunneling events are collectively enhanced. Here, we operate at $\omega_0 = 2\pi \times 26(1)\,\mathrm{kHz}$ and $\tilde{\Delta}_{\mathrm{c}} = -2\pi \times 1.4(2)\,\mathrm{MHz}$. In this chapter, the error bars correspond always to the standard error of the mean.

with $\max(n_{\mathrm{ph}})$, $t_{\max}$ and τ being free fit parameters. An exemplary fit (red dashed curve) is presented in Fig. 5.6(a) and accurately captures the functional form of the observed photon pulse.

In Fig. 5.6(b), we present the fitted values for the peak photon number $\max(n_{\mathrm{ph}})$ and the corresponding time delay $t_{\max}$ for different initial atom numbers N. The former exhibits a clear super-linear growth, whereas the latter monotonically decreases with increasing N. We fit the experimental data with power-law functions of the form $y(N) = a(N - N_{\mathrm{th}})^p + b$. Here, $N_{\mathrm{th}} \approx 30000$ represents an experimentally determined threshold atom number above which we observe superradiant Raman scattering in our system, see Fig. 5.7(a). Our experimental observations of $\max(n_{\mathrm{ph}})$ and $t_{\max}$ are well captured by power-law functions with $p = 1.8(3)$ [green curve] and $p = -1.3(3)$ [red curve in Fig. 5.6(b)], respectively. These fit results are compatible within errors with the expected scaling $\max(n_{\mathrm{ph}}) \propto N^2$ and $t_{\max} \propto N^{-1}$ of superradiant Raman scattering, see Eq. (2.26).

Indeed, these observations demonstrate that cavity-assisted tunneling in our system is induced by superradiant Raman scattering, which is collectively enhanced by the number of participating atoms N. In contrast, a collection of N independent emitters undergoing spontaneous scattering would yield a different scaling behavior with $\max(n_{\mathrm{ph}}) \propto N$ and $t_{\max} \propto 1$, as discussed in detail in section 2.2.2.

5.3.2 The properties of dynamical tunneling in our system

We further characterize the key properties of the tunneling events induced by superradiant Raman scattering in our system. In Fig. 5.7(a), we plot the measured fraction of transferred atoms to the sites $|\pm1, \pm1\rangle_1$ as a function of the initial atom number N. We observe that tunneling can occur only above an initial atom number of approximately $N_{\mathrm{th}} \approx 30000$, and the transfer fractions saturates at $N_1/N \approx 0.8$.

This limited transfer clearly goes beyond the fundamental description of the Tavis-Cummings model, as both mean-field (see Fig. 2.3) and exact numerical simulations (Fig. 2.4) predict a complete population transfer, i.e., $N_1/N = 1$.

We attribute the observed behavior to the combined influence of residual spin dephasing and interaction-induced self-trapping in the momentum lattice. Spin dephasing arises from spatio-temporal fluctuations of the bias magnetic field B, which leads to dynamical variations in the offset between the two spin manifolds ω_0. At the same time, repulsive contact interactions in real space result in effective attractive interactions in the momentum-space picture; this induces self-trapping of atoms at the initial lattice site $|0,0\rangle_0$ [243, 244] when the tunneling rates are below the effective attractive interaction strength $\tilde{u} \approx 2\pi \times 0.2\,\mathrm{kHz}$ (see appendix A.2 for a detailed discussion). To capture these effects, we phenomenologically introduce dephasing term with rate Γ_ϕ in our numerical simulations (Eqs. A.2). We find reasonable agreement with our experimental observations when considering dephasing rates around $\Gamma_\phi = 2\pi \times 0.25\,\mathrm{kHz} \approx \tilde{u}$ [black curve in Fig. 5.7(a)], whereas an idealized simulation with $\Gamma_\phi = 0$ (blue curve) fails to reproduce our data.

Furthermore, we extract the photon pulse area $\langle N_{\mathrm{ph}}\rangle = 2\kappa \int n_{\mathrm{ph}}(t)dt$ to account for the total number of photons leaking from the cavity during the tunneling event $|0,0\rangle_0 \to |\pm1,\pm1\rangle_1$. In Fig. 5.7(b), we observe a one-to-one correspondence between $\langle N_{\mathrm{ph}}\rangle$ and the number of transferred atoms N_1, which we quantify by a linear fit yielding a slope of 1.09(2) (solid line). This one-to-one correspondence is a direct consequence of total angular momentum conservation in the system: a tunneling process transferring N_1 atoms from $|0,0\rangle_0$ (Zeeman sublevel $m = -1$) to $|\pm1,\pm1\rangle_1$ ($m = 0$) changes the atomic angular momentum by $+\hbar N_1$, which is only compensated by scattering N_1 σ_+-polarized drive photons into the π-polarized cavity field, see also Fig. 5.2(b).

These observations further confirm the utility of the leaking cavity field as a reliable observable for investigating the tunneling dynamics in the momentum lattice.

Coherence-dependent tunneling

Finally, we leverage our observations to gain insight into the properties of the tunneling rate in our system. We use the fitted maximal photon numbers $\max(n_{\mathrm{ph}})$ in Fig. 5.6(b) to estimate the peak tunneling amplitude $|t_{\mathrm{SR,max}}| = \eta\sqrt{\max(n_{\mathrm{ph}})/8}$ using Eq. (5.12). In Fig. 5.7(c), we plot $|t_{\mathrm{SR,max}}|$ as a function of the initial number of atoms N. We observe that the peak tunneling rates linearly increase with N, reaching values around $|t_{\mathrm{SR,max}}| \lesssim 2\pi \times 0.4\,\mathrm{Hz}$. This behavior further emphasizes the collective nature of cavity-assisted tunneling in our system, which is inherently connected to the collective enhancement of superradiant Raman scattering. Importantly, the inferred values of $|t_{\mathrm{SR,max}}|$ consistently exceed the phenomenological spin dephasing rates $\Gamma_\phi = 2\pi \times 0.15\,\mathrm{kHz}$, enabling tunneling in the momentum lattice even in the presence of technical imperfections.

Tunneling in our system is dynamical in nature, as it evolves self-consistently with the emerging cavity field and is collectively enhanced by the number of participating atoms. When considering only two modes and adiabatically eliminating the cavity

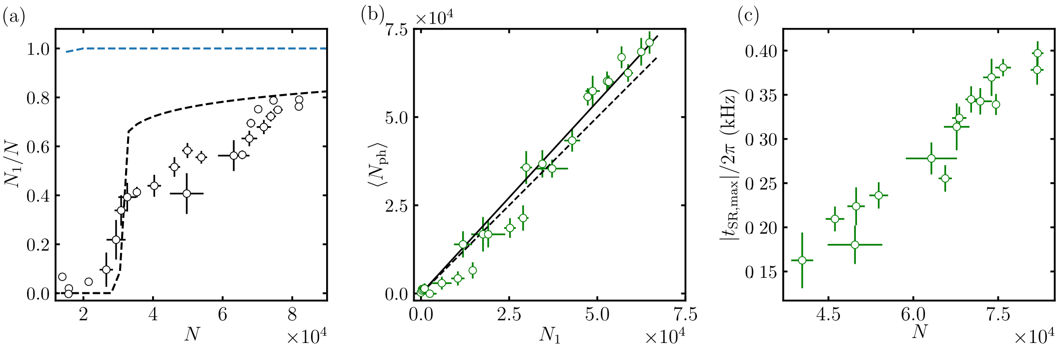

Figure 5.7: Probing the nature of dynamical tunneling. **(a)** Tunneling efficiency N_1/N as a function of atom number N, showcasing a threshold of $N_{\mathrm{th}} \approx 3 \times 10^4$ and a maximal efficiency around $N_1/N \approx 0.8$. Our results are captured by mean-field simulations with an effective spin dephasing rate of $\Gamma_\phi = 2\pi \times 0.25\,\mathrm{kHz}$ (gray), whereas dephasing-free simulation with $\Gamma_\phi = 0$ (blue line) predicts always optimal tunneling efficiencies with $N_1/N \approx 1$. **(b)** One-to-one relation between the number of atoms N_1 in $|\pm1, \pm1\rangle_1$ and the photon pulse area $\langle N_{\mathrm{ph}} \rangle$, arising from total angular momentum conservation. A linear fit yields a slope of 1.09(2) (solid), compatible to the theoretical expectation of 1 (dashed line). **(c)** Inferred peak tunneling amplitude $|t_{\mathrm{SR,max}}|$ as a function of N, highlighting the collective nature of tunneling in our system.

field ($\frac{d}{dt}\hat{a} = 0$), we obtain

$$|t_{\mathrm{SR}}(t)| = \frac{\eta |\langle \hat{a}(t) \rangle|}{\sqrt{8}} \approx \frac{\eta^2}{4\sqrt{\tilde{\Delta}_{\mathrm{c}}^2 + \kappa^2}} \left| \left\langle \hat{\psi}_1^\dagger \hat{\psi}_0(t) \right\rangle \right|, \tag{5.20}$$

with the bosonic operator $\hat{\psi}_0$ ($\hat{\psi}_1^\dagger$) annihilating (creating) particles in the initial (final) lattice site $|0,0\rangle_0$ ($|\pm1,\pm1\rangle_1$), see Eq. (5.16). The tunneling rate in the momentum lattice evolves together with the coherences between neighboring lattice sites $\langle \hat{\psi}_1^\dagger \hat{\psi}_0(t) \rangle$, which in turn dynamically change during a superradiant Raman scattering. Hence, dynamical tunneling in our system is qualitatively different from conventional density-dependent hopping in Hubbard systems [242], where the effective tunneling rates depend on local occupations such as $\langle \hat{\psi}_0^\dagger \hat{\psi}_0(t) \rangle$.

5.4 Observing hopping cascades in a momentum lattice

The observations discussed in the previous sections showcase independent tunneling events occurring sequentially in time. In this section, we discuss an extension of our experimental scheme to a regime featuring current cascades in the momentum lattice, where the tunneling events between different sites mutually stimulate each other. To experimentally access this regime, we reduce the offset energy ω_0 between the two spin manifolds $|0\rangle$ and $|1\rangle$ to values comparable to the recoil frequency ω_{rec}, as illustrated in the coupling scheme in Fig. 5.8(a). Thereby, we shift multiple states in the momentum lattice close to degeneracy. We prepare

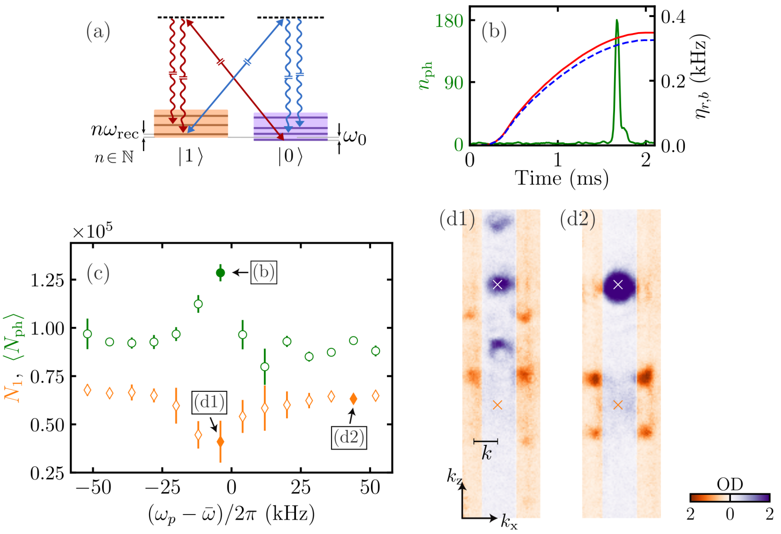

Figure 5.8: Cavity-assisted hopping cascade. **(a)** Coupling scheme. The splitting between the two spin manifolds ω_0 is reduced below the recoil energy ω_{rec}, shifting several lattice sites close to degeneracy. **(b)** Representative cavity photon pulse (green). The couplings $\eta_{r,b}$ (red, blue curves) are increased with a small technical imbalance $(\eta_r - \eta_b)/(\eta_r + \eta_b) = 0.034(3)$. **(c)** Photon excess measurement. Photon pulse area $\langle N_{\mathrm{ph}}\rangle$ (circles) and final number of atoms N_1 in $|\pm1,\pm1\rangle_1$ (diamonds) as functions of the peak emission frequency ω_p. Close to the two-photon resonance $\omega_p = \bar{\omega}$, we observe a large excess of photons $\langle N_{\mathrm{ph}}\rangle \gg N_1$, which is due to a single cavity pulse stimulating multiple tunneling events in the momentum lattice. **(d)** Representative time-of-flight images, with the white and orange crosses denoting the position of the sites $|0,0\rangle_0$ and $|0,0\rangle_1$, which are separated by a Stern-Gerlach gradient along z. The purple (orange) color map indicates regions solely occupied by atoms in $|0\rangle$ ($|1\rangle$). The square labels in (c) indicate the data points corresponding to panels (b), (d1) and (d2). Here, we operate at $\Delta_c = -2\pi \times 3.4(2)$ MHz and $N = 9.1(1) \times 10^4$ atoms.

$N = 9.1(1) \times 10^4$ atoms in the central lattice site $|0,0\rangle_0$, and increase the Raman couplings to $\eta_{r,b} \approx 2\pi \times 0.34\,\mathrm{kHz}$ within $t_{\mathrm{ramp}} = 2.1\,\mathrm{ms}$.

In Fig. 5.8(b), we plot a representative cavity pulse $n_{\mathrm{ph}}(t)$. The photon pulse reaches large peak values $\max(n_{\mathrm{ph}}) \approx 180$ and displays an asymmetric shape, clearly deviating from the hyperbolic secant expected for conventional two-level superradiant scattering, cf. Eq. (2.26). We numerically integrate the photon traces to obtain the total number of emitted cavity photons $\langle N_{\mathrm{ph}}\rangle$ and extract the peak frequency of emission ω_{p} from the corresponding spectrograms $\tilde{n}_{\mathrm{ph}}(t,\omega)$ for different realizations. In Fig. 5.8(c), we observe a clear excess of detected photons $\langle N_{\mathrm{ph}}\rangle$ in comparison to the number of atoms N_1 occupying the mode $|\pm1,\pm1\rangle_1$, in direct contrast to the results discussed in Fig. 5.7(b). This effect is amplified as the emission frequency ω_{p} approaches the two-photon resonance $\omega_{\mathrm{p}} - \bar{\omega} \to 0$. Concurrently, we observe finite populations in lattice sites with up to $10\hbar\omega_{\mathrm{rec}}$ kinetic energy (e.g., $|1,3\rangle_1$) in the corresponding time-of-flight images [see Fig. 5.8(d1)]. For comparison, away from the two-photon resonance the time-of-flight images solely indicate occupation of the sites $|0,0\rangle_0$ and $|\pm1,\pm1\rangle_1$ [Fig. 5.8(d2)]. The small distance between the cavity

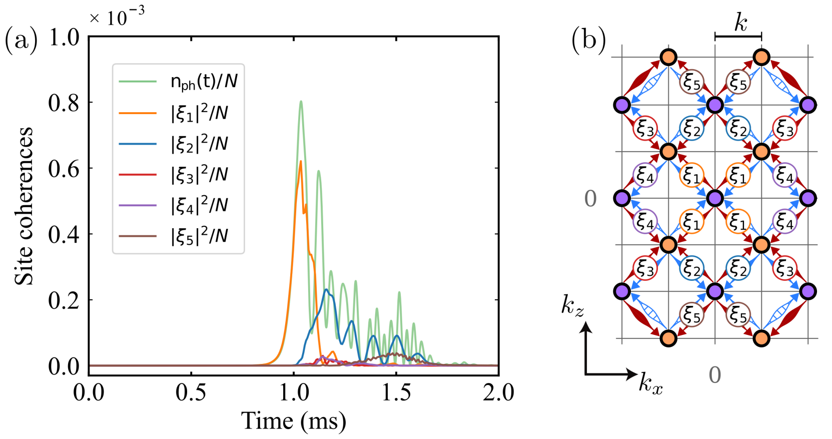

Figure 5.9: Gross-Pitaevskii equation simulations of hopping cascade. **(a)** Numerical results showing the cavity photon number $n_{\mathrm{ph}}(t)$ and the coherences between neighboring lattice sites $|\xi_j|^2$ for the experimental parameters of Fig. 5.8. These simulations help us to discern a cascade of tunneling events, where the next hopping event is stimulated by the previous one is concluded, and coherences between multiple sites are simultaneously established. **(b)** Schematic representation of the relevant two-site coherences ξ_j in the momentum lattice, as defined in Eq. (A.11). For details on these calculations, see Ref. [245]

mirrors $L \approx 175\ \mu$m limits the field of view along x-direction to lattice sites with $k_x \lesssim k_{\mathrm{rec}}$.

To better interpret the observe dynamics, we perform ab initio simulations of the underlying Gross-Pitaevskii equations, as discussed in the appendix A.3. The corresponding simulation results are presented in Fig. 5.9(a). We also observe a strong asymmetric cavity pulse (green curve) accompanied by the buildup of coherences between multiple neighboring lattice sites ζ_j. These coherences are defined in Eq. (A.11) of the appendix A.3, and schematically illustrated in Fig. 5.9(b). Within the duration of the cavity pulse, finite coherences between multiple lattice sites are simultaneously established, in contrast to the subsequent tunneling events at larger offsets ω_0. We attribute this to the tunneling rate $\max(t_{\mathrm{SR}}) \approx 2\pi \times 1.5\,\mathrm{kHz}$ starting to become comparable with the splitting between adjacent sites in the momentum lattice.

Together with the supporting Gross-Pitaevskii simulations, cf. appendix A.3, our experimental observations in this regime demonstrate a cascade of tunneling events in an extended momentum-space lattice, where the subsequent hopping event starts before the previous one is fully concluded.

5.5 Discussion and outlook

We experimentally demonstrated a new scheme for engineering dynamical tunneling in a momentum-space lattice, which is based on recoil-resolved superradiant Raman scattering of a spinor BEC coupled to an optical cavity. Due to inherent cavity losses, the resulting lattice dynamics are non-Hermitian and directional. By exploiting energy conservation in the total light-matter system, we locally resolved the tunneling events in real time through frequency-selective measurements of the leaking cavity field. Specifically, the tunneling rates evolve in conjunction with the coherences between the participating lattice sites. Furthermore, we experimentally demonstrated the superradiant nature of the associated cavity field. We extended our observations to a regime featuring mutually stimulating tunneling cascades.

As an extension, combining real-time probing and continuous feedback [246] on the relative phase of the two Raman drives could facilitate the realization of non-trivial tunneling phases in different plaquettes of the momentum grid [247]. This, in turn, could pave the way for the observation of synthetic magnetic fields and topologically protected states in a non-Hermitian system [35, 248, 249]. Additionally, an extension to running-wave Raman drives can result in emergent spin-orbit coupling in a driven-dissipative setting [208, 250, 251]. Finally, exploring the interplay between cavity-assisted tunneling and Bose-Hubbard physics [65] holds the potential to realize unconventional strongly-correlated phases and dynamics [252], such as topological insulators [253] or density-dependent gauge fields [254].

6 Spin- and momentum-correlated atom pairs mediated by photon exchange

Understanding and controlling the mechanisms behind the generation of correlated particle pairs is essential for advancing fundamental physics and quantum-enhanced technologies. Vacuum fluctuations are at the origin of elementary particle-antiparticle pairs and Hawking radiation in cosmology [255, 256], while quasiparticle pairing in condensed-matter systems drives strongly-correlated phenomena such as superconductivity [7] and superfluidity [257]. In the context of quantum technologies, entangled pairs of photons produced via parametric down-conversion in nonlinear crystals have enabled quantum-enhanced sensing and metrology [24, 258]. A prominent example is the recent upgrade of the Laser Interferometer Gravitational-Wave Observatory (LIGO), where the injection of squeezed states of light [259] has helped to double the detection sensitivity across the bandwidths relevant for gravitational-wave events [260].

In recent years, approaches resembling nonlinear optical systems have been explored with ultracold atomic gases to correlate massive particles either in their external or internal degrees of freedom. Atom pairs in multiple momentum modes have been generated in colliding Bose-Einstein condensates (BECs) [261–270] and Floquet-engineered systems via parametric amplification [225, 271]. Notably, correlated atom pairs in well-defined internal and external modes can be generated by spin-changing collisions in a spin-1 BEC [34], with three available internal levels $m = \{-1, 0, 1\}$. As illustrated in Fig. 6.1(a), a pair of atoms in the central $m = 0$ spin level can interact via local collisions, and populate the levels $m = -1$ and $m = +1$, conserving both the total center of mass and angular momentum. Since their first experimental observation [272], collisional spin-mixing dynamics has been successfully employed to demonstrate spin squeezing [273–275], probe entanglement between spatially separated condensates [276–278] and implement quantum-enhanced atomic interferometry [279, 280]. Yet, spin-changing collisions are associated with small effective scattering lengths on the order of few Bohr radii, restricting the dynamics to characteristic timescales around ~ 100 ms $-$ 1 s [34]. In particular, atom interferometry for applications in precision magnetometry and gravitometry could benefit from a faster and more controlled production of correlated pairs in well-defined spin and momentum modes [281, 282].

Experiments with cold atoms coupled to optical cavities are versatile platforms to induce strong and tunable light-matter interactions [57, 76], which can be exploited to synthesize correlated atom pairs. This has been demonstrated in pioneering experiments with circular Rydberg atoms exchanging photons in a microwave cavity [283]. More recently, these techniques have been extended to generate pairs and control correlations within the effective spin modes of thermal atomic ensembles [80, 81, 84].

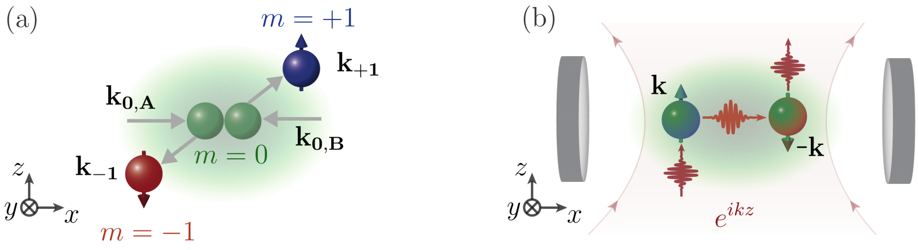

Figure 6.1: Collisional and photon-mediated spin-mixing dynamics. **(a)** Spin-changing collisions. Pairs of spin-1 atoms in the intermediate spin level $m = 0$ (green) interact via local s-wave collisions and form correlated pairs of in $m = +1$ (blue) and $m = -1$ (red circles), with momenta $\mathbf{k_{+1}}$ and $\mathbf{k_{-1}}$. This process conserves both total angular and center of mass momentum ($\mathbf{k}_{0,\mathrm{A}} + \mathbf{k}_{0,\mathrm{B}} = \mathbf{k_{+1}} + \mathbf{k_{-1}}$), with $\mathbf{k}_{0,\mathrm{A}}$ and $\mathbf{k}_{0,\mathrm{B}}$ being the initial momenta. **(b)** Cavity-assisted spin-mixing dynamics. A zero-momentum atom in $m = 0$ can scatter a photon from a running-wave drive into the empty cavity mode, and flip its spin to $m = 1$ while obtaining effective recoil momentum along the drive direction ($\mathbf{k}$). This virtual cavity photon is rescattered by a second $m = 0$ atom into the drive, which in turn changes its spin to $m = -1$ and obtains net recoil momentum $-\mathbf{k}$. This mechanism gives rise to nonlocal spin- and momentum-correlated atom pairs, also conserving both total angular and center of mass momentum ($\mathbf{k}_{\mathrm{tot}} = \mathbf{0} = \mathbf{k} - \mathbf{k}$).

In this chapter, we present the first experimental realization of correlated atom pairs in well-defined spin and momentum modes created via coherent light-matter interactions in an optical cavity. The pairs are experimentally generated within tens of microseconds using a spinor Bose-Einstein condensate and exploiting the coherent exchange of cavity photons. The fast timescales allow us to extricate the pair dynamics from typical dissipative mechanisms in atomic systems, such as heating, three-body losses, and trapping effects [95, 192].

We illustrate the central ideas behind the experiments in Fig. 6.1(b): We consider a spin-1 BEC prepared in a well-defined zero-momentum mode in the $m = 0$ Zeeman sublevel, which is illuminated by a running-wave drive transverse to the cavity. Far detuned from the cavity resonance, an atom in $m = 0$ scatters a photon from the drive into the cavity and flips its spin to $m = +1$ while obtaining net photon recoil momentum ($\mathbf{k}$) along the drive direction. Due to the large associated energy cost, this photon only virtually occupies the cavity and is re-scattered by a second $m = 0$ atom into the drive, which in turn flips its spin to $m = -1$ and obtains net recoil opposite to the drive direction ($-\mathbf{k}$). In our experiment, we directly observe such spin-and momentum-correlated pairs in $m = \pm 1$, and $\pm\mathbf{k}$ or $\mp\mathbf{k}$. Leveraging on the optical control over coherent and dissipative processes, we present the first observation of coherent pair oscillations involving well-defined momentum modes. We observe a collective enhancement in pair production, which is directly related to superradiant Raman scattering in our system. This phenomenon bears similarities to parametric amplification in nonlinear optics. Our observations are in quantitative agreement with Truncated Wigner simulations taking the vacuum fluctuations of the system into account. We examine the quantum statistics of the pairs and demonstrate their correlated nature by probing inter-spin correlations in momentum space. Our results provide prospects for rapid entanglement generation in quantum degenerate gases and for applications in atomic interferometry.

Outline of this chapter

In section 6.1, we introduce the theoretical framework to model pair production in our system. We derive the many-body Hamiltonian, discuss the second-order phase transition giving rise to pair production and present our truncated Wigner simulations to model the open-system dynamics. In section 6.2, we present the experimental protocols and the first observations of coherent pair oscillations involving well-defined momentum modes. In section 6.3, we investigate the collective enhancement of pair production and draw parallels to parametric amplification in nonlinear optics. In section 6.4, we demonstrate independent experimental control over the unitary pair dynamics and the leading dissipative channel associated with superradiant scattering. Furthermore, we investigate the quantum statistics of the emergent pairs and probe their momentum-space correlations in sections 6.5 and 6.6, respectively. Finally, in section 6.7, we summarize our findings and discuss possible routes for the observation of quantum correlations in our system.

Parts of this chapter have been published in Ref. [91]

> F. Finger*, R. Rosa-Medina*, N. Reiter, P. Christodoulou, T. Donner, and T. Esslinger. *Spin- and momentum-correlated atom pairs mediated by photon exchange.* arXiv 2303.11326 (2023)
> * These authors contributed equally to this work

6.1 Theoretical description

Here, we present the theoretical framework to describe the generation of spin- and momentum-correlated atom pairs in our system. In section 6.1.1, we discuss the experimental coupling scheme and the microscopic mechanism underlying pair production in our system. In section 6.1.2, we derive the associated many-body Hamiltonian after adiabatically eliminating the cavity field. Additionally, in section 6.1.3, we discuss the two competing second-order transitions leading to pair production via two discernible channels in our system. Finally, in section 6.1.4, we present our truncated Wigner simulations, which incorporate quantum fluctuations and model the open system dynamics beyond mean-field effects.

6.1.1 Coupling scheme

In the experiments discussed in this chapter, we initialize a ^{87}Rb BEC in the $m = 0$ Zeeman sublevel of the $F = 1$ hyperfine manifold, with a tunable offset magnetic field B along the z direction defining the quantization axis. The atoms are illuminated by a y-polarized running-wave drive propagating in the z direction and are dispersively coupled the z-polarized fundamental cavity mode, see illustration in Fig. 6.2(a). For our choice of quantization axis, the relevant cavity mode is π polarized while the drive field can be decomposed in a balanced superposition of σ_+ and σ_- photons.

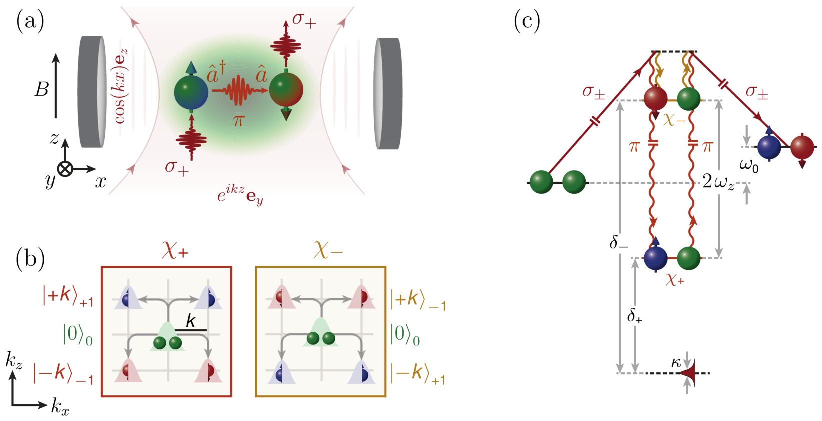

Figure 6.2: Experimental setup and coupling scheme. (a) Setup. A BEC is illuminated by a y-polarized running-wave drive with wavenumber k (propagating in z direction); the atoms are coupled to the z-polarized cavity mode, with the magnetic field B defining the quantization axis. An atom in the Zeeman sublevel $m = 0$ (green) flips its spin to $m = 1$ (blue) while scattering a σ_+ photon into the π-polarized cavity mode ($\hat{a}^\dagger$). This photon is rescattered by a second $m = 0$ atom into the drive ($\hat{a}$), changing its state to $m = -1$ (red circle). **(b)** Momentum-space picture. Pair are generated via two discernible channels $\chi_\pm$, depending on the first atom absorbing a $\sigma_\pm$ drive photon and changing its spin to $m = \pm 1$. The corresponding spin-momentum modes $|\tilde{k}\rangle_\mathrm{m}$ are defined in the main text. **(c)** Energy diagram. The pair-production mechanism comprises two coupled Raman scattering processes, each involving a drive (straight arrows) and a cavity (curly arrows) photon. The intermediate modes are split by twice the linear Zeeman shift ω_z and give rise to two discernible channels. The corresponding coupling rates $\chi_\pm$ depend on the Raman detunings $\delta_\pm$ and the cavity loss rate κ. The offset ω_0 is set by the kinetic and internal energy of the pairs.

We operate the drive at the tune-out wavelength of the $F = 1$ manifold, $\lambda_\mathrm{d} = \lambda_\mathrm{TO} \approx 790.019$ nm, in order to suppress spurious scalar light-matter interactions, see section 2.1.2 for details.

This coupling scheme can convert a pair of zero-momentum atoms in $m = 0$ into a correlated pair in $m = \pm 1$ with opposite recoil momenta $\pm\hbar k$ along z direction, with $k = 2\pi/\lambda_\mathrm{d}$ being the drive's wavenumber. The underlying mechanism is a *photon exchange* involving the drive and the vacuum mode of the cavity [80], as illustrated in Fig. 6.2(a): During this process, one atom in the mode $|k_z = 0\rangle_{m=0} \equiv |0\rangle_0$ scatters either a σ_+- or σ_--polarized photon from the drive into the π-polarized cavity mode and flips its spin to either $m = +1$ or $m = -1$. The atom obtains a recoil momentum $\hbar k$ along $+z$ occupying the modes $|{+k}\rangle_{+1}$ or $|{+k}\rangle_{-1}$, respectively. The emitted virtual cavity photon (π-polarized) is rescattered into the running-wave drive by a second atom in $|0\rangle_0$, which obtains recoil momentum along $-z$ and populates the complementary spin state $m = -1$ or $m = +1$, i.e., the modes $|{-k}\rangle_{-1}$ or $|{-k}\rangle_{+1}$. Due to the cavity mode structure [$\propto \cos(kx)$], the pairs additionally occupy a symmetric superposition with $\pm\hbar k$ recoil momentum along the cavity direction (x), cf. Fig. 6.2(a). In Fig. 6.2(b), we schematically depict the different atomic modes in momentum space.

Our coupling scheme gives rise to correlated atom pairs in well-defined external and internal modes through two distinct channels with coupling rates χ_+ and χ_-, depending on whether the first atom occupies the mode $|{+k}\rangle_{+1}$ or $|{+k}\rangle_{-1}$. Regardless of the coupling channel, the pair creation processes conserve both the total center of mass and angular momentum of the atoms, similar to collisional spin-mixing dynamics [34].

6.1.2 Derivation of the effective Hamiltonian

We derive the Hamiltonian of the system following the general framework for dispersive atom-light interactions discussed in section 2.1. The negative part of the total electric field is given by

$$\hat{\mathbf{E}}^{(-)} = \frac{E_d}{2} e^{ikz} e^{-i\omega_\mathrm{d} t} \mathbf{e}_y + E_0 \hat{a} \cos(kx) \mathbf{e}_z. \tag{6.1}$$

The operator $\hat{a}$ annihilates a z-polarized cavity photons in the fundamental mode of the cavity, with $E_0 = 402$ V/m being the corresponding vacuum electric field. We consider a classical y-polarized running-wave drive with mode structure $f(z) = e^{ikz}$, frequency ω_d and tunable electric field amplitude E_d, as illustrated in Fig. 6.2(a). Due to their small detuning, we assume a common wavenumber $k = 2\pi/\lambda_\mathrm{d}$ for the drive and the cavity fields.

Analogously to Eq. (2.15), we derive the single-particle Hamiltonian

$$\hat{H}_\mathrm{SP} = \hat{H}_\mathrm{at} + \hat{H}_\mathrm{cav} + \hat{H}_v, \tag{6.2}$$

in a rotating frame induced by the generator $\hat{H}_\mathrm{rot} = \hbar\omega_\mathrm{d}\hat{a}^\dagger\hat{a} - \hbar\omega_z\hat{F}_z$, with $\hat{F}_z$ being the z component of the spin-1 operator describing the $F = 1$ manifold, i.e., $\hat{\mathbf{F}} = (\hat{F}_x, \hat{F}_y, \hat{F}_z)^T$. In this rotating frame, the stationary cavity field oscillates at ω_d, while the atomic spin rotates with linear Zeeman splitting ω_z. The energy of a single atom

$$\hat{H}_\mathrm{at} = \frac{\hat{p}^2}{2M} + \hbar q \hat{F}_z^2, \tag{6.3}$$

is determined by its kinetic energy and the quadratic Zeeman splitting $q = 2\pi B^2 \times 72\,\mathrm{Hz/G^2}$. The bare energy of the cavity photons

$$\hat{H}_\mathrm{cav} = -\hbar\delta_c\hat{a}^\dagger\hat{a}, \tag{6.4}$$

is given by their detuning $\delta_c = \omega_\mathrm{d} - \omega_c$ with respect to the cavity resonance ω_c.

In Eq. (6.2), we consider exclusively atom-light interactions $\hat{H}_v$ mediated by the vectorial polarizability α_v, as the trasnverse drive is operated at the tune-out wavelength λ_TO, where the scalar polarizability vanishes $\alpha_s = 0$ [110]. This yields

$$\begin{aligned} \hat{H}_v &= -i\frac{\alpha_v}{2F}\left(\hat{\mathbf{E}}^{(+)} \times \hat{\mathbf{E}}^{(-)}\right) \cdot \hat{\mathbf{F}} \\ &= \frac{\alpha_v E_0 E_\mathrm{d} \cos(kx)}{8}\left[\left(\hat{a}^\dagger e^{ikz} - \hat{a} e^{-ikz}\right)\left(\hat{F}_+ e^{i\omega_z t} + \hat{F}_- e^{-i\omega_z t}\right)\right]. \end{aligned} \tag{6.5}$$

Mode expansion and many-body Hamiltonian

We derive the many-body Hamiltonian using a six-mode expansion in momentum and spin space. The considered modes $|k_z\rangle_m$ are $|0\rangle_0$ with a spatially homogeneous single-particle wavefunction $\psi \propto 1$ in the Zeeman sublevel $m = 0$, the four modes $|\pm k\rangle_{m=\pm 1}$ occupied by pairs with $\psi \propto \cos(kx) e^{\pm ikz}$, cf. Fig. 6.2(b), and an additional higher-order momentum mode $|\pm 2k_x\rangle_0$ in $m = 0$ with $\psi \propto \cos^2(kx)$. The latter can participate in the dynamics due to the interaction between pairs in $m = \pm 1$, as observed in section 6.2. The corresponding spinor field operator is given by

$$\begin{aligned} \hat{\Psi}(\mathbf{x}) &= \left(\hat{\Psi}_{+1}(\mathbf{x}),\, \hat{\Psi}_0(\mathbf{x}),\, \hat{\Psi}_{-1}(\mathbf{x})\right)^T \\ &= \begin{pmatrix} \frac{k}{\sqrt{2}\pi} \cos(kx)(e^{ikz}\hat{c}_{+k,+1} + e^{-ikz}\hat{c}_{-k,+1}) \\ \frac{k}{2\pi}\hat{c}_{0,0} + \frac{\sqrt{2}k}{\sqrt{3}\pi}\cos^2(kx)\hat{c}_{\pm 2k_x,0} \\ \frac{k}{\sqrt{2}\pi} \cos(kx)(e^{-ikz}\hat{c}_{-k,-1} + e^{ikz}\hat{c}_{+k,-1}) \end{pmatrix}, \end{aligned} \tag{6.6}$$

with the bosonic operators $\hat{c}_{k_z,m}$ annihilating atoms in the modes $|k_z\rangle_m$. The corresponding single-particle wave functions are normalized in a unit cell of size $\mathcal{R} = [-\pi/k, \pi/k)^2$. Within this mode expansion, we can derive the many-body Hamiltonian in second quantization

$$\begin{aligned} \hat{H}_{\mathrm{mb}} &= \hat{H}_{\mathrm{cav}} + \int_{\mathcal{R}} \hat{\Psi}^\dagger(\mathbf{x}) \left[\hat{H}_{\mathrm{at}} + \hat{H}_v\right] \hat{\Psi}(\mathbf{x}) d\mathbf{x} \\ &= -\hbar\delta_c \hat{a}^\dagger \hat{a} + \frac{\hbar\omega_0}{2} \sum_{\tilde{m}=\pm 1} \left(\hat{c}^\dagger_{+k,\tilde{m}}\hat{c}_{+k,\tilde{m}} + \hat{c}^\dagger_{-k,-\tilde{m}}\hat{c}_{-k,-\tilde{m}}\right) + 4\hbar\omega_{\mathrm{rec}}\hat{c}^\dagger_{\pm 2k_x,0}\hat{c}_{\pm 2k_x,0} \\ &+ \hbar\eta \left[\hat{a}^\dagger e^{i\omega_z t}\left(\hat{c}^\dagger_{+k,+1}\hat{c}_0 + \hat{c}^\dagger_0 \hat{c}_{-k,-1}\right) + \hat{a}^\dagger e^{-i\omega_z t}\left(\hat{c}^\dagger_0 \hat{c}_{-k,+1} + \hat{c}^\dagger_{+k,-1}\hat{c}_0\right) + \text{h.c.}\right], \end{aligned} \tag{6.7}$$

where we use the shorthand notation $\hat{c}_0 = \left(\hat{c}_{0,0} + \sqrt{2/3}\hat{c}_{\pm 2k_x,0}\right)$ and apply a global phase rotation $\hat{a} \to \hat{a}e^{i\pi/2}$. The Raman coupling rate is given by $\eta = \beta\alpha_v E_0 E_{\mathrm{d}}/8\hbar$, with $\beta \approx 0.91$ arising from the overlap integrals between the harmonically confined atomic cloud and the different electric fields, see section 4.1.2. The bare energy of atoms in the modes $|\pm k\rangle_{\pm 1}$ is determined by the second order Zeeman splitting and the kinetic energy, $\hbar\omega_0/2 = \hbar q + 2\hbar\omega_{\mathrm{rec}}$, with $\omega_{\mathrm{rec}} = \hbar k^2/(2M) = 2\pi \times 3.73\,\mathrm{kHz}$ being photon recoil frequency. Additionally, the energy offset $4\hbar\omega_{\mathrm{rec}}$ of the mode $|\pm 2k_x\rangle_0$ is directly associated to its $\lambda_{\mathrm{d}}/2$-periodic modulation along the cavity direction.

The Hamiltonian derived in Eq. (6.7) constitutes a two-channel Tavis-Cummings model, cf. Eq. (2.19) in section 6.1.3: as illustrated in the level scheme in Fig. 6.2(c), we identify two different channels giving rise to cavity-assisted Raman transitions between the modes $|0\rangle_0 \to |+k\rangle_{+1}$ and $|0\rangle_0 \to |+k\rangle_{-1}$. These processes are associated with the emission of an energy-conserving cavity photons $\hat{a}^\dagger e^{i\omega_z t}$ (orange) and $\hat{a}^\dagger e^{-i\omega_z t}$ (yellow wiggly arrows) with approximate frequencies $\omega_{\mathrm{d}} + \omega_z$ and $\omega_{\mathrm{d}} - \omega_z$, respectively. As discussed in section 2.2 of chapter 2, such cavity-assisted two-photon transitions can give rise to superradiant Raman scattering if the corresponding two-photon Raman detunings $\delta_+ = -\delta_c - \omega_z$ and $\delta_- = -\delta_c - \omega_z$ are small compared to the cavity linewidth κ.

In the experiments discussed in this chapter, we operate the drive in the opposite limit of large two-photon detunings, $|\delta_\pm| \gg \kappa$, where a steady-state occupation of the cavity mode is strongly suppressed. This motivates us to adiabatically eliminate the cavity field following the formalism for open quantum systems introduced in Ref. [122]. We obtain the effective Hamiltonian for the atomic degrees of freedom

$$\begin{aligned}
\hat{H} &= \hat{H}_0 + \hat{H}_+ + \hat{H}_-, \quad \text{with} \\
\hat{H}_0 &= \sum_{\tilde{m}=\pm 1} \frac{\hbar\omega_0}{2} \left(\hat{c}^\dagger_{+k,\tilde{m}} \hat{c}_{+k,\tilde{m}} + \hat{c}^\dagger_{-k,-\tilde{m}} \hat{c}_{-k,-\tilde{m}} \right) + 4\hbar\omega_{\mathrm{rec}} \hat{c}^\dagger_{\pm 2k_x,0} \hat{c}_{\pm 2k_x,0} \\
\hat{H}_+ &= \hbar\chi_+ \left(2\hat{c}^\dagger_{-k,-1} \hat{c}^\dagger_{+k,+1} \hat{c}_0 \hat{c}_0 + \hat{c}^\dagger_0 \hat{c}_{+k,+1} \hat{c}^\dagger_{+k,+1} \hat{c}_0 + \hat{c}^\dagger_{-k,-1} \hat{c}_0 \hat{c}^\dagger_0 \hat{c}_{-k,-1} + \text{h.c.} \right), \\
\hat{H}_- &= \hbar\chi_- \left(2\hat{c}^\dagger_{-k,+1} \hat{c}^\dagger_{+k,-1} \hat{c}_0 \hat{c}_0 + \hat{c}^\dagger_{-k,+1} \hat{c}_0 \hat{c}^\dagger_0 \hat{c}_{-k,+1} + \hat{c}^\dagger_0 \hat{c}_{+k,-1} \hat{c}^\dagger_{+k,-1} \hat{c}_0 + \text{h.c.} \right).
\end{aligned} \tag{6.8}$$

The various energy scales of the system are schematically depicted in Fig. 6.2(c). The first term, $\hat{H}_0$, describes the energy cost $\hbar\omega_0 = 2\hbar q + 4\hbar\omega_{\mathrm{rec}}$ for creating a single atom pair occupying the modes $|+k\rangle_{\pm 1}$ and $|-k\rangle_{\mp 1}$; for more details see Eq. (6.7). The effective interaction terms, $\hat{H}_\pm$, describe the two discernible pair-production channels with the corresponding intermediate states being separated by twice the linear Zeeman splitting ω_z, cf. Fig. 6.2(c). These two channels describe the formation of spin- and momentum-correlated atom pairs in the modes $|+k\rangle_{\pm 1}$ and $|-k\rangle_{\mp 1}$ ($\hat{c}^\dagger_{-k,\mp 1} \hat{c}^\dagger_{+k,\pm 1}$) out of two atoms in $|0\rangle_0$ ($\hat{c}_0 \hat{c}_0$), respectively. The corresponding coherent coupling rates are

$$\chi_\pm = \eta^2 \frac{\delta_\pm}{\delta_\pm^2 + \kappa^2}. \tag{6.9}$$

Remarkably, both the strength and the sign of $\chi_\pm$ can be independently controlled by adjusting the two-photon coupling η and the corresponding Raman detunings $\delta_\pm = -\delta_c \mp \omega_z = \omega_c - (\omega_{\mathrm{d}} \pm \omega_z)$. In the Hamiltonian in Eq. (6.8), we directly see that negative coupling rates $\chi_\pm < 0$ can energetically favor the formation of atom pairs in the corresponding modes, when becoming comparable with the pair energy cost ($\hbar\omega_0$). The remaining terms in $\hat{H}_\pm$ describe effective spin-exchange interactions between atoms in the adjacent Zeeman sublevels, i.e., $m = 0 \leftrightarrow m = 1$ and $m = 0 \leftrightarrow m = -1$. They are also mediated by the exchange of virtual cavity photons and conserve atomic population in the different modes when disregarding occupation of $|\pm 2k_x\rangle_0$.

6.1.3 Parametric amplification of pair production

In this section, we discuss the second-order phase transitions underlying the formation of pairs in our system. Negative coherent couplings $\chi_\pm < 0$ soften the bare pair energy and induce two concurring phase transitions to phases featuring macroscopic numbers of pairs in the corresponding channels. Following Refs. [80, 279], we linearize the many-body Hamiltonian in Eq. (6.8) assuming that the mode $|0\rangle_0$ remains *undepleted*[1] throughout the dynamics, i.e., occupied by N atoms. We set $\hat{c}_0 = \sqrt{N}$ and obtain

$$\begin{aligned}\hat{H}_{\text{eff}} =& \hat{H}^{+}_{\text{eff}} + \hat{H}^{-}_{\text{eff}},\\ \hat{H}^{\pm}_{\text{eff}} =& \hbar\left(\frac{\omega_0}{2} + 2N\chi_\pm\right)\left(\hat{c}^\dagger_{+k,\pm1}\hat{c}_{+k,\pm1} + \hat{c}^\dagger_{-k,\mp1}\hat{c}_{-k,\mp1}\right)\\ &+\hbar\chi_\pm 2N\left(\hat{c}^\dagger_{+k,\pm1}\hat{c}^\dagger_{-k,\mp1} + \hat{c}_{k,\pm1}\hat{c}_{-k,\mp1}\right)\\ =& \hbar(\omega_0 + 4N\chi_\pm)(\hat{K}_{z,\pm} - 1/2) + 4\hbar N\chi_\pm\hat{K}_{x,\pm}.\end{aligned} \tag{6.10}$$

Here, we introduce two sets of Hermitian operators

$$\begin{aligned}\hat{K}_{x,\pm} &= \frac{1}{2}\left(\hat{c}^\dagger_{+k,\pm1}\hat{c}^\dagger_{-k,\mp1} + \hat{c}_{+k,\pm1}\hat{c}_{-k,\mp1}\right),\\ \hat{K}_{y,\pm} &= \frac{1}{2i}\left(\hat{c}^\dagger_{+k,\pm1}\hat{c}^\dagger_{-k,\mp1} - \hat{c}_{+k,\pm1}\hat{c}_{-k,\mp1}\right),\\ \hat{K}_{z,\pm} &= \frac{1}{2}\left(1 + \hat{c}^\dagger_{+k,\pm1}\hat{c}_{+k,\pm1} + \hat{c}^\dagger_{-k,\mp1}\hat{c}_{-k,\mp1}\right),\end{aligned} \tag{6.11}$$

which define two independent SU(1,1) algebras $\{\hat{K}_{x,\pm}, \hat{K}_{y,\pm}, \hat{K}_{z,\pm}\}$ [284]. The operators $\hat{K}_{z,\pm}$ count excitations (pairs) on top of the undepleted $|0\rangle_0$ mode, whereas the raising $\hat{K}^{+}_{\pm} = (\hat{K}_{x,\pm} + i\hat{K}_{y,\pm})$ and lowering operators $\hat{K}^{-}_{\pm} = (\hat{K}_{x,\pm} - i\hat{K}_{y,\pm})$ create and annihilate them, respectively. Within the undepleted pump-mode approximation in Eq. (6.11), the two pair channels χ_+ and χ_- become fully decoupled from each other, as they are described by the Hamiltonians $\hat{H}^{+}_{\text{eff}}$ and $\hat{H}^{-}_{\text{eff}}$, respectively.

Analogously to the generalized Dicke model in section 4.1.4, the excitations can be examined via linear stability analysis of the corresponding Heisenberg equations of motion

$$\begin{aligned}\frac{d}{dt}\begin{pmatrix}\hat{K}_{x,\pm}\\ \hat{K}_{y,\pm}\\ \hat{K}_{z,\pm}\end{pmatrix} &= \frac{i}{\hbar}\begin{pmatrix}[\hat{H}^{\pm}_{\text{eff}}, \hat{K}_{x,\pm}]\\ [\hat{H}^{\pm}_{\text{eff}}, \hat{K}_{y,\pm}]\\ [\hat{H}^{\pm}_{\text{eff}}, \hat{K}_{z,\pm}]\end{pmatrix}\\ &= \mathbf{M}_\pm\begin{pmatrix}\hat{K}_{x,\pm}\\ \hat{K}_{y,\pm}\\ \hat{K}_{z,\pm}\end{pmatrix} = \begin{pmatrix}0 & -A_\pm & 0\\ A_\pm & 0 & B_\pm\\ 0 & B_\pm & 0\end{pmatrix}\begin{pmatrix}\hat{K}_{x,\pm}\\ \hat{K}_{y,\pm}\\ \hat{K}_{z,\pm}\end{pmatrix},\end{aligned} \tag{6.12}$$

with $A_\pm = \omega_0 + 4N\chi_\pm$ and $B_\pm = 4N\chi_\pm$.

We diagonalize the dynamical matrix $\mathbf{M}_\pm$ for each channel and obtain three non-degenerate complex eigenvalues

$$\begin{aligned}\lambda_{1,\pm} &= 0,\\ \lambda_{2,\pm} &= \sqrt{-\omega_0(\omega_0 + 8N\chi_\pm)} := +\lambda_\pm,\\ \lambda_{3,\pm} &= -\sqrt{-\omega_0(\omega_0 + 8N\chi_\pm)} := -\lambda_\pm,\end{aligned} \tag{6.13}$$

---

[1] This *undepleted pump-mode approximation* is widely used to model optical parametric amplifiers and is valid as long as the pump laser depletion is small in comparison to the occupation of the photon pairs [24].

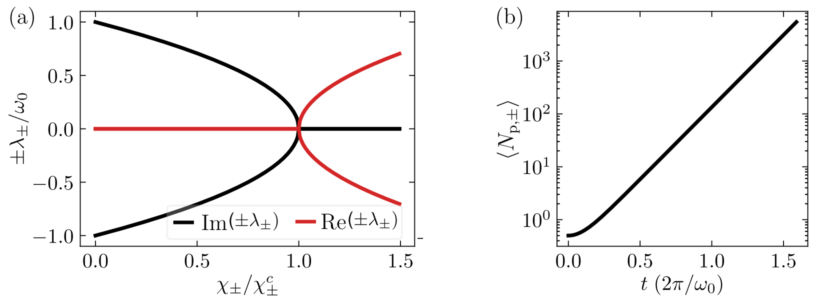

Figure 6.3: Second-order phase transitions and pair production within the undepleted pump-mode approximation. **(a)** Imaginary Im($\pm\lambda_\pm$) and real part Re($\pm\lambda_\pm$) of the system's eigenfrequencies $\pm\lambda_\pm$ as a function of the coupling strength for each of the two channels $\chi_\pm$. At small couplings, the imaginary part Im($\pm\lambda_\pm$) $\approx \pm\omega_0$ characterizes the bare energy of the pairs, which progressively softens and vanishes at the critical coupling $\chi^c_\pm$. Above this value, the eigenfrequencies obtain a positive real part Re($+\lambda_\pm$) > 0, indicating a dynamical instability and a second-order transition to a phase featuring pairs in the corresponding channel. **(b)** Expected evolution of the mean pair number $\langle N_{\mathrm{p},\pm}\rangle$ following an instantaneous coupling quench ($\chi_\pm = 2\chi^c_\pm$). The semi-log scale shows the exponential buildup of pairs within the undepleted pump-mode approximation, cf. Eq. (6.16).

which we plot in Fig. 6.3(a). In the limit of weak couplings $\chi_\pm \approx 0$, the eigenvalues $\pm\lambda_\pm \approx \pm i\omega_0$ are purely imaginary, and reflect the bare energy associated with creating and annihilating a single pair excitation in the system. For increasingly large negative couplings $\chi_\pm < 0$, the imaginary part of the eigenvalues Im($\pm\lambda_\pm$) progressively softens (black curves), reaching zero at

$$N\chi^c_\pm = -\frac{\omega_0}{8}, \tag{6.14}$$

which we identify as the *critical coupling* of the system. Above this value, the eigenvalue $+\lambda_\pm$ obtains a positive real part Re($+\lambda_\pm$) > 0 (red curves), which gives rise to a dynamical instability amplifying the formation of pairs in the corresponding modes. This behavior indicates the existence two second-order phase transitions at $\chi^c_\pm$ in the thermodynamic limit ($N \to \infty$). The collective enhancement of atom-light interactions is manifested in the scaling of the critical coupling $\chi^c_\pm \propto 1/N$ with the number of atoms N; this is similar to the scaling of the critical coupling associated with Dicke phase transition, cf. Eq. (4.16) in chapter 4.

We emphasize that the spin-exchange processes between the adjacent Zeeman sublevels $m = 0 \leftrightarrow 1$ and $m = 0 \leftrightarrow -1$ are essential for inducing the corresponding phase transitions, see Eq. (6.8). If absent, the dynamical matrix $M_\pm$ would have the entry $A_\pm = \omega_0$ and mode softening would be suppressed in the eigenvalues in Eq. (6.13). Note that this mechanism bears close similarities to the softening of low-momentum modes in extended $m = 0$ Bose-Einstein condensates arising from collisional spin-exchange interactions; they can be examined using Bogoliubov theory [285] and lead to spatially modulated magnons occupying the $m = \pm 1$ sublevels [286].

To gain further insights into the system's dynamics, we calculate the matrix of eigenvectors $\mathbf{\Lambda}_\pm$ of $\mathbf{M}_\pm$ and compute the time evolution of the relevant SU(1,1) operators

$$\begin{pmatrix} \hat{K}_{x,\pm}(t) \\ \hat{K}_{y,\pm}(t) \\ \hat{K}_{z,\pm}(t) \end{pmatrix} = \Lambda_\pm \begin{pmatrix} e^{\lambda_{0,\pm} t} & 0 & 0 \\ 0 & e^{-\lambda_\pm t} & 0 \\ 0 & 0 & e^{\lambda_\pm t} \end{pmatrix} \Lambda_\pm^{-1} \begin{pmatrix} \hat{K}_{x,\pm}(0) \\ \hat{K}_{y,\pm}(0) \\ \hat{K}_{z,\pm}(0) \end{pmatrix}. \tag{6.15}$$

As all the atoms are prepared in the $m = 0$ Zeeman sublevel, we assume that the pair modes are initially empty and set $\langle \hat{K}_{z,\pm}(0) \rangle = 1/2$, $\langle \hat{K}_{x,\pm}(0) \rangle = \langle \hat{K}_{y,\pm}(0) \rangle = 0$. Additionally, the initial pair occupation is set to $\langle \hat{K}_{z,\pm}(0) \rangle = 1/2$ to reproduce the 'quantum one-half' noise associated with the vacuum fluctuations, see section 6.1.4. We estimate the evolution of the average number of pairs in the $\chi_\pm$ channel as

$$\langle N_{\mathrm{p},\pm}(t) \rangle = \left\langle \hat{K}_{z,\pm}(t) \right\rangle = \frac{(\chi_\pm/\chi_\pm^{\mathrm{c}})^2}{16(\chi_\pm/\chi_\pm^{\mathrm{c}} - 1)} \left[e^{\mathrm{Re}(\lambda_\pm)t} + e^{-\mathrm{Re}(\lambda_\pm)t} - 1 \right] + \frac{1}{2}, \tag{6.16}$$

Upon quenching the system above the critical coupling, $\chi_\pm/\chi_\pm^{\mathrm{c}} > 1$, we anticipate an exponential increase in the number of pairs, proportional to $e^{\mathrm{Re}(\lambda_\pm)t}$, provided that the undepleted pump-mode approximation remains valid, i.e., $\langle N_{\mathrm{p},\pm}(t) \rangle \ll N$. In Fig. 6.3(b), we show an exemplary time evolution of $\langle N_{\mathrm{p},\pm}(t) \rangle$ in this regime for $\chi_\pm/\chi_\pm^{\mathrm{c}} = 2$, highlighting their exponential growth within characteristic timescales of $1/\lambda_\pm$. Given its similarity to parametric processes in nonlinear optical media [24], we refer to pair production in this regime as *parametric amplification*.

Bose-Einstein statistics and two-mode squeezed vacuum states

Within the undepleted pump-mode approximation, the generation of atom pairs via the two discernible channels χ_+ and χ_- is described by the sum of two independent Hamiltonians $\hat{H}_{\mathrm{eff}} = \hat{H}_{\mathrm{eff}}^+ + \hat{H}_{\mathrm{eff}}^-$, cf. Eq. (6.11). Hence, in this limit, the many-body state of the system is expected to be in a product state of the two channels. Its exact form is given by

$$\begin{gathered} |\psi\rangle = |\mathrm{TMSV}\rangle_+ \otimes |\mathrm{TMSV}\rangle_- , \quad \text{with} \\ |\mathrm{TMSV}\rangle_\pm = \frac{1}{\sqrt{1 + \langle N_{\mathrm{p},\pm} \rangle}} \sum_{\tilde{N}=0}^{\infty} \left(\frac{\langle N_{\mathrm{p},\pm} \rangle}{1 + \langle N_{\mathrm{p},\pm} \rangle} \right)^{\frac{\tilde{N}}{2}} \left| \tilde{N}, \tilde{N} \right\rangle_\pm . \end{gathered} \tag{6.17}$$

The states $|\mathrm{TMSV}\rangle_\pm$ are so-called *two-mode squeezed vacuum* states (TMSV) [287], associated with the $\chi_\pm$ channel. They describe a weighted superposition of twin-Fock states $|\tilde{N}, \tilde{N}\rangle_\pm$ with an equal number of particles $\tilde{N}$ in the relevant modes in $m = +1$ and $m = -1$. The Fock states associated with the two channels are defined as $|N_{+1}, N_{-1}\rangle_\pm = (\hat{c}^\dagger_{\pm_k,1})^{N_{+1}} (\hat{c}^\dagger_{\mp_k,-1})^{N_{+1}} |\mathrm{vac}, \mathrm{vac}\rangle_\pm$, with $|\mathrm{vac}, \mathrm{vac}\rangle_\pm$ denoting the vacuum state in the corresponding modes. A detailed derivation in the context of spin-changing collisions using Bogoliubov theory for a single-channel configuration can be found in appendix C of Ref. [288].

From Eq. (6.17), we can directly evaluate the probability distribution associated with the occupation of pairs N_{p} in the two channels

$$p_\pm(N_{\mathrm{p}}, \langle N_{\mathrm{p},\pm} \rangle) = \frac{\langle N_{\mathrm{p},\pm} \rangle^{N_{\mathrm{p}}}}{(1 + \langle N_{\mathrm{p},\pm} \rangle)^{N_{\mathrm{p}}+1}}. \tag{6.18}$$

It resembles a *Bose-Einstein distribution*, which describes an ensemble of non-interacting bosonic particles at thermal equilibrium. This thermal-like distribution features a highly skewed occupation, peaking at the vacuum state with $N_\mathrm{p} = 0$ and gradually decaying towards larger pair numbers. A defining feature of Bose-Einstein distributions is their large occupation fluctuations, as indicated by the standard deviation being equal to the mean pair occupation, i.e., $\sigma(N_{\mathrm{p},\pm}) = \langle N_{\mathrm{p},\pm}\rangle$.

We can approximate the distribution in Eq. (6.18) as a thermal Boltzmann distribution, $p_\pm \approx e^{-\beta_\pm N_\mathrm{p}}/\mathcal{Z}_\pm$, with canonical partition sum $\mathcal{Z}_\pm = \mathrm{Tr}(e^{-\beta_\pm N_\mathrm{p}})$ [288]. By assuming thermodynamic equilibrium [289] and identifying $\beta_\pm = \hbar\omega_0/(k_\mathrm{B} T_{\mathrm{eff},\pm})$, we can calculate the effective pair temperature for the two channels

$$T_{\mathrm{eff},\pm} = \frac{\hbar\omega_0 \langle N_{\mathrm{p},\pm}\rangle}{k_\mathrm{B}}, \tag{6.19}$$

with k_B being the Boltzmann constant.

6.1.4 Open system dynamics and truncated Wigner simulations

Our theoretical discussions so far have focused on the many-body Hamiltonian, which is responsible for the coherent production of atom pairs in our system. Yet, due to the decay of the cavity field at rate κ, our experimental setup is inherently an open quantum system. Starting from Eq. (2.21), we employ the effective operator formalism presented in Ref. [122] and derive effective Lindblad terms describing the atomic degrees of freedom of our system. For each of the two channels, we obtain

$$\mathcal{L}_\pm = \sqrt{\gamma_\pm}\left(\hat{c}^\dagger_{+k,\pm1}\hat{c}_0 + \hat{c}^\dagger_0\hat{c}_{-k,\mp1}\right). \tag{6.20}$$

In direct correspondence to our discussion of Eq. (2.28) in section 2.2.4, the operators $\mathcal{L}_\pm$ describe superradiant Raman decay processes, where atoms scatter photons into the cavity mode while irreversibly changing their spin state $m \to m\pm1$ and obtaining net recoil momentum $+\hbar k$ along the drive direction z. These real photons are leaked from the cavity before they can be further rescattered by a second atom, hindering the formation of pairs. Accordingly, they can be directly measured outside the cavity, for instance through our heterodyne detection scheme, see section 3.2.1. The corresponding single-particle dissipative rates are

$$\gamma_\pm = \frac{2\kappa}{\delta_\pm^2 + \kappa^2}. \tag{6.21}$$

The dynamics of the open quantum system is determined by the master equation

$$\frac{d\hat{\rho}_\mathrm{at}}{dt} = -\frac{i}{\hbar}\left[\hat{H}, \hat{\rho}_\mathrm{at}\right] + \sum_{j\in\{+,-\}} \mathcal{L}_j\hat{\rho}_\mathrm{at}\mathcal{L}_j^\dagger - \frac{1}{2}\left(\mathcal{L}_j^\dagger\mathcal{L}_j\hat{\rho}_\mathrm{at} + \hat{\rho}_\mathrm{at}\mathcal{L}_j^\dagger\mathcal{L}_j\right), \tag{6.22}$$

with $\hat{\rho}_\mathrm{at}$ defining the density matrix of the atoms within our six-mode expansion.

In correspondence to our theoretical treatment of superradiant Raman scattering in section 2.2.1, we define expectation values for the different modes $\psi_{\tilde{k},m} = \langle\hat{c}_{\tilde{k},m}\rangle$.

We derive a set of six complex-valued equations of motion (EOMs)

$$\begin{aligned}
\frac{d}{dt}\psi_{0,0} &= [-i\chi_+(2\psi_0^*\psi_{\text{-}k,\text{-}1}\psi_{k,1} + \psi_{k,1}^*\psi_0\psi_{k,1} + \psi_{\text{-}k,\text{-}1}^*\psi_0\psi_{\text{-}k,\text{-}1}) \\
&\quad - i\chi_-(2\psi_0^*\psi_{k,\text{-}1}\psi_{\text{-}k,1} + \psi_{\text{-}k,1}^*\psi_0\psi_{\text{-}k,1} + \psi_{k,\text{-}1}\psi_0\psi_{k,\text{-}1}^*) \\
&\quad + \gamma_+(\psi_{k,1}^*\psi_{k,1}\psi_0 - \psi_{\text{-}k,\text{-}1}^*\psi_{\text{-}k,\text{-}1}\psi_0) + \gamma_-(\psi_{k,\text{-}1}^*\psi_{k,\text{-}1}\psi_0 - \psi_{\text{-}k,1}^*\psi_{\text{-}k,1}\psi_0)], \\
\frac{d}{dt}\psi_{\pm k,\pm 1} &= -i\frac{\omega_0}{2}\psi_{\pm k,\pm 1} \pm (\gamma_+ \mp i\chi_+)(\psi_0^*\psi_0\psi_{\pm k,\pm 1} + \psi_{\mp k,\mp 1}^*\psi_0\psi_0), \\
\frac{d}{dt}\psi_{\mp k,\pm 1} &= -i\frac{\omega_0}{2}\psi_{\mp k,\pm 1} \pm (\gamma_- \mp i\chi_-)(\psi_0^*\psi_0\psi_{\mp k,\pm 1} + \psi_{\pm k,\mp 1}^*\psi_0\psi_0), \\
\frac{d}{dt}\psi_{\pm 2k_x,0} &= -4i\omega_{\text{rec}}\psi_{\pm 2k_x,0} \\
&\quad + \sqrt{\frac{2}{3}}[-i\chi_+(2\psi_0^*\psi_{\text{-}k,\text{-}1}\psi_{k,1} + \psi_{k,1}^*\psi_0\psi_{k,1} + \psi_{\text{-}k,\text{-}1}^*\psi_0\psi_{\text{-}k,\text{-}1}) \\
&\quad - i\chi_-(2\psi_0^*\psi_{k,\text{-}1}\psi_{\text{-}k,1} + \psi_{\text{-}k,1}^*\psi_0\psi_{\text{-}k,1} + \psi_{k,\text{-}1}\psi_0\psi_{k,\text{-}1}^*) \\
&\quad + \gamma_+(\psi_{\text{-}k,\text{-}1}^*\psi_0\psi_{\text{-}k,\text{-}1} - \psi_{k,1}\psi_0\psi_{k,1}^*) + \gamma_-(\psi_{\text{-}k,1}^*\psi_0\psi_{\text{-}k,1} - \psi_{k,\text{-}1}\psi_0\psi_{k,\text{-}1}^*)],
\end{aligned} \tag{6.23}$$

with $\psi_0 = \psi_{0,0} + \sqrt{2/3}\psi_{\pm 2k_x,0}$.

Truncated Wigner simulations

We employ *truncated Wigner simulations* to model the dynamics of our system in the presence of technical and quantum fluctuations. We closely follow the methodology originally proposed for interacting Bose gases in Ref. [290]. Within this approximation, the system is truncated to relevant empty excitation modes $\hat{c}_q$ that are represented by stochastic complex variables ψ_q, with $q = \{\tilde{k}, m\}$ following the notation of Eqs. (6.23). If the occupation of the different modes is initially uncorrelated, they can be sampled from suitable Gaussian-shaped Wigner distributions with mean $\langle\psi_q\rangle = 0$ and variance $\sigma^2(\psi_q) = 1/2$. This yields initial occupations of

$$\langle\hat{c}_q^\dagger\hat{c}_q\rangle = \langle\psi_q^*\psi_q\rangle = 1/2 \tag{6.24}$$

for the empty excitation modes, which are typically referred to as *quantum one-half fluctuations* and interpreted as the degree of vacuum noise in the system [291]. This method has been successfully employed to capture the fluctuation dynamics associated with spin-changing collisions in Bose-Einstein condensates satisfying the single spatial-mode approximation [279, 292].

In practice, we initialize all the atoms in the mode $\hat{c}_{0,0}$ associated with the zero-momentum BEC in $m = 0$ by setting $\psi_{0,0}(t = 0) = \sqrt{N}$. The remaining modes are sampled S times from complex-valued normal distributions with mean $\mu = 0$ and variance $\sigma^2 = 1/2$. The mean-field EOMs in Eqs. (6.23) are then evolved for these different initial conditions, employing MATLAB's built-in methods as discussed in section 2.2.1. Additionally, we incorporate the technical fluctuations of the initial atom number in our simulations. For this purpose, we sample the atom number for each simulation from a Gaussian distribution with a mean N and standard deviation

$\sigma(N) = 0.045N$ to reflect the experimental conditions described in section 3.2.3. Finally, we can compute the expectation value $\langle \hat{O}(t) \rangle_S$, standard deviation $\sigma_S[\hat{O}_j(t)]$ and correlations $\langle \hat{O}_j(t) \hat{O}_k(t) \rangle_S$ of relevant observables $\hat{O}_j(t)$ and $\hat{O}_k(t)$ at any given time t by averaging over S realizations. To ensure numerical convergence, we typically consider $S = 500$ stochastically sampled initial conditions.

6.2 Observing coherent pair dynamics

Here, we discuss the experimental observation of coherent pair dynamics in our system. In section 6.2.1, we introduce the relevant protocol and present experimental observations, highlighting the emergence of pairs involving either a single or two discernible channels. In section 6.2.2, we explore the time evolution of the pair dynamics, observing coherent pair oscillations involving well-defined spin and momentum modes.

6.2.1 Experimental protocol and first observations

Our experiments start with a ^{87}Rb Bose-Einstein condensate, consisting of up to $N \approx 80000$ atoms coupled to the fundamental mode of our high-finesse optical cavity. The atoms are initialized in the $m = 0$ Zeeman sublevel of the $F = 1$ hyperfine ground-state manifold, with a variable magnetic field B along the z direction defining the quantization axis, cf. Fig. 6.2(a). We quench the laser power of the running-wave transverse drive for variable evolution time t at a fixed cavity detuning δ_c. Unlike the experiments discussed in the previous chapters, we do not actively stabilize the drive power, which would be technically involved for the relevant timescales $t \approx 100\,\mu\text{s}$. The passive stability of the drive power $\Delta P_\text{d}/P_\text{d} \approx 0.01$ is incorporated in the calibration of the corresponding coupling strengths.

Single-channel and two-channel configurations

In a first set of experiments, we prepare $N = 5.3(3) \times 10^4$ atoms in $m = 0$ and quench the drive to $\chi_+ = -2\pi \times 0.54(2)\,\text{Hz}$ for $t = 60\,\mu\text{s}$ at fixed two-photon detuning $\delta_+ = -2\pi \times 18.7(2)$ MHz. We consider two representative magnetic fields $B \approx 10.1$ G [Fig. 6.4(a)] and $B \approx 1.45$ G [Fig. 6.4(b)], yielding linear Zeeman splittings of $\omega_z = -2\pi \times 7.09(1)$ MHz and $\omega_z = -2\pi \times 1.01(1)$ MHz, respectively:

- For $\omega_z = -2\pi \times 7.09(1)$ MHz, we only observe the formation of atom pairs in the modes $|{+k}\rangle_{+1}$ and $|{-k}\rangle_{-1}$, as shown by the exemplary momentum distribution in Fig. 6.4(a1). The large Zeeman splitting results in a substantial two-photon detuning for the complementary pair channel, $\delta_- = -2\pi \times 32.9(2)$ MHz, as depicted in the level scheme in Fig. 6.4(b1). This condition predominantly favors the formation of pairs via the χ_+-channel, as the coupling to the complementary χ_--channel remains notably smaller, with $\chi_- = 0.57\chi_+$.

- For $\omega_z = -2\pi \times 1.01(1)$ MHz, we observe simultaneous occupation of pairs in the modes $|{+k}\rangle_{\pm1}$ and $|{-k}\rangle_{\mp1}$, as shown by the single-shot momentum distribution in Fig. 6.4(a2). In this case, the two-photon detunings for both

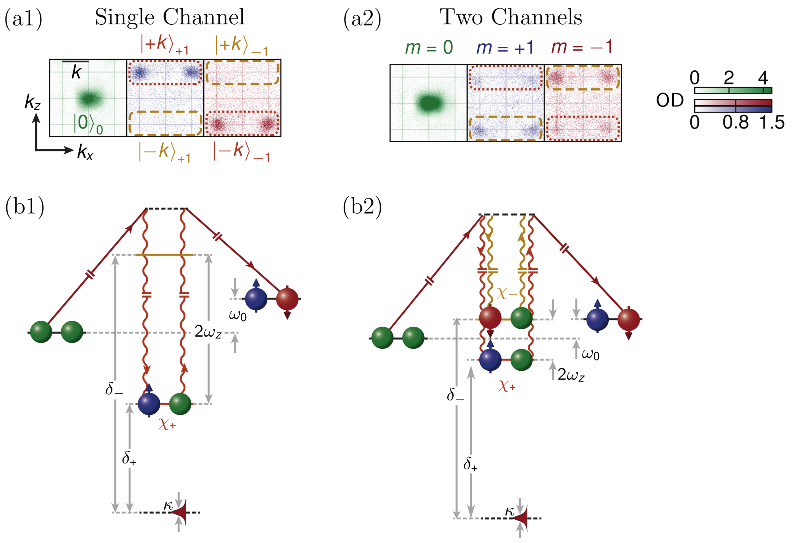

Figure 6.4: Observation of atom pairs in single-channel and two-channel configurations. **(a)** Exemplary spin-resolved momentum distributions for the single-channel (a1) and two-channel (a2) configuration. The orange and yellow boxes indicate the modes $|\pm k\rangle_{\pm 1}$ and $|\pm k\rangle_{\mp 1}$ associated with the χ_+ and χ_- channel, respectively. **(b)** Energy level diagrams for both configurations. In the single-channel case (b1), the Raman detunings for the two channels differ significantly, $|\delta_+| \ll |\delta_-|$, due to the large first order Zeeman splitting ω_z. This setting favors pair production solely via the χ_+ channel. In the two-channel configuration (b2), the small values of ω_z yield $\delta_+ \approx \delta_-$ and concurrent pair generation via two discernible channels χ_+ (yellow) and χ_- (orange arrows). For a detailed description of the coupling scheme, see Fig. 6.2(c).

channels become comparable, with $\delta_+ = -2\pi \times 18.7(2)$ MHz and $\delta_- = -2\pi \times 20.7(2)$ MHz. This results in similar coherent couplings $\chi_- = 0.90\chi_+$, see Eq. (6.9), and in concurrent occupation of both channels. The level scheme in Fig. 6.4(b2) illustrates this situation.

In the following, we make extensive use of these two settings, which we refer to as the *single-channel* and *two-channel configurations*, respectively.

6.2.2 Probing coherent pair oscillations

We can gain a deeper understanding of the pair dynamics, and its interplay with depletion and dissipation effects by investigating the full population evolution of the different modes. For clarity, we concentrate on the single-channel configuration involving the modes $|+k\rangle_{+1}$ and $|-k\rangle_{-1}$. We initialize $N = 8.1(3) \times 10^4$ atoms in the mode $|0\rangle_0$, and quench coupling to $\chi_+ = -2\pi \times 0.59(3)$ Hz over a variable evolution time t, while keeping $\delta_+ = -2\pi \times 22.7(1)$ MHz and $\omega_z = -2\pi \times 7.09(1)$ MHz constant. We infer the number of pairs by counting the atoms in $|-k\rangle_{-1}$, as this mode can be only occupied after the exchange of virtual cavity photons. This is different for the mode $|+k\rangle_{+1}$, which can be also populated following superradiant Raman scattering.

In Fig. 6.5(a), we plot the short-time evolution of the average number of pairs

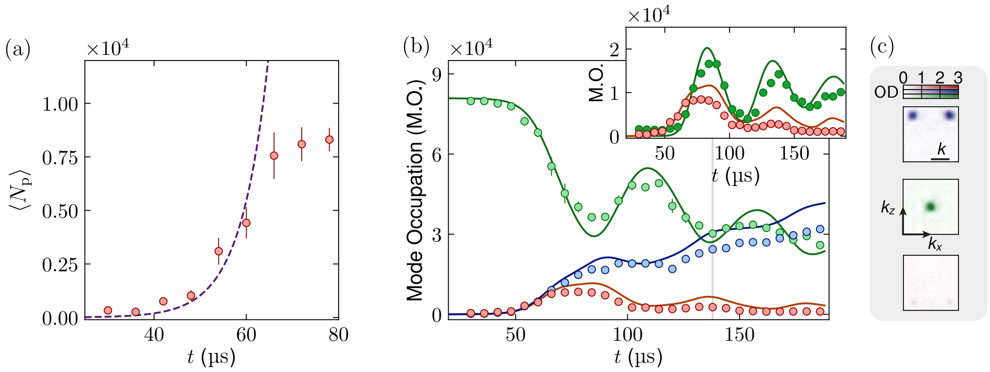

Figure 6.5: Coherent pair oscillations. **(a)** Short-time evolution of the average number of pair $\langle N_\mathrm{p}\rangle$ for a single-channel configuration. The dashed curve shows the expected exponential growth for an undepleted pump mode and captures our observations for $t \lesssim 60\,\mu\mathrm{s}$. **(b)** Long-time evolution of mode occupations for $|0\rangle_0$ (green), $|{+k}\rangle_{+1}$ (blue) and $|{-k}\rangle_{-1}$ (red data points) exhibiting coherent pair oscillations. The solid curves show the results from truncated Wigner simulations, and quantitatively agree with our observations. As shown in the inset, we also observe delayed oscillations of the higher-order momentum mode $|{\pm 2k_x}\rangle_0$ (dark green points). For longer times, photon loss leads to an imbalance between the populations in $|{+k}\rangle_{+1}$ and $|{-k}\rangle_{-1}$. **(c)** Representative momentum-space distribution with large imbalance at $t = 138\,\mu\mathrm{s}$ [gray line in (b)]. Throughout this chapter, the error bars represent the standard error of the mean.

$\langle N_\mathrm{p}\rangle$. We observe the onset of pair production around $t \approx 40\,\mu\mathrm{s}$ followed by an exponential population increase for $t \lesssim 60\,\mu\mathrm{s}$ which is compatible with the expectations for an undepleted pump mode from Eq. (6.16) [dashed curve in Fig. 6.5(a)]. As time elapses, we observe coherent oscillations redistributing the atoms between the different available modes, cf. Fig. 6.5(b). These pair oscillations are a direct consequence of the system being quenched across a second-order phase transition: in a restricted phase space with N atoms, the system undergoes periodic oscillations around a new ground-state configuration with finite pair numbers [34]. While similar to pair oscillations arising from spin-mixing interactions in spinor Bose-Einstein condensates [272], our observations also demonstrate coherent pair dynamics involving well-defined momentum modes.

To experimentally discern the oscillatory dynamics presented in Fig. 6.5(b), it was crucial to improve the shot-to-shot atom number stability in the $m = 0$ Zeeman sublevel to $\Delta N/N < 0.05$. This is achieved by using the new preparation scheme discussed in section 2.2.4. Prior to this improvement, we were only able to observe the initial nonlinear growth of pairs within $t \lesssim 80\,\mu\mathrm{s}$, followed by a decay attributed to superradiant Raman scattering.

For longer times, we observe a gradual accumulation of atoms in $|{+k}\rangle_{+1}$ as shown by the representative momentum-space distribution in Fig. 6.5(c). This results in an increasingly large population imbalance between $|{+k}\rangle_{+1}$ and $|{-k}\rangle_{-1}$. Concurrently, the oscillations are damped on a timescale $T_\mathrm{coh} \approx 150\,\mu\mathrm{s}$, which we identify as the coherence time in our system. We attribute both effects to the intrinsic open nature of our system, as photons are sporadically lost at the cavity mirrors through superradiant Raman scattering, inhibiting the reabsorption of cavity photons and thereby the formation of the second pair constituent $|-k\rangle_{-1}$. We account for this effect in our truncated Wigner simulations [see Eqs. (6.23)], which quantitatively reproduce the observed population dynamics including the growing mode imbalance, cf. solid lines in Fig. 6.5(b). The coupling χ_+ is the only free parameter of our simulations and is optimized to $\chi_+ = 0.89\eta_{+,\mathrm{exp}}$ of the experimentally calibrated value η_{exp} via least-square minimization; we attribute this minor discrepancy to the imperfect alignment between the BEC and the cavity mode.

Importantly, this small deviation is compatible with the systematic uncertainty of the atom-number calibration in our system ($\sim 15\%$) and thereby the strength of the collective atom-light interactions $N\chi_+$. Hence, our experimental results are in quantitative agreement with our truncated Wigner simulations taking vacuum fluctuations into account. For comparison, the short-time pair dynamics in experiments coupling thermal atomic gases to optical cavities are captured by theory only after rescaling the collective coupling by a factor of $\sim\sqrt{6}$ [80]; this discrepancy is attributed to spurious coupling inhomogeneities associated with thermal broadening.

The population oscillations of the mode $|0\rangle_0$ exhibit a higher contrast than their counterparts in $|\pm k\rangle_{\pm 1}$. This is due to the pair dynamics coherently occupying higher-order momentum modes at late times, similar to our observations of superradiant tunneling in an extended momentum-space lattice in section 5.2 of chapter 5. In the inset of Fig. 6.5(b), we show the mode occupation (M.O.) of the density-modulated state $|\pm 2k_x\rangle_0$ in $m = 0$ (dark green), which exhibits delayed oscillations in comparison to the mode $|-k\rangle_{-1}$ (orange data points). This behavior is reproduced by our truncated Wigner simulations (solid lines). The underlying higher-order pair process involves an atom in $|-k\rangle_{-1}$ with symmetric momentum $k_x = \pm k$ along x, which scatters a photon from the drive into cavity, flipping its spin state back to $m = 0$ and obtaining additional momentum along $k_{\mathrm{x}} = \pm 2k$ the cavity direction (mode $|\pm 2k_x\rangle_0$); this virtual cavity photon is rescattered into the drive by a second atom in $|+k\rangle_{+1}$ which also occupies $|\pm 2k_x\rangle_0$. The long-time pair dynamics is not necessarily restricted to the above-mentioned modes, as even higher-order states can be occupied provided that the total momentum of the system is conserved. Since our field of view is limited to $|k_x| \lesssim 2.2k$ due to the small separation between cavity mirrors ($l = 176\,\mu\mathrm{m}$), the systematic study of higher-order pair dynamics should be the subject of future experiments.

6.3 Parametric amplification of pair production of atom pairs in well-defined modes

Here, we discuss the collective enhancement of pair production in our system. In section 6.3.1, we draw parallels to parametric amplification in nonlinear optical systems and provide experimental evidence demonstrating the collective enhancement of pair production. In section 6.3.2, we discuss the various relevant time scales of our system: the rapid generation of pairs ($\sim 40\,\mu\mathrm{s}$) ensures that the atoms remain in well-defined momentum modes throughout the course of the dynamics.

6.3.1 Collectively enhanced pair production via superradiant photon exchange

Our system bears a close resemblance to $\chi^{(3)}$-parametric amplifiers. In these optical systems, a strong coherent pump laser beam irradiates a nonlinear crystal. There two 'pump photons' are converted into correlated 'signal' and 'idler photon' pairs through a four-wave mixing process, as schematically depicted in Fig. 6.6(a). Within the undpleted pump-mode approximation [24], the Hamiltonian describing the creation of signal and idler photon pairs reads

$$\hat{H}_{\mathrm{PA}} = \sum_j \hbar g_j N_{\mathrm{p}} (\hat{a}^\dagger_{\mathrm{s},j} \hat{a}^\dagger_{\mathrm{i},j} + \hat{a}_{\mathrm{s},j} \hat{a}_{\mathrm{i},j}), \tag{6.25}$$

with the operators $\hat{a}^\dagger_{\mathrm{s},j}$ and $\hat{a}^\dagger_{\mathrm{i},j}$ creating signal and idler photons in well-defined optical modes j, and g_j being the corresponding single-particle coupling rates. Within this approximation, the pump-mode creation operator is approximated as $\hat{a}^\dagger_{\mathrm{p}} = \sqrt{N_{\mathrm{p}}}$, with N_{p} being the average number of pump-mode photons. For efficient parametric amplification, the output modes should fulfill the *phase-matching condition* and conserve total momentum $2\mathbf{k}_{\mathrm{p}} = \mathbf{k}_{\mathrm{s},j} + \mathbf{k}_{\mathrm{i},j}$ both inside and outside the nonlinear crystal [293]. A hallmark feature of parametric amplifiers is the amplification of vacuum fluctuations resulting in the exponential generation of signal and idler pairs when increasing the power of the laser beam $P_{\mathrm{pump}} \propto N_{\mathrm{p}}$ above a loss-dependent threshold, as schematically depicted in Fig. 6.6(b). This behavior arises from the collectively enhanced pair production rates $g_j N_{\mathrm{p}}$ when increasing the number of involved pump photons N_{p}, see Eq. (6.25).

Our system constitutes an atomic parametric amplifier, with the nonlinear interactions induced by the collective exchange of cavity photons: the initial zero-momentum BEC in $m = 0$ corresponds to the macroscopically occupied pump mode, whereas the atoms in $m = +1$ and $m = -1$ compare to idler and signal modes, respectively[2]. In particular, we expect parametric amplification of signal and idler pairs when varying the initial atom number N, provided the undepleted pump-mode approximation remains valid.

To assess this experimentally, we prepare a BEC of variable atom number N in the mode $|0\rangle_0$ and quench the coupling $\chi_+ = -2\pi \times 0.64(1)\,\mathrm{Hz}$ for a fixed evolution time of $t_{\mathrm{fix}} = 65\,\mathrm{\mu s}$. For clarity, we operate in the single-channel configuration with large Zeeman splitting $\omega_z = 2\pi \times 7.09(1)\,\mathrm{MHz}$ and set $\delta_+ = -2\pi \times 20.7(3)\,\mathrm{MHz}$. In Fig. 6.6(c), we observe a super-linear increase of the mean pair number $\langle N_{\mathrm{p}} \rangle$ when adjusting the initial atom number N. This behavior is due to collective enhancement of the pair production, which results in coupling rates $N\chi_\pm$ akin to the third-order susceptibility $\chi^{(3)}$. From the analytic solution for an undepleted pump mode in Eq. (6.16), we expect the number of pairs to scale as $\langle N_{\mathrm{p}} \rangle \propto e^{\alpha\sqrt{N}}$ with N. This holds for fixed evolution times t_{fix} and $|\chi_+| \gg |\chi_+^{\mathrm{c}}|$, with $\alpha \approx t_{\mathrm{fix}}\sqrt{\omega_0|\chi_+|}$. In the inset of Fig. 6.6(c), we plot the same experimental data using a semi-log scale and verify the aforementioned scaling with N, both for the experimental data and our

---

[2] We note that designating the $m = -1$ and $m = +1$ sublevels as signal and idler modes is somewhat arbitrary. However, we have adopted this nomenclature motivated by the larger internal energy of $m = -1$ atoms, mirroring the convention where signal photons have higher frequencies.

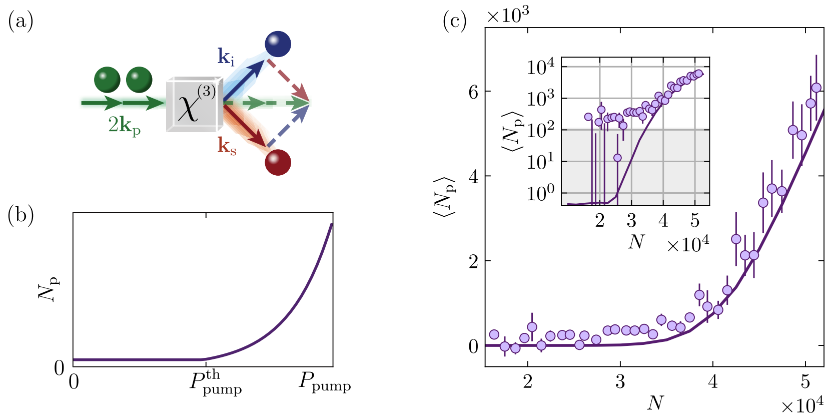

Figure 6.6: Parametric amplification of atom pairs. **(a)** Schematics of an optical parametric amplifier, which converts two pump photons with individual momenta $\mathbf{k}_\mathrm{p}$ (green) into a correlated pair of signal (blue) and idler photons (red circles), with $\mathbf{k}_\mathrm{s}$ and $\mathbf{k}_\mathrm{i}$. This process occurs via the nonlinear interactions $\chi^{(3)}$, and conserves total momentum. **(b)** A hallmark of parametric amplification is the super-linear growth of photon pairs N_p, when increasing the pump power P_p above a loss-dependent threshold P^th_p. **(c)** Observed mean number of atom pairs $\langle N_\mathrm{p}\rangle$ as a function of the atom number N at fixed evolution times $t_\mathrm{fix} = 65\,\mu\mathrm{s}$. We observe a super-linear growth, indicating parametric amplification. This is captured by our truncated Wigner simulations (solid line). The inset shows the data in a semi-log scale, highlighting the scaling $\langle N_\mathrm{p}\rangle \propto \exp\left(\sqrt{N}\right)$ and the technical detection noise of $\sigma_\mathrm{det} \approx 200$ atoms (shaded area), see section 3.2.2.

truncated Wigner simulations (solid lines). For small atom numbers $N \lesssim 30000$, the experimentally determined pair number exhibits an offset of $\langle N_\mathrm{p}\rangle \approx 200$ pairs while the simulations continue decreasing and reach the level associated to quantum fluctuations $\langle N_\mathrm{p}\rangle \approx 1/2$ below the critical atom number of $N^c \approx 24000$. The deviation from the theoretical expectations at small pair numbers is due to our technical imaging detection noise, which is also on the order of $\sigma_\mathrm{det} \approx 200$ atoms [shaded area in the inset of Fig. 6.6(c)]. For additional details on the imaging detection limits, see section 3.2.2.

The observed super-linear scaling demonstrates the collective nature of pair production in our system. We refer to the underlying mechanism as *superradiant photon exchange*, due to the similarities with collectively enhanced superradiant Raman scattering, which we examined in section 5.3 of the previous chapter.

6.3.2 Relevant time scales of the system

Collective amplification in our system is only possible if the emergent pairs remain in well-defined spin and momentum modes throughout the course of the dynamics [270, 294], which we can verify by assessing and comparing the different timescales of our experiments. In our system, the characteristic timescale to produce pairs, $T_\mathrm{int} = 2\pi/(N\max|\chi_\pm|)$, is determined by the collective couplings $N\chi_\pm$. For typical experimental values $N = 8 \times 10^4$ and $\chi_+ = -2\pi \times 0.5\,\mathrm{Hz}$, we obtain $T_{\text{int}} \approx 35\,\mu\text{s}$, which is in agreement with the onset of pair production observed in Fig. 6.5(a). Simultaneously, the lifetime of the modes associated with the pairs is constrained by the harmonic trapping potential, as the paired states with $\pm\hbar k$ are not its eigenstates. Following Ref. [270], we estimate their lifetime as $T_{\text{LT}} = \min(T_{\text{exp}},\ T_{\text{sep}})$, with $T_{\text{exp}} = 2\pi/\max(\omega_{hx}, \omega_{hz})$ and $T_{\text{sep}} = R_{\text{TF}}/v_{\text{rec}}$ being the characteristic timescales for the expansion in the harmonic trap and for the separation between the pairs and the zero-momentum BEC, respectively. Using the calibrated trap frequencies $[\omega_{hx},\ \omega_{hy},\ \omega_{hz}] = 2\pi \times [204(3),\ 34(2),\ 185(1)]$ Hz, the recoil velocity $v_{\text{rec}} = 0.0058$ m/s and a typical Thomas-Fermi radius of $R_{\text{TF}} \approx 5.8\,\mu\text{m}$, we obtain $T_{\text{exp}} \approx 5\,\text{ms}$ and $T_{\text{LT}} = T_{\text{sep}} \approx 1\,\text{ms}$. Finally, as already discussed in the context of Fig. 6.5(b), the coherence time of the observed pair oscillations is given by $T_{\text{coh}} \approx 150\,\mu\text{s}$ for our typical experimental parameters. For a more systematic estimation of the pair lifetime, see also the calculations in appendix A.3 regarding the lifetimes in momentum-space lattices.

The large separation of timescales in our system, quantified as $T_{\text{LT}}/T_{\text{int}} \approx 25 \gg 1$ and $T_{\text{LT}}/T_{\text{coh}} \approx 6.7 \gg 1$, ensures that pairs are produced in well-defined individual momentum modes and remain in such throughout the dynamics. For comparison, the experiments generating correlated momentum pairs through collisions in metastable helium BECs display a ratio of $T_{\text{LT}}/T_{\text{int}} \approx 0.7$ [270]. Meanwhile, the experiments using Floquet engineering in a two-dimensional BEC to create correlated matter-wave jets exhibit $T_{\text{LT}}/T_{\text{int}} \lesssim 3$ [294]. These experiments operate in the spontaneous scattering regime and in the weak collective regime for pair production, respectively. Conversely, our experiments operate in the so-called strong collective regime for pair production.

6.4 Controlling coherent and dissipative pair dynamics

Here, we investigate the interplay between unitary pair dynamics and the leading dissipative processes in our system, which arise from superradiant scattering. We introduce the corresponding experimental protocol in section 6.4.1 and present our observations in section 6.4.2. Our results highlight our ability to independently control coherent and dissipative processes, and to discern them through a combination of atomic and photonic observables.

6.4.1 Motivation and experimental protocol

In our experiment, we can optically control the coherent interaction rates $\chi_{\pm} = \eta^2\delta_{\pm}/(\delta_{\pm}^2 + \kappa^2)$ giving rise to pairs by adjusting the Raman coupling η and the corresponding detunings $\delta_{\pm}$, cf. Eq. (6.9). As the pair dynamics takes place within tens to hundreds of microseconds, we can separate this process from typical dissipation sources in cold-atom experiments such as heating, three-body losses, and trapping effects [95, 192]. Additionally, operating the drive at the tune-out wavelength λ_{TO} suppresses spurious optical potentials and minimizes spontaneous emission for any given Raman coupling η [204]. We experimentally verify that the transverse drive does not induce significant losses by monitoring the atom-number evolution while illuminating with the maximum experimentally used laser power ($P_{\text{d}} \approx 120\,\text{mW}$).

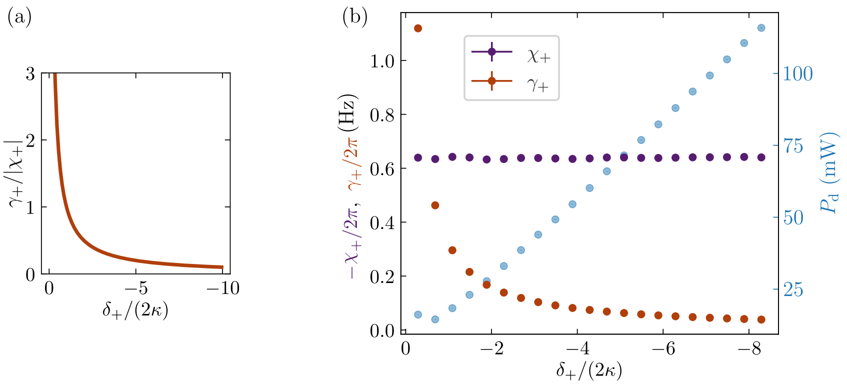

Figure 6.7: Protocol for controlling the coherent and dissipative dynamics. **(a)** Expected scaling of the ratio between dissipative γ_+ and coherent couplings χ_+, when adjusting the two-photon detuning δ_+. **(b)** Experimental protocol. For larger values of $|\delta_+|$, we also increase the drive laser power P_d (blue) in order to obtain constant coherent couplings rates $\chi_{+,\mathrm{fix}} = -2\pi \times 0.64(1)$ Hz (purple data points). Concurrently, the dissipative coupling γ_+ (red points) monotonically decreases with $|\delta_+|$, facilitating independent control over the dissipative dynamics.

The measured $1/e$ lifetime of 47(7) ms for the atoms in the trap is orders of magnitude larger than the relevant experimental timescales of $t \lesssim 200\,\mu\mathrm{s}$.

Nonetheless, the dynamics is purely unitary only in the asymptotic limit of large two-photon detunings, with $|\delta_\pm|/\kappa \to \infty$. For finite $\delta_\pm$, the system inherently features competing superradiant Raman scattering, which leads to a dissipative population transfer towards the modes $|{+k}\rangle \pm 1$ at rates $\gamma_\pm = 2\eta^2\kappa/(\delta_\pm^2 + \kappa^2)$, as derived in Eq. (6.21). Due to their different scaling

$$\frac{\gamma_\pm}{\chi_\pm} = \frac{2\kappa}{\delta_\pm},$$

we can experimentally adjust the ratio between dissipative and coherent processes by varying $\delta_\pm$. In particular, we can strongly mitigate superradiant Raman scattering by operating the drive at $|\delta_\pm| \gg 2\kappa$, as plotted in Fig. 6.7(a).

In order to examine this competition, we modify the experimental protocol to maintain the coherent coupling rate χ_+ constant over a broad range of two-photon detunings, δ_+, as demonstrated in Fig. 6.7(b): given that the coupling rate scales as $\chi_+ \approx \eta^2/\delta_+ \propto P_\mathrm{d}/\delta_+$, with $P_\mathrm{d} \propto \eta^2$ being the drive laser power, we progressively increase P_d for larger $|\delta_+|$ (blue data points). This results in equal coherent couplings $\chi_{+,\mathrm{fix}} = -2\pi \times 0.64(3)$ Hz for a wide range of detunings (purple data points). Simultaneously, the dissipative coupling scales as $\gamma_+ = 2\chi_{+,\mathrm{fix}}\kappa/\delta_+$ and gradually decreases with increasing $|\delta_+|$ (red data points).

6.4.2 Investigating the interplay between coherent and dissipative dynamics

We experimentally study the relationship between the coherent and dissipative dynamics of our system in a single-channel configuration with $\omega_z = -2\pi \times 7.09(1)$ MHz.

As discussed in the previous section, we quench the coherent coupling to a fixed value $\chi_{+,\mathrm{fix}} = -2\pi \times 0.64(3)\,\mathrm{Hz}$ for $t = 80\,\mathrm{\mu s}$. We initialize $N = 5.3(3) \times 10^4$ atoms and monitor the dynamics for different two-photon detunings δ_+, see Fig. 6.8. The measured mean number of pairs $\langle N_\mathrm{p} \rangle$ remains small close to the two-photon resonance ($\delta_+ = 0$) and increases monotonically for large detunings $|\delta_+|/(2\kappa) \gg 1$, as shown in Fig. 6.8(a). Simultaneously, the mean population imbalance $\langle N_\mathrm{imb} \rangle$ between $|{+k}\rangle_1$ and $|{-k}\rangle_{-1}$ (gray data points) exhibits the opposite trend and gradually decreases towards zero for large detunings, cf. Fig. 6.8(b).

In Fig. 6.8(b), we also present the total number of photons $\langle N_\mathrm{ph} \rangle$ leaked from the cavity (orange data points), as estimated from our heterodyne detection, see section 3.2.1 for technical details: we estimate it as $\langle N_\mathrm{ph} \rangle = 2\kappa \int n_\mathrm{ph}(t)dt$, with $n_\mathrm{ph}(t)$ being the mean number of photons at the characteristic frequency $\omega_\mathrm{d} - \omega_z$ associated with superradiant Raman scattering between the modes $|0\rangle_0 \to |{+k}\rangle_{+1}$. The qualitative agreement between $\langle N_\mathrm{ph} \rangle$ and $\langle N_\mathrm{imb} \rangle$ verifies that superradiant Raman scattering is indeed the primary dissipation source in our system within the relevant timescales. The experimental results are well captured by our truncated Wigner simulations [solid lines in Figs. 6.8(a,b)]. The discrepancy of the simulated pair number $\langle N_\mathrm{p} \rangle$ at $|\delta_+|/(2\kappa) \lesssim 1$ is attributed to the limited validity of the adiabatic cavity field elimination in this regime (dashed line).

Furthermore, we monitor the time evolution of the different modes at fixed coherent coupling $\chi_{+,\mathrm{fix}}$ for three representative detunings δ_+. For the largest value $\delta_+/(2\kappa) = -6.3$ [Fig. 6.8(c1)], we observe high-contrast coherent oscillations of the pump-mode occupation $|0\rangle_0$ (green data points). These oscillations become less pronounced at the intermediate detuning $\delta_+/(2\kappa) = -4.3$ [Fig. 6.8(c2)], and are almost completely suppressed for the smallest value $\delta_+/(2\kappa) = -2.3$, cf. Fig. 6.8(c3). Conversely, the accumulation of atoms in the mode $|{+k}\rangle_{+1}$ (blue data points) due to superradiant Raman scattering is accelerated close to the two-photon resonance. It is worth noting that the number of atoms within our field of view does not remain constant through the course of the dynamics. We estimate an upper bound $N_\mathrm{H}(t) = \max(N) - N(t)$ for the 'hidden modes'[3] outside of our field of view ($|k_x| \lesssim 2.2k$), cf. gray datapoints in Figs. 6.8(c1-3). For all examined detunings, $N_\mathrm{H}(t)$ monotonically increases and follows the same qualitative trend as $|{+k}\rangle_{+1}$. This behavior suggests that the occupation of higher-order momentum modes is primarily due to irreversible superradiant Raman scattering. A likely candidate is the $m = +1$ mode with $k_z = +k$ and symmetric momentum $k_x = \pm 3k$ along the cavity axis, which can be occupied through superradiant Raman scattering following transient pair production in $|{\pm 2k_x}\rangle_0$. For all the two-photon detunings considered in Fig. 6.8(b), the total number of photons leaking out of the cavity $\langle N_\mathrm{ph} \rangle$ exceeds the imbalance $\langle N_\mathrm{imb} \rangle$ after $t = 80\,\mathrm{\mu s}$. However, the former is approximately equal to $\langle N_\mathrm{ph} \rangle \approx \langle N_\mathrm{imb} \rangle + N_\mathrm{H}(80\,\mathrm{\mu s})$, further supporting this conjecture.

---

[3] In these considerations, we implicitly neglect atom loss due to the large $1/e$-lifetime of the trapped atoms, 47(7) ms. As the measured atom numbers do not depend on the spin composition (see section 3.2.2), we can associate $N_\mathrm{H}(t)$ with the occupation of modes outside our field of view.

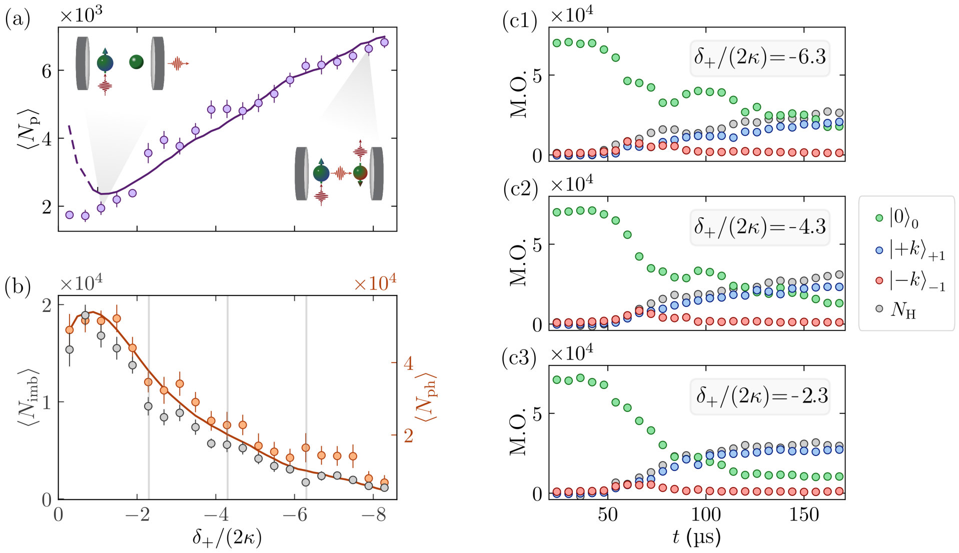

Figure 6.8: Experimental control over coherent and dissipative dynamics. **(a)** Mean number of pairs $\langle N_\mathrm{p}\rangle$ as a function of the two-photon detuning δ_+, for $t = 80\,\mu\mathrm{s}$ and fixed coherent couplings $\chi_{+,\mathrm{fix}} = -2\pi \times 0.64(3)\,\mathrm{Hz}$. **(b)** Corresponding mode imbalance $\langle N_\mathrm{imb}\rangle$ (gray) and average number of photons leaked from the cavity $\langle N_\mathrm{ph}\rangle$ (orange data points). The formation of pairs becomes pronounced (suppressed) at small (large) cavity detunings δ_+, which is attributed to the dominant coherent (dissipative) dynamics in this regime, see illustrations in (a). The solid lines are obtained from truncated Wigner simulations, with the dashed line in (a) indicating the regime where the adiabatic cavity field elimination becomes invalid, i.e., $|\delta_+| < 2\kappa$. **(c)** Evolution of the mode occupation (M.O.) for three representative detunings $\delta_+/(2\kappa) = -6.3$ (c1), -4.3 (c2) and -2.3 (c3) [gray lines in (b)], showing a suppression of coherent pair oscillations at small $|\delta_+|$. The gray data points N_H indicate occupation of modes outside our field of view due to superradiant Raman scattering.

6.5 Characterizing the pair quantum statistics

Our results so far have provided experimental evidence for the coherent oscillations and parametric amplification of atom pairs in well-defined spin and momentum modes. These findings can be captured within mean-field approaches, as they originate directly from the system's nonlinear equations of motion [cf. Eq. (6.23)] and rely on estimating the expectation values of different operators, such as the mean pair number. However, it is often challenging to detect beyond mean-field effects in many-body cavity QED systems with degenerate Bose gases [58]. The fluctuations of relevant observables tend to be suppressed by $1/N$ when the steady state of the atomic ensemble resembles a coherent state with N atoms.

In this section, we experimentally investigate the emergent pair statistics and observe distributions that are fundamentally different from the expectation for semi-classical coherent states. In section 6.5.1, we present our experimental observations both for the single-channel and two-channel configurations. We observe wide pair histograms resembling thermal Bose-Einstein distributions and infer the associated temperature of the pairs. In section 6.5.2, we estimate the relative importance of

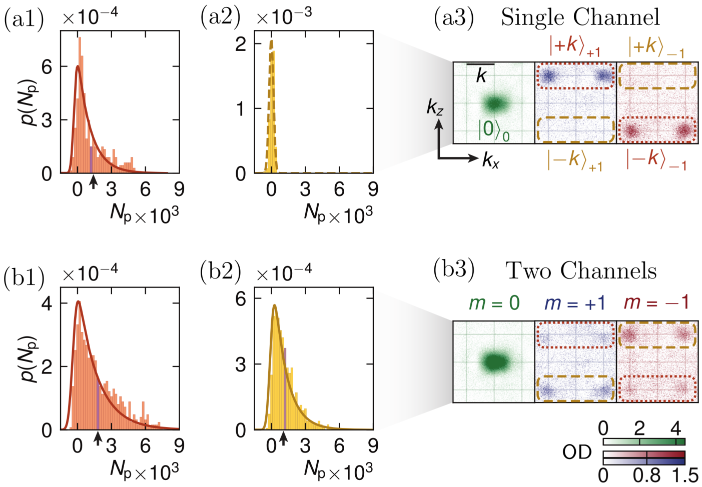

Figure 6.9: Pair statistics. **(a)** Histograms of the pair number for a single-channel configuration, showing the distributions associated with the χ_+ channel (a1) and the absence of pairs via χ_- (a2). **(b)** Histograms for the two-channel case, showing the concurrent pair distributions via χ_+ (b1) and χ_- processes (b2). The solid lines show the fitted Bose-Einstein distributions convolved with our Gaussian detection noise. The purple bin and black arrow indicate the mean $\langle N_\mathrm{p}\rangle$ and standard deviation $\sigma(N_\mathrm{p})$, respectively, demonstrating large fluctuations $\sigma(N_\mathrm{p}) \approx \langle N_\mathrm{p}\rangle$. The Gaussian fit (dashed line) in (a2) is consistent with a zero-pair distribution, see main text. For (a) and (b), the exact evolution times are $t =$ 60 µs and 62 µs, respectively. In (a3) and (b3), we present representative time-of-flight images, highlighting the modes giving rise to pairs for both configurations.

thermal and quantum fluctuations for the emergent pair dynamics.

6.5.1 Measuring the pair statistics

To characterize the pair statistics, we accumulate hundreds of realizations under equal experimental conditions for the single-channel [Fig. 6.9(a)] and two-channel configurations [Fig. 6.9(b)]. Based on our analysis of the population dynamics in section 6.2.2, we choose an evolution time of $t \approx$ 60 µs to ensure that pair production occurs in a regime of parametric amplification. The remaining experimental parameters are the same as in Fig 6.4. For both configurations, we present the pair statistics associated with χ_+ and χ_- processes in orange [Figs. 6.9(a1,b1)] and yellow histograms [Figs. 6.9(a2,b2)], respectively. When a channel becomes active, we observe large shot-to-shot fluctuations of the pair occupations. The skewed distributions peak close to $N_\mathrm{p} = 0$ and slowly decay for higher pair numbers. As discussed in section 6.1.3, we expect the pair statistics to be captured by a Bose-Einstein distribution, cf. Eq. (6.18), provided the undepleted pump-mode approximation remains valid. To assess this, we need to consider the technical detection noise which is on the order of $\sigma_\mathrm{det} \approx 200$ atoms, see section 3.2.2. This uncorrelated noise is well-captured by a Gaussian distribution $G(N_\mathrm{p}, \sigma_\mathrm{G}, \mu)$, with mean μ and standard deviation σ_G. We fit the pair histograms in each occupied channel with a convolution of a Bose-Einstein distribution $p_{\pm}(N_\mathrm{p}, \langle N_{\mathrm{p},\pm}\rangle)$ and a normalized Gaussian distribution to account for detection noise

$$P_{\pm}(N_\mathrm{p}, \langle N_{\mathrm{p},\pm}\rangle, \sigma_\mathrm{G}, \mu) = p_{\pm}(N_\mathrm{p}, \langle N_{\mathrm{p},\pm}\rangle) * G(N_\mathrm{p}, \sigma_\mathrm{G}, \mu). \tag{6.26}$$

These thermal fits accurately capture the form of the observed histograms, as shown by the solid curves in Figs. 6.9(a1, b1, b2), indicating that the underlying pair distributions are compatible with Bose-Einstein statistics. For the case of an unoccupied pair channel in Fig. 6.9(a2), the distribution is captured by a Gaussian fit (dashed curve) and yields $\sigma_\mathrm{G} \approx \sigma_\mathrm{det}$.

For a more quantitative comparison, we estimate the mean and standard deviation of the pair occupation in our system. Assuming uncorrelated physical and technical fluctuations, we calculate the standard deviation as $\sigma(N_\mathrm{p}) = \sqrt{\sigma^2_\mathrm{exp}(N_\mathrm{p}) - \sigma^2_\mathrm{G}}$, where $\sigma_\mathrm{exp}(N_\mathrm{p})$ is the experimentally measured standard deviation. For the single-channel configuration, we obtain $\langle N_{\mathrm{p},+}\rangle = 1150(50)$ and $\sigma(N_{\mathrm{p},+}) = 1400(50)$, as indicated by the dark bin and arrow in Fig. 6.9(a1), respectively. Additionally, for the two-channel configuration, we obtain $\langle N_{\mathrm{p},+}\rangle = 1750(50)$ and $\sigma(N_{\mathrm{p},+}) = 1800(50)$ [Fig. 6.9(b1)], and $\sigma(N_{\mathrm{p},-}) = 1100(50)$ [Fig. 6.9(b2)] for the two active pair channels. Hence, for all the observed configurations we infer large standard deviations, $\sigma(N_\mathrm{p}) \approx \langle N_\mathrm{p}\rangle$, which are consistent with a Bose-Einstein distribution and greatly exceed the expectation for semi-classical coherent spin states $\sigma(N_\mathrm{p})|_\mathrm{coh} = \langle N_\mathrm{p}\rangle^{1/2}$.

As the pair statistics follows a thermal-like distribution, we can estimate an effective temperature using Eq. (6.19) and assuming thermal equilibrium. For the characteristic bare pair energies of $\omega_0 \approx 2\pi \times 15\,\mathrm{kHz}$ and the typical average number of pair numbers $\langle N_\mathrm{p}\rangle \approx 1000$, we obtain

$$T_\mathrm{eff} \approx 500\,\mu\mathrm{K}. \tag{6.27}$$

For comparison, the effective pair temperature in our system greatly exceeds the spin temperature for a comparable number of pairs produced by spin-changing collisions, with $T_\mathrm{eff} \lesssim 10\,\mathrm{nK}$ [288]. It is also significantly higher than the temperature $T \approx 100\,\mathrm{nK}$ of the external degrees of freedom in our harmonically trapped BEC. This disparity originates from the lower energy scales associated with the latter systems, $\omega_0 \lesssim 2\pi\times 1\,\mathrm{Hz}$ and $\omega_\mathrm{Trap} \approx 2\pi\times 100\,\mathrm{Hz}$, respectively. In future experiments, it will be interesting to explore systematically the time evolution of the pair distributions both at short and long times [295]; this could help to elucidate the pair thermalization dynamics in the presence of tunable coherent and dissipative channels.

Our observations of the pair statistics are consistent with the many-body system occupying a two-mode squeezed vacuum state, i.e., a superposition of twin-Fock states in the corresponding modes as shown by Eq. (6.17). Multimode parametric amplification in the two-channel configuration is not expected to alter the resulting distributions for an undepleted pump mode as long as the different channels remain discernible [296].

6.5.2 The role of thermal and quantum fluctuations

As an atomic parametric amplifier, our system is capable of enhancing both thermal and quantum fluctuations, giving rise to states featuring macroscopic pair occupations [297]. In this section, we make a quantitative estimation of the initial thermal occupation of the relevant momentum modes and conclude that the pair dynamics indeed primarily amplifies quantum fluctuations.

We estimate an upper bound for the thermal occupation of the different momentum modes forming the pairs in our system. By considering $N \approx 8 \times 10^4$ and an average trap frequency $\bar{\omega} = (\omega_{hx}\omega_{hy}\omega_{hz})^{1/3} = 2\pi \times 109\,\mathrm{Hz}$, we obtain a critical condensation temperature of $T_c \approx\ 210\,\mathrm{nK}$ [111]. Thus, for typical experimental temperatures of $T \lesssim\ 100\,\mathrm{nK}$, we expect a condensate fraction of $N_\mathrm{c}/N \gtrsim 0.9$ [298]. The momentum-space width of the initial BEC and the momentum modes associated with pairs is on the order of $\delta k = 2\pi/R_\mathrm{TF} \approx 0.12k$, with $R_\mathrm{TF} \approx 5.8\,\mu\mathrm{m}$ being the Thomas-Fermi radius of the harmonically confined BEC. The momentum modes $|\pm k\rangle_{\pm 1}$ in the Zeeman sublevels $m = \pm 1$ associated with pairs are localized around $(k_x, k_x, k_z) = (\pm k, 0, \pm k)$, with k being the photon recoil momentum. Taking into account their finite spread δk, the probability to thermally occupy one of these modes is

$$P = 2 \int_{k-\delta k}^{k+\delta k} \int_{-\delta k}^{\delta k} \int_{k-\delta k}^{k+\delta k} p(\mathbf{k}, T)\ \mathrm{d}k_x\, \mathrm{d}k_y\, \mathrm{d}k_z \approx 2.8 \times 10^{-4}, \tag{6.28}$$

with $p(\mathbf{k}, T) = \mathcal{N}\left[\exp\left(\frac{E(\mathbf{k})}{k_B T}\right) + 1\right]^{-1}$ being the momentum-space probability distribution for the thermal ^{87}Rb atoms of mass M at $T =\ 100\,\mathrm{nK}$. Here, $E(\mathbf{k}) = \hbar^2\mathbf{k}^2/(2M)$ is the kinetic energy associated with the momenta $\hbar\mathbf{k} = \hbar(k_x, k_y, k_z)$, k_B is the Boltzmann constant and $\mathcal{N}$ a normalization factor. The factor of 2 in Eq. (6.28) accounts for the two momentum states $k_x = k$ and $k_x = -k$ contributing to form a pair.

In our experiments, we prepare the initial BEC in the $m = 0$ Zeeman sublevel by applying a strong magnetic-field gradient to clean spurious atoms in $m = \pm 1$ [78]. Making a conservative estimate, we assume that the spurious occupation of these Zeeman sublevels, $N_{\pm 1}$, is less than $3\sigma_\mathrm{det} \approx 600$ atoms which lies within the 99.7% confidence interval of our technical detection noise, see section 3.2.2. The corresponding upper bound for the number of thermal atoms in $m = \pm 1$ is obtained as $N_{\pm 1}^T < \frac{(N - N_\mathrm{c})}{N} \times 3\sigma_\mathrm{det} = 60$.

Hence, we estimate an initial thermal occupation of $\langle N_T \rangle = P N_{\pm 1}^T < 0.016$ for the relevant spin and momentum modes $|\pm k\rangle_{\pm 1}$ that form pairs in our system. This upper bound for thermal fluctuations is orders of magnitude smaller than the expected occupation associated with quantum fluctuations $\langle N_\mathrm{QF} \rangle \approx 1/2$, which is estimated using the truncated Wigner approximation [290], cf. Eq. (6.24). This comparison strongly suggests that the emergent spin and momentum pairs in our BEC primarily result from parametric amplification of vacuum fluctuations.

6.6 Probing momentum-space correlations

Here, we move beyond the studies of individual modes and investigate the correlated nature of the pairs by probing their momentum-space noise correlations. In section 6.6.1, we discuss the evaluation protocol for examining noise correlations in our experiment. In section 6.6.2, we provide extensive experimental observations that showcase the correlated formation of atom pairs in both the single-channel and two-channel configurations.

6.6.1 Extracting momentum-space correlation maps

Since first proposed in Ref. [38], noise correlations have been successfully employed to probe and diagnose many-body physics in cold-atom experiments. Examples range from the observation of bosonic bunching [299] and fermionic antibunching in optical lattices [300], to measurements of out-of-equilibrium dynamics in quenched many-body quantum systems [301, 302]. To evaluate the correlations between atoms in the $m = +1$ and $m = -1$ sublevels, we introduce the *inter-spin noise correlation map*

$$\mathcal{C}^{+1,-1}(k^z_{+1}, k^z_{-1}) = \frac{\langle n_{+1} n_{-1}\rangle - \langle n_{+1}\rangle \langle n_{-1}\rangle}{\sigma(n_{+1})\sigma(n_{-1})} = \frac{\langle \delta(n_{+1})\delta(n_{-1})\rangle}{\sigma(n_{+1})\sigma(n_{-1})}, \tag{6.29}$$

with $n_m \equiv n_m(k^z_m)$ indicating the momentum-space density distribution of spin state m along the relevant z direction. The corresponding momentum-space coordinates are k^z_m. We define $\sigma(n_m) = \langle n^2_m \rangle - \langle n_m \rangle^2$ and $\delta(n_m) = n_m - \langle n_m \rangle$. If the occupations in $m = \pm 1$ fluctuate in an uncorrelated fashion around their respective expectation values, i.e., $\langle \delta(n_{+1})\delta(n_{-1})\rangle = 0$, we expect $\mathcal{C}^{+1,-1}(k^z_{+1}, k^z_{-1}) = 0$. Conversely, correlated density fluctuations at specific momenta (k^z_{+1}, k^z_{-1}) give rise to positive inter-spin correlations $\mathcal{C}^{+1,-1}(k^z_{+1}, k^z_{-1}) > 0$, whereas anticorrelated fluctuations result in $\mathcal{C}^{+1,-1}(k^z_{+1}, k^z_{-1}) < 0$. The normalization factor in Eq. (6.29) ensures that the correlations are bounded to $\mathcal{C}^{+1,-1} \in [-1, 1]$.

To experimentally evaluate the correlation map, we first extract the two-dimensional density distributions $n_m(k_x, k_z)$ in $m =\in \{+1, -1\}$ by imaging after Stern-Gerlach separation, see section 3.2.2. We obtain one-dimensional momentum-space distributions along the relevant z direction

$$n_m(k^z_m) = \sum_{k_x \in R_1} n_m(k_x, k^z_m) + \sum_{k_x \in R_2} n_m(k_\mathrm{x}, k^z_m), \tag{6.30}$$

by integrating the distribution along k_x within two regions of interest $R_1 = [0.8, 1.2]k$ and $R_2 = [-1.2, 0.8]k$. Thereby, we neglect the central unoccupied region $k_x \in (-0.8, 0.8)k$ in $m = \pm 1$, which would otherwise propagate additional spurious technical fringes into the correlation analysis. After calibrating the recoil momentum k in the time-of-flight images, we extract the inter-spin correlation map using Eq. (6.29) and averaging over $S \approx 500$ experimental realizations. For the typical times of flight, $t_\mathrm{TOF} \approx 6\,\mathrm{ms}$, we obtain a momentum-space resolution of $\delta k_z \approx 0.018k$ which is limited by the effective pixel size of our imaging system.

6.6.2 Correlated generation of spin and momentum pairs

We study the correlations in our system both for the single-channel and two-channel configurations. For this purpose, we prepare $N = 7.2(6) \times 10^4$ atoms in $|0\rangle_0$ and quench the coupling to $\chi_+ = -2\pi \times 0.41(1)\,\mathrm{Hz}$ for $t = 62\,\mathrm{\mu s}$ at large two-photon

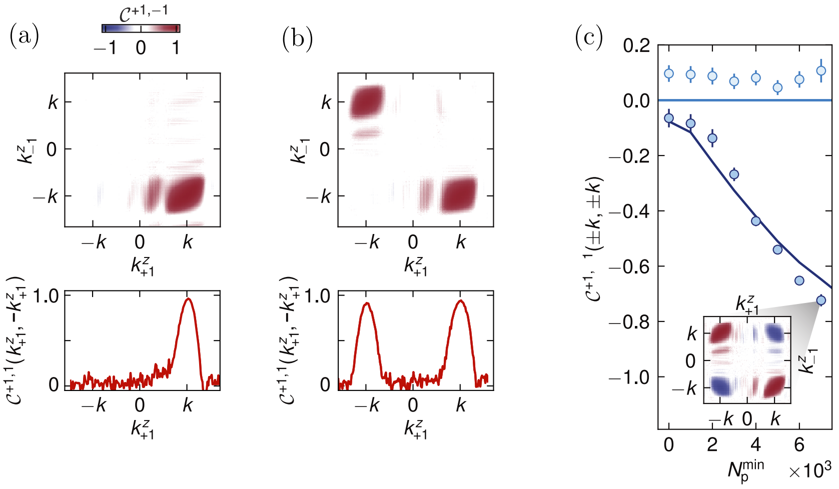

Figure 6.10: Inter-spin correlations. **(a,b)** Momentum-space correlation maps $\mathcal{C}^{+1,-1}(k^z_{+1}, k^z_{-1})$ for the single-channel (a) and two-channel configuration (b), demonstrating the correlated nature of the emergent pairs. The lower panels show one-dimensional cuts along $k^z_{-1} = -k^z_{+1}$, and indcate correlation widths $\sim 0.4k$ (FWHM). **c)** Anticorrelation peaks $\mathcal{C}^{+1,-1}(\pm k, \pm k) = [\mathcal{C}^{+1,-1}(k, k) + \mathcal{C}^{+1,-1}(-k, -k)]/2$ for realizations with $N_\mathrm{p} > N_\mathrm{p}^\mathrm{min}$ for a single-channel (light blue) and two-channel configuration (dark blue). The anticorrelations increase with $N_\mathrm{p}^\mathrm{min}$ due to pump-mode depletion. The inset displays a representative correlation map for $N_\mathrm{p}^\mathrm{min} = 7 \times 10^3$. The solid lines show the results from our truncated Wigner simulations and the error bars are obtained via jackknife resampling [303].

detunings $\delta_+ = -2\pi \times 25.7$ MHz. For the two configurations, the linear Zeeman splittings are set to $\omega_z = -2\pi \times 7.09(1)$ MHz and $\omega_z = -2\pi \times 0.90(1)$ MHz, respectively. The corresponding correlation maps $\mathcal{C}^{+1,-1}(k^z_{+1}, k^z_{-1})$ are shown in Figs. 6.10(a) and (b), and are obtained by averaging over $S = 563$ and $S = 569$ realizations, respectively. In the single-channel configuration, we observe large positive correlations on the order of $\mathcal{C}^{+1,-1}(+k, -k) \approx 0.96$ around $(k^z_{+1}, k^z_{-1}) = (+k, -k)$, demonstrating that pairs occupy the modes $|+k\rangle_{+1}$ and $|-k\rangle_{-1}$ in a correlated fashion, cf. Fig. 6.10(a). When the two channels become active we find comparable positive correlation peaks around $(+k, -k)$ and $(-k, +k)$ [Fig. 6.10(b)], indicating the correlated generation of $m = \pm 1$ pairs via the two discernible channels χ_+ and χ_-.

For both configurations, the correlation maps have an asymmetric structure and exhibit a smaller width along the diagonal $(k^z_{+1}, k^z_{-1}) = (k^z_{+1}, -k^z_{+1})$. This asymmetric behavior is intrinsic to our evaluation, as the two finite-sized clouds are being displaced from each other in opposite directions when modifying their coordinates along this diagonal. In the lower panels of Figs. 6.10(a) and (b), we present the corresponding cuts of the correlation maps $\mathcal{C}^{+1,-1}(k^z_{+1}, -k^z_{+1})$. In both cases, we observe correlation widths around $0.4k$ (FWHM), which are compatible with the observed momentum spread of the corresponding modes $\sim 0.3k$. We attribute the additional side patterns beside the correlation peaks to residual density-dependent imaging artifacts associated with intensity fringes of the imaging beam when passing through the narrow slit of our optical cavity ($l = 176\,\mu\text{m}$), see section 3.2.2.

We re-evaluate the correlation maps after post-selecting the experimental data for realizations above a minimum pair number N_p^min, see Fig. 6.10(c). For the two-channel configuration (dark blue data points), we observe more pronounced anticorrelation peaks around equal momenta $(+k, +k)$ and $(-k, -k)$ when increasing N_p^min; this is also directly shown by the exemplary correlation map in the inset of Fig. 6.10(c). This trend is quantitatively captured by our truncated Wigner simulations (solid line). In contrast, the correlations around equal momenta remain negligible for the single-channel case (light blue data points). We attribute the emergent anticorrelations to the competition between the two channels in the presence of pump-mode depletion, which inhibits large simultaneous occupation of these modes. This trend indicates that the many-body state cannot be merely expressed as a product state of two-mode squeezed vacuum states in the individual channels

$$|\psi\rangle \neq |\text{TMSV}\rangle_+ \otimes |\text{TMSV}\rangle_- \,, \tag{6.31}$$

especially in a regime of large pair occupations.

In future studies, it will be important to carefully characterize the nature of these mode anticorrelations and to examine whether the non-separability of the two channels can give rise to metrologically useful quantum entanglement in our system. Such a task is challenging, as analytically calculating the exact many-body state of the system beyond the undepleted-pump approximation might require to exactly diagonalize the system in a regime of large pair numbers, i.e., $N_\text{p} > N_\text{p}^\text{min} \approx 2000$.

6.7 Discussion and outlook

In this chapter, we have experimentally demonstrated the creation of spin- and momentum-correlated atom pairs via superradiant photon-exchange processes in a degenerate Bose gas. Our scheme primarily amplifies vacuum fluctuations to induce nonlocal spin-mixing dynamics within tens of microseconds. Different from previous implementations [80, 81], our experiments give rise to atom pairs in well-defined spin and momentum modes via two discernible coupling channels. We reported on the first experimental observation of coherent pair oscillations involving momentum modes. Our results are in quantitative agreement with truncated Wigner simulations taking vacuum fluctuations into account. Furthermore, we demonstrated independent control over coherent and dissipative processes, and discerned them via combined measurements of atomic and photonic observables. Crucially, the dynamics remains coherent for long times ($T_\text{coh} \approx 150\,\mu\text{s}$) in comparison to the typical pair generation timescales ($T_\text{int} \approx 35\,\mu\text{s}$). Hence, our system constitutes a very good candidate for applications in atomic interferometry [258]. As both the sign and strength of the photon-mediated interactions can be optically controlled, our experiments offer prospects for implementing time-reversal protocols in SU(1,1) atom interferometers [279, 304]. Additionally, our results showcase a new mechanism that can be potentially employed for fast entanglement generation in spatially separated atomic clouds [305, 306]. In particular, combining two-channel pair production with mode-selective spin rotations offers a promising route for performing Bell tests with massive particles [307, 308]. Finally, inducing pair production through multiple transverse laser drives offers a pathway to extend the experiments presented in chapter 5 to a unitary regime. This approach could facilitate the observation of cavity-assisted correlated tunneling in extended momentum-space lattices.

6.7.1 Towards the detection of quantum correlations

The pair mechanism in our experiments closely resembles the production of entangled pairs of signal and idler photons in optical parametric amplifiers [24]. However, our observations in section 6.6 do not discern if the observed pair correlations are of classical or quantum-mechanical origin. To establish the presence of genuine quantum correlations in our system, it is essential to identify suitable criteria and examine their experimental feasibility. This endeavor is associated with additional technical challenges that need to be addressed in future experiments.

A straightforward approach could be to examine *relative number squeezing*, as also studied in experiments employing spin-changing collisions to generate correlated pairs of $m = \pm 1$ atoms in single-mode BECs [275, 309]. For a single-channel configuration, we can define the corresponding spin squeezing parameter [310] as

$$\zeta_{\mathrm{s}}^2 = \frac{\sigma^2(\hat{J}_z)}{\sigma^2(\hat{J}_z)|_{\mathrm{coh}}} = \frac{2\sigma^2(\hat{J}_z)}{\langle N_{\mathrm{p}} \rangle} \implies \mathcal{G} = \frac{1}{\zeta_{\mathrm{s}}^2} = \frac{\langle N_{\mathrm{p}} \rangle}{2\sigma^2(\hat{J}_z)}, \tag{6.32}$$

with the population imbalance defined as $\hat{J}_z = (\hat{N}_{+1} - \hat{N}_{-1})/2$, and the operators $\hat{N}_{+1}$ and $\hat{N}_{-1}$ counting the atoms in the two correlated modes $|+k\rangle_{+1}$ and $|-k\rangle_{-1}$, respectively. An uncorrelated coherent spin state is associated with the variance $\sigma^2(\hat{J}_z)|_{\mathrm{coh}} = \langle \hat{N}_{+1} + \hat{N}_{-1} \rangle /4 = \langle N_{\mathrm{p}} \rangle /2$, with $\langle N_{\mathrm{p}} \rangle$ being the total number of atom pairs. Conversely, squeezing is signaled by the relative number fluctuations $\sigma^2(\hat{J}_z)$ becoming smaller than the value for a coherent state, i.e., $\zeta_{\mathrm{s}}^2 < 1$. Equivalently, we define the metrological gain as $\mathcal{G} = 1/\zeta_{\mathrm{s}}^2$ in Eq. (6.32), which diagnoses relative number squeezing for $\mathcal{G} > 1$.

An alternative criterion involves examining the *violation of the Cauchy-Schwarz inequality.* This approach has been pioneered by Clauser to demonstrate entanglement in two-photon cascades [311], and has been recently employed to probe quantum-correlated atom pairs arising from binary collisions in metastable Helium BECs [270, 312]. For a single-channel configuration, the Cauchy-Schwarz ratio is defined as

$$\mathcal{C} = \frac{\langle : \hat{N}_{+1} \hat{N}_{1} : \rangle}{\sqrt{\langle : \hat{N}_{+1}^2 : \rangle \, \langle : \hat{N}_{-1}^2 : \rangle}}, \tag{6.33}$$

with $\langle : \, : \rangle$ denoting the quantum-mechanical expectation value after normal ordering. The Cauchy-Schwarz ratio quantifies the relation between average inter- and average intra-spin correlations in our system. For classically correlated systems we expect $\mathcal{C} \leq 1$ as a direct consequence of the mathematical Cauchy-Schwarz inequality. In contrast, values of $\mathcal{C} > 1$ indicate the presence of quantum correlations [313]. As discussed in Ref. [314], this criterion only entails genuine quantum entanglement in the sense of non-separability the underlying many-body state, if the system is composed by indistinguishable particles. This is indeed the case for our system, which consists of a spinor Bose-Einstein condensate initialized in a single well-defined mode $|0\rangle_0$.

We assess the viability of these two criteria using our truncated Wigner simulations. For the single-channel configuration, we numerically simulate the pair dynamics using typical experimental parameters $N = 50000$, $\omega_z = -2\pi \times 7.09\,\mathrm{MHz}$, $\delta_+ = -2\pi \times 25\,\mathrm{MHz}$. In Fig. 6.11(a), we observe an exponential increase of the mean pair number $\langle N_\mathrm{p} \rangle$ (purple curve) for $t \approx 50\,\mathrm{\mu s}$, which later saturates due to pump-mode depletion. Concurrently, the average imbalance $\langle N_\mathrm{imb} \rangle = \langle \hat{N}_{+1} - \hat{N}_{-1} \rangle$ also increases, indicating spurious superradiant Raman scattering. Our simulations indicate that on average $\chi_+/\gamma_+ = \delta_+/(2\kappa) \approx 10$ pairs are created before the first photon is lost from the cavity around $t \approx 25\,\mathrm{\mu s}$ ($\langle N_\mathrm{imb} \rangle \approx 1$).

In Fig. 6.11(b), we plot the metrological gain $\mathcal{G}$ as a function of the average number of pairs $\langle N_\mathrm{p} \rangle$. For small pair numbers, we observe a rapid increase of quantum correlations peaking at $\mathcal{G} \approx 10$ around $\langle N_\mathrm{p} \rangle \approx 10$, i.e., at the average time when the first photon is lost from the cavity. For larger pair numbers and evolution times, we observe a monotonic decrease of $\mathcal{G}$, reaching classical values $\mathcal{G} < 1$ for $\langle N_\mathrm{p} \rangle \gtrsim 100$. We attribute this decay to parasitic photon loss, as shown by the growing imbalance $\langle N_\mathrm{imb} \rangle$ in this regime. In Fig. 6.11(c), we evaluate the Cauchy-Schwarz ratio $\mathcal{C}$ as function of $\langle N_\mathrm{p} \rangle$ using our numerical simulations (solid curve) and an analytic estimate for a two-mode squeezed vacuum (TMSV) state (dashed curve). At small pair numbers $\langle N_\mathrm{p} \rangle \approx 100$, we observe a clear violation of the Cauchy-Schwarz inequality with $\mathcal{C} \approx 1.005$. The monotonic reduction of $\mathcal{C}$ for intermediate pair numbers ($\langle N_\mathrm{p} \rangle \lesssim 1000$) is primarily caused by a $1/N_\mathrm{p}$ scaling of quantum correlations [314]. Indeed, we observe $\mathcal{C}_\mathrm{TMSV} \approx 1 + 0.5/\langle N_\mathrm{p} \rangle$ for a TMSV state indicating asymptotically classical correlations $\mathcal{C}_\mathrm{TMSV} \to 1$ for $\langle N_\mathrm{p} \rangle \to \infty$. At large pair numbers ($\langle N_\mathrm{p} \rangle \gtrsim 1500$), our numerical simulations show $\mathcal{C} < 1$ signaling the onset of classical correlations. This is attributed to photon loss in our system, as the Cauchy-Schwarz ratio for a TMSV state remains always $\mathcal{C}_\mathrm{TMSV} > 1$.

Establishing quantum correlations in our experiment using these two criteria presents considerable challenges, mainly associated with the technical limitations in the atom number detection. As shown in Fig. 6.11, we can obtain a large metrological gain $\mathcal{G} \approx 10$ and a measurable 2%-violation of the Cauchy-Schwarz inequality $\mathcal{C} > 1.01$ only for small $\langle N_\mathrm{p} \rangle < 50$. However, such small pair numbers currently lie below the imaging detection noise that is around $\sigma_\mathrm{det} \approx 200$ atoms, see section 3.2.2. To address this limitation, we are currently upgrading the absorption imaging setup to improve the detection sensitivity by at least an order of magnitude. This would involve replacing the current CCD camera, which has a limiting quantum efficiency of around 0.25 [138]. A complementary approach could involve increasing the available drive laser power to induce pair production at even larger two-photon detunings, further suppressing competing superradiant scattering. On a theoretical level, it is crucial to continue searching for suitable entanglement witnesses for our experiment.

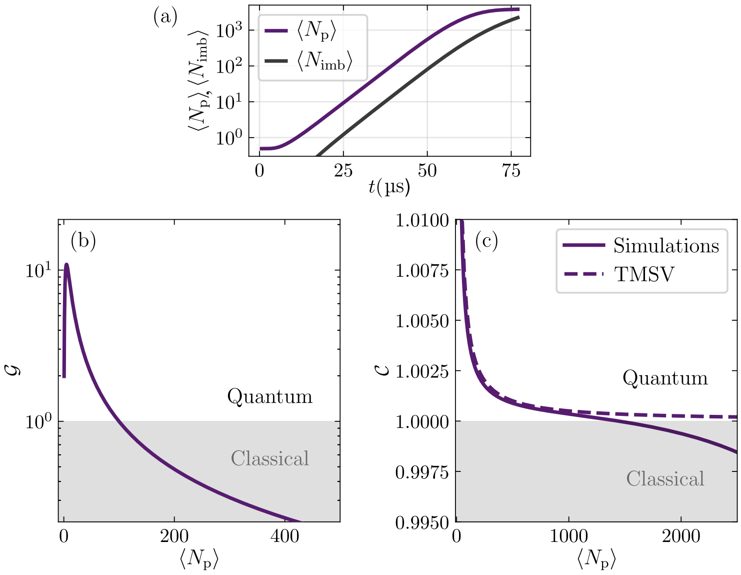

Figure 6.11: Towards the detection of quantum correlations. **(a)** Evolution of the average pair number $\langle N_\mathrm{p}\rangle$ and mode imbalance $\langle N_\mathrm{imb}\rangle$ obtained from our truncated Wigner simulations for a single-channel configuration. **(b)** Simulated metrological gain $\mathcal{G}$ associated with relative number squeezing of the pair constituents. For $\langle N_\mathrm{p}\rangle \ll 100$, we expect quantum correlations as signaled by $\mathcal{G} > 1$. **(c)** Cauchy-Schwarz ratio $\mathcal{C}$ obtained from simulations (solid) and analytic estimations for a TMSV state (dashed line). It shows a $1/\langle N_\mathrm{p}\rangle$-decay of quantum correlations ($\mathcal{C} > 1$) with increasing $\langle N_\mathrm{p}\rangle$. For large pair numbers, both criteria indicate a crossover to a classical regime $\mathcal{G} < 1$ and $\mathcal{C} < 1$, which is attributed to spurious photon losses.

7 Antiferromagnetic phases in a Bose-Hubbard model with cavity-mediated interactions

Experiments with ultracold atoms in optical lattices have greatly extended the scope of quantum simulation of many-body systems [39]. Two key strengths are the high degree of tunability of the different energy scales, and the possibility to address and probe the atoms' motional and spin degrees of freedom. This has enabled experimental access to strongly correlated phenomena, such as quantum magnetism and complex out-of-equilibrium dynamics [21]. While contact interactions naturally occur in ultracold atomic samples [315], long-range interactions are more elusive. Nonetheless, systems that are traditionally used to engineer long-range interactions, such as dipolar quantum gases, heteronuclear molecules, and Rydberg atoms, suffer from small long-range interaction strengths, low densities, and short lifetimes, respectively [51–56].

Quantum gases coupled to optical cavities provide an alternative experimental platform to create photon-mediated global-range interactions between the atoms, whose strength and sign are controlled by tailored driving fields [57, 58]. They have enabled theoretical [316–324] and experimental [65–67] investigations of lattice supersolid and charge density wave phases in single-component spin systems. The atomic ground-state phases and excitation spectrum can be accessed non-destructively in real time by the light leaking from the cavity [67]. Recently, it has become experimentally feasible to include the internal atomic spin degree of freedom in such systems, which has resulted in the observation of spin-dependent [78] and spin-changing self-organization [79, 89]. In combination with optical lattices, this approach can pave the way for realizing strongly correlated magnetic phases with photon-mediated interactions.

In this chapter, we propose and theoretically investigate an extended two-component Bose-Hubbard model with cavity-mediated global-range interactions – the lattice counterpart of the experiments performed in Ref. [78] with a bulk Bose gas. In Fig. 7.1(a), we illustrate the key ideas behind our approach to engineer cavity-mediated interactions that have a 'density' and a 'spin' contribution. We consider a balanced spin mixture comprising the spin states $|\uparrow\rangle$ and $|\downarrow\rangle$, which is confined in a deep two-dimensional $\lambda_\mathrm{d}/2$-periodic optical lattice to form a Mott insulator. The atoms are coupled to a high-finesse optical cavity and illuminated by a transverse drive (TD) propagating in z direction, with a tunable polarization angle ϕ in the xy plane.

Deep in the dispersive regime, the drive can scatter photons into the y-polarized cavity mode (operator $\hat{a}_y$) and mediate two distinct types of global-range interactions

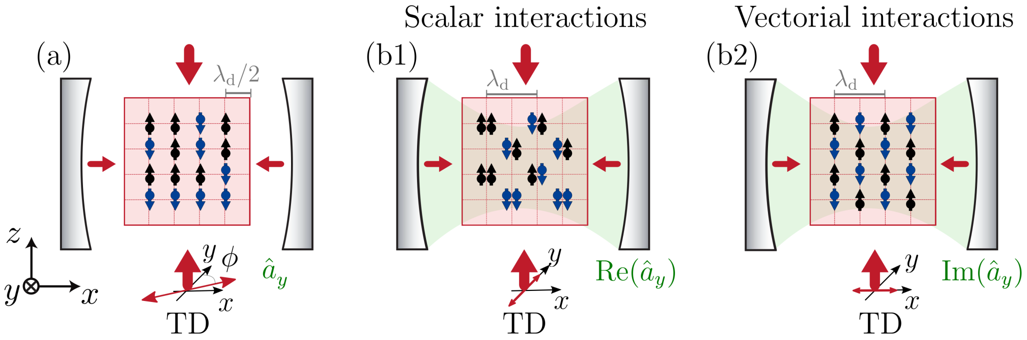

Figure 7.1: A Bose-Hubbard model with cavity-mediated density and spin interactions. **(a)** A two-component Mott insulator (spin states $|\uparrow\rangle$ and $|\downarrow\rangle$) is confined by a deep $\lambda_\mathrm{d}/2$-periodic optical lattice inside a high-finesse optical cavity. The atoms can scatter photons from a transverse drive (TD) field with a tunable polarization angle ϕ into the y-polarized cavity mode ($\hat{a}_y$). **(b)** Cavity-mediated global-range interactions. (b1) Scalar light-matter interactions dominate for TD polarizations aligned close to the y axis, coupling atoms to the real quadrature of the cavity mode [Re($\hat{a}_y$)]. The interference potential between the TD and cavity fields induces a dynamical λ_d-periodic checkerboard modulation, which can overcome the repulsive contact interactions and induce density-modulated states. (b2) Vectorial light-matter interactions dominate for nearly x-polarized TD fields, coupling the atoms to the imaginary quadrature of the cavity mode [Im($\hat{a}_y$)]. This gives rise to $\lambda_\mathrm{d}/2$-shifted interference potentials for the two spin states $|\uparrow\rangle$ and $|\downarrow\rangle$, facilitating the formation of λ_d-periodic antiferromagnetic phases.

between the atoms:

- When the drive polarization is aligned close to the y axis ($\phi = 0$), scalar light-matter interactions dominate and couple the atomic density to the real quadrature of the cavity field [Re($\hat{a}_y$)]. The interference potential between the TD and cavity fields induces a common λ_d-periodic checkerboard modulation for the atoms, independently of their spin degree of freedom. In the insulating regime, this favors the formation density-modulated charge density waves, as schematically depicted in Fig. 7.1(b1).

- For a polarization angle close to the x axis ($\phi = \pi/2$), vectorial atom-light interactions become dominant and couple the atomic spin to the imaginary quadrature of the cavity field [Im($\hat{a}_y$)]. The dynamic interference potential gives rise to $\lambda_\mathrm{d}/2$-shifted checkerboard modulations for the atoms in the two spin states $|\uparrow\rangle$ and $|\downarrow\rangle$, which preferably occupy lattice sites of opposite parity, favoring a global antiferromagnetic ordering in the system. This effect is illustrated in Fig. 7.1(b2).

The interplay of these two adjustable global-range interaction scales with tunneling and contact interactions in the optical lattice gives rise to a rich phase diagram. Using a mean-field Gutzwiller approach at unity filling, we calculate the phase diagram of the system and identify density-modulated and magnetically ordered phases, both in the superfluid and insulating regimes of the Hubbard model. Notably, the interplay between short- and vectorial global-range interactions induces the formation of an antiferromagnetic Mott insulator at arbitrarily small coupling strengths. To further elucidate the nature of this magnetically ordered phase, we construct an effective perturbative Hamiltonian for its low-energy excitations, and identify a spin-exchange branch with a tunable energy gap. Finally, we provide a detailed route for the experimental implementation of this model in our experiment. We discuss how to control the different energy scales via experimental parameters, and address suitable observables and open technical challenges. While some magnetically ordered phases have been discussed in bosonic [325, 326] and fermionic systems [327, 328], our comprehensive theoretical study of the different phases and excitations in an experimentally accessible regime constitutes an important stepping stone for their successful experimental realization.

Outline of this chapter

In this chapter, we discuss a feasible proposal to engineer extended Bose-Hubbard models with cavity-mediated global-range interactions, addressing both the atoms' density and spin degrees of freedom. In section 7.1, we present the relevant experimental scheme and map our system to an extended two-component Hubbard model. In section 7.2, we calculate the mean-field phase diagram using a Gutzwiller ansatz at unity filling. Furthermore, in section 7.3, we study the low-lying excitations above this phase and discover a spin-exchange branch featuring a tunable energy gap. We discuss a route towards experimental implementation in section 7.4, highlighting the control over the system's parameters, the different experimental observables, and the technical challenges. Finally, in section 7.5, we summarize our findings and discuss future directions.

This work originated from the master thesis project of Leon Carl [329], which was jointly supervised by Tena Dubcek, Rodrigo Rosa-Medina, Tilman Esslinger, and Sebastian D. Huber. Parts of this chapter have been published in Ref. [92]

> L. Carl, R. Rosa-Medina, S. D. Huber, T. Esslinger, N. Dogra*, T. Dubcek*.
> *Phases, instabilities and excitations in a two-component lattice model with photon-mediated interactions.* Physical Review Research **5**, L032003 (2023).
> * These authors contributed equally to this work

7.1 Coupling scheme and mapping to an extended Hubbard model

Here, we discuss the theoretical framework to map our experimental system to an extended Bose-Hubbard model. In section 7.1.1, we present the relevant coupling scheme and derive the associated single-particle Hamiltonian. When eliminating the cavity field, the system can be mapped to an extended Bose-Hubbard model featuring tunable density- and spin-dependent global-range interactions, as discussed in section 7.1.2. A detailed derivation can be also found in the master thesis of Leon Carl in Ref. [329].

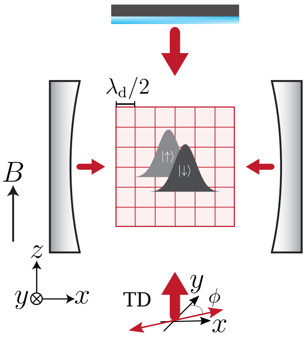

Figure 7.2: Coupling scheme. A two-component BEC comprising the spin states $|\uparrow\rangle$ and $|\downarrow\rangle$ is confined by a two-dimensional optical lattice in the xz plane, with lattice spacing $\lambda_\mathrm{d}/2$; a bias magnetic field B along the z direction defines the quantization axis. The atoms are coupled to a high-finesse optical cavity and illuminated by a standing-wave transverse drive (TD) field with a tunable polarization angle ϕ in the xy plane. The TD propagates in the z direction and scatters photons into the the y-polarized cavity mode, mediating global-range interactions between the atoms.

7.1.1 Coupling scheme

We consider a balanced spin mixture of two Bose-Einstein condensates (BECs) coupled to the fundamental mode of our high-finesse optical cavity. The two spin components $|\uparrow\rangle = |F=1, m=1\rangle$ and $|\downarrow\rangle = |F=1, m=-1\rangle$ belong to the $F=1$ hyperfine ground-state manifold of ^{87}Rb, with the quantization axis defined by a magnetic field B in the z-direction. The mixture is loaded into a two-dimensional $\lambda_\mathrm{d}/2$-periodic square optical lattice extending in the xz plane, as schematically depicted in Fig. 7.2.

The lattice arm along the z-direction has a tunable linear polarization in the xy-plane, which is controlled by the angle ϕ, cf. Fig. 7.2. As in the experiments discussed in the previous chapters, it also fulfills a dual role as a transverse drive (TD) field. The negative part of the total electric field is given by

$$\hat{\mathbf{E}}^{(-)} = E_\mathrm{d}\cos(kz)\left[\cos(\phi)\mathbf{e}_y + \sin(\phi)\mathbf{e}_x\right]e^{-i\omega_\mathrm{d}} + E_0\cos(kx)\mathbf{e}_y\hat{a}_y. \tag{7.1}$$

The first contribution describes the standing-wave TD field with amplitude E_d, frequency ω_d and spatial profile $f(z) = \cos(kz)$; the second term describes a y-polarized cavity field (annihilation operator $\hat{a}_y$), with vacuum field strength E_0 and spatial mode profile $g(x) = \cos(kx)$. Due to their small frequency difference, we assume a common wavenumber $k = 2\pi/\lambda_\mathrm{d}$ for both fields. For sufficiently large Zeeman splitting, we can neglect spin-changing processes due to cavity-assisted Raman transitions and thereby the involvement of the z-polarized cavity mode in Eq. (7.1).

We consider a transverse drive with wavelength $\lambda_\mathrm{d} = 784.7\,\mathrm{nm}$, in order to induce concurring scalar and vectorial light-matter interactions in the dispersive regime, cf. Tab. 2.1. At this wavelength, the ratio between the corresponding polarizabilities is $\xi = \frac{\alpha_v}{2\alpha_s} = -0.464$. Closely following Eq. (2.12), we derive the single-particle Hamiltonian of the system in a rotating frame at the frequency of the transverse drive ω_d

$$\hat{H}_\mathrm{sp} = \hat{H}_\mathrm{at} + \hat{H}_\mathrm{cav} + \hat{H}_\mathrm{LM}. \tag{7.2}$$

The atomic and cavity Hamiltonian are given by

$$\begin{aligned}\hat{H}_\mathrm{at} &= \frac{\hat{\mathbf{p}}^2}{2M} + \hat{V}_\mathrm{lat}(x,z) = \frac{\hat{\mathbf{p}}^2}{2M} - V_\mathrm{2D}\left[\cos^2\left(\frac{2\pi}{\lambda_\mathrm{d}}x\right) + \cos^2\left(\frac{2\pi}{\lambda_\mathrm{d}}z\right)\right] \\ \hat{H}_\mathrm{cav} &= -\hbar\left[\Delta_c - U_0\cos^2\left(\frac{2\pi}{\lambda}x\right)\right]\hat{a}_y^\dagger\hat{a}_y.\end{aligned} \tag{7.3}$$

The bare atomic Hamiltonian, $\hat{H}_\mathrm{at}$, describes ^{87}Rb atom with mass M and momentum $\hat{\mathbf{p}} = (\hat{p}_x + \hat{p}_z)$ moving in the 2D square attractive lattice potential with depth $V_\mathrm{2D} > 0$. The bare energy of the cavity field, $\hat{H}_\mathrm{cav}$, is determined by the drive-cavity detuning $\Delta_c = \omega_\mathrm{d} - \omega_c < 0$, with ω_c being the cavity resonance frequency. Additionally, the presence of an atom dispersively shifts the cavity resonance [108], where $U_0 = -2\pi \times 56\,\mathrm{Hz}$ is the maximal dispersive shift at λ_d.

The light-matter interactions comprise scalar and vectorial contributions

$$\begin{aligned}\hat{H}_\mathrm{LM} &= \alpha_s\hat{\mathbf{E}}^{(+)}\cdot\hat{\mathbf{E}}^{(-)} - i\frac{\alpha_v}{2F}\left(\hat{\mathbf{E}}^{(+)}\times\hat{\mathbf{E}}^{(-)}\right)\cdot\hat{\mathbf{F}} \\ &= \hbar\eta_s\cos\left(\frac{2\pi}{\lambda_\mathrm{d}}x\right)\cos\left(\frac{2\pi}{\lambda_\mathrm{d}}z\right)\hat{X} + \hbar\eta_v\cos\left(\frac{2\pi}{\lambda_\mathrm{d}}x\right)\cos\left(\frac{2\pi}{\lambda_\mathrm{d}}z\right)\hat{P}\hat{F}_z.\end{aligned} \tag{7.4}$$

The scalar component couples the atomic motional degrees of freedom to the real quadrature of the cavity field, $\hat{X} = \left(\hat{a}_y + \hat{a}_y^\dagger\right)/\sqrt{2}$. This gives rise to a dynamical λ_d-periodic density modulation, which is independent of the atomic spin degree of freedom. Concurrently, the vectorial component is mediated by the imaginary quadrature of the cavity field, $\hat{P} = i\left(\hat{a}_y^\dagger - \hat{a}_y\right)/\sqrt{2}$, and gives rise to phase-shifted λ_d-periodic modulations for atoms in the two spin states. This is due to $\hat{F}_z\left|\uparrow\right\rangle = +\left|\uparrow\right\rangle$ and $\hat{F}_z\left|\downarrow\right\rangle = -\left|\downarrow\right\rangle$, with $\hat{F}_z$ being the z-component of the $F=1$ atomic spin operator $\hat{\mathbf{F}}$. The associated coupling strengths are $\eta_s = \eta\cos(\phi)$ and $\eta_v = \eta\xi\sin(\phi)$, respectively, with the two-photon scattering rate defined as $\eta = \sqrt{2}\alpha_s E_0 E_p/\hbar = \mathrm{sgn}(\alpha_s)\sqrt{2|U_0 V_\mathrm{2D}|}$.

Importantly, both the two-photon coupling rate η and the relative contributions of vectorial and scalar processes, $\eta_v/\eta_s = \xi\tan(\phi)$, can be independently adjusted by means of the TD lattice depth V_2D and the polarization angle ϕ, respectively. As illustrated in Fig. 7.1(b), a y-polarized ($\phi = 0$) TD field exclusively induces scalar light-matter coupling ($\eta_v = 0$), while in the limit of an x-polarized drive ($\phi = \pi/2$), only vectorial light-matter interactions prevail ($\eta_s = 0$).

7.1.2 Mapping to an extended Bose-Hubbard Hamiltonian

We derive the many-body Hamiltonian for two-component Bose-Einstein condensate. From Eq. (7.2), we obtain the many-body Hamiltonian in second quantization

$$\begin{aligned}\hat{H}_{\mathrm{MB}} = &\int \hat{\Psi}^{\dagger}\left(\frac{\hat{\mathbf{p}}^2}{2m}+\hat{V}_{\mathrm{lat}}(x,z)\right)\hat{\Psi}\,dxdz-\sum_{m\in\{\uparrow,\downarrow\}}\mu_m\int\hat{\Psi}_m^{\dagger}\hat{\Psi}_m\,dxdz\\ &+\frac{1}{2}\sum_{m\in\uparrow,\downarrow}g_{2\mathrm{D},m}\int\Psi_m^{\dagger}\Psi_m^{\dagger}\Psi_m\Psi_m\,dxdz+g_{2\mathrm{D},\uparrow\downarrow}\int\Psi_{\uparrow}^{\dagger}\Psi_{\downarrow}^{\dagger}\Psi_{\uparrow}\Psi_{\downarrow}\,dxdz\\ &+\int\hat{\Psi}^{\dagger}\cos(kx)\cos(kz)\left(\eta_s\hat{X}+\eta_v\hat{P}\hat{F}_z\right)\hat{\Psi}\,dxdz\\ &-\int\hat{\Psi}^{\dagger}U_0\cos(kx)^2\hat{a}^{\dagger}\hat{a}\hat{\Psi}\,dxdz-\Delta_c\hat{a}^{\dagger}\hat{a},\end{aligned} \tag{7.5}$$

where $\hat{\Psi}(x,z)=[\hat{\Psi}_{\uparrow}(x,z),\hat{\Psi}_{\downarrow}(x,z)]^T$ is the bosonic field operator associated with the spin mixture. For each spin state $m\in\{|\uparrow\rangle,|\downarrow\rangle\}$, we introduce the associated chemical potential $\mu_{\uparrow(\downarrow)}$. The terms in the second line account for on-site contact interactions. Closely following the experiments discussed in Ref. [65], we consider an additional $\lambda_y/2=670\,\mathrm{nm}/2$ periodic deep optical lattice propagating in the y-direction. This lattice confines the dynamics to the xz plane, effectively modifying the strengths of contact interaction. This is accounted by integrating over the corresponding localized Wannier function $w_0^{(y)}(y)$, see Ref. [319]. The contact interaction strengths in Eq. (7.5) are given by $g_{2\mathrm{D},m}=\frac{4\pi a_m}{M}\int|w_0^{(y)}(y)|^4\,dy$ and $g_{2\mathrm{D},\uparrow\downarrow}=\frac{2\pi a_{\uparrow\downarrow}}{M}\int|w_0^{(y)}(y)|^4\,dy$ for intra- and inter-spin species collisions, respectively. Here, a_m and $a_{\uparrow\downarrow}$ denote the corresponding s-wave scattering lengths.

For sufficiently deep lattice potentials [330], we can expand the many-body function in a localized basis consisting of Wannier functions the lowest energy band

$$\hat{\Psi}_m(x,z)=\sum_{\mathbf{i}}w_{\mathbf{i}}(x,z)\hat{b}_{\mathbf{i},m}, \tag{7.6}$$

with $w_{\mathbf{i}}(x,z)$ and $\hat{b}_{\mathbf{i},m}$ representing the Wannier function localized at site $\mathbf{i}=(i_x,i_z)$ and the corresponding bosonic annihilation operator for the spin state m. Considering only nearest-neighbor tunneling, we derive the following lattice Hamiltonian

$$\begin{aligned}\hat{H}_{\mathrm{MB}}=&-\hbar t\sum_{m\in\{\uparrow,\downarrow\},\langle\mathbf{i},\mathbf{j}\rangle}(\hat{b}_{\mathbf{i},m}^{\dagger}\hat{b}_{\mathbf{j},m}+\hat{b}_{\mathbf{j},m}^{\dagger}\hat{b}_{\mathbf{i},m})+\sum_{m\in\{\uparrow,\downarrow\},\mathbf{i}}\frac{\hbar U_m}{2}\hat{n}_{\mathbf{i},m}(\hat{n}_{\mathbf{i},m}-1)+\hbar U_{12}\sum_{\mathbf{i}}\hat{n}_{\mathbf{i},\uparrow}\hat{n}_{\mathbf{i},\downarrow}\\ &-\sum_{m\in\{\uparrow,\downarrow\},\mathbf{i}}\mu_m\hat{n}_{\mathbf{i},m}-\hbar\tilde{\Delta}_c\hat{a}_y^{\dagger}\hat{a}_y+\hbar\eta_s M_0\hat{\Theta}_D\hat{X}+\hbar\eta_v M_0\hat{\Theta}_S\hat{P},\end{aligned} \tag{7.7}$$

where $\langle\mathbf{i},\mathbf{j}\rangle$ denotes a pair of neighbouring sites. The corresponding tunneling rate

$$\hbar t=\int w_{\mathbf{i}}(x,z)\left(-\frac{1}{2m}\left(\frac{\partial^2}{\partial_x^2}+\frac{\partial^2}{\partial_y^2}\right)+V_{\mathrm{lat}}(x,z)\right)w_{\mathbf{j}}(x,z)\,dxdz \tag{7.8}$$

is independent of the spin and tunneling direction, as the underlying square lattice $\hat{V}_{\text{lat}}(x,z)$ is spin-insensitive and symmetric along x and z. The intra- and inter-spin contact interactions are given by

$$\begin{aligned} \hbar U_m &= g_{2\text{D},m} \int |w_0(x,z)|^4 \, dxdz, \\ \hbar U_{12} &= g_{2\text{D},\uparrow\downarrow} \int |w_0(x,z)|^4 \, dxdz, \end{aligned} \tag{7.9}$$

respectively. The scalar and vectorial components of light-matter interactions couple to the operators

$$\begin{aligned} \hat{\Theta}_D &= \sum_{\mathbf{i}} (-1)^{|\mathbf{i}|} \left(\hat{n}_{\mathbf{i},\uparrow} + \hat{n}_{\mathbf{i},\downarrow}\right), \\ \hat{\Theta}_S &= \sum_{\mathbf{i}} (-1)^{|\mathbf{i}|} \left(\hat{n}_{\mathbf{i},\uparrow} - \hat{n}_{\mathbf{i},\downarrow}\right), \end{aligned} \tag{7.10}$$

respectively. Finally, the presence of N atoms in the cavity yields a collective dispersive shift $\tilde{\Delta}_c = (\Delta_c - U_0 M_1 N)$ of the cavity resonance. The corresponding overlap integrals are defined as

$$\begin{aligned} M_0 &= \int w_{\mathbf{0}}(x,z)\cos(kx)\cos(kz) w_{\mathbf{0}}(x,z) \, dxdz, \\ M_1 &= \int w_{\mathbf{0}}(x,z)\cos(kx)^2 w_{\mathbf{0}}(x,z) \, dxdz. \end{aligned} \tag{7.11}$$

Extended Bose-Hubbard model

To obtain an atom-only description, we adiabatically eliminate the cavity field [122]. This is valid for the typical parameters of our experiment, as the cavity losses $\kappa = 2\pi \times 1.25\,\text{MHz}$ and detuning $\left|\tilde{\Delta}_c\right| \gtrsim 2\pi \times 5\,\text{MHz}$ significantly exceed the atomic energy scales (t, U_m, U_{12}), which are all on the order of $\lesssim 2\pi \times 5\,\text{kHz}$ [108]. We set the corresponding Heisenberg equation of motion to zero and obtain

$$\begin{aligned} \frac{d}{dt}\hat{a}_y &= i\tilde{\Delta}_c \hat{a}_y - i\frac{M_0}{\sqrt{2}}\left(\eta_s \hat{\Theta}_D + i\eta_v \hat{\Theta}_S\right) - \kappa \hat{a}_y \overset{!}{=} 0 \\ \Rightarrow \hat{a}_y &= \frac{M_0}{\sqrt{2}} \frac{1}{\tilde{\Delta}_c + i\kappa}\left(\eta_s \hat{\Theta}_D + i\eta_v \hat{\Theta}_S\right). \end{aligned} \tag{7.12}$$

By inserting this expression into the many-body Hamiltonian in Eq. (7.7), we obtain an effective *extended Bose-Hubbard model*

$$\begin{aligned} \hat{H} &= \hat{H}_{\text{BH}} + \hat{H}_{\text{LM}}, \quad \text{with} \\ \hat{H}_{\text{BH}} &= -\hbar t \sum_{m,<\mathbf{i},\mathbf{j}>} (\hat{b}^\dagger_{\mathbf{i},m}\hat{b}_{\mathbf{j},m} + \text{h.c.}) + \frac{\hbar U}{2}\sum_{\mathbf{i},m} \hat{n}_{\mathbf{i},m}\left(\hat{n}_{\mathbf{i},m} - 1\right) + \hbar U_{12}\sum_{\mathbf{i}} \hat{n}_{\mathbf{i},\uparrow}\hat{n}_{\mathbf{i},\downarrow}, \\ \hat{H}_{\text{LM}} &= -\hbar\frac{U_s}{K}\hat{\Theta}_D^2 - \hbar\frac{U_v}{K}\hat{\Theta}_S^2. \end{aligned} \tag{7.13}$$

The first term, $\hat{H}_{\mathrm{BH}}$, describes a two-component Bose-Hubbard model with tunneling rate $t > 0$ and repulsive intra- and inter-spin contact interactions, $U > 0$ and $U_{12} > 0$. We assume the former to be identical for $|\uparrow\rangle$ and $|\downarrow\rangle$, as is the case for ^{87}Rb in the $F = 1$ manifold. As we will operate at fixed unity filling, we set the chemical potential to $\mu_\uparrow = \mu_\downarrow = 0$.

The second term, $\hat{H}_{\mathrm{LM}}$, consists of spin-independent ('scalar') and spin-dependent ('vectorial') global-range interactions that are mediated by the intra-cavity field. The former are associated with the operator $\hat{\Theta}_D^2$; its expectation value is maximized if the atoms arrange in spin-independent density modulation with all atoms occupying either even or odd lattice sites, cf. Eq. (7.10). The latter are associated with the operator $\hat{\Theta}_S^2$ [cf Eq. (7.10)]; its expectation value is in turn maximized for a global antiferromagnetic ordering, with all atoms in $|\uparrow\rangle$ occupying even sites and all atoms in $|\downarrow\rangle$ occupying odd sites, or vice-versa. The corresponding interaction strengths $U_s = U_L \cos^2(\phi)$ and $U_v = U_L \xi^2 \sin^2(\phi)$ can be tuned with respect to each other via the TD polarization angle ϕ. The overall interaction strength of global-range interactions is given by

$$\frac{U_L}{K} = -\frac{M_0^2 \tilde{\Delta}_c}{\kappa^2 + \tilde{\Delta}_c^2} \eta^2, \tag{7.14}$$

for a system comprising K lattice sites, and can be experimentally controlled by adjusting the effective cavity detuning $\tilde{\Delta}_c$.

The extended Bose-Hubbard Hamiltonian in Eq. (7.13) possess several symmetries. First, it is invariant under a global spin-flip $\hat{b}_{\mathbf{i},\uparrow} \to \hat{b}_{\mathbf{i},\downarrow}$, and two global continuous phase transformations, $\hat{b}_{\mathbf{i},m} \to e^{i\phi_m} \hat{b}_{\mathbf{i},m}$ for each spin state $m \in \{\uparrow, \downarrow\}$. Furthermore, the scalar and vectorial global-range interactions introduce an additional $\mathbb{Z}_2$-symmetry associated to the two sublattices defined by even and odd sites. Henceforth, the Hamiltonian has a $\mathcal{U}(1) \times \mathcal{U}(1) \times \mathbb{Z}_2 \times \mathbb{Z}_2$-symmetry.

7.2 Ground state phase diagram

We discuss the mean-field phase diagram of the extended Bose-Hubbard model derived in Eq. (7.13). In section 7.2.1, we introduce a Gutzwiller mean-field ansatz and define the corresponding order parameters of the system. The phase diagrams are calculated in section 7.2.2 for the relevant case of unity filling. Remarkably, we observe an emergent antiferromagnetic Mott insulator for arbitrarily small photon-mediated interactions, which arises due to their cooperation with repulsive contact interactions. The corresponding calculations were carried out by Nishant Dogra and Leon Carl.

7.2.1 Gutzwiller ansatz and order parameters

To explore the zero-temperature phase diagram, we consider Gutzwiller mean-field approach at fixed lattice fillings [331–333]. This is well justified for our experiment, as we typically operate at large particle numbers around $N \approx 10^4$ [65, 78]. The extended Bose-Hubbard Hamiltonian in Eq. (7.13) remains invariant under a displacement by λ_{d} both in x and z directions. Hence, we consider a translationally

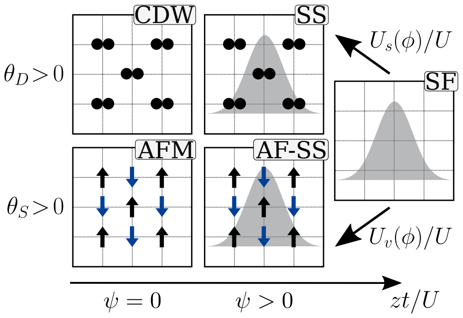

Figure 7.3: Mean-field order parameters and ground-state phases. The order parameters θ_D and θ_S characterize the global density and spin modulation, respectively. The degree of superfluidity in the system is quantified by ψ. When the tunneling rates t dominate over the contact interactions U, the system occupies a superfluid phase (SF) with $\psi > 0$. As the cavity-mediated scalar interactions (U_s/U) or vectorial interactions (U_v/U) are increased, we expect lattice supersolid (SS) or antiferromagnetic lattice supersolid (AF-SS) phases, respectively. They are characterized by $\theta_D > 0$ and $\theta_S > 0$. Decreasing t/U leads to insulating configurations ($\psi = 0$), with the system occupying either a charge density wave (CDW) or an antiferromagnetic Mott insulator (AFM). The arrows indicate the two spin states, while the circles represent the spin-insensitive density configurations.

invariant ground state on each of the even (e) and odd (o) sublattices,

$$|\Psi_{\mathrm{G}}\rangle = \prod_{e=0}^{K/2} \prod_{o=0}^{K/2} |\phi_e\rangle\,|\phi_o\rangle\,. \tag{7.15}$$

For each site $i \in \{e, o\}$, we introduce the corresponding wavefunction

$$|\phi_i\rangle = \sum_{n=0}^{n_{\max}} \sum_{m=0}^{m_{\max}} a_i(n,m)\,|n,m\rangle_i \tag{7.16}$$

where $|n,m\rangle_i = \frac{(\hat{b}^\dagger_{i,\uparrow})^n}{\sqrt{n!}} \frac{(\hat{b}^\dagger_{i,\downarrow})^m}{\sqrt{m!}} |0\rangle$ is the local Fock state with $n \leq n_{\max}$ atoms in the spin state $|\uparrow\rangle$ and $m \leq m_{\max}$ atoms in state $|\downarrow\rangle$ on a single site. Within our Gutzwiller ansatz, the real coefficients $\mathbf{a}_e \equiv (a_e(n,m))_{n,m}$ and $\mathbf{a}_o \equiv (a_o(n,m))_{n,m}$ are optimized to minimize the effective mean-field energy density

$$\mathcal{E}(\mathbf{a}_e, \mathbf{a}_o) = \frac{\langle \Psi_{\mathrm{G}} | \hat{H} | \Psi_{\mathrm{G}} \rangle}{K/2}, \tag{7.17}$$

with K being the total number of lattice sites.

Mean-field order parameters

In order to diagnose the different phases of our system, we introduce various mean-field order parameters, see Fig. 3.4. First, we define average *superfluid order param-*

eter as

$$\psi = \frac{1}{4}\sum_{i,m} \psi_{i,m} = \frac{1}{4}\sum_{i,m} |\,\langle \Psi_{\mathrm{G}}|\hat{b}^{\dagger}_{i,m}|\Psi_{\mathrm{G}}\rangle\,|, \tag{7.18}$$

with $m \in \{\uparrow,\downarrow\}$ and $i \in \{e, o\}$. This order parameter differentiates between insulating ($\psi = 0$) and phase-coherent superfluid phases ($\psi > 0$). Starting from Eq. (7.10), we introduce *density* and *spin order parameters*

$$\begin{aligned} \theta_D &= |\,\langle \Psi_{\mathrm{G}}|(\hat{n}_{e,\uparrow} + \hat{n}_{e,\downarrow}) - (\hat{n}_{o,\uparrow} + \hat{n}_{o,\downarrow})|\Psi_{\mathrm{G}}\rangle\,|, \\ \theta_S &= |\,\langle \Psi_{\mathrm{G}}|(\hat{n}_{e,\uparrow} - \hat{n}_{e,\downarrow}) - (\hat{n}_{o,\uparrow} - \hat{n}_{o,\downarrow})|\Psi_{\mathrm{G}}\rangle\,|. \end{aligned} \tag{7.19}$$

The operator $\hat{n}_{i,m} = \hat{b}^{\dagger}_{i,m}\hat{b}_{i,m}$ counts the number of particles in the site $i \in \{e, o\}$ with $m \in \{\uparrow,\downarrow\}$. As illustrated in Fig. 7.3, the scalar global-range interactions $U_s(\phi)$ favor a finite density order parameter ($\theta_D > 0$); this order parameter indicates global occupation imbalance between even and odd lattice sites. Concurrently, the vectorial interactions $U_v(\phi)$ favor a finite spin order parameter ($\theta_S > 0$). It is associated with the atoms in the spin state $|\uparrow\rangle$ ($|\downarrow\rangle$) preferably occupying even (odd) lattice sites or vice versa, signaling global *antiferromagnetic ordering* in our system [cf. Fig. 7.3].

Numerical methods

To calculate the phase diagram of the system, we consider the Gutzwiller ansatz introduced in Eq. (7.15) and truncate the local occupation per spin state to $n_{\max} = m_{\max} = 3$. Using the built-in MATLAB function *fmincon*, we minimize the energy functional in Eq. (7.17) under the constraint of fixed density for each spin state. This results in a total of 28 variational parameters. Through empirical analysis, we find that density and spin orders do not coexist in our system, allowing us to choose simpler ansatzes for the corresponding ground-state phases. This reduces the number optimization parameters to 15-18 depending on the phase of the system. A detailed discussion of this approach can be found in Ref. [92].

7.2.2 Phase diagram at unity filling

We calculate the phase diagram of the system for a balanced spin mixture at unity filling, by imposing the constraint

$$\rho_m = \frac{N_m}{(K/2)} = \langle \phi_e|\hat{n}_{e,m}|\phi_e\rangle + \langle \phi_o|\hat{n}_{o,m}|\phi_o\rangle = 1, \tag{7.20}$$

with $m = \{\uparrow,\downarrow\}$. The choice to operate at fixed density is motivated by cold-atom experiments, although a qualitatively similar phase diagram arises in a grand canonical ensemble [325].

For clarity, we consider equal intra- and inter-spin contact interactions ($U = U_{12}$), which is a reasonable approximation for ^{87}Rb atoms in the $F = 1$ manifold with $U_{12}/U \approx 1.0093$ [334]. In Fig. 7.4, we present the different mean-field order parameters in the $(zt/U, U_L/U)$ parameter space, where $z = 4$ is the number of nearest neighbors in the square lattice. We consider two qualitatively different scenarios:

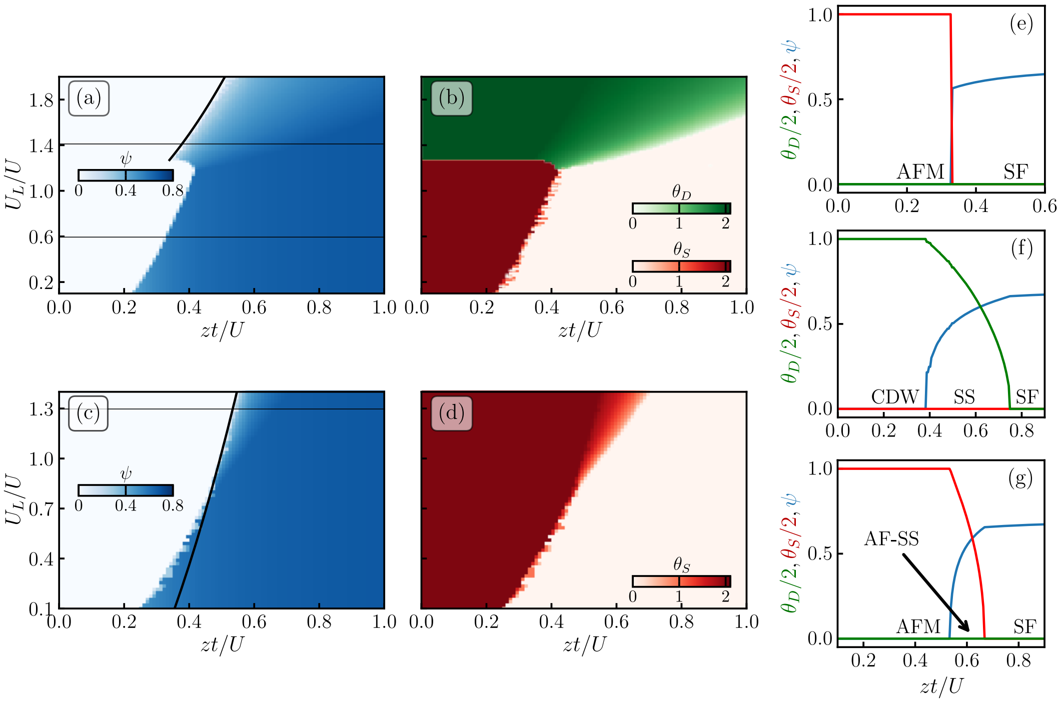

Figure 7.4: Mean-field phase diagrams at unity filling, displaying the order parameters ψ, θ_D, and θ_S in the $(zt/U, U_L/U)$ parameter space. We consider two representative ratios between the scalar and vectorial global-range interactions: $U_s/U_v \approx 4.64$ **(a, b)** and $U_s/U_v \approx 0.33$ **(c, d)**. The superfluid order parameter ψ (a, c) indicates the transition between insulating and phase-coherent configurations. The density θ_D and spin order parameter θ_S (b, d) characterize the globally ordered phases arising from scalar and vectorial interactions, respectively. **(e-g)** Cuts along the phase diagrams for $U_s/U_v \approx 4.64$ at constant $U_L/U = 0.59$ (e) and $U_L/U = 1.41$ (f), and for $U_s/U_v \approx 0.33$ at $U_L/U = 1.3$ (g), as indicated by the horizontal lines in (a, c). In the insulating regime, we identify an antiferromagnetic Mott insulator, which is stabilized for arbitrarily small values of U_L/U. The solid lines in (a, c) are perturbative estimations, which accurately capture second-order transitions in our system, cf. Ref. [92].

one with dominant scalar interactions $U_s/U_v \approx 4.64$ [Fig. 7.4(a,b)] and another with larger vectorial interactions $U_s/U_v \approx 0.33$ [Fig. 7.4(c,d)]. For our experimental parameters, they can be achieved by choosing TD polarization angles of $\phi = \pi/4$ and $\phi = 5\pi/12$, respectively. The different mean-field phases are also schematically depicted in Fig. 7.3.

For $U_s > U_v$ [Fig. 7.4(a,b)], we observe two distinct Mott insulating phases ($\psi = 0$) at low tunneling rates zt/U: for large global-range interactions U_L, we obtain a spin-degenerate *charge density wave* (CDW), with $\theta_D > 0$ and $\theta_S = 0$. For small values of U_L, the system arranges in an *antiferromagnetic Mott insulator* (AFM), with $\theta_S > 0$ and $\theta_D = 0$. Remarkably, the system favors an AFM for arbitrarily small vectorial interactions U_v, which we attribute to their interplay with the contact interactions U. The latter prevent the formation of a CDW and overcome the kinetic energy cost to form a unity filling Mott insulator (MI); in this regime, the AFM configuration is favored among all possible MIs by the global-range interactions U_v. Additionally, we identify a discontinuity in θ_D and θ_S when modifying U_L/U at fixed zt/U, signaling a first order AFM– CDW phase transition around $U_L/U \approx 1.27$. As tunneling increases, the system becomes *superfluid* ($\psi > 0$). We observe a first-order AFM-SF phase transition at small U_L/U, signaled by a discontinuous jump in the corresponding order parameters, cf. horizontal cut in Fig. 7.4(e). For large U_L, the system can simultaneously exhibit superfluidity ($\phi > 0$) and density ordering ($\theta_D > 0$), which we denote as a *lattice supersolid* (SS) phase. When increasing the tunneling rate zt at large U_L/U, we observe a continuous second-order SS-SF transition, as shown by the cut in Fig 7.4(f).

In the regime $U_v > U_s$ [Fig. 7.4(c,d)], the system exhibits solely spin ordered phases with $\theta_S > 0$, and $\theta_D = 0$, as the vectorial global-range and the contact interactions dominate over their scalar counterpart. For small global-range interactions $U_L/U < 0.8$, we identify a first-order AFM– SF phase transition, signaled by a discontinuous jump of ψ and θ_S. For larger values of U_L, we observe a second-order transition from AFM to a spin-ordered superfluid phase, which we denote as *antiferromagnetic lattice supersolid phase* (AF-SS) [Fig. 7.4(g)]. The second-order phase transitions from AFM to AF-SS and CDW to SS are supported by perturbative estimations [335], cf. black lines in Fig. 7.4(a,c) and Ref. [92] for detailed calculations.

As the global-range interactions couple every pair of lattice sites, they are captured well by our mean-field Gutzwiller ansatz [336]. However, we expect the method to progressively lose validity as the tunneling is increased, since the local-basis truncation ($n_{\max} = m_{\max} = 3$) disregards large local occupations which are present deep in the superfluid regime [333]. This is reflected by the saturation of the corresponding order parameter ψ in Figs. 7.4(e-g). In the Supplemental Material of Ref. [92], we further validate our results using two complementary approaches. First, we consider a self-consistent mean-field method in a grand canonical ensemble [337] and obtain a comparable ground-state phases. Second, the qualitative behavior of the different transitions observed in Figs. 7.4(e-g) also agrees with exact diagonalization calculations, which are however limited to small system sizes with $N = K \leq 10$ due to the increasing computational cost.

7.3 Excitations above the antiferromagnetic Mott insulator

In this section, we investigate the low-energy excitations of the system above the antiferromagnetic Mott insulator state. In section 7.3.2, we examine the excitation branches in the zero-tunneling limit: in addition to the well-known particle-hole excitations in Hubbard systems, we also identify a tunable spin-exchange branch. Furthermore, in section 7.3.2, we present the results of perturbative calculations at finite tunneling, which showcase the softening of the different excitation branches. These calculations were carried out by Tena Dubcek.

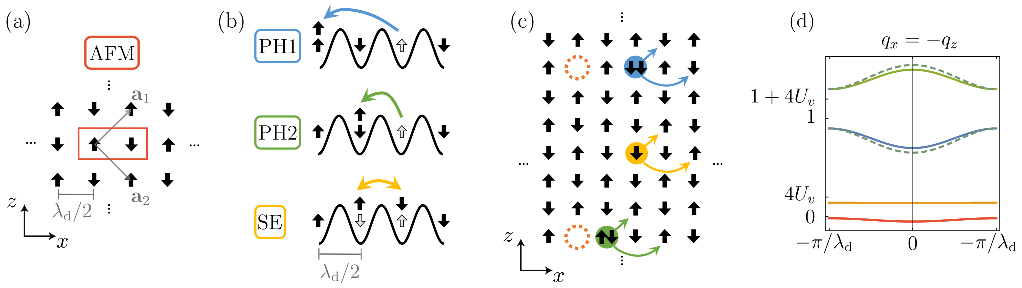

Figure 7.5: Excitations on top of the antiferromagnetic Mott insulator (AFM). **(a)** Unit cell of the λ_d-periodic AFM ground state containing two atoms (red box) and spanned by the unit vectors $\mathbf{a_1}$ and $\mathbf{a_2}$. **(b)** The excitations in the zero-tunneling limit involve two neighboring unit cells and can be grouped into two particle-hole branches PH1 (blue) and PH2 (green), as well as a gapped spin-exchange excitation SE (yellow). The gap of the latter can be independently controlled by adjusting U_v. **(c)** Delocalization of the two components (quasiparticles) of each excitation branch at finite tunneling. **(d)** Exemplary band structure for $t/U = U_v/U = 0.05$ at quasimomenta $q_x = -q_z$. The dashed lines indicate the bands when mixing of the particle-like components is considered, cf. Ref. [92].

7.3.1 Excitation branches in the zero-tunneling limit

The low-energy excitations of strongly correlated many-body systems provide important insights their microscopic behavior, as they define their dynamical response to external forces and drive transitions between different macroscopic ground-state phases. In the previous section, we identified an emergent antiferromagnetic Mott insulator (AFM), stabilized by the interplay of contact and global-range interactions. Here, we study the excitations on top of the AFM phase which have no counterpart neither in single-component BH models [65, 319] nor in bulk spinor Bose gases [78].

Due to its underlying periodicity, we can define the AFM ground state and the different elementary excitations on a square superlattice, with unit vectors $\mathbf{a}_1 = (\mathbf{e}_x + \mathbf{e}_z)\,\lambda_d/2$ and $\mathbf{a}_2 = (\mathbf{e}_x - \mathbf{e}_z)\,\lambda_d/2$. As illustrated in Fig. 7.5(a), the unit cell associated with an AFM ground state contains two spins, either at $[R_\uparrow = 0,\, R_\downarrow = \lambda_d/2\mathbf{e}_x]$ or $[R_\downarrow = 0, R_\uparrow = \lambda_d/2\mathbf{e}_x]$, depending on the way the global site symmetry is broken. In this framework, the excitations on top of the AFM can be understood as two correlated quasiparticles, which are always created in pairs within two adjacent unit cells.

In the limit of vanishing tunneling, $zt/U \to 0$, we identify three different low-energy branches, see Fig. 7.5(b). We identify two first particle-hole branches PH1 and PH2, which are composed by a particle (P) and hole (H) quasiparticle created in lattice sites with the same and opposite parity, respectively. For clarity, we consider the case of vanishing scalar interactions ($U_s = 0$). By evaluating the many-body Hamiltonian in Eq. (7.13) for $t = 0$, we obtain the energy gaps of these excitations

$$\begin{aligned} \Delta E_{\text{PH1}} &= \hbar U, \\ \Delta E_{\text{PH2}} &= \hbar(U + 4U_v). \end{aligned} \tag{7.21}$$

In addition, we identify a *spin-exchange* (SE) excitation, which involves a pairwise exchange of two atoms with different spins occupying neighboring lattice sites, as shown in Fig. 7.5(b). This excitation breaks the global antiferromagnetic order in the system and is associated with an energy gap of

$$\Delta E_{\mathrm{SE}} = 8\hbar U_v \tag{7.22}$$

for $t = 0$. Importantly, the energy gap of the SE excitation can be independently controlled with respect to the gaps of the particle-hole excitations (PH1 and PH2) by adjusting the strength of the vectorial long-range interactions U_v.

7.3.2 Spectrum at finite tunneling rates

At finite tunneling rates, the quasiparticles forming each excitation branch (such as particles and holes) can independently tunnel and delocalize within the lattice, shifting their energies compared to the $t = 0$ limit. This phenomenon is schematically depicted in Fig. 7.5(c) for the different excitation branches.

Using a perturbative approach, we derive an effective excitation Hamiltonian

$$H_{\mathrm{eff}} = \sum_{\mathbf{n}',\mathbf{n}} \sum_{\beta} h^{\beta}_{\mathbf{n}\mathbf{n}'} \left(\hat{b}^{\beta}_{\mathbf{n}'}\right)^{\dagger} \hat{b}^{\beta}_{\mathbf{n}} + \text{h.c.}, \tag{7.23}$$

describing the delocalization of the different qusiparticles β within doublets of adjacent spin sites $\mathbf{n}$. The corresponding annihilation operators are $\hat{b}^{\beta}_{\mathbf{n}}$. The coefficients $h^{\beta}_{\mathbf{n}\mathbf{n}'}$ characterize the effective tunneling strengths ($\mathbf{n}' \neq \mathbf{n}$) and energies ($\mathbf{n}' = \mathbf{n}$) of the quasiparticles. They are obtained via first-order perturbation theory, by including up to fourth-order tunneling processes between nearest and next-nearest neighbors. The detailed calculations can be found in the Supplemental Material of Ref. [92]. Our approach is quantitatively valid, as long as the tunneling rate t is small compared to the energy gaps between the initial/final states and each of the adiabatically eliminated virtual states, i.e., for $t \ll 4U_v$ and $t \ll U$.

We diagonalize the excitation Hamiltonian in the reciprocal quasimomentum space (q_x, q_z). In Fig. 7.5(d), we present a representative band structure at finite tunneling $t/U = 0.05$ for commensurate quasimomenta $q_x = -q_z$. The bandwidth of the SE branches (yellow curve) scales as $\sim t^4$, resulting in an extremely flat band in the considered regime, $t \approx U_v << U$. The bandwidths of the two PH branches scale as $\sim t^2$ (blue and green curves), and increase if weak mixing through a first-order tunneling process is considered (dashed lines). All these bands are eight times degenerate, four times due to the C4 symmetry invariance of the two quasiparticles (e.g. particle left, right, above or below the hole) and two times due to the underlying $\mathbb{Z}_2$ symmetry of the AFM phase.

From our perturbative calculations, we find that the SE excitation energy obtains a second-order leading correction at finite tunneling. At vanishing quasimomenta $q_x = q_z = 0$ (long-wave limit), we obtain

$$\frac{\Delta E_{\mathrm{SE}}(t)}{\hbar U} = 8 \left[\frac{U_v}{U} - \frac{2(3 - 4U_v/U)}{(1 - 4U_v/U)(1 + 4U_v/U)} \left(\frac{t}{U}\right)^2 \right]. \tag{7.24}$$

Specifically, this equation indicates that the SE branch progressively softens with increasing tunneling rates ($\Delta E_{\mathrm{SE}}(t > 0) < \Delta E_{\mathrm{SE}}(0)$), provided the global-range interactions are sufficiently small ($U_v/U < 1/4$).

In future projects, it would be particularly interesting to explore the interplay between the spin-exchange excitations and the different macroscopic phases of the system. In particular, we should investigate whether a complete (partial) softening of the SE branch in the vicinity of the superfluid phase is the microscopic mechanism underlying a second (first) order AF-SS to SF (AFM to SF) transition observed in Fig. 7.4(d). However, due to the large tunneling rates in this regime ($t/U \gtrsim 0.5$), it would be necessary to consider higher-order interaction terms in Eq. (7.23), which can give rise to additional mixing and level crossing between the different excitation branches.

7.4 Experimental feasibility and challenges

Here, we discuss the technical details regarding a potential experimental implementation of the extended Bose-Hubbard model discussed in this chapter. In section 7.4.1, we examine how the different energy scales of the system can be independently controlled in the experiment and outline the methods to infer the various order parameters by combining photonic and atomic observables. In section 7.4.2, we address various technical challenges associated with the inhomogeneous density distribution of the trapped BEC and the immiscibility of the two spin components. We propose a feasible potential experimental protocol to overcome potential limitations and access the different ground-state phases in our experiment.

7.4.1 Experimental parameters and observables

The proposal discussed in this chapter can be directly implemented and explored in our experiment, by leveraging on the experimental procedures and observables developed in previous works [65, 67, 78]. Specifically, we can prepare a balanced mixture of atoms in the $|F = 1, m = +1\rangle$ and $|F = 1, m = -1\rangle$ Zeeman sublevels [78] by means of radio-frequency spin rotations starting from a BEC in the state $|F = 1, m = 0\rangle$, cf. section 3.2.3. As shown in Fig. 7.6(a), we can proceed by confining the spin mixture in a deep optical lattice ($V_y \gtrsim 25\,\mathrm{E_{rec,y}}$) with a periodicity of $\lambda_y/2 = 670\,\mathrm{nm}/2$ along the y-direction [65]. Thereby, we split the BEC in a stack of independent two-dimensional pancakes in the xz-plane, which solely interacting via cavity-mediated global range interactions. To initialize the different phases of the system, we can then adiabatically increase the depth V_{2D} of the square optical lattice in the xz plane at fixed cavity detunings $\tilde{\Delta}_c$.

Controlling the different energy scales of the system

We can independently control the relevant energy scales of the extended Bose-Hubbard Hamiltonian derived in Eq. (7.13) by adjusting complementary experimental parameters. In a single experimental realization, we can control the ratio between the tunneling and contact interactions by modifying the lattice depth V_{2D}.

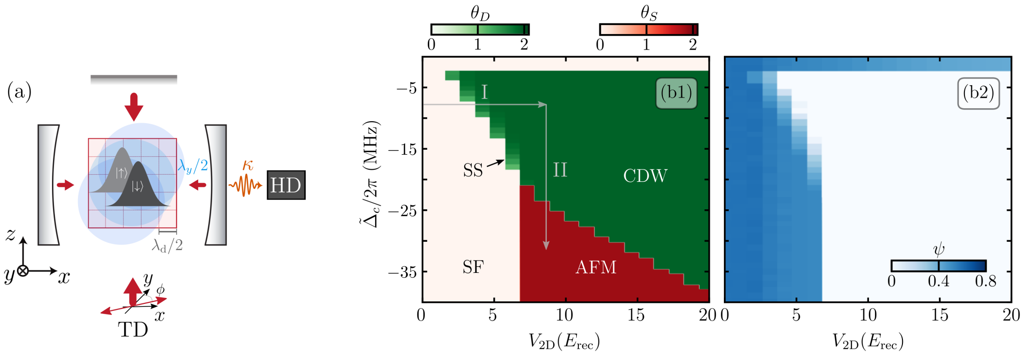

Figure 7.6: Towards experimental implementation. **(a)** Proposed experimental scheme. The two-component BEC is confined in a stack of two-dimensional pancakes in the xz plane using an auxiliary $\lambda_y/2$-periodic optical lattice. To initialize the dynamics, we increase the depth V_2D of a $\lambda_\mathrm{d}/2$-periodic square lattice and monitor the leaking cavity field with our heterodyne (HD) detection. **(b)** Unity filling phase diagram in the experimental parameter space (V_2D, $\tilde{\Delta}_c$) for $U_s/U_v = 4.64$ ($\phi = \pi/4$) and $N = 20000$ atoms. We plot the corresponding density (θ_D) and spin order parameters (θ_S) in (b1), and the superfluid order parameter ψ in (b2). The gray arrows in (b1) indicate a proposed two-step protocol (paths I and II) to access the CDW and AFM phases in a single experimental realization. For the abbreviations, see Fig. 7.3.

In the limit of deep lattices $V_\mathrm{2D} \gg E_\mathrm{rec}$, we can approximate the Wannier functions in Eqs. (7.8) and (7.9) as localized Gaussian wave packets [338], and obtain

$$\frac{t}{U} = \frac{\sqrt{2}}{a_\mathrm{s} k_y} \left(\frac{V_\mathrm{2D}}{E_\mathrm{rec}}\right)^{1/4} \left(\frac{V_y}{E_{\mathrm{rec},y}}\right)^{-1/4} e^{-\sqrt{2V_\mathrm{2D}/E_\mathrm{rec}}}, \tag{7.25}$$

with a_s and $k_y = 2\pi/\lambda_y$ being the s-wave scattering length and the wavenumber associated with the auxiliary lattice in y direction. As expected, the ration t/U is reduced by increasing V_2D, facilitating access to superfluid-Mott insulator phase transition [39].

Furthermore, for any given value of V_2D, we can independently tune the overall strength of cavity-mediated interactions U_L by modifying the effective cavity detuning $\tilde{\Delta}_c$, see Eq. (7.14). Specifically, they scale as $U_L \propto 1/\tilde{\Delta}_c$ for $|\tilde{\Delta}_c| \gg \kappa$. Finally, we can control the relative strength of scalar and vectorial interactions, $U_s = U_L \cos^2(\phi)$ and $U_v = U_L \xi^2 \sin^2(\phi)$ by changing the TD polarization angle ϕ at the beginning of each experimental realization.

To exemplify the high degree of experimental tunability, we calculate the mean-field phase diagram for $N = 20000$ atoms at unity filling in the $(V_\mathrm{2D}, \tilde{\Delta}_c)$ parameter space for $\phi = \pi/4$ ($U_s = 4.64 U_v$). In Figs. 7.6(b1) and (b2), we present the corresponding density and spin order parameters (θ_D and θ_S), as well as the superfluid order parameter (ψ). At large negative cavity detunings $\tilde{\Delta}_c$, we observe a superfluid-insulator phase transition around $V_\mathrm{2D} \gtrsim 6\,\mathrm{E_{rec}}$ [Fig. 7.6(b2)], accompanied by the formation of an antiferromagnetic Mott insulator (AFM) with $\theta_S > 0$ [Fig. 7.6(b1)]. As Δ_c is decreased (U_L increased), we observe emergent density-ordered lattice supersolid (SS) and charge-density-wave (CDW) phases with $\theta_D > 0$.

Experimental observables

The different ground-state phases can be detected by a combination of atomic and photonic observables in our experiment. As discussed in see section 3.2.2, we can measure the momentum-space distribution of the atoms via absorption imaging after free time-of-flight expansion. Specifically, we can count the number of coherent atoms N_{coh} in the different momentum peaks following an analogous evaluation to Fig. 4.6(b) in chapter 4. The superfluid order parameter can be then estimated as $\psi \approx \sqrt{N_{\mathrm{coh}}/N}$ [196].

Additionally, we can directly assess density and spin ordering in our system by leveraging on our heterodyne detection of the leaking cavity field, cf. section 3.2.1. By eliminating the y-polarized cavity field using Eq. (7.12), we obtain the following relations for the density and spin order parameters

$$\begin{aligned} \theta_D &= \frac{\langle \hat{\Theta}_D \rangle}{N} \approx \frac{\tilde{\Delta}_c^2 + \kappa^2}{\eta_s N M_0 \tilde{\Delta}_c} \mathrm{Re}\left(\langle \hat{a}_y \rangle\right), \\ \theta_S &= \frac{\langle \hat{\Theta}_S \rangle}{N} \approx \frac{\tilde{\Delta}_c^2 + \kappa^2}{\eta_v N M_0 \tilde{\Delta}_c} \mathrm{Im}\left(\langle \hat{a}_y \rangle\right), \end{aligned} \tag{7.26}$$

for $|\tilde{\Delta}_c| \gg \kappa$. From Eq. (7.26), we conclude that the density and spin order parameters are directly proportional to the real and imaginary quadratures of the y-polarized cavity field, $\theta_D \propto \mathrm{Re}(\langle \hat{a}_y \rangle)$ and $\theta_S \propto \mathrm{Im}(\langle \hat{a}_y \rangle)$, respectively.

This relation allows us to discern spin- and density-ordered superradiant phases in single experimental realizations. To probe these phases, we propose to first increase the lattice depth V_{2D} at small cavity detunings $\tilde{\Delta}_c$ to access the CDW phase (ramp I), see Fig. 7.6(b1). Using our heterodyne detection, we can measure the phase ϕ of the leaking cavity field. In a second step (ramp II), we can then access the AFM phase by increasing $\tilde{\Delta}_c$ at fixed values of V_{2D}. From Eq. (7.26), we expect the first order CDW-AFM transition to be signaled by an abrupt jump of the phase of the cavity field to either $\phi + \pi/2$ or $\phi - \pi/2$, depending on the $\mathbb{Z}_2$-symmetry broken configuration. A similar technique has been successfully employed in Ref. [339] to diagnose the discontinuous phase transition between two emergent centro-symmetric crystals in a Bose-Einstein condensate coupled to an optical cavity.

7.4.2 Experimental challenges and future directions

Inhomogeneous density distributions

The calculations performed in this chapter were carried out for an idealized experimental system with homogeneous density distributions at unity filling. However, the harmonically trapped BEC in our experiment inherently follows a parabolic Thomas-Fermi distribution [111]. For our typical trap frequencies $[\omega_{hx},\ \omega_{hy},\ \omega_{hz}] = 2\pi \times [200,\ 30,\ 180]$ Hz and atom numbers $N = 20000$, we calculate the site occupation $n(x, y)$ of the central pancake layer in the xy plane and present it in Fig. 7.7(a). We observe a rapidly varying Thomas-Fermi distribution extending over ~ 15 sites in each direction, with the occupation peaking around $n(0, 0) \approx 9.5$ at the central

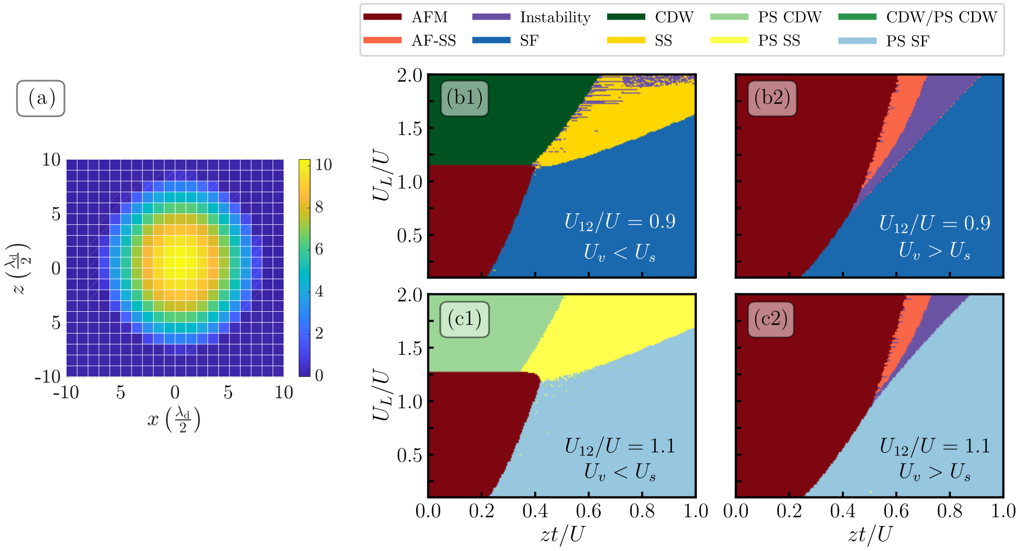

Figure 7.7: Spatial inhomogeneities and immiscibility. **(a)** Thomas-Fermi distribution of the central 2D pancake ($y = 0$) for $N = 20000$ atoms and typical trap frequencies $[\omega_{hx}, \omega_{hy}, \omega_{hz}] = 2\pi \times [200, 30, 180]$ Hz. The density distribution is integrated within $\lambda_\mathrm{d}/2 \times \lambda_\mathrm{d}/2$ regions to obtain the average site occupation $n(x, y)$, which peaks around $n(0, 0) \approx 9.5$ at the trap center. **(b, c)** Mean-field phase diagrams at unity filling for different ratios of inter- and intra-spin interactions, $U_{12}/U = 0.9$ (b) and $U_{12}/U = 1.1$ (c). As in Fig. 7.4, we consider $U_s/U_v = 4.64$ (b1, c1) and $U_s/U_v = 0.33$ (b2, c2). For the experimentally relevant case of $U_{12} > U$ (c), the two spin components become immiscible, giving rise to phase-separated (PS) phases in SF, SS, and CDW configurations. Additionally, the global-range interactions introduce an extended instability region within the AF-SS phase.

lattice site[1].

For a conventional Bose-Hubbard system, featuring solely tunneling and contact interactions, the spatial inhomogeneities can be considered within a local-density approximation. Within this approach, we can assume a spatially varying chemical potential $\mu(x, z)$ to capture the phases in regions with different average occupations [36, 37]. However, cavity-mediated global-range interactions invalidate the local-density approximation, as they directly couple regions of the lattice with different average occupations. In a spinless extended Bose-Hubbard system, the interplay between U_L and the harmonic trapping potential can give rise to coexistence of Mott insulating (MI) and CDW phases, as discussed in Ref. [67]. In an intuitive picture, the system has to pay an additional energy cost to arrange the atoms away from the trap center, which has to be compensated by the energy gain associated with the formation of a CDW. In a spin mixture, we conjecture that a similar mechanism might give rise to coexistence between the different insulating phases, such as the AFM, CDW and MI.

---

[1] In the experiments discussed in Ref. [65], the peak occupation was reduced to $n(0, 0) \approx 2.8$ atoms by relaxing the harmonic confinement and magnetically levitating the BEC in the Zeeman sublevel $m = -1$. However, this approach is not feasible for our proposal as a homogeneous spin mixture in $m = \pm 1$ cannot be magnetically levitated. An alternative approach to reduce both $n(0, 0)$ and spatial inhomogeneities, could be to confine the BEC in a spin-independent optical box trap at the center of the cavity [340].

Immiscibility of the spin mixture

In the phase diagrams presented in section 7.2, we explicitly assume equal inter- (U_{12}) and intra-spin (U) contact interactions. This assumption is only approximately valid for a spin mixture of ^{87}Rb atoms in the $|F=1, m=+1\rangle$ and $|F=1, m=-1\rangle$ Zeeman sublevels, which features $U_{12}/U = a_{\uparrow\downarrow}/a_\mathrm{s} \approx 1.0093$ [334, 341]. Indeed, due to $U_{12} > U > 0$, we expect that the $m = \pm 1$ mixture becomes *immiscible* and give rise to fully *phase separated* states [342–344]. These states are characterized by the two spin components occupying opposite regions of the trapping potentials, as first observed in Ref. [345].

To incorporate phase separation in our calculations, we modify the Gutzwiller ansatz presented in Eq. (7.15). Specifically, the system is divided into halves (A, B) which have higher spin-up ($\rho_\uparrow^A > \rho_\downarrow^A$) or spin-down densities ($\rho_\downarrow^B > \rho_\uparrow^B$), respectively. We further impose total atom number conservation in each half ($\rho \equiv \rho_\uparrow^{A,B} + \rho_\downarrow^{A,B} = 2$) to ensure unity filling. Besides homogeneous and phase separated configurations (PS) [346], our system can also exhibit phase instabilities (PI) due to the interplay of short- and global-range interactions [322]. Such PI are signaled by a negative compressibility, $\partial_\rho \mu < 0$ [347], where $\mu(\rho) = \partial_\rho \mathcal{E}(\rho)$ is the chemical potential as a function of the density ρ. We calculate the derivative numerically by using the energy densities $\mathcal{E}(\rho)$ extracted from Eq. (7.17) and allowing for density variations. A detailed discussion of this approach can be found in Ref. [92].

In Figs. 7.7(b,c), we present the phase diagrams for different inter- to intra-spin interaction ratios U_{12}/U, and scalar to vectorial global-range interaction ratios U_s/U_v at unity filling:

- The phase diagrams for $U_{12} < U$ [Figs. 7.7(b)] are qualitatively similar to the uniform mixture at $U_{12}/U = 1$ discussed in Fig. 7.4. For dominating scalar interactions [Figs. 7.7(b1)], we find extended SF, AFM, CDW and SS phases. Additionally, we observe a scattered region of PI in the SS phase. Our observations of PI are qualitatively different from the results for spinless systems [322, 347], which predict stable SS phases at integer filling in 2D systems. Meanwhile, for dominating vectorial interactions [Figs. 7.7(b2)], we find extended regions of PI in the AF-SS phase.

- When considering stronger inter-spin interactions, $U_{12} > U$, several fully phase separated (PS) ground-state configurations arise, cf. Figs. 7.7(c). For dominating scalar interactions [Fig. 7.7(c1)], we observe a fully PS CDW and PS SS. Moreover, for larger vectorial interactions [Fig. 7.7(c2)], we also observe shrinkage of the AF-SS region with increasing U_{12}/U , explained by the growing local cost of double site occupation with atoms of opposite spin. Additionally, we find a fully PS SF for all U_s/U_v ratios.

We note here a limitation of our numerical simulations. The identification of the different phases relies on minimization in a high-dimensional parameter space. This can lead to spurious solutions, such as the scattered instability points in Fig. 7.7(b1) and the irregular phase boundaries in Figs. 7.7(b2,c2).

Towards experimental implementations

In our experiment, the $m = \pm 1$ spin mixture can be readily initialized in a shallow two-dimensional lattice ($V_{\mathrm{2D}} \lesssim 5\,\mathrm{E}_{\mathrm{rec}}$), giving rise to a superfluid phase. Due to the $m = \pm 1$ immiscibility and the large tunneling rates, we expect the atoms to arrange themselves in a phase separated superfluid (PS SF) configuration, as shown in Figs. 7.7(c). Phase separation can be particularly detrimental for the experimental observation of spin-ordered phases. For the protocol (gray arrows) suggested in Fig. 7.6(b1), the system would be prepared in a PS CDW, with the atoms in $m = +1$ and $m = -1$ occupying opposite regions of the trap. When ramping then the cavity detuning towards the AFM phase, we expect the system to remain trapped in a metastable PS CDW phase [67], as the system is in an insulating configuration and multiple hopping events are required to rearrange the atoms towards a magnetically ordered AFM.

To overcome this potential limitation and study the AFM-CDW phase transition, we propose a complementary experimental protocol. Initially, we create a Mott insulator state in the $m = 0$ Zeeman sublevel by increasing the lattice depths V_{2D} while maintaining large cavity detunings $\tilde{\Delta}_c$. Then, we employ a resonant radio frequency pulse [78] to prepare a homogeneous $m = \pm 1$ mixture within the lattice. As tunneling is suppressed deep in the insulating regime, we expect to access the AFM phase before the atoms in $m = \pm 1$ significantly separate. Finally, we can probe the AFM-CDW transition by adiabatically ramping the cavity detuning towards $\tilde{\Delta}_c \to 0$.

7.5 Discussion and outlook

In this chapter, we theoretically investigated an experimentally feasible two-component spin Bose-Hubbard model, featuring tunable vectorial and scalar cavity-assisted global-range interactions. Employing a Gutzwiller ansatz at unity filling, we obtained a rich phase diagram showcasing density- and spin-modulated phases, both in superfluid and insulating regimes. Notably, we identified an emergent antiferromagnetic Mott insulator (AFM) that is stabilized even for arbitrarily small vectorial interactions, owing to their interplay with repulsive contact interactions. Furthermore, we investigated the low-lying excitations above the AFM phase and identified a spin-exchange branch with an independently tunable energy gap. At finite tunneling strengths, the different excitation branches delocalize in the lattice, which was examined using an effective perturbative Hamiltonian. To gain deeper insights into the mechanisms underlying the various phase transitions of our system, future investigations could incorporate higher-order quasiparticle interactions in the effective theory.

The different ground-state phases can be readily detected in our experiment by combining cavity field heterodyne detection and time-of-flight absorption imaging, as the density- and spin-modulated phases couple to orthogonal quadratures of the cavity field. The larger inter-spin contact interactions for ^{87}Rb atoms in the $F = 1$ manifold give rise to phase separated superfluid and density-modulated phases, which pose additional challenges to the experimental protocols required to access the magnetically ordered AFM and AF-SS phases.

As a direct extension, it would be interesting to systematically investigate the first-order CDW-AFM transition. Two key questions there are the lifetime and decay of metastable states [67] and the spread of correlated quasiparticle excitations, which might exhibit an unbounded velocity due to global-range interactions [348, 349]. Moreover, regions of phase coexistence could arise when considering the harmonic trapping potential [316, 321]. In the absence of optical lattices, cavity dissipation directly couples the density- and spin-modulated states, leading to chiral instabilities and limit cycles [108, 350, 351]. Our lattice system offers experimentally tunable access to the boundary between density- and spin-modulated insulating phases, and can help clarify the fate of these instabilities in the Hubbard regime. This could provide deeper insights into non-Hermitian dynamics in strongly correlated quantum systems. Finally, the inclusion of spin-changing processes, such as cavity-mediated Raman transitions [89, 90], can introduce another competing energy scale in the system and give rise to exotic magnetic phases like spin-density waves or chiral states [76].

8 Conclusions and future directions

Throughout the course of this dissertation, we successfully harnessed vectorial atom-light interactions to induce cavity-assisted Raman transitions in a degenerate Bose gas. This approach proved to be a rich experimental playground for exploring emergent spin dynamics induced by superradiant Raman scattering. We developed several experimental schemes to selectively address well-defined external and internal modes of a Bose-Einstein condensate (BEC) and monitor the emergent phases and microscopic dynamics through complementary measurements of the cavity field and the atomic density distribution. We conducted three experimental projects, demonstrating our ability to control dissipative and coherent dynamics in our system.

In the first project, we realized a Dicke superradiant phase transition induced by cavity-assisted Raman transitions. By independently controlling the co- and counter-rotating interactions, we observed a dissipation-induced phase and a discontinuous superradiant transition in an extended bistability regime. The underlying mechanism is a collective decay of the light-matter excitations, which we resolved by probing the cavity spectrum. In the second project, we moved beyond Dicke physics and engineered dynamical tunneling in a synthetic lattice in momentum space. Collective hopping is implemented via superradiant Raman scattering in a non-Hermitian setting. By employing frequency-resolved measurements of the leaking cavity field, we locally resolved individual tunneling events . Our results highlight the cavity field spectrum as a suitable observable for monitoring collective excitations and out-of-equilibrium dynamics in real time, and in a non-destructive fashion. In the final experimental project, we engineered spin- and momentum-correlated atom pairs through the exchange of virtual cavity photons. We observed coherent pair oscillations within tens of microseconds and demonstrated the collective character of the dynamics. Our scheme offers the possibility to independently control the coherent pair dynamics and competing dissipative superradiant scattering. Furthermore, we characterized the pair quantum statistics and verified their correlated nature by probing momentum-resolved noise correlations. These observations pave the way for the fast generation of entangled matter-wave pairs.

Our results demonstrate a comprehensive approach for engineering, controlling and probing many-body spin dynamics in driven-dissipative settings, opening new exciting possibilities for cavity QED experiments. In the following sections, we discuss some of the potential directions for future experiments.

In section 8.1, we present an experimental scheme that combines cavity-assisted Raman transitions and Hubbard physics in optical lattices. This setting is expected to give rise to emergent spin-wave phases both in superfluid and insulating regimes. To address current technical limitations, in section 8.2, we propose a cavity-based detection scheme to resolve small atom numbers in different Zeeman sublevels by exploiting the vectorial polarizability of the atoms. Finally, in section 8.3, we discuss two possible extensions of the coherent pair dynamics. First, we consider the formation of pairs in an optical lattice to obtain control over the underlying dispersion relation and potentially simulate random spin models in momentum space. Second, we present preliminary observations of cavity-assisted spin-exchange dynamics in a two-component BEC, and discuss the possibility to implement a quantum simulator for photon-mediated Cooper pairing.

8.1 Extended Hubbard models with cavity-assisted Raman transitions

In chapter 7, we proposed and theoretically investigated an extended Bose-Hubbard model showcasing spin-dependent global-range interactions mediated by cavity photons. An important aspect of such lattice systems is that they provide access to phases and transitions in a strongly correlated regime, where inter-particle interactions become significant [21]. Specifically, the interplay between short- and global-range interactions stabilizes an antiferromagnetic insulator for the system considered in chapter 7, even for arbitrarily small cavity-mediated interactions.

To further explore emergent magnetic phases in Hubbard systems, we propose to combine them with cavity-assisted Raman transitions. We consider a scenario analogous to the experiments discussed in chapter 4, as illustrated in Fig. 8.1(a). A BEC in the Zeeman sublevel $m = -1$ (spin state $|{\downarrow}\rangle$) is confined in the fundamental mode of the cavity by a two-dimensional optical lattice in the xz plane, with site spacing $\lambda_\mathrm{d}/2$. The quantization axis is defined by a magnetic field in $-z$ direction. The atoms are illuminated by two y-polarized standing-wave drives propagating along z, with frequencies $\omega_{\mathrm{r,b}}$ and Raman couplings $\eta_{\mathrm{r,b}}$. As discussed in section 4.2.2, this coupling configuration induces spin-changing self-organization mediated by the z-polarized cavity mode ($\hat{a}$). The corresponding superradiant phase is characterized by a self-consistent cavity field at $\bar{\omega} = (\omega_r + \omega_b)/2$ and by the atoms occupying a superposition of the Zeeman sublevels $m = -1$ ($|{\downarrow}\rangle$) and $m = 0$ ($|{\uparrow}\rangle$), see level scheme in Fig. 8.1(b).

For a sufficiently deep optical lattice V_{2D} [65], we can expand the atomic field operators in Wannier states and obtain a tight-binding representation. Following an analogous approach to section 7.1.2, we derive an extended Bose-Hubbard model incorporating cavity-assisted Raman transitions, $\hat{H} = \hat{H}_{\mathrm{BH}} + \hat{H}_{\mathrm{R}}$, with

$$\begin{aligned}\hat{H}_{\mathrm{BH}} =& -\hbar t \sum_{m,\langle \mathbf{i},\mathbf{j}\rangle} (\hat{b}^\dagger_{\mathbf{i},m} \hat{b}_{\mathbf{j},m} + \mathrm{h.c.}) + \frac{\hbar U}{2} \sum_{\mathbf{i},m} \hat{n}_{\mathbf{i},m}\left(\hat{n}_{\mathbf{i},m} - 1\right) + \hbar U_{12} \sum_{\mathbf{i}} \hat{n}_{\mathbf{i},\uparrow} \hat{n}_{\mathbf{i},\downarrow} \\ & + \hbar \Delta\mu \sum_{\mathbf{i}} \left(\hat{n}_{\mathbf{i},\uparrow} - \hat{n}_{\mathbf{i},\downarrow}\right) \\ \hat{H}_{\mathrm{R}} =& -\hbar \frac{U_{\mathrm{R}}}{K} \left[\sum_{\mathbf{i}} (-1)^{|\mathbf{i}|} \left(\hat{b}_{\mathbf{i},\uparrow} \hat{b}_{\mathbf{i},\downarrow} + \hat{b}_{\mathbf{i},\downarrow} \hat{b}_{\mathbf{i},\uparrow} \right) \right]^2 .\end{aligned} \tag{8.1}$$

The operators $\hat{b}^\dagger_{\mathbf{i},m}$ and $\hat{n}_{\mathbf{i},m} = \hat{b}^\dagger_{\mathbf{i},m} \hat{b}_{\mathbf{i},m}$ create and count atoms on the site $\mathbf{i} = (i_x, i_z)$ and spin state $m \in \{\downarrow, \uparrow\}$, respectively. The first term, $\hat{H}_{\mathrm{BH}}$, describes

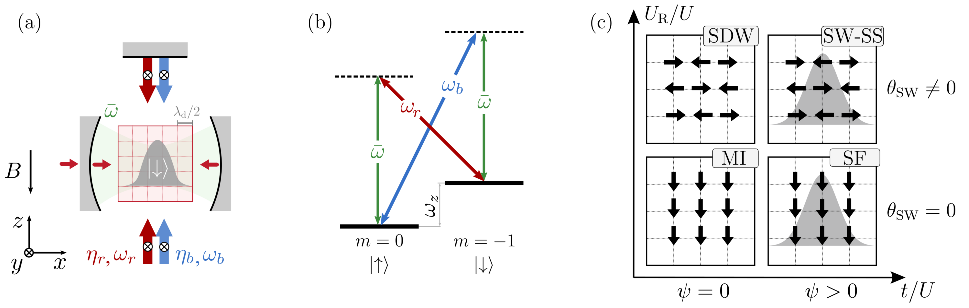

Figure 8.1: Extended Bose-Hubbard models with cavity-assisted Raman transitions. **(a)** Experimental setup. A BEC in the spin state $|{\downarrow}\rangle$ ($m = -1$) is confined in the cavity by a $\lambda_d/2$-periodic 2D optical lattice (xz plane). The atoms are illuminated by two standing-wave drives propagating along z (y polarization), with Raman couplings $\eta_{r,b}$ and frequencies $\omega_{r,b}$. **(b)** Coupling scheme. The drives induce cavity-assisted Raman transitions between the levels $|{\downarrow}\rangle$ ($m = -1$) and $|{\uparrow}\rangle$ ($m = 0$), which are offset by ω_z. When entering the superradiant phase, a coherent z-polarized cavity field builds up at the intermediate frequency $\bar{\omega} = (\omega_b + \omega_r)/2$. **(c)** Expected phases and order parameters. The order parameter ψ quantifies the degree of superfluidity, while θ_{SW} describes the global transverse spin-wave order. When the tunneling rate t is small compared to the contact interactions U, the system occupies a spin-polarized Mott insulator (MI) with $\psi = 0$. As t is increased, the system enters a superfluid (SF) phase ($\psi > 0$). When increasing the cavity-mediated interactions U_R, we expect a spin-density wave insulator (SDW) or a spin-wave lattice supersolid (SWF) depending on t/U. They both exhibit $\theta_{SW} \neq 0$, and $\psi = 0$ or $\psi > 0$, respectively.

a two-component Bose-Hubbard model with nearest-neighbor tunneling rate $t > 0$, and repulsive intra- and inter-spin contact interactions $U > 0$ and $U_{12} > 0$. They are defined in Eqs. (7.8) and (7.9), respectively. For uniform fillings, the relative chemical potential between the two spin states, $\Delta\mu = (\omega_b - \omega_r)/2 - \omega_z$, can be experimentally controlled by adjusting the linear Zeeman splitting ω_z. This is analogous to the energy offset $\hbar\omega_0$ in the bulk system, cf. Eq. (4.8).

The second term, $\hat{H}_R$, arises from cavity-assisted Raman transitions and induces spin-changing global-range interactions. When the two drives are balanced, $\eta = \eta_r = \eta_b$, the corresponding coupling

$$\frac{U_R}{K} = \eta^2 M_0^2 \frac{(-\tilde{\Delta}_c)}{\kappa^2 + \tilde{\Delta}_c^2}, \tag{8.2}$$

can be independently controlled via the effective cavity detuning $\tilde{\Delta}_c = \bar{\omega} - \omega_c$, with ω_c being the dispersively shifted cavity resonance. The overlap integral M_0 is defined in Eq. (7.11), while K indicates the total number of sites. For positive couplings, $U_R > 0$, the global-range interactions favor the formation of two $\mathbb{Z}_2$ symmetry-broken *transverse spin waves*: the atoms on even and odd lattice sites preferably occupy symmetric superpositions of the two spin states with opposite orientations, i.e., $|{\rightarrow}\rangle = (|{\uparrow}\rangle + |{\downarrow}\rangle)/\sqrt{2}$ and $|{\leftarrow}\rangle = -(|{\uparrow}\rangle + |{\downarrow}\rangle)/\sqrt{2}$, or vice versa.

Following the theoretical investigations in Refs. [325, 327], we introduce the mean-field order parameter

$$\theta_{\mathrm{SW}} = \frac{1}{N} \left\langle \hat{b}_{\mathbf{i},\uparrow}\hat{b}_{\mathbf{i},\downarrow} + \hat{b}_{\mathbf{i},\downarrow}\hat{b}_{\mathbf{i},\uparrow} \right\rangle \approx \frac{\tilde{\Delta}_c^{\;2} + \kappa^2}{\eta N M_0 \tilde{\Delta}_c} \mathrm{Re}(\langle \hat{a} \rangle), \tag{8.3}$$

which quantifies the degree of transverse spin-wave order in the system. Importantly, θ_{SW} can be measured in real time by monitoring the real quadrature $\mathrm{Re}(\langle \hat{a} \rangle)$ of the leaking cavity field, with $\mathrm{Re}(\langle \hat{a} \rangle) > 0$ and $\mathrm{Re}(\langle \hat{a} \rangle) < 0$ being associated with the two symmetry-broken configurations.

As also studied in Ref. [325], we conjecture the existence of four different ground-state phases depending on the relative ratios between the tunneling rate, global- and short-range interactions. They are illustrated in the schematic phase diagram in Fig. 8.1(c). For negligible global-range interactions, $U_{\mathrm{R}}/U \to 0$, the system is expected to remain in $|{\downarrow}\rangle$ and occupy either a spin-polarized superfluid (SF) or a Mott insulator (MI). These phases are characterized by the superfluid order parameter ψ in Eq. (7.18) assuming either finite or vanishing values, respectively. Increasing U_{R} above a critical value should favor the emergence of transverse spin-wave order in the system, as indicated by $\theta_{\mathrm{SW}} \neq 0$. Depending on the value of t/U, we anticipate that the system will either organize in a spin-wave lattice supersolid (SW-SS) or a spin-density wave insulator (SDW), characterized by $\psi > 0$ and $\psi = 0$, respectively. The latter is reminiscent of a charge-density wave in long-range interacting spinless systems [65]. As also discussed in section 7.4.2, the harmonically trapped BEC in our experiment inherently follows an inhomogeneous density distribution, see Fig.7.7(a) in chapter 7. Similar to a spinless system [67], such inhomogeneities can potentially stabilize extended regions of phase coexistence involving MI and SDW phases.

Experimentally, it might be advantageous to operate the transverse drive close to the tune-out wavelength of ^{87}Rb in the $F = 1$ manifold, which is approximately $\lambda_{\mathrm{TO}} \approx 790.019\,\mathrm{nm}$, cf. Fig. 2.1(a). Thereby, the vectorial polarizability becomes dominant, $|\alpha_v/\alpha_s| \gg 1$, and we can gain controlled access to extended SW-SS regions at small lattice depths. Additionally, it would be interesting to induce either controlled polariton damping or superradiant Raman scattering between the two spin levels, as explored in chapters 4 and 5 for bulk systems. This could shed light on collective dissipative dynamics in strongly correlated systems.

8.2 Cavity-based detection schemes

In future experiments, it would be extremely beneficial to accurately measure the number of atoms in the different Zeeman sublevels m of the $F = 1$, especially in the context of the pair production experiments presented in chapter 6. As discussed in section 6.7, we require to accurately measure $N_{\mathrm{p}} \lesssim 100$ pairs in the levels $m = +1$ and $m = -1$ to access a regime exhibiting significant quantum correlations. For this purpose, it is essential to reduce our current technical detection noise (~ 200 atoms) by at least one order of magnitude. To complement the current efforts to upgrade the absorption imaging setup, we discuss here preliminary ideas for cavity-based detection schemes. Atom counting protocols in cavity-QED experiments typically rely on probing the dispersive shift of a given cavity resonance in the presence of

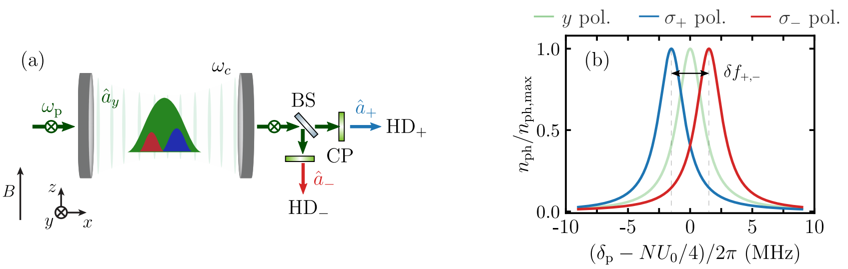

Figure 8.2: Cavity-assisted detection scheme of atoms in different spin states. **(a)** Experimental setup. We prepare atoms in the Zeeman sublevels $m = 0$ (green), $+1$ (blue) and -1 (red) inside the cavity, with a magnetic field B along z defining the quantization axis. The y-polarized cavity mode (operator $\hat{a}_y$, resonance frequency ω_c) is probed using a weak beam with frequency ω_p. By a combination of beamsplitters (BS) and circular polarizers (CP), the cavity output is separated into $\sigma_\pm$-polarized components ($\hat{a}_\pm$) that are detected in two interdependent heterodyne setups HD$_\pm$. **(b)** Vectorial dispersive shift. The cavity transmission spectrum $n_\mathrm{ph}(\delta_\mathrm{p})$ is probed by adjusting the probe-cavity detuning δ_p. Apart from a common scalar shift, $-NU_0/4$, the transmission spectra of σ_+ (blue) and σ_- photons (red curve) exhibit a relative vectorial shift, δf_{+-}, which scales with the atom number imbalance $N_{+1} - N_{-1}$ in $m = \pm 1$. For these calculations, we choose N=50000, $N_{+1} - N_{-1} = 50$ and a cavity detuning of $\delta_{D_2} = -2\pi \times 1\,\mathrm{GHz}$ from the D_2 line.

atoms [352, 353], which arises from the scalar atom-light interactions. In this section, we present a scheme exploiting the vectorial polarizability of the atoms to achieve spin-resolved atom number measurements in $m = \pm 1$. The proposed technique shares similarities with free-space Faraday rotation schemes, which have been successfully employed to monitor the dynamics of spinor BECs in a non-destructive fashion, as detailed in Refs. [354, 355].

We prepare atoms in the three different Zeeman sublevels $m = 0$ (green), $m = +1$ (blue) and $m = -1$ (red shape) of the $F = 1$ manifold and probe the y-polarized cavity mode ($\hat{a}_y$), as schematically depicted in Fig. 8.2(a). For clarity, we first neglect the birefringence of our optical cavity which can induce additional complications that we address in the end of this section. For a quantization axis along the z direction, the negative part of the electric field associated with the y-polarized cavity mode

$$\hat{\mathbf{E}}^{(-)} = E_0 \hat{a}_y \cos(kx) \mathbf{e}_y = \frac{E_0}{\sqrt{2}} (\hat{a}_+ \mathbf{e}_+ + \hat{a}_- \mathbf{e}_-) \cos(kx) \tag{8.4}$$

can be decomposed in a superposition of $\sigma_\pm$-polarized photons. The corresponding unit vectors and photon annihilation operators are $\mathbf{e}_\pm$ and $\hat{a}_\pm$, respectively, while E_0 represents the vacuum electric field. The wavenumber of the cavity mode is given by $k = \omega_\mathrm{c}/c$, with ω_c being the cavity resonance frequency. We probe the cavity resonance using a weak y-polarized laser at frequency ω_p and separate the leaking field in $\sigma_\pm$ components using a suitable combination of beamsplitters and circular polarizers [101]. These components can be detected using independent heterodyne setups HD$_\pm$, as depicted in Fig. 8.2(a).

We assume dispersive light-matter interactions and use Eq. (2.12) to derive the corresponding single-particle Hamiltonian

$$\begin{aligned}\hat{H}_{\mathrm{SP}} = &\left[\hbar\omega_{\mathrm{c}} + \left(\frac{\alpha_s E_0^2}{2} - \frac{\alpha_v E_0^2}{2}\hat{F}_z\right)\cos(kx)\right]\hat{a}_+^\dagger \hat{a}_+ \\ &+ \left[\hbar\omega_{\mathrm{c}} + \left(\frac{\alpha_s E_0^2}{2} + \frac{\alpha_v E_0^2}{2}\hat{F}_z\right)\cos(kx)\right]\hat{a}_-^\dagger \hat{a}_-,\end{aligned} \tag{8.5}$$

with $\hat{F}_z$ being the z projection of the $F = 1$ spin operator. In Eq. (8.5), we directly see that the scalar polarizability α_s induces a common dispersive shift of the cavity resonance frequencies for σ_+ and σ_- polarizations, irrespective of the atomic spin state; the corresponding maximal dispersive shift is given by $U_0/2 = \alpha_s E_0^2/(2\hbar)$, with the factor of 1/2 arising from the decomposition of the cavity mode into two circular polarizations. In contrast, the vectorial polarizability α_v is associated with the atoms in $m = +1$ ($\langle \hat{F}_z \rangle = 1$) and $m = -1$ ($\langle \hat{F}_z \rangle = -1$) interacting differently with σ_+ and σ_- photons. Specifically, an atom in $m = \pm 1$ shifts the cavity resonance of the σ_+- and σ_--polarized mode by $\mp U_v$ and $\pm U_v$, respectively, with the maximal *vectorial dispersive shift* being defined as $U_v = \alpha_v E_0^2/(2\hbar)$.

To obtain a many-body description, we consider the exemplary situation of pair production in a single-channel configuration discussed in section 6.1.2. Using the mode expansion in Eq. (6.6), we derive the many-body Hamiltonian in a rotating frame at the frequency of the probe beam ω_{p}

$$\begin{aligned}\hat{H}_{\mathrm{MB}} \approx &\left[-\hbar\delta_{\mathrm{p}} + \frac{\hbar U_0}{4}\hat{N} - \frac{3\hbar U_v}{8}\left(\hat{c}_1^\dagger \hat{c}_1 - \hat{c}_{-1}^\dagger \hat{c}_{-1}\right)\right]\hat{a}_+^\dagger \hat{a}_+ \\ &+ \left[-\hbar\delta_{\mathrm{p}} + \frac{\hbar U_0}{4}\hat{N} + \frac{3\hbar U_v}{8}\left(\hat{c}_1^\dagger \hat{c}_1 - \hat{c}_{-1}^\dagger \hat{c}_{-1}\right)\right]\hat{a}_-^\dagger \hat{a}_-.\end{aligned} \tag{8.6}$$

Here, we introduce the probe-cavity detuning $\delta_{\mathrm{p}} = \omega_{\mathrm{p}} - \omega_{\mathrm{c}}$, use the shorthand notation $\hat{c}_m^\dagger$ for the operators creating atoms in the corresponding modes of the different Zeeman sublevels m and define $\hat{N} = \sum_m \hat{c}_m^\dagger \hat{c}_m$. From Eq. (8.6), we expect the resonance condition for $\sigma_\pm$-polarized photons to be shifted as

$$\tilde{\delta}_\pm = -\frac{U_0}{4}N \pm \frac{3}{8}U_v(N_1 - N_{-1}), \tag{8.7}$$

with $N_{\pm 1}$ being the number of atoms in $m = \pm 1$. Apart from a common dispersive shift scaling with the total atom number N, we obtain a differential frequency shift for σ_+ and σ_- photons

$$\delta f_{+-} = \tilde{\delta}_+ - \tilde{\delta}_- = -\frac{3}{4}U_v(N_1 - N_{-1}), \tag{8.8}$$

which can differentiate between atoms in $m = +1$ and $m = -1$, as it scales with their difference $N_1 - N_{-1}$.

To obtain an experimentally resolvable differential signal, it is important that δf_{+-} becomes comparable with the cavity linewidth, i.e., $|\delta f_{+-}| \gtrsim \kappa = 2\pi \times 1.25\,\mathrm{MHz}$. This can be achieved by probing a cavity mode close to atomic resonance. For an atomic detuning[1] of $\delta_{D_2} = \omega_\mathrm{c} - \omega_{D_2} = -2\pi \times 1\,\mathrm{GHz}$ with respect to the D_2 line of ^{87}Rb, we obtain $U_0 \approx -2\pi \times 161\,\mathrm{kHz}$ and $U_v \approx -2\pi \times 161\,\mathrm{kHz}$. In Fig. 8.2(b), we plot the Lorentzian-shaped cavity spectra for σ_+ (blue) and σ_- photons (red) for $N = 50000$ atoms. There, we directly see that the relative splitting $\delta f_{+-} \approx 2\pi \times 3\,\mathrm{MHz}$ is clearly discernible for small $m = \pm 1$ imbalances of $N_1 - N_{-1} = 50$ atoms. For comparison, the y-polarized cavity mode (green) is solely affected by the scalar dispersive shift.

A key strength of this technique is that the frequency shift δf_{+-} is a differential signal that is obtained by simultaneously monitoring the spectra of σ_+- and σ_--polarized photons. Hence, it is robust against long-term drifts of the cavity resonance frequency ω_c and the total atom number N. As δf_{+-} scales with the atom number difference $N_1 - N_{-1}$, this observable is particularly suitable to diagnose relative number squeezing in $m = +1$ and $m = -1$. For more details on this criterion, see discussion in section 6.7.1. In the derivation of δf_{+-}, we implicitly assume that all linearly polarized cavity eigenmodes are degenerate. This is not the case for our experiment [137], as the two linearly polarized eigenmodes of our birefringent cavity, $\hat{a}_1$ and $\hat{a}_2$, are split by $\delta_\mathrm{B} = 2\pi \times 2.2\,\mathrm{MHz}$ and rotated by $\phi = 22°$ with respect to the y and z axes, respectively. As the y-polarized cavity field is not an eigenmode, birefringence would lift the degeneracy between σ_+- and σ_--polarized photons and further admix them with π-polarized light. To circumvent this complication, we could rotate the bias magnetic field by ϕ in the yz plane and thereby also the quantization axis. In this setting, pair production would be mediated by the cavity eigenmode $\hat{a}_2$ (π polarization), while we could probe the eigenmode $\hat{a}_1$ (superposition of degenerate σ_+ and σ_- photons) to examine the differential shift δf_{+-}.

To integrate such cavity-based detection schemes in our experiment, we plan to install an additional laser system to produce a stabilized probe beam at frequency ω_p, which will be operated at small atomic detunings with respect to the D_2 line. At the same time, we will continue exploring different cavity-based detection techniques. One promising approach might involve using co-propagating Raman beams to selectively shelve the atoms in a given Zeeman sublevel $|F = 1, m\rangle$ in the $F = 2$ hyperfine manifold. Given the large ground-state hyperfine splitting, $\Delta_\mathrm{HFS} = 2\pi \times 6.835\,\mathrm{GHz}$, we expect to be able to measure the dispersive shift in $F = 2$, regardless of occupation in $F = 1$.

8.3 Quantum simulation using photon-mediated atom pairs

This section outlines future directions for quantum simulation experiments that build upon the cavity-mediated correlated atom pairs discussed in chapter 6. In section 8.3.1, we discuss a feasible scheme to engineer random spin models in momentum space. Our proposal combines correlated atom pairs with well-defined quasi-momentum states in an optical lattice. Furthermore, in section 8.3.2, we present preliminary direct observations of photon-mediated spin-exchange interactions in a two-component Bose gas. The underlying mechanism could facilitate the simulation of photon-mediated Cooper pairs in our experiment.

---

[1] This detuning is at the boundary of the dispersive regime's validity, since the excited state hyperfine splitting ($\Delta_{\mathrm{HFS}'} = 2\pi \times 0.5\,\mathrm{GHz}$) starts to become comparable with δ_{D_2}, as shown in Fig. 3.1(b). In future experiments, we will also explore similar schemes in the resonant regime of cavity QED [101], where we expect larger differential mode splittings for $\sigma_\pm$-photons.

8.3.1 Implementing random spin models in momentum space

The Sachdev-Ye-Kitaev (SYK) model [356, 357] is one of the most prominent examples of random spin models. The corresponding Hamiltonian

$$\hat{H}_{\mathrm{SYK}} = \sum_{jklm} \hbar J_{jklm} \hat{d}_m^\dagger \hat{d}_l^\dagger \hat{d}_k \hat{d}_j, \tag{8.9}$$

describes an ensemble of N all-to-all coupled fermions with creation operators $\hat{d}_l^\dagger$ and $l \in \{1, ..., N\}$. The random couplings J_{jklm} are sampled from Gaussian distributions with $\langle J_{jklm} \rangle = 0$, $\mathrm{var}(J_{jklm}) = \mathcal{J}/N^{2/3}$ and disorder strength $\mathcal{J}$. This model is characterized by the lack of quasiparticle excitations due its exponentially dense low energy spectrum, and was first introduced in the context of non-Fermi liquids and strange metals [358]. Due to their all-to-all connectivity, such random spin models inherently describe a zero-dimensional system. Recently, the SYK model has also attracted substantial interest as a minimal model for holographic quantum gravity [357, 359], owing to the exponentially fast scrambling of quantum correlations and the AdS/CFT correspondence [360]. As natural materials do not conventionally feature such properties, there are growing efforts to simulate random spin models in different platforms, ranging from nuclear-spin chains [361] to cavity-QED experiments with cold atoms [362].

Here, we discuss an experimental scheme to realize a bosonic spin model with pseudo-random, all-to-all interactions. The fundamental idea relies on distributing the occupation of a Bose-Einstein condensate (BEC) among multiple quasimomenta q of the band structure associated with an optical lattice, which we interpret as 'sites' in our system. For a sufficiently filled Bloch band, the cavity-assisted pair production mechanism induces correlated hopping of atoms from the sites q and q' into the sites $q + k$ and $q' - k$, respectively. The corresponding hopping rates $J_{q,q'}$ depend on the initial momenta, q and q', while the tunneling distance k is determined by an external laser drive, as illustrated in Fig. 8.3(a).

Following the experiments described in chapter 6, we consider a BEC initialized in the $m = 0$ Zeeman sublevel and additionally confined in a one-dimensional optical lattice with site spacing $\lambda_L/2$, wavenumber $k_L = 2\pi/\lambda_L$ and lattice depth V_L, as depicted in Fig. 8.3(b). The atoms are illuminated by a running-wave transverse drive propagating along the z direction with wavenumber k, which induces cavity-assisted pair production. As illustrated in the dispersion relation in Fig. 8.3(c), this coupling scheme converts two atoms in $m = 0$ (green) with quasimomenta q and q' into correlated atom pairs in $m = +1$ (blue) and $m = -1$ (red) with quasimomenta $q + k$ and $q' - k$, respectively. The associated coupling rates $J_{q,q'}$ depend on the initial quasimomenta, q and q', due to the varying overlap integrals between different Bloch states and the laser drive.

To obtain a quantitative description, we start from the single-particle Hamiltonian

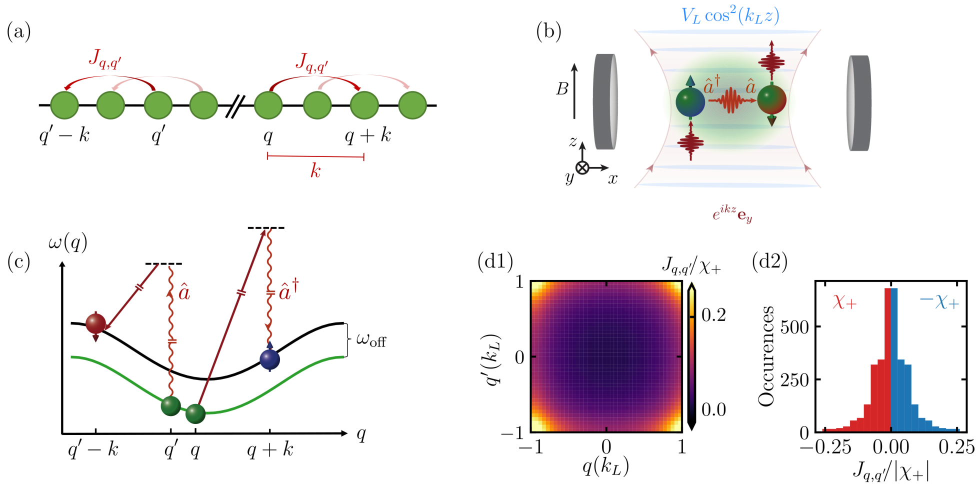

Figure 8.3: Random spin model in momentum space. **(a)** Proposed lattice model. Atoms in two arbitrary sites q and q' interact via the coupling term $J_{q,q'}$, which pairwise transfers them to different sites $q+k$ and $q'-k$ at the distance k. **(b)** Experimental setup. A BEC in the spin state $m=0$ is confined in a 1D optical lattice, with lattice depth V_L and site spacing $\lambda_L/2=\pi/k_L$. The atoms are coupled to the cavity by a running-wave drive with wavenumber k. Pairs of atoms in $m=+1$ (blue) and $m=-1$ (orange spheres) are created by the exchange virtual cavity photons (operator $\hat{a}$). **(c)** Coupling scheme, depicting the generation of $m=\pm1$ pairs out of atoms in $m=0$ (green spheres) with different quasimomenta q and q'. The dispersion relation $\omega(q)$ for atoms in $m=\pm1$ (black) is offset by $\omega_{\rm off}$ from that of $m=0$ (green curve). **(d)** Preliminary calculations. (d1) $J_{q,q'}$ distribution for $V_L=3E_{\rm rec}$ and $k=2k_L$. (d2) The corresponding histogram peaks at $J_{q,q'}=0$ and decreases at larger couplings. Notably, the sign of the distribution can be controlled by the sign of the corresponding coherent coupling χ_+, with $J_{q,q'}<0$ (red) or $J_{q,q'}>0$ (blue histogram).

in Eq. (6.2), and expand the $F=1$ field operator into Bloch functions

$$\hat{\Psi}(\mathbf{x})=\left(\hat{\Psi}_{+1}(\mathbf{x}),\,\hat{\Psi}_0(\mathbf{x}),\,\hat{\Psi}_{-1}(\mathbf{x})\right)^T=\begin{pmatrix}\frac{k}{\sqrt{2}\pi}\cos\left(kx\right)\sum_q e^{iqz}u_q(z)\hat{c}_{q,+1}\\ \frac{k}{2\pi}\sum_q e^{iqz}u_q(z)\hat{c}_{q,0}\\ \frac{k}{\sqrt{2}\pi}\cos\left(kx\right)\sum_q e^{iqz}u_q(z)\hat{c}_{q,-1}\end{pmatrix},\quad(8.10)$$

where the bosonic operators $\hat{c}^\dagger_{q,m}$ create atoms in spin state $m\in\{-1,0,1\}$ with quasimomenta q in the lowest Bloch band (s-band). The orbitals $u_q(z)=u_q(z+2\pi/k_L)$ are $2\pi/k_L$-periodic in real space. The single-particle states in $m=\pm1$ are modulated along the x direction according to the cavity mode structure [$\propto\cos(kx)$]. Following Ref. [122], we adiabatically eliminate the cavity field and obtain an atom-only description, $\hat{H}=\hat{H}_0+\hat{H}_{\rm int}$, with

$$\begin{aligned}\hat{H}_0&=\sum_{q\in\mathrm{BZ}}\hbar\omega_q(V_L)\hat{c}^\dagger_{q,0}\hat{c}_{q,0}+\hbar\left[\omega_q(V_L)+\omega_{\rm off}\right]\left(\hat{c}^\dagger_{q,+1}\hat{c}_{q,+1}+\hat{c}^\dagger_{q,-1}\hat{c}_{q,-1}\right)\\ \hat{H}_{\rm int}&=\sum_{q,q'\in\mathrm{BZ}}\hbar J_{q,q'}(V_L,k)\left(\hat{c}^\dagger_{q+k,+1}\hat{c}^\dagger_{q'-k,-1}\hat{c}_{q,0}\hat{c}_{q',0}+\mathrm{h.c.}\right).\end{aligned}\quad(8.11)$$

The first contribution, $\hat{H}_0$, describes the offset energy of the atoms. While the atoms in $m = 0$ directly follow the lowest-band dispersion relation $\omega_q(V_L)$, the atoms in $m = \pm 1$ are additionally offset by $\omega_{\text{off}} = \omega_{\text{rec}}(k) + q$, with q and $\omega_{\text{rec}}(k)$ being the quadratic Zeeman splitting and the recoil frequency associated with the $\cos(kx)$ density modulation, respectively. The interaction Hamiltonian, $\hat{H}_{\text{int}}$, describes cavity-assisted pair production in quasimomentum space, with coupling rates $J_{q,q'}(V_L, k) = 2\chi_+ M_{q+k,q} M_{q'-k,q'}$. Here, we consider a single-channel configuration with bulk coupling rate χ_+ and neglect additional spin-exchange terms for clarity, see Eqs. (6.9) and (6.8). The interactions further depend on the overlap integrals $M_{q+k,q} = \langle q + k | \, e^{ikz} \, | q \rangle$ between the initial and final Bloch states which are coupled by the running-wave transverse drive. The exact form of $M_{q+k,q}(V_L, k)$ also depends on details of the experimental implementation, such as the lattice depth V_L and the drive wavenumber k.

We numerically examine the coupling distribution $J_{q,q'}$ for a typical lattice depth of $V_L = 3E_{\text{rec}}$ and select a drive wavevector of $k = 2k_L$, as shown in Fig. 8.3(d1). For this specific scenario, we obtain a coupling distribution $J_{q,q'}$ that is highly concentrated at the boundaries of the Brillouin zone, $q = \mp k_L = \mp k/2$ and $q' = \pm k_L = \pm k/2$, and rapidly decays for varying quasimomenta. The larger couplings at these boundaries arise because the corresponding final quasimomenta $q + k = k_L$ and $q' - k = -k_L$ are the only ones situated within the first Brillouin zone. For larger lattice depths V_L, we observe a broadening of the distributions due to hybridization between the s- and p-bands at the edges of the Brillouin zone. To visualize the coupling distribution, we present the histogram of $J_{q,q'}/|\chi_+|$ in Fig. 8.3(d2) [red histogram]. This distribution has its peak at $J_{q,q'} = 0$ and monotonically decreases for larger $J_{q,q'}$. Unlike the SYK model presented in Eq. (8.8), the couplings in Fig. 8.3(d2) consistently maintain the same sign, which can be globally adjusted by changing the sign of the bulk pair coupling $\chi_+ < 0$ (red) or $\chi_- < 0$ (blue histograms).

In future experiments, we plan to initialize a partially filled lowest Bloch band in the vicinity of the superfluid–Mott insulator phase transition [363]. Close to the phase transition, the superfluid features strong onsite repulsive interactions spreading its momentum distribution among different quasimomenta q. This can be potentially combined with Bloch oscillations under a gradient potential [364] in order to precisely control the initial momentum distribution in the lattice. Furthermore, we aim to explore methods to control the coupling distribution $J_{q,q'}$ and establish genuine bosonic random spin models. Specifically, a distribution with expectation value $\langle J_{q,q'} \rangle = 0$ and significant fluctuations can be obtained by exposing the atoms to two transverse drives with opposite two-photon detunings δ_+ and $-\delta_+$. This results in commensurate coupling distributions with different signs, $\chi_+ \propto \delta_+ < 0$ (red) and $-\chi_+ \propto -\delta_+ > 0$ (blue histogram), leading to $\langle J_{q,q'} \rangle = 0$ for the entire system, as shown in Fig. 8.3(d2).

There are many open questions that present opportunities for collaboration between theory and experiment. While random spin models with bosonic degrees of freedom are known to exhibit rapid scrambling dynamics [365], their relevance in the context of holographic duality is still unclear. On a more pragmatic note, it is also uncertain whether stringent Gaussian coupling distributions are required to obtain exponential scrambling dynamics, as suggested in a recent cavity-QED proposal [366]. The early-time scrambling dynamics and late-time chaotic behavior in random spin models can be diagnosed via exponentially decaying out-of-time-order correlators (OTOCs) and long-range spectral correlations [366, 367], respectively. Experimentally, accessing such observables is far from trivial and will require the development of suitable protocols.

8.3.2 Engineering and observing spin-exchange processes

The cavity-assisted pair production scheme introduced in chapter 6 provides a flexible mechanism to control photon-mediated spin interactions involving well-defined internal and external modes. In this section, we propose and experimentally demonstrate a straightforward extension facilitating the direct observation of photon-mediated spin-exchange interactions.

We consider a two-component Bose-Einstein condensate (BEC) initialized in the Zeeman sublevels $m = -1$ and $m = 0$ of the $F = 1$ hyperfine manifold, with a magnetic field B along z defining the quantization axis, see illustration in Fig. 8.4(a). From now on, we refer to them as the spin levels $|\downarrow\rangle$ and $|\uparrow\rangle$, respectively. The atoms are coupled to the cavity by a running-wave drive propagating in z direction with wavenumber k and linear y polarization. Similar to the scheme discussed in section 6.1.1, a zero-momentum atom in $|\downarrow\rangle$ (mode $|k_z = 0\rangle_\downarrow$) can scatter a σ_+-polarized drive photon into the π-polarized cavity mode ($\hat{a}^\dagger$) and flip its spin to $|\uparrow\rangle$ while obtaining net photon recoil momentum $+\hbar k$ along z (mode $|+k\rangle_\uparrow$). This virtual cavity photon is rescattered by a second atom in $|\uparrow\rangle$ (mode $|0\rangle_\uparrow$) into the drive, which in turn changes its spin to $|\downarrow\rangle$ and obtains $-\hbar k$ momentum along z, occupying the mode $|-k\rangle_\downarrow$. Due to the drive polarization, the complementary process of an atom in $|0\rangle_\uparrow$ first scattering a σ_--polarized drive photon is also possible, and yields correlated occupation of the modes $|+k\rangle_\downarrow$ and $|-k\rangle_\uparrow$. As the total population in $|\uparrow\rangle$ and $|\downarrow\rangle$ is conserved [80], we refer to them as photon-mediated *spin-exchange processes.*

To obtain a quantitative description, we expand the $F = 1$ field operator as

$$\begin{aligned}\hat{\Psi}(\mathbf{x}) &= \left(\hat{\Psi}_{+1}(\mathbf{x}),\, \hat{\Psi}_0(\mathbf{x}),\, \hat{\Psi}_{-1}(\mathbf{x})\right)^T \\ &= \begin{pmatrix} 0 \\ \frac{k}{2\pi}\hat{c}_{0,\uparrow} + \frac{k}{\sqrt{2}\pi}\cos{(kx)}(e^{-ikz}\hat{c}_{-k,\uparrow} + e^{ikz}\hat{c}_{+k,\uparrow}) \\ \frac{k}{2\pi}\hat{c}_{0,\downarrow} + \frac{k}{\sqrt{2}\pi}\cos{(kx)}(e^{-ikz}\hat{c}_{-k,\downarrow} + e^{ikz}\hat{c}_{+k,\downarrow}) \end{pmatrix},\end{aligned} \tag{8.12}$$

with the bosonic operators $\hat{c}_{k_z,m}$ annihilating atoms in the modes $|k_z\rangle_m$, with $m \in \{\uparrow, \downarrow\}$ and $k_z \in \{0, -k, +k\}$. The corresponding single-particle wave functions are normalized within an unit cell of size $[-\pi/k, \pi/k)^2$, while the additional modulation $[\propto \cos(kx)]$ is inherited from the cavity mode structure. Following the experiments discussed in chapters 4 and 5, we operate at large magnetic fields B to suppress superradiant scattering and pair production involving the Zeeman sublevel $m = +1$. Accordingly, we set $\hat{\Psi}_{+1}(\mathbf{x}) = 0$. To obtain an effective many-body description, we start from the single-particle Hamiltonian in Eq. (6.2). By using the mode expansion in Eq. (8.12) and adiabatically eliminating the cavity field [122], we obtain the atom-

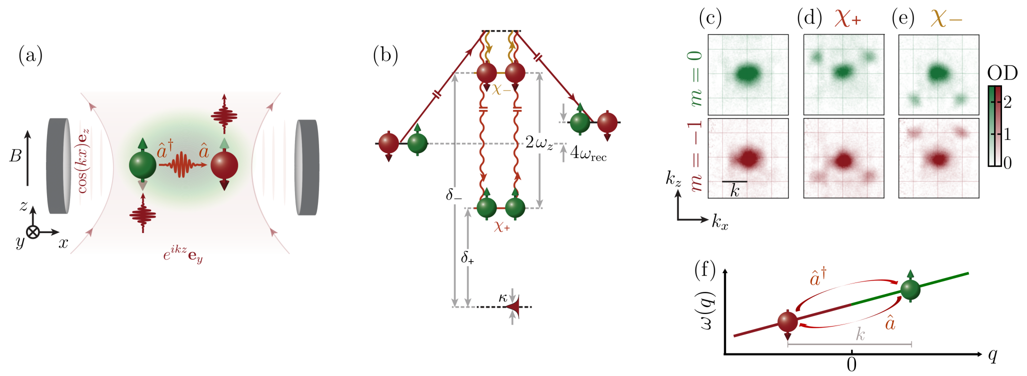

Figure 8.4: Observation of photon-mediated spin-exchange (SE) interactions. **(a)** Experimental setup. A two-component BEC in the Zeeman sublevels $m = -1$ ($|{\downarrow}\rangle$) and $m = 0$ ($|{\uparrow}\rangle$) is coupled to the cavity by a running-wave drive propagating in z direction (wavenumber k). SE processes are mediated by virtual cavity photons (operator $\hat{a}$). **(b)** Energy diagram. The SE mechanism comprises two coupled Raman scattering processes, each involving a drive (straight) and a cavity (curly arrows) photon. The intermediate modes are split by twice the linear Zeeman shift ω_z, giving rise to two discernible channels. The corresponding coupling rates $\chi_\pm$ depend on the two-photon detunings $\delta_\pm$ and the cavity loss rate κ. The final state is offset by $4\hbar\omega_{\mathrm{rec}}$, with ω_{rec} being the recoil frequency. **(c-e)** Representative spin-resolved momentum distributions. (c) The system is prepared in a balanced mixture in $m = -1$ (red) and $m = 0$ (green colormap). When quenching the coupling, we observe correlated occupation of the modes $|{+k}\rangle_\uparrow$ and $|{-k}\rangle_\downarrow$ (d) or $|{+k}\rangle_\downarrow$ and $|{-k}\rangle_\uparrow$ (e). This indicates SE interactions via the χ_+ and χ_- channels, respectively. **(f)** Towards quantum simulation of the BCS pairing mechanism. We consider a linear dispersion relation $\omega(q)$ in an optical lattice, occupied by atoms in $|{\uparrow}\rangle$ (green) and $|{\downarrow}\rangle$ (red line). The photon-mediated SE interactions resonantly pair atoms at opposite quasimomenta $-q$ and q, which emulates essential features of phonon-mediated Cooper pairs in solid-state systems.

only Hamiltonian

$$\begin{aligned}\hat{H} =& \sum_{\tilde{k}\in\{k,-k\}} 2\hbar\omega_{\mathrm{rec}} \left(\hat{c}^\dagger_{\tilde{k},\uparrow}\hat{c}_{\tilde{k},\uparrow} + \hat{c}^\dagger_{-\tilde{k},\downarrow}\hat{c}_{-\tilde{k},\downarrow}\right) \\ &+ \hbar\chi_+ \left(\hat{c}^\dagger_{-k,\downarrow}\hat{c}^\dagger_{+k,\uparrow}\hat{c}_{0,\uparrow}\hat{c}_{0,\downarrow} + \text{h.c.}\right) + \hbar\chi_- \left(\hat{c}^\dagger_{-k,\uparrow}\hat{c}^\dagger_{+k,\downarrow}\hat{c}_{0,\downarrow}\hat{c}_{0,\uparrow} + \text{h.c.}\right).\end{aligned} \tag{8.13}$$

The first term describes the bare energy associated with spin-exchanged pairs, which amounts to $4\hbar\omega_{\mathrm{rec}}$ and is fully determined by the photon recoil frequency ω_{rec}. The second and third terms describe two spin-exchange channels with coupling rates $\chi_\pm$ that can be independently controlled via of the corresponding two-photon detunings $\delta_\pm$, see Eq. (6.9). For $\chi_\pm < 0$, the two channels favor the correlated occupation of the modes $|{\pm k}\rangle_\uparrow$ and $|{\mp k}\rangle_\downarrow$. The different energy scales of the system are visualized in the energy level diagram in Fig. 8.4(b).

Preliminary experimental observations

To investigate photon-mediated spin-exchange interactions in our experiment, we initialize a balanced spin mixture comprising $N/2 = 3.5(2)\times10^4$ atoms in each of the modes $|0\rangle_\downarrow$ and $|0\rangle_\uparrow$. This is shown by the exemplary momentum-space distribution of the atoms in Fig. 8.4(c). We operate at large linear Zeeman splitting $\omega_z \approx -2\pi \times 20\,\mathrm{MHz}$ to suppress pair production and induce spin-exchange interactions in a single-channel configuration. In a first experiment, we set the relevant two-photon detuning to $\delta_+ = -2\pi \times 16\,\mathrm{MHz}$ ($\delta_- = -2\pi \times 36\,\mathrm{MHz}$) and quench the coupling to $\chi_+ = -2\pi \times 0.5\,\mathrm{Hz}$ for $t = 65\,\mu\mathrm{s}$. In the representative momentum distribution in Fig. 8.4(d), we observe correlated occupation of the modes $|{+k}\rangle_\uparrow$ and $|{-k}\rangle_\downarrow$, signaling spin-exchange interactions via the χ_+ channel. To complement these observations, we set the two-photon detuning to $\delta_- = -2\pi \times 10\,\mathrm{MHz}$ ($\delta_+ = +2\pi \times 10\,\mathrm{MHz}$) and perform an analogous quench experiment. As shown in Fig. 8.4(e), we observe correlated occupation of the modes $|{+k}\rangle_\downarrow$ and $|{-k}\rangle_\uparrow$, indicating spin-exchange interactions via the complementary χ_- channel.

These preliminary observations demonstrate our ability to optically engineer and directly observe spin-exchange processes mediated by virtual cavity photons.

Towards the simulation of photon-mediated BCS pairing

Controlling spin-exchange interactions can be particularly useful in the context of quantum simulation experiments. We propose a scenario similar to section 8.3.1, where the atoms are loaded in a one-dimensional lattice along the drive direction. We consider a tunable dispersion relation $\omega(q)$ for the atoms in the different quasimomentum states q. Specifically, we assume a linear dispersion $\omega(q) \propto q$ and initialize the atoms in $|\uparrow\rangle$ and $|\downarrow\rangle$ solely at positive ($q > 0$) and negative quasimomenta ($q < 0$), respectively, as illustrated in Fig. 8.4(d). While experimentally involved, such asymmetric band structures have been recently Floquet-engineered using two-tone phase modulation in an optical lattice [368].

We expand the system in Bloch waves [Eq. (8.10)] and consider a single-channel configuration with $|\chi_+| \gg |\chi_-|$. We derive the corresponding many-body Hamiltonian in quasimomentum space

$$\hat{H} \approx \sum_q \hbar\omega(q) \left(\hat{c}^\dagger_{q,\uparrow}\hat{c}_{q,\uparrow} + \hat{c}^\dagger_{q,\downarrow}\hat{c}_{q,\downarrow}\right) + \sum_{q<0} \hbar\chi_+ \left(\hat{c}^\dagger_{-q-k,\downarrow}\hat{c}^\dagger_{q+k,\uparrow}\hat{c}_{-q,\uparrow}\hat{c}_{q,\downarrow} + \mathrm{h.c.}\right), \tag{8.14}$$

where we retain only resonant spin-exchange terms. The Hamiltonian in Eq. (8.14) is a bosonic version of the paradigmatic Barden-Cooper-Schrieffer (BCS) model [7], which provided the first microscopic theory of conventional superconductivity and superfluidity. This model describes a system of two-spin electrons with effective attractive interactions $\chi_+ < 0$ mediated by the exchange of virtual phonons. They give rise to bound electron pairs of opposite spin ($|\uparrow\rangle$, $|\downarrow\rangle$) and momenta ($q + k$, $-q - k$) in the vicinity of the Fermi surface [369]. The emergent Cooper pairs are protected by a self-consistent pairing gap $\Delta_\mathrm{BCS} = \chi_+ \sum_q \langle \hat{c}_{-q,\uparrow}\hat{c}_{q,\downarrow}\rangle < 0$.

In future experiments, we aim to employ our system as an analog quantum simulator of the BCS pairing mechanism. As first proposed in Ref. [132], cavity-QED experiments with ultracold atoms offer a high degree of control over the single-particle dispersion $\omega(q)$ and the spin-exchange coupling rate χ_+. Furthermore, both ground-state paired states and dynamical superfluid phases can be experimentally accessed by adiabatic preparation and quench experiments, respectively. The observation of such dynamical phases has been recently reported in Ref. [370]; that experiment relies on controlling spin-exchange interactions in a thermal atomic cloud and encoding the Cooper pairs in effective pseudospins of the ensemble. In contrast, our system offers the possibility to naturally encode photon-mediated Cooper pairing in well-defined spin and momentum modes of a degenerate quantum gas. A central question to investigate in future experiments is to what extent the underlying bosonic character of the unpaired atoms in $|\downarrow\rangle$ and $|\uparrow\rangle$ gives rise to qualitatively different emergent phenomena, as compared to conventional Cooper pairs in electron systems.

8.3.3 Further directions

The future directions of our experiment are not limited to the previously discussed proposals. As a final thought, the correlated spin- and momentum-pairs can also serve as a suitable input state for matter-wave interferometry [371]. A promising direction could be to employ time-reversal protocols to implement active SU(1,1) atomic interferometers [304, 372]. For this endeavor, we could benefit from generating pairs in the $F = 2$ hyperfine manifold [372], given that the associated negative quadratic Zeeman splitting $q < 0$ facilitates access to both positive and negative pair energy offsets $\hbar\omega_0 = 2\hbar q + 4\hbar\omega_{\mathrm{rec}}$. By simultaneously quenching $\omega_0 \to -\omega_0$ and the coupling $\chi_+ \to -\chi_+$ in a single-channel configuration, we can evolve the system with the negative Hamiltonian $-\hat{H}$ effectively realizing a time-reversal operation, see Eq. (6.8). To perform quantum-enhanced sensing [281], it will be essential to generate and accurately resolve few hundreds of atom pairs featuring genuine quantum correlations, as discussed in section 6.7.1. A remaining experimental challenge is to devise suitable interferometric protocols to detect relative phase shifts of the atomic wave functions in the different spin states, in the presence of conservative forces such as gravity or magnetic field gradients. For this purpose, we can potentially leverage the opposite motion of the paired atoms in the $m = +1$ and $m = -1$ Zeeman sublevels along the drive direction.

In conclusion, while this dissertation has shed light on various aspects of coherent and dissipative collective phenomena using cavity-assisted Raman transitions, it offers only a glimpse into the vast landscape that awaits exploration.

A Complementary theoretical calculations for momentum-space lattices

Here, we present complementary theoretical calculations for our experiments on dynamical tunneling in a momentum-space lattice, discussed in chapter 5. In appendix A.1, we derive the mean-field Langevin equations of motion in a four-mode expansion which are used to model the first few tunneling events in our system. In appendix A.2, we discuss the role of repulsive contact interactions which give rise to effective attractive interactions in momentum space and self-trapping in the momentum lattice. Finally, in appendix A.3, we discuss the Gross-Pitaevskii equation simulations used to benchmark the dynamics in our system.

This appendix has been adapted from the Supplemental Material of Ref. [90]

> R. Rosa-Medina*, F. Ferri*, F. Finger, N. Dogra, K. Kroeger, R. Lin, R. Chitra, T. Donner and T. Esslinger. *Observing Dynamical Currents in a Non-Hermitian Momentum Lattice.* Physical Review Letters **128**, 143602 (2022)
> * These authors contributed equally to this work

A.1 Equations of motion of the open system

We derive mean-field equations of motion (EOM) for the expectation values of the cavity field $\alpha = \langle \hat{a} \rangle / \sqrt{N}$, atomic populations $\rho_{jj} = \left\langle \hat{\psi}_j^\dagger \hat{\psi}_j \right\rangle / N$ and atomic coherences $\rho_{jk} = \left\langle \hat{\psi}_j^\dagger \hat{\psi}_k \right\rangle / N$, with $\{j, k\} \in \{0, 1, 2, 3\}$. Using the master equation describing photon loss in Eq. (2.21) and the few-mode Hamiltonian in Eq. (5.17), we obtain a set of eleven complex coupled EOM

$$\begin{aligned}
\frac{d}{dt}\alpha &= -(\kappa - i\tilde{\Delta}_\mathrm{c})\alpha + i\sqrt{N}\eta\left(\frac{1}{\sqrt{2}}\rho_{01}^* - \frac{1}{\sqrt{2}}\rho_{02} - \frac{1}{2}\rho_{13}^* + \frac{1}{2}\rho_{23}\right), \\
\frac{d}{dt}\rho_{00} &= i\sqrt{\frac{N}{2}}\eta\left(\alpha\rho_{01} - \alpha^*\rho_{01}^* + \alpha\rho_{02}^* - \alpha^*\rho_{02}\right), \\
\frac{d}{dt}\rho_{11} &= i\sqrt{N}\eta\left(-\frac{1}{\sqrt{2}}\alpha\rho_{01} + \frac{1}{\sqrt{2}}\alpha^*\rho_{01}^* - \frac{1}{2}\alpha\rho_{13} + \frac{1}{2}\alpha^*\rho_{13}^*\right), \\
\frac{d}{dt}\rho_{22} &= i\sqrt{N}\eta\left(-\frac{1}{\sqrt{2}}\alpha\rho_{02}^* + \frac{1}{\sqrt{2}}\alpha^*\rho_{02} - \frac{1}{2}\alpha\rho_{23}^* + \frac{1}{2}\alpha^*\rho_{23}\right), \\
\frac{d}{dt}\rho_{33} &= i\frac{\sqrt{N}}{2}\eta\left(\alpha\rho_{13} - \alpha^*\rho_{13}^* + \alpha\rho_{23}^* - \alpha^*\rho_{23}\right),
\end{aligned} \tag{A.1}$$

$$
\begin{aligned}
\frac{d}{dt}\rho_{01} &= -[\Gamma_\phi + i(\omega_0 + 2\omega_{\mathrm{rec}})]\rho_{01} + i\sqrt{N}\eta\left[\frac{1}{\sqrt{2}}\alpha^*\left(\rho_{00}-\rho_{11}\right) + \frac{1}{\sqrt{2}}\alpha\rho_{12}^* - \frac{1}{2}\alpha\rho_{03}\right], \\
\frac{d}{dt}\rho_{02} &= -[\Gamma_\phi + i(\omega_0 + 2\omega_{\mathrm{rec}})]\rho_{02} + i\sqrt{N}\eta\left[-\frac{1}{\sqrt{2}}\alpha\left(\rho_{00}-\rho_{22}\right) - \frac{1}{\sqrt{2}}\alpha^*\rho_{12} + \frac{1}{2}\alpha^*\rho_{03}\right], \\
\frac{d}{dt}\rho_{03} &= -(\Gamma_\phi + i4\omega_{\mathrm{rec}})\rho_{03} + i\sqrt{N}\eta\left(-\frac{1}{2}\alpha^*\rho_{01} + \frac{1}{2}\alpha\rho_{02} - \frac{1}{\sqrt{2}}\alpha^*\rho_{13} + \frac{1}{\sqrt{2}}\alpha\rho_{23}\right), \\
\frac{d}{dt}\rho_{12} &= i\sqrt{N}\eta\left(-\frac{1}{\sqrt{2}}\alpha\rho_{02} - \frac{1}{\sqrt{2}}\alpha\rho_{01}^* + \frac{1}{2}\alpha^*\rho_{13} + \frac{1}{2}\alpha^*\rho_{23}^*\right), \\
\frac{d}{dt}\rho_{13} &= -[\Gamma_\phi + i(2\omega_{\mathrm{rec}} - \omega_0)]\rho_{13} + i\sqrt{N}\eta\left[\frac{1}{2}\alpha^*\left(\rho_{33}-\rho_{11}\right) - \frac{1}{\sqrt{2}}\alpha^*\rho_{03} + \frac{1}{2}\alpha\rho_{12}\right], \\
\frac{d}{dt}\rho_{23} &= -[\Gamma_\phi + i(2\omega_{\mathrm{rec}} - \omega_0)]\rho_{23} + i\sqrt{N}\eta\left[-\frac{1}{2}\alpha\left(\rho_{33}-\rho_{22}\right) + \frac{1}{\sqrt{2}}\alpha^*\rho_{03} - \frac{1}{2}\alpha^*\rho_{12}^*\right].
\end{aligned}
$$

Here, we employ the mean-field decoupling $\left\langle \hat{a}\hat{\psi}_j^\dagger\hat{\psi}_k \right\rangle \approx N^{3/2}\alpha\rho_{jk}$ and set $\rho_{jk}^* = \rho_{kj}$. Importantly, by explicitly simulating the evolution of the atomic coherences, we can additionally incorporate spin dephasing between the two manifolds $|0\rangle$ and $|1\rangle$. We estimate its rate to be on the order of $\Gamma_\phi = 2\pi \times 0.2\,\mathrm{kHz}$ in our experiment, which we attribute to the combined effect of atomic collisions and magnetic field fluctuations [89].

Numerical simulations

Similar to the procedure outlined in section 2.2.1, we numerically evaluate the mean-field EOMs derived in Eqs. (A.2). We employ the built-in MATLAB solver 'ode45' which is based on a Runge-Kutta (4,5) method [121], choose adaptive time steps and constrain the relative error tolerance in each step to 10^{-8}. To initialize the mean-field dynamics, we sample small fluctuations on top of the expectation value of the cavity field. This sampling ensures an initial cavity field at $t = 0$ compatible with a coherent vacuum state. For the simulations presented in Figs. 5.4 and 5.7, we initialize the atoms in a zero-momentum BEC in the central lattice site $|0,0\rangle_0$ ($\rho_{00} = 1$) and increase the smooth s-shaped ramps, identical to the experimental protocol, see Eq. (5.18). Additionally, we choose spin dephasing rates of $\Gamma_\phi = 2\pi \times 0.15$ kHz and $2\pi \times 0.25$ kHz, respectively.

A.2 Role of contact interactions in momentum-space lattices

Here, we discuss the influence of the repulsive contact interactions of a ^{87}Rb BEC on the dynamics in a momentum-space lattice. We assume that all atoms in each momentum state occupy the same spatial mode. We employ the mode expansion in Eq. (5.8), and obtain a momentum-space representation of the Hamiltonian describing contact interactions

$$\hat{H}_u = g \int_R \hat{\Psi}^\dagger(\hat{\mathbf{x}})\hat{\Psi}^\dagger(\hat{\mathbf{x}})\hat{\Psi}(\hat{\mathbf{x}})\hat{\Psi}(\hat{\mathbf{x}})d\mathbf{x} = u \sum_{\mathbf{j_1},\mathbf{j_2},\mathbf{j_3},\mathbf{j_4}} \hat{c}^\dagger_{\mathbf{j_1}}\hat{c}^\dagger_{\mathbf{j_2}}\hat{c}_{\mathbf{j_3}}\hat{c}_{\mathbf{j_4}}, \tag{A.2}$$

where we introduce the short-hand notation $\hat{c}_{\mathbf{j}} = \hat{c}^\sigma_{(2j+\sigma,2k+\sigma)}$, with $\{j,k\} \in \mathbb{Z}$ and $\sigma \in \{0,1\}$ for the operators in the momentum grid. Momentum conservation is ensured by $\mathbf{j_1}+\mathbf{j_2} = \mathbf{j_3}+\mathbf{j_4}$. The strength of the contact interactions $g = 4\pi\hbar^2 a_\mathrm{s}/M$ depends on the s-wave scattering length of ^{87}Rb atoms in the $F = 1$ hyperfine manifold $a_\mathrm{s} = 100.4a_\mathrm{B}$ [34], with a_B being the Bohr radius. The effective interaction strength in the momentum grid ($u = g\rho/N$) scales with the average atomic density ρ.

Closely following the approach of previous works on momentum-space lattices in Refs. [243, 244, 373], we neglect four-wave mixing processes [261] and retain only mode-conserving contributions of the form $\hat{c}^\dagger_{\mathbf{j}}\hat{c}^\dagger_{\mathbf{k}}\hat{c}_{\mathbf{j}}\hat{c}_{\mathbf{k}}$, $\hat{c}^\dagger_{\mathbf{j}}\hat{c}^\dagger_{\mathbf{k}}\hat{c}_{\mathbf{k}}\hat{c}_{\mathbf{j}}$ and $\hat{c}^\dagger_{\mathbf{j}}\hat{c}^\dagger_{\mathbf{j}}\hat{c}_{\mathbf{j}}\hat{c}_{\mathbf{j}}$. By employing the standard bosonic commutation relations, we can obtain a simplified Hamiltonian

$$\hat{H}_u \approx u \sum_{\mathbf{j}} \Big[\hat{n}_{\mathbf{j}}(\hat{n}_{\mathbf{j}}-1)/2 + \sum_{\mathbf{k}\neq\mathbf{j}} \hat{n}_{\mathbf{j}}\hat{n}_{\mathbf{k}}\Big] = u\hat{N}(\hat{N}-1/2) - u/2\sum_{\mathbf{j}} \hat{n}^2_{\mathbf{j}}, \tag{A.3}$$

where we introduce the density $\hat{n}_{\mathbf{j}} = \hat{c}^\dagger_{\mathbf{j}}\hat{c}_{\mathbf{j}}$ and total particle number operators $\hat{N} = \sum_{\mathbf{j}} \hat{n}_{\mathbf{j}}$. For repulsive contact interactions $u > 0$, as it is the case for the $F = 1$ manifold of ^{87}Rb ($a_\mathrm{s} > 0$), the Hamiltonian of Eq. (A.3) yields effective on-site attractive interactions in the momentum grid. This term can induce dephasing of the population dynamics [373] or give rise to self-trapping in the initial state of the momentum lattice [243, 244], if it becomes dominant over the effective tunneling strength t of the system ($uN > 4t$).

In our experiment, we estimate the effective interactions in the momentum grid to be on the order of $uN/\hbar = g\rho/\hbar \approx 2\pi\times 0.8\,\mathrm{kHz}$, where ρ is the typical average density of $2.1\times 10^{20}\,\mathrm{m}^{-3}$. As the self-consistent tunneling rates in Eq. (5.12) can reach larger values, i.e., $\hbar\cdot\max(|t_\mathrm{SR}|) > uN/4$, we expect that the BEC does not remain self-trapped in the initial momentum state $|0,0\rangle_0$, which is consistent with our experimental observations. To phenomenologically capture the influence of contact interactions, we consider spin dephasing rates on the order of $\Gamma_\phi = uN/(4\hbar) = 2\pi\times 0.2\,\mathrm{kHz}$ in the mean-field simulations using Eqs. (A.2).

A.3 Gross-Pitaevskii equation simulations

Here, we present ab initio Gross-Pitaevskii (GP) equation simulations to benchmark the dynamics in the momentum lattice. We present the corresponding equation of motion and employ them to assess the lifetime of the momentum lattice due to oscillatory dynamics in the harmonic trap. A detailed derivation and discussion of the GP equations of motion for our system can be found in the Supplemental Material of Ref. [90] and in the PhD thesis of Rui Lin [245].

A.3.1 Equations of motion and numerical simulations

We consider the two-component mean-field Hamiltonian

$$\hat{\mathcal{H}} = N \int \Phi^{\dagger} \hat{H}^{(1)} \Phi dx dz + \frac{g_0}{2} N(N-1) \int |\phi_0 + \phi_1|^4 dx dz, \tag{A.4}$$

with $\Phi = (\phi_0, \phi_1)^{\mathrm{T}}$ describing the mean-field wavefunctions of the spin levels $|0\rangle$ $[\phi_0(x,z)]$ and $|1\rangle$ $[\phi_1(x,z)]$. The two-dimensional wavefunctions are normalized as $\int \Phi^{\dagger}\Phi dx dz = 1$. The second term in Eq. (A.4) describes contact interactions between the atoms, where we assume identical inter- and intra-spin coupling constants g_0. This is a good approximation for ^{87}Rb atoms in the $F = 1$ manifold [34]. Additionally, the first term integrates over the single-particle Hamiltonian, which is given by

$$\begin{aligned} \hat{H}^{(1)} \quad = \quad & \left[\frac{\hat{p}^2}{2M} + \frac{M}{2}(\omega_{hx}^2 x^2 + \omega_{hz}^2 z^2)\right] - \omega_0 \sigma_z \\ & + \eta(\alpha + \alpha^*) \cos(kx) \cos(kz) \sigma_y + i\eta(\alpha - \alpha^*) \cos(kx) \sin(kz) \sigma_x, \end{aligned} \tag{A.5}$$

where σ_j refer to the Pauli matrices, with $j \in \{x, y, z\}$. This Hamiltonian contains the same contributions as the one presented in Eq. (5.3), but further considers the harmonic confinement and omits the constant term arising from scalar light-matter interactions. Specifically, the first line includes the kinetic term, the harmonic trap with typical experimental trapping frequencies $[\omega_{hx}, \omega_{hz}] = 2\pi \times [218, 172]$ Hz, and the splitting between the two spin levels ($\propto \omega_0$). The second line describes cavity-assisted Raman transitions between the two spin levels, and coincides with the Hamiltonian in Eq. (5.6) in the limit of balanced drives $\eta := \eta_r = \eta_b$. The contact interaction strength $N g_0 = 1210\hbar^2/m$ is optimized, such that the initial Thomas-Fermi radii coincide with the experimental values $[r_{\mathrm{TF},x}, r_{\mathrm{TF},z}] = [4.3, 5.5]\,\mu$m. The cavity field is treated as a coherent light field and represented by a complex number α. The corresponding GP equation of motion reads

$$\begin{aligned} \partial_t \alpha &= [i\tilde{\Delta}_c - \kappa]\alpha - i\eta N \theta, \\ \theta &= \int \Phi^{\dagger} \left[\cos(kx)\cos(kz)\sigma_y + i\cos(kx)\sin(kz)\sigma_x\right] \Phi dx dz. \end{aligned} \tag{A.6}$$

To numerically evolve the GP equations of motion, we employ the *Multiconfigurational Time-Dependent Hartree Method for Indistinguishable Particles* [374], which is implemented in the MCTDH-X software [375]. We prepare the system in a slightly perturbed BEC state in a harmonic trap, which we empirically choose such that the first superradiant pulse occurs at a time comparable to the one observed in the experiment.

A.3.2 Dynamics due to harmonic confinement and contact interactions

Harmonically confined Bose-Einstein condensates exhibit oscillatory motion when prepared away from their equilibrium configuration [111], for example through excited breathing modes [376]. As the states in the momentum lattice differ from the

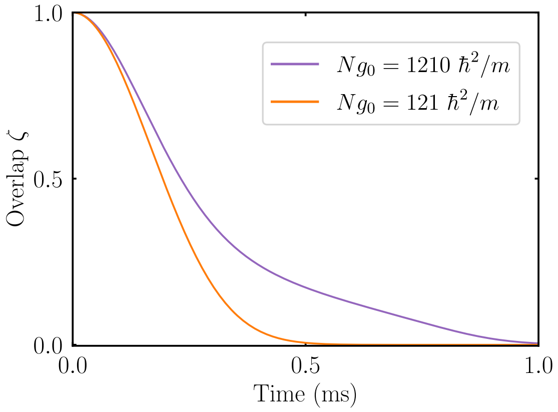

Figure A.1: Lifetime in the momentum lattice. From our GP simulations, we extract the overlap ζ between the mode associated with the lattice sites $|\pm1,\pm1\rangle_1$ and the instantaneous state evolving in an harmonic trap. As shown in the purple (orange) curve, the overlap vanishes at $T_{\mathrm{LT}} \approx 1\,\mathrm{ms}$ ($T_{\mathrm{LT}} \approx 0.5\,\mathrm{ms}$) for the experimentally relevant (weaker) contact interactions indicating the lifetime in the momentum lattice.

equilibrium Thomas-Fermi distribution, we expect them to oscillate in real space in the trap. This moves the corresponding momentum components out of the grid nodes at integer multiples of the recoil momentum k, progressively rendering the tight-binding picture invalid. Naively, we expect the lifetime in the momentum lattice to be comparable with the inverse trap frequency. Nevertheless, our Gross-Pitaevskii simulations indicate that contact interactions can increase this lifetime.

To quantify the role of contact interactions where we prepare an initial wavefunction

$$\phi(x,z) = \psi(x,z)\cos(kx)\cos(kz). \tag{A.7}$$

The envelop function $\psi(x,z)$ describes a Thomas-Fermi profile or a Gaussian profile, depending on whether contact interactions are considered or not. This state resembles the atomic state after the first tunneling event in the momentum lattice, i.e., $|\pm1,\pm1\rangle_1$. We evolve the state in the harmonic trap while enforcing a vanishing cavity field. The same simulation is performed for both the experimentally relevant contact interaction strength $Ng_0 = 1210\ \hbar^2/m$ and for a significantly smaller value $Ng_0 = 121\ \hbar^2/m$. During the simulation, we extract the overlap between the instantaneous wavefunction and the initial one

$$\zeta = \left| \int dk_x dk_z \phi^*(k_x,k_z;t=0)\phi(k_x,k_z;t) \right| = \left| \int dx dz \phi^*(x,z;t=0)\phi(x,z;t) \right|, \tag{A.8}$$

and show it in Fig. A.1. For the relevant interaction strength, we infer a lifetime of $T_{\mathrm{LT}} \approx 1\,\mathrm{ms}$, which is approximately twice longer than for a system with weak contact interactions. In Fig. A.2, we show representative real- and momentum-space distributions for the two cases at different stages of the evolution. Contact interactions effectively diffuse the lattice peaks in momentum space, which slows down the evolution of the atomic distribution away from the grid nodes of the momentum-space lattice. The lifetime T_{LT} is compatible with the maximal time delay observed between subsequent superradiant pulses in Figs. 5.4 and 5.5.

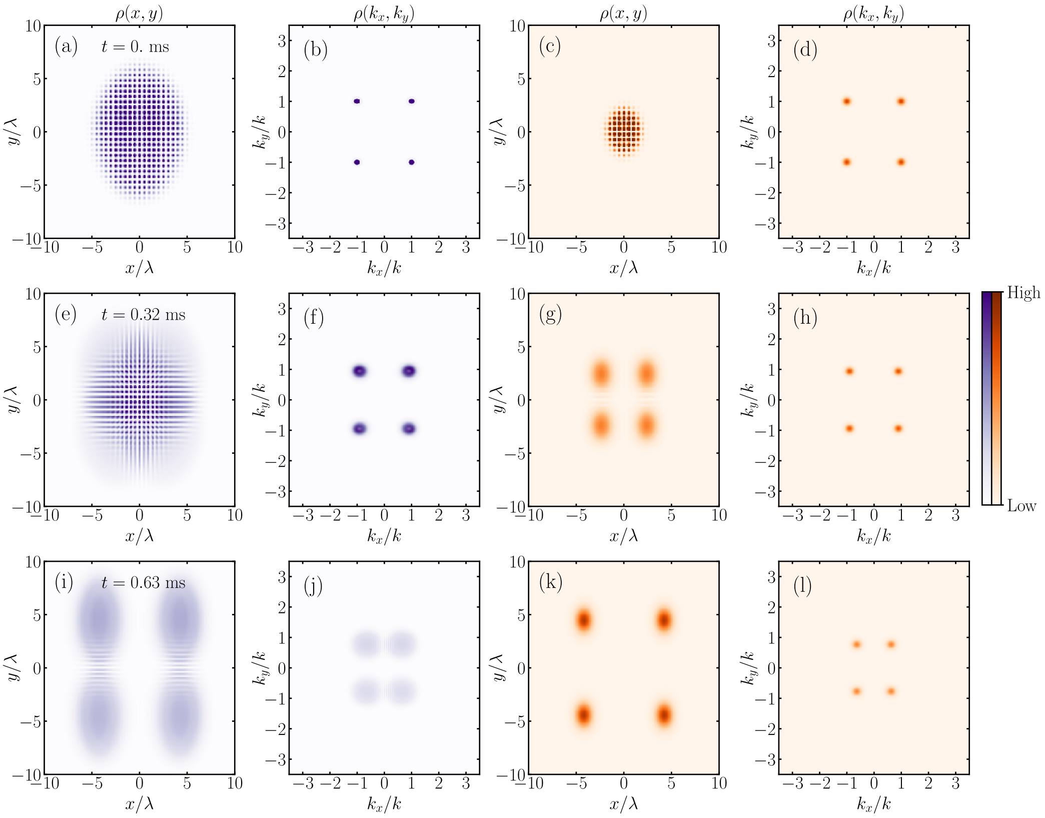

Figure A.2: Representative snapshots of the evolution of the real-and momentum-space distributions. We consider 2D harmonically confined atomic cloud initialized in the state $\phi(x, z)$ for the experimentally relevant trap frequencies $[\omega_{hx}, \omega_{hz}] = 2\pi \cdot [218, 172]$ Hz [cf. Eq. (A.7)]. The purple (orange) colormap corresponds to the experimentally relevant (smaller) contact interactions, which are on the order of $Ng_0 = 1210\ \hbar^2/m$ ($Ng_0 = 121\ \hbar^2/m$).

A.3.3 Cascaded hopping in the momentum lattice

Finally, we introduce the atomic coherences between different lattice sites in order to simulate and visualize the cascaded dynamics in Fig. 5.9. The atomic order parameter θ associated with the GP equations of motion can be evaluated as

$$\begin{aligned} \theta &= \sum_{\substack{j,l\in\mathbb{Z}\\ s_{1,2}=\pm 1}} \theta_{j,l,s_1,s_2} \\ N\theta_{j,l,s_1,s_2} &= -\frac{1}{\sqrt{8}}\left[\left\langle \hat{c}^{1\dagger}_{(2j+s_1,2l+s_2)}\hat{c}^{0}_{(2j,2l)}\right\rangle - is_2\left\langle \hat{c}^{0\dagger}_{(2j,2l)}\hat{c}^{1}_{(2j+s_1,2l+s_2)}\right\rangle\right], \end{aligned} \tag{A.9}$$

which is a sum of local two-site coherences $\langle \hat{c}^{1\dagger}_{(2j+s_1,2l+s_2)}\hat{c}^{0}_{(2j,2l)}\rangle$ in the momentum lattice. As the GP simulations operate in the continuum, we approximate these coherences by integrals over the the corresponding Brillouin zones

$$\left\langle \hat{c}^{1\dagger}_{(2j+s_1,2l+s_2)}\hat{c}^{0}_{(2j,2l)}\right\rangle = \int_{-k}^{k}\int_{-k}^{k} dk_x dk_z \phi_1^*(k_x-(2j+s_1)k, k_z-(2l+s_2)k)\phi_0(k_x-2jk, k_z-2lk), \tag{A.10}$$

Finally, we scale the coherences by a factor of $\eta N/(\tilde{\Delta}_c + i\kappa)$ to obtain a result commensurate with the cavity field α, and group them according to the associated tunneling events in the momentum lattice

$$\begin{aligned} \xi_1 &= \frac{\eta N}{\tilde{\Delta}_c + i\kappa}\left(\theta_{0,0,+1,+1} + \theta_{0,0,+1,-1} + \theta_{0,0,-1,+1} + \theta_{0,0,-1,-1}\right), \\ \xi_2 &= \frac{\eta N}{\tilde{\Delta}_c + i\kappa}\left(\theta_{0,2,+1,-1} + \theta_{0,2,-1,-1} + \theta_{0,-2,+1,+1} + \theta_{0,-2,-1,+1}\right), \\ \xi_3 &= \frac{\eta N}{\tilde{\Delta}_c + i\kappa}\left(\theta_{2,2,-1,-1} + \theta_{2,-2,-1,+1} + \theta_{-2,2,+1,-1} + \theta_{-2,-2,+1,+1}\right), \\ \xi_4 &= \frac{\eta N}{\tilde{\Delta}_c + i\kappa}\left(\theta_{2,0,-1,+1} + \theta_{2,0,-1,-1} + \theta_{-2,0,+1,+1} + \theta_{-2,0,+1,-1}\right), \\ \xi_5 &= \frac{\eta N}{\tilde{\Delta}_c + i\kappa}\left(\theta_{0,2,+1,+1} + \theta_{0,2,-1,+1} + \theta_{0,-2,+1,-1} + \theta_{0,-2,-1,-1}\right). \end{aligned} \tag{A.11}$$

These two-site coherences are schematically illustrated in Fig. 5.9(b), and mutually stimulate each other in the parameter regime where we observe hopping cascades, see Fig. 5.8.

Bibliography

[1] W. N. Cottingham and D. A. Greenwood. *An Introduction to the Standard Model of Particle Physics.* Cambridge University Press, 2 edition (2007).

[2] P. W. Anderson. *More Is Different.* Science **177**, 393–396 (1972).

[3] S. Kivelson and S. A. Kivelson. *Defining emergence in physics.* NPJ Quantum Materials **1**, 16024 (2016).

[4] L. Landau. *On the theory of phase transitions.* In *Collected Papers of L.D. Landau*, pages 193–216. Pergamon (1965).

[5] N. W. Aschcroft and N. D. Mermin. *Solid State Physics.* Harcourt College Publishers (1975).

[6] S. Sachdev. *Quantum magnetism and criticality.* Nature Physics **4**, 173–185 (2008).

[7] J. Bardeen, L. N. Cooper, and J. R. Schrieffer. *Microscopic Theory of Superconductivity.* Physical Review **106**, 162–164 (1957).

[8] A. Rivas and S. F. Huelga. *Time Evolution in Open Quantum Systems*, pages 19–31. Springer Berlin Heidelberg, Berlin, Heidelberg (2012).

[9] T. F. Nova, A. S. Disa, M. Fechner, and A. Cavalleri. *Metastable ferroelectricity in optically strained* $SrTiO_3$. Science **364**, 1075–1079 (2019).

[10] X. Li, T. Qiu, J. Zhang, E. Baldini, J. Lu, A. M. Rappe, and K. A. Nelson. *Terahertz field–induced ferroelectricity in quantum paraelectric* $SrTiO_3$. Science **364**, 1079–1082 (2019).

[11] D. Fausti, R. I. Tobey, N. Dean, S. Kaiser, A. Dienst, M. C. Hoffmann, S. Pyon, T. Takayama, H. Takagi, and A. Cavalleri. *Light-Induced Superconductivity in a Stripe-Ordered Cuprate.* Science **331**, 189–191 (2011).

[12] M. Mitrano, A. Cantaluppi, D. Nicoletti, S. Kaiser, A. Perucchi, S. Lupi, P. Di Pietro, D. Pontiroli, M. Riccò, S. R. Clark, D. Jaksch, and A. Cavalleri. *Possible light-induced superconductivity in* K_3C_{60} *at high temperature.* Nature **530**, 461–464 (2016).

[13] W. M. Yen. *Introduction: Advances in the laser spectroscopy of solids*, pages 1–28. Springer Berlin Heidelberg, Berlin, Heidelberg (1989).

[14] R. P. Feynman. *Simulating physics with computers.* International Journal of Theoretical Physics **21**, 467–488 (1982).

[15] I. M. Georgescu, S. Ashhab, and F. Nori. *Quantum simulation.* Rev. Mod. Phys. **86**, 153–185 (2014).

[16] G. S. Paraoanu. *Recent Progress in Quantum Simulation Using Superconducting Circuits.* Journal of Low Temperature Physics **175**, 633–654 (2014).

[17] R. Blatt and C. F. Roos. *Quantum simulations with trapped ions.* Nature Physics **8**, 277–284 (2012).

[18] A. Browaeys and T. Lahaye. *Many-body physics with individually controlled Rydberg atoms.* Nature Physics **16**, 132–142 (2020).

[19] A. Aspuru-Guzik and P. Walther. *Photonic quantum simulators.* Nature Physics **8**, 285–291 (2012).

[20] J. Bloch, A. Cavalleri, V. Galitski, M. Hafezi, and A. Rubio. *Strongly correlated electron–photon systems.* Nature **606**, 41–48 (2022).

[21] C. Gross and I. Bloch. *Quantum simulations with ultracold atoms in optical lattices.* Science **357**, 995–1001 (2017).

[22] F. Schäfer, T. Fukuhara, S. Sugawa, Y. Takasu, and Y. Takahashi. *Tools for quantum simulation with ultracold atoms in optical lattices.* Nature Reviews Physics **2**, 411–425 (2020).

[23] A. J. Daley, I. Bloch, C. Kokail, S. Flannigan, N. Pearson, M. Troyer, and P. Zoller. *Practical quantum advantage in quantum simulation.* Nature **607**, 667–676 (2022).

[24] R. W. Boyd. *Nonlinear Optics.* Academic Press, Burlington, third edition edition (2008).

[25] K. Poulios, R. Keil, D. Fry, J. D. A. Meinecke, J. C. F. Matthews, A. Politi, M. Lobino, M. Gräfe, M. Heinrich, S. Nolte, A. Szameit, and J. L. O'Brien. *Quantum Walks of Correlated Photon Pairs in Two-Dimensional Waveguide Arrays.* Phys. Rev. Lett. **112**, 143604 (2014).

[26] I. Carusotto and C. Ciuti. *Quantum fluids of light.* Reviews of Modern Physics **85**, 299–366 (2013).

[27] C. Ciuti, P. Schwendimann, and A. Quattropani. *Theory of polariton parametric interactions in semiconductor microcavities.* Semiconductor Science and Technology **18**, S279 (2003).

[28] J. Kasprzak, M. Richard, S. Kundermann, A. Baas, P. Jeambrun, J. M. J. Keeling, F. M. Marchetti, M. H. Szymańska, R. André, J. L. Staehli, V. Savona, P. B. Littlewood, B. Deveaud, and L. S. Dang. *Bose–Einstein condensation of exciton polaritons.* Nature **443**, 409–414 (2006).

[29] A. Amo, J. Lefrère, S. Pigeon, C. Adrados, C. Ciuti, I. Carusotto, R. Houdré, E. Giacobino, and A. Bramati. *Superfluidity of polaritons in semiconductor microcavities.* Nature Physics **5**, 805–810 (2009).

[30] A. Amo and J. Bloch. *Exciton-polaritons in lattices: A non-linear photonic simulator.* Comptes Rendus Physique **17**, 934–945 (2016). Polariton physics / Physique des polaritons.

[31] T. Ozawa, H. M. Price, A. Amo, N. Goldman, M. Hafezi, L. Lu, M. C. Rechtsman, D. Schuster, J. Simon, O. Zilberberg, and I. Carusotto. *Topological photonics.* Rev. Mod. Phys. **91**, 015006 (2019).

[32] C. E. Rüter, K. G. Makris, R. El-Ganainy, D. N. Christodoulides, M. Segev, and D. Kip. *Observation of parity–time symmetry in optics.* Nature Physics **6**, 192–195 (2010).

[33] R. Ma, B. Saxberg, C. Owens, N. Leung, Y. Lu, J. Simon, and D. I. Schuster. *A dissipatively stabilized Mott insulator of photons.* Nature **566**, 51–57 (2019).

[34] D. M. Stamper-Kurn and M. Ueda. *Spinor Bose gases: Symmetries, magnetism, and quantum dynamics.* Rev. Mod. Phys. **85**, 1191–1244 (2013).

[35] T. Ozawa and H. M. Price. *Topological quantum matter in synthetic dimensions.* Nature Reviews Physics **1**, 349–357 (2019).

[36] W. S. Bakr, A. Peng, M. E. Tai, R. Ma, J. Simon, J. I. Gillen, S. Fölling, L. Pollet, and M. Greiner. *Probing the Superfluid–to–Mott Insulator Transition at the Single-Atom Level.* Science **329**, 547–550 (2010).

[37] J. F. Sherson, C. Weitenberg, M. Endres, M. Cheneau, I. Bloch, and S. Kuhr. *Single-atom-resolved fluorescence imaging of an atomic Mott insulator.* Nature **467**, 68–72 (2010).

[38] E. Altman, E. Demler, and M. D. Lukin. *Probing many-body states of ultracold atoms via noise correlations.* Physical Review A **70**, 013603 (2004).

[39] M. Greiner, O. Mandel, T. Esslinger, T. W. Hänsch, and I. Bloch. *Quantum phase transition from a superfluid to a Mott insulator in a gas of ultracold atoms.* Nature **415**, 39–44 (2002).

[40] M. Greiner, C. A. Regal, and D. S. Jin. *Emergence of a molecular Bose–Einstein condensate from a Fermi gas.* Nature **426**, 537–540 (2003).

[41] S. Jochim, M. Bartenstein, A. Altmeyer, G. Hendl, S. Riedl, C. Chin, J. Hecker Denschlag, and R. Grimm. *Bose-Einstein Condensation of Molecules.* Science **302**, 2101–2103 (2003).

[42] D. Greif, T. Uehlinger, G. Jotzu, L. Tarruell, and T. Esslinger. *Short-Range Quantum Magnetism of Ultracold Fermions in an Optical Lattice.* Science **340**, 1307–1310 (2013).

[43] A. Mazurenko, C. S. Chiu, G. Ji, M. F. Parsons, M. Kanász-Nagy, R. Schmidt, F. Grusdt, E. Demler, D. Greif, and M. Greiner. *A cold-atom Fermi–Hubbard antiferromagnet.* Nature **545**, 462–466 (2017).

[44] Z. Hadzibabic, P. Krüger, M. Cheneau, B. Battelier, and J. Dalibard. *Berezinskii–Kosterlitz–Thouless crossover in a trapped atomic gas.* Nature **441**, 1118–1121 (2006).

[45] S. Krinner, D. Stadler, D. Husmann, J.-P. Brantut, and T. Esslinger. *Observation of quantized conductance in neutral matter.* Nature **517**, 64–67 (2015).

[46] S. Krinner, T. Esslinger, and J.-P. Brantut. *Two-terminal transport measurements with cold atoms.* Journal of Physics: Condensed Matter **29**, 343003 (2017).

[47] M. Prüfer, P. Kunkel, H. Strobel, S. Lannig, D. Linnemann, C.-M. Schmied, J. Berges, T. Gasenzer, and M. K. Oberthaler. *Observation of universal dynamics in a spinor Bose gas far from equilibrium.* Nature **563**, 217–220 (2018).

[48] S. Erne, R. Bücker, T. Gasenzer, J. Berges, and J. Schmiedmayer. *Universal dynamics in an isolated one-dimensional Bose gas far from equilibrium.* Nature **563**, 225–229 (2018).

[49] C. Eigen, J. A. P. Glidden, R. Lopes, E. A. Cornell, R. P. Smith, and Z. Hadzibabic. *Universal prethermal dynamics of Bose gases quenched to unitarity.* Nature **563**, 221–224 (2018).

[50] J. Dalibard. *Collisional dynamics of ultra-cold atomic gases.* In *Bose-Einstein Condensation in Atomic Gases*, pages 321–349. IOS Press (1999).

[51] T. Lahaye, C. Menotti, L. Santos, M. Lewenstein, and T. Pfau. *The physics of dipolar bosonic quantum gases.* Reports on Progress in Physics **72**, 126401 (2009).

[52] L. Chomaz, I. Ferrier-Barbut, F. Ferlaino, B. Laburthe-Tolra, B. L. Lev, and T. Pfau. *Dipolar physics: a review of experiments with magnetic quantum gases.* Reports on Progress in Physics **86**, 026401 (2022).

[53] S. A. Moses, J. P. Covey, M. T. Miecnikowski, D. S. Jin, and J. Ye. *New frontiers for quantum gases of polar molecules.* Nature Physics **13**, 13–20 (2017).

[54] J. L. Bohn, A. M. Rey, and J. Ye. *Cold molecules: Progress in quantum engineering of chemistry and quantum matter.* Science **357**, 1002–1010 (2017).

[55] A. Browaeys, D. Barredo, and T. Lahaye. *Experimental investigations of dipole–dipole interactions between a few Rydberg atoms.* Journal of Physics B: Atomic, Molecular and Optical Physics **49**, 152001 (2016).

[56] X. Wu, X. Liang, Y. Tian, F. Yang, C. Chen, Y.-C. Liu, M. K. Tey, and L. You. *A concise review of Rydberg atom based quantum computation and quantum simulation.* Chinese Physics B **30**, 020305 (2021).

[57] H. Ritsch, P. Domokos, F. Brennecke, and T. Esslinger. *Cold atoms in cavity-generated dynamical optical potentials.* Rev. Mod. Phys. **85**, 553–601 (2013).

[58] F. Mivehvar, F. Piazza, T. Donner, and H. Ritsch. *Cavity QED with quantum gases: new paradigms in many-body physics.* Advances in Physics **70**, 1–153 (2021).

[59] K. Hepp and E. H. Lieb. *On the superradiant phase transition for molecules in a quantized radiation field: the Dicke maser model.* Annals of Physics **76**, 360 – 404 (1973).

[60] Y. K. Wang and F. T. Hioe. *Phase Transition in the Dicke Model of Superradiance.* Phys. Rev. A **7**, 831–836 (1973).

[61] F. Dimer, B. Estienne, A. S. Parkins, and H. J. Carmichael. *Proposed realization of the Dicke-model quantum phase transition in an optical cavity QED system.* Phys. Rev. A **75**, 013804 (2007).

[62] K. Baumann, C. Guerlin, F. Brennecke, and T. Esslinger. *Dicke quantum phase transition with a superfluid gas in an optical cavity.* Nature **464**, 1301–1306 (2010).

[63] R. Mottl, F. Brennecke, K. Baumann, R. Landig, T. Donner, and T. Esslinger. *Roton-Type Mode Softening in a Quantum Gas with Cavity-Mediated Long-Range Interactions.* Science **336**, 1570–1573 (2012).

[64] K. Baumann, R. Mottl, F. Brennecke, and T. Esslinger. *Exploring Symmetry Breaking at the Dicke Quantum Phase Transition.* Phys. Rev. Lett. **107**, 140402 (2011).

[65] R. Landig, L. Hruby, N. Dogra, M. Landini, R. Mottl, T. Donner, and T. Esslinger. *Quantum phases from competing short- and long-range interactions in an optical lattice.* Nature **532**, 476–479 (2016).

[66] J. Klinder, H. Keßler, M. R. Bakhtiari, M. Thorwart, and A. Hemmerich. *Observation of a Superradiant Mott Insulator in the Dicke-Hubbard Model.* Phys. Rev. Lett. **115**, 230403 (2015).

[67] L. Hruby, N. Dogra, M. Landini, T. Donner, and T. Esslinger. *Metastability and avalanche dynamics in strongly correlated gases with long-range interactions.* Proceedings of the National Academy of Sciences **115**, 3279–3284 (2018).

[68] J. Léonard, A. Morales, P. Zupancic, T. Esslinger, and T. Donner. *Supersolid formation in a quantum gas breaking a continuous translational symmetry.* Nature **543**, 87–90 (2017).

[69] V. D. Vaidya, Y. Guo, R. M. Kroeze, K. E. Ballantine, A. J. Kollár, J. Keeling, and B. L. Lev. *Tunable-Range, Photon-Mediated Atomic Interactions in Multimode Cavity QED.* Phys. Rev. X **8**, 011002 (2018).

[70] X. Zhang, Y. Chen, Z. Wu, J. Wang, J. Fan, S. Deng, and H. Wu. *Observation of a superradiant quantum phase transition in an intracavity degenerate Fermi gas.* Science **373**, 1359–1362 (2021).

[71] V. Helson, T. Zwettler, F. Mivehvar, E. Colella, K. Roux, H. Konishi, H. Ritsch, and J.-P. Brantut. *Density-wave ordering in a unitary Fermi gas with photon-mediated interactions.* Nature **618**, 716–720 (2023).

[72] F. Brennecke, R. Mottl, K. Baumann, R. Landig, T. Donner, and T. Esslinger. *Real-time observation of fluctuations at the driven-dissipative Dicke phase transition.* Proceedings of the National Academy of Sciences **110**, 11763–11767 (2013).

[73] N. Dogra, M. Landini, K. Kroeger, L. Hruby, T. Donner, and T. Esslinger. *Dissipation-induced structural instability and chiral dynamics in a quantum gas.* Science **366**, 1496–1499 (2019).

[74] Keßler, Hans and Kongkhambut, Phatthamon and Georges, Christoph and Mathey, Ludwig and Cosme, Jayson G. and Hemmerich, Andreas. *Observation of a Dissipative Time Crystal.* Phys. Rev. Lett. **127**, 043602 (2021).

[75] D. Dreon, A. Baumgärtner, X. Li, S. Hertlein, T. Esslinger, and T. Donner. *Self-oscillating pump in a topological dissipative atom–cavity system.* Nature **608**, 494–498 (2022).

[76] F. Mivehvar, H. Ritsch, and F. Piazza. *Cavity-Quantum-Electrodynamical Toolbox for Quantum Magnetism.* Phys. Rev. Lett. **122**, 113603 (2019).

[77] F. Le Kien, P. Schneeweiss, and A. Rauschenbeutel. *Dynamical polarizability of atoms in arbitrary light fields: general theory and application to cesium.* The European Physical Journal D **67**, 92 (2013).

[78] M. Landini, N. Dogra, K. Kroeger, L. Hruby, T. Donner, and T. Esslinger. *Formation of a Spin Texture in a Quantum Gas Coupled to a Cavity.* Phys. Rev. Lett. **120**, 223602 (2018).

[79] R. M. Kroeze, Y. Guo, V. D. Vaidya, J. Keeling, and B. L. Lev. *Spinor Self-Ordering of a Quantum Gas in a Cavity.* Phys. Rev. Lett. **121**, 163601 (2018).

[80] E. J. Davis, G. Bentsen, L. Homeier, T. Li, and M. H. Schleier-Smith. *Photon-Mediated Spin-Exchange Dynamics of Spin-1 Atoms.* Physical Review Letters **122**, 010405 (2019).

[81] E. J. Davis, A. Periwal, E. S. Cooper, G. Bentsen, S. J. Evered, K. Van Kirk, and M. H. Schleier-Smith. *Protecting Spin Coherence in a Tunable Heisenberg Model.* Physical Review Letters **125**, 060402 (2020).

[82] M. A. Norcia, R. J. Lewis-Swan, J. R. K. Cline, B. Zhu, A. M. Rey, and J. K. Thompson. *Cavity-mediated collective spin-exchange interactions in a strontium superradiant laser.* Science **361**, 259–262 (2018).

[83] J. A. Muniz, D. Barberena, R. J. Lewis-Swan, D. J. Young, J. R. K. Cline, A. M. Rey, and J. K. Thompson. *Exploring dynamical phase transitions with cold atoms in an optical cavity.* Nature **580**, 602–607 (2020).

[84] A. Periwal, E. S. Cooper, P. Kunkel, J. F. Wienand, E. J. Davis, and M. Schleier-Smith. *Programmable interactions and emergent geometry in an array of atom clouds.* Nature **600**, 630–635 (2021).

[85] E. Davis. *Engineering and imaging nonlocal spin dynamics in an optical cavity.* Doctoral thesis, Stanford University (2020).

[86] J. G. Bohnet, Z. Chen, J. M. Weiner, D. Meiser, M. J. Holland, and J. K. Thompson. *A steady-state superradiant laser with less than one intracavity photon.* Nature **484**, 78–81 (2012).

[87] M. A. Norcia and J. K. Thompson. *Cold-Strontium Laser in the Superradiant Crossover Regime.* Phys. Rev. X **6**, 011025 (2016).

[88] R. H. Dicke. *Coherence in Spontaneous Radiation Processes.* Phys. Rev. **93**, 99–110 (1954).

[89] F. Ferri, R. Rosa-Medina, F. Finger, N. Dogra, M. Soriente, O. Zilberberg, T. Donner, and T. Esslinger. *Emerging Dissipative Phases in a Superradiant Quantum Gas with Tunable Decay.* Phys. Rev. X **11**, 041046 (2021).

[90] R. Rosa-Medina, F. Ferri, F. Finger, N. Dogra, K. Kroeger, R. Lin, R. Chitra, T. Donner, and T. Esslinger. *Observing Dynamical Currents in a Non-Hermitian Momentum Lattice.* Physical Review Letters **128**, 143602 (2022).

[91] F. Finger, R. Rosa-Medina, N. Reiter, P. Christodoulou, T. Donner, and T. Esslinger. *Spin-and momentum-correlated atom pairs mediated by photon exchange.* arXiv preprint arXiv:2303.11326 (2023).

[92] L. Carl, R. Rosa-Medina, S. D. Huber, T. Esslinger, N. Dogra, and T. Dubcek. *Phases, instabilities and excitations in a two-component lattice model with photon-mediated interactions.* Phys. Rev. Res. **5**, L032003 (2023).

[93] E. L. Raab, M. Prentiss, A. Cable, S. Chu, and D. E. Pritchard. *Trapping of Neutral Sodium Atoms with Radiation Pressure.* Phys. Rev. Lett. **59**, 2631–2634 (1987).

[94] S. Chu, J. E. Bjorkholm, A. Ashkin, and A. Cable. *Experimental Observation of Optically Trapped Atoms.* Phys. Rev. Lett. **57**, 314–317 (1986).

[95] R. Grimm, M. Weidemüller, and Y. B. Ovchinnikov. *Optical Dipole Traps for Neutral Atoms.* Advances In Atomic, Molecular, and Optical Physics **42**, 95–170 (2000).

[96] E. M. Purcell, H. C. Torrey, and R. V. Pound. *Resonance Absorption by Nuclear Magnetic Moments in a Solid.* Phys. Rev. **69**, 37–38 (1946).

[97] M. Brune, F. Schmidt-Kaler, A. Maali, J. Dreyer, E. Hagley, J. M. Raimond, and S. Haroche. *Quantum Rabi Oscillation: A Direct Test of Field Quantization in a Cavity.* Phys. Rev. Lett. **76**, 1800–1803 (1996).

[98] S. Gleyzes, S. Kuhr, C. Guerlin, J. Bernu, S. Deléglise, U. Busk Hoff, M. Brune, J.-M. Raimond, and S. Haroche. *Quantum jumps of light recording the birth and death of a photon in a cavity.* Nature **446**, 297–300 (2007).

[99] R. J. Thompson, G. Rempe, and H. J. Kimble. *Observation of normal-mode splitting for an atom in an optical cavity.* Phys. Rev. Lett. **68**, 1132–1135 (1992).

[100] A. Boca, R. Miller, K. M. Birnbaum, A. D. Boozer, J. McKeever, and H. J. Kimble. *Observation of the Vacuum Rabi Spectrum for One Trapped Atom.* Phys. Rev. Lett. **93**, 233603 (2004).

[101] F. Brennecke, T. Donner, S. Ritter, T. Bourdel, M. Köhl, and T. Esslinger. *Cavity QED with a Bose–Einstein condensate.* Nature **450**, 268–271 (2007).

[102] H. Konishi, K. Roux, V. Helson, and J.-P. Brantut. *Universal pair polaritons in a strongly interacting Fermi gas.* Nature **596**, 509–513 (2021).

[103] G. Grynberg, A. Aspect, C. Fabre, and C. Cohen-Tannoudji. *Introduction to Quantum Optics: From the Semi-classical Approach to Quantized Light.* Cambridge University Press (2010).

[104] M. O. Scully and M. S. Zubairy. *Atom–field interaction – semiclassical theory*, page 145–192. Cambridge University Press (1997).

[105] Y.-J. Lin, R. L. Compton, K. Jiménez-García, J. V. Porto, and I. B. Spielman. *Synthetic magnetic fields for ultracold neutral atoms.* Nature **462**, 628–632 (2009).

[106] J. de Hond, J. Xiang, W. C. Chung, E. Cruz-Colón, W. Chen, W. C. Burton, C. J. Kennedy, and W. Ketterle. *Preparation of the Spin-Mott State: A Spinful Mott Insulator of Repulsively Bound Pairs.* Phys. Rev. Lett. **128**, 093401 (2022).

[107] I. B. Spielman. *Raman processes and effective gauge potentials.* Phys. Rev. A **79**, 063613 (2009).

[108] N. Dogra. *Interaction- and dissipation-induced phenomena in a quantum gas coupled to a cavity.* PhD thesis, ETH Zurich (2019).

[109] D. A. Steck. *Rubidium 87 D line data.* (2001).

[110] F. Schmidt, D. Mayer, M. Hohmann, T. Lausch, F. Kindermann, and A. Widera. *Precision measurement of the Rb 87 tune-out wavelength in the hyperfine ground state F = 1 at 790 nm.* Physical Review A **93**, 022507 (2016).

[111] F. Dalfovo, S. Giorgini, L. P. Pitaevskii, and S. Stringari. *Theory of Bose-Einstein condensation in trapped gases.* Rev. Mod. Phys. **71**, 463–512 (1999).

[112] Y. V. Nazarov and J. Danon. *Second quantization*, page 63–86. Cambridge University Press (2013).

[113] M. Tavis and F. W. Cummings. *Exact Solution for an N-Molecule—Radiation-Field Hamiltonian.* Phys. Rev. **170**, 379–384 (1968).

[114] M. Hosseini, Y. Duan, K. M. Beck, Y.-T. Chen, and V. Vuletić. *Cavity Cooling of Many Atoms.* Phys. Rev. Lett. **118**, 183601 (2017).

[115] F. Brennecke. *Collective interaction between a Bose-Einstein condensate and a coherent few-photon field.* PhD thesis, ETH Zürich (2009).

[116] H.-P. Breuer and F. Petruccione. *The Theory of Open Quantum Systems.* Oxford University Press (2007).

[117] S. B. Jäger, T. Schmit, G. Morigi, M. J. Holland, and R. Betzholz. *Lindblad Master Equations for Quantum Systems Coupled to Dissipative Bosonic Modes.* Phys. Rev. Lett. **129**, 063601 (2022).

[118] D. Manzano. *A short introduction to the Lindblad master equation.* AIP Advances **10**, 025106 (2020).

[119] R. Kubo. *Generalized Cumulant Expansion Method.* Journal of the Physical Society of Japan **17**, 1100–1120 (1962).

[120] M. Gross and S. Haroche. *Superradiance: An essay on the theory of collective spontaneous emission.* Physics Reports **93**, 301–396 (1982).

[121] L. F. Shampine and M. W. Reichelt. *The MATLAB ODE Suite.* SIAM Journal on Scientific Computing **18**, 1–22 (1997).

[122] F. Reiter and A. S. Sørensen. *Effective operator formalism for open quantum systems.* Physical Review A **85**, 032111 (2012).

[123] *Lindblad master equation solver.* Lindblad Master Equation Solver - QuTiP 4.7 Documentation (2022).

[124] K. Stitely, F. Finger, R. Rosa-Medina, F. Ferri, T. Donner, T. Esslinger, S. Parkins, and B. Krauskopf. *Quantum Fluctuation Dynamics of Dispersive Superradiant Pulses in a Hybrid Light-Matter System.* arXiv preprint arXiv:2302.08078 (2023).

[125] P. Kirton and J. Keeling. *Superradiant and lasing states in driven-dissipative Dicke models.* New Journal of Physics **20**, 015009 (2018).

[126] K. Debnath, Y. Zhang, and K. Mølmer. *Lasing in the superradiant crossover regime.* Phys. Rev. A **98**, 063837 (2018).

[127] G. Vrijsen, O. Hosten, J. Lee, S. Bernon, and M. A. Kasevich. *Raman Lasing with a Cold Atom Gain Medium in a High-Finesse Optical Cavity.* Physical Review Letters **107**, 063904 (2011).

[128] M. A. Norcia, M. N. Winchester, J. R. K. Cline, and J. K. Thompson. *Superradiance on the millihertz linewidth strontium clock transition.* Science Advances **2** (2016).

[129] T. Laske, H. Winter, and A. Hemmerich. *Pulse Delay Time Statistics in a Superradiant Laser with Calcium Atoms.* Phys. Rev. Lett. **123**, 103601 (2019).

[130] B. Sundar, D. Barberena, A. P. n. Orioli, A. Chu, J. K. Thompson, A. M. Rey, and R. J. Lewis-Swan. *Bosonic Pair Production and Squeezing for Optical Phase Measurements in Long-Lived Dipoles Coupled to a Cavity.* Phys. Rev. Lett. **130**, 113202 (2023).

[131] E. Colella, R. Citro, M. Barsanti, D. Rossini, and M.-L. Chiofalo. *Quantum phases of spinful Fermi gases in optical cavities.* Physical Review B **97**, 134502 (2018).

[132] R. J. Lewis-Swan, D. Barberena, J. R. K. Cline, D. J. Young, J. K. Thompson, and A. M. Rey. *Cavity-QED Quantum Simulator of Dynamical Phases of a Bardeen-Cooper-Schrieffer Superconductor.* Physical Review Letters **126**, 173601 (2021).

[133] I. D. Leroux, M. H. Schleier-Smith, and V. Vuletić. *Implementation of Cavity Squeezing of a Collective Atomic Spin.* Phys. Rev. Lett. **104**, 073602 (2010).

[134] Z. Chen, J. G. Bohnet, S. R. Sankar, J. Dai, and J. K. Thompson. *Conditional Spin Squeezing of a Large Ensemble via the Vacuum Rabi Splitting.* Phys. Rev. Lett. **106**, 133601 (2011).

[135] A. W. Öttl. *Correlations and Counting Statistics of an Atom Laser.* Phd thesis, ETH Zürich (2006).

[136] S. Ritter. *Probing coherence during Bose-Einstein condensation.* PhD thesis, ETH Zürich (2007).

[137] A. Öttl, S. Ritter, M. Köhl, and T. Esslinger. *Hybrid apparatus for Bose-Einstein condensation and cavity quantum electrodynamics: Single atom detection in quantum degenerate gases.* Review of Scientific Instruments **77**, 063118 (2006).

[138] L. Hruby. *Metastability and quench dynamics in a long-range interacting Hubbard model.* PhD thesis, ETH Zürich (2018).

[139] R. Mottl. *Roton-type mode softening in a dissipative quantum many-body system with cavity-mediated long-range interactions.* PhD thesis, ETH Zürich (2014).

[140] P. D. Lett, R. N. Watts, C. I. Westbrook, W. D. Phillips, P. L. Gould, and H. J. Metcalf. *Observation of Atoms Laser Cooled below the Doppler Limit.* Phys. Rev. Lett. **61**, 169–172 (1988).

[141] M. Greiner, I. Bloch, T. W. Hänsch, and T. Esslinger. *Magnetic transport of trapped cold atoms over a large distance.* Phys. Rev. A **63**, 031401 (2001).

[142] T. Esslinger, I. Bloch, and T. W. Hänsch. *Bose-Einstein condensation in a quadrupole-Ioffe-configuration trap.* Phys. Rev. A **58**, R2664–R2667 (1998).

[143] T. Stöferle. *Exploring Atomic Quantum Gases in Optical Lattices.* Phd thesis, ETH Zürich (2005).

[144] B. Tabbert and A. Goushcha. *Optical Detectors*, pages 543–619. Springer Berlin Heidelberg, Berlin, Heidelberg (2012).

[145] R. Landig. *Quantum phases emerging from competing short-and long-range interactions in an optical lattice.* PhD thesis, ETH Zürich (2016).

[146] X. Li. *Emergent structures and dynamics in a quantum gas with cavity-mediated long-range interactions.* Doctoral thesis, ETH Zurich, Zurich (2021-10-01).

[147] J. Maas. *Realization of a polarization-resolved heterodyne detection system.* Master thesis, ETH Zürich (2018).

[148] G. Reinaudi, T. Lahaye, Z. Wang, and D. Guéry-Odelin. *Strong saturation absorption imaging of dense clouds of ultracold atoms.* Opt. Lett. **32**, 3143–3145 (2007).

[149] B. Gadway, D. Pertot, R. Reimann, M. G. Cohen, and D. Schneble. *Analysis of Kapitza-Dirac diffraction patterns beyond the Raman-Nath regime.* Opt. Express **17**, 19173–19180 (2009).

[150] R. J. Fletcher, M. Robert-de Saint-Vincent, J. Man, N. Navon, R. P. Smith, K. G. H. Viebahn, and Z. Hadzibabic. *Connecting Berezinskii-Kosterlitz-Thouless and BEC Phase Transitions by Tuning Interactions in a Trapped Gas.* Physical Review Lett. **114**, 255302 (2015).

[151] K. Baumann. *Experimental realization of the Dicke quantum phase transition.* PhD thesis, ETH Zürich (2011).

[152] K. Kröger. *Real-Time Feedback and Cavity-Mediated Spin Interactions in a Quantum Gas.* Doctoral thesis, ETH Zürich, Zurich (2020).

[153] S. Sachdev. *Quantum Phase Transitions.* Cambridge University Press, 2 edition (2011).

[154] L. D. Carr. *Understanding quantum phase transitions.* Taylor and Francis (2010).

[155] M. Müller, S. Diehl, G. Pupillo, and P. Zoller. *Engineered Open Systems and Quantum Simulations with Atoms and Ions.* In P. Berman, E. Arimondo, and C. Lin, editors, *Advances in Atomic, Molecular, and Optical Physics*, volume 61 of *Advances In Atomic, Molecular, and Optical Physics*, pages 1 – 80. Academic Press (2012).

[156] A. J. Daley. *Quantum trajectories and open many-body quantum systems.* Advances in Physics **63**, 77–149 (2014).

[157] L. M. Sieberer, M. Buchhold, and S. Diehl. *Keldysh field theory for driven open quantum systems.* Reports on Progress in Physics **79**, 096001 (2016).

[158] M. Soriente, T. L. Heugel, K. Arimitsu, R. Chitra, and O. Zilberberg. *Distinctive class of dissipation-induced phase transitions and their universal characteristics.* Phys. Rev. Research **3**, 023100 (2021).

[159] M. Soriente, T. Donner, R. Chitra, and O. Zilberberg. *Dissipation-Induced Anomalous Multicritical Phenomena.* Phys. Rev. Lett. **120**, 183603 (2018).

[160] S. Diehl, E. Rico, M. A. Baranov, and P. Zoller. *Topology by dissipation in atomic quantum wires.* Nature Physics **7**, 971–977 (2011).

[161] J. T. Barreiro, M. Müller, P. Schindler, D. Nigg, T. Monz, M. Chwalla, M. Hennrich, C. F. Roos, P. Zoller, and R. Blatt. *An open-system quantum simulator with trapped ions.* Nature **470**, 486–491 (2011).

[162] Y. Lin, J. P. Gaebler, F. Reiter, T. R. Tan, R. Bowler, A. S. Sørensen, D. Leibfried, and D. J. Wineland. *Dissipative production of a maximally entangled steady state of two quantum bits.* Nature **504**, 415–418 (2013).

[163] H. Krauter, C. A. Muschik, K. Jensen, W. Wasilewski, J. M. Petersen, J. I. Cirac, and E. S. Polzik. *Entanglement Generated by Dissipation and Steady State Entanglement of Two Macroscopic Objects.* Phys. Rev. Lett. **107**, 080503 (2011).

[164] I. Bloch, J. Dalibard, and W. Zwerger. *Many-body physics with ultracold gases.* Reviews of Modern Physics **80**, 885–964 (2008).

[165] I. Bloch, J. Dalibard, and S. Nascimbène. *Quantum simulations with ultracold quantum gases.* Nature Physics **8**, 267–276 (2012).

[166] J.-R. Li, J. Lee, W. Huang, S. Burchesky, B. Shteynas, F. Ç. Top, A. O. Jamison, and W. Ketterle. *A stripe phase with supersolid properties in spin–orbit-coupled Bose–Einstein condensates.* Nature **543**, 91–94 (2017).

[167] S. Diehl, A. Micheli, A. Kantian, B. Kraus, H. P. Büchler, and P. Zoller. *Quantum states and phases in driven open quantum systems with cold atoms.* Nature Physics **4**, 878–883 (2008).

[168] T. Langen, R. Geiger, and J. Schmiedmayer. *Ultracold Atoms Out of Equilibrium.* Annual Review of Condensed Matter Physics **6**, 201–217 (2015).

[169] R. Labouvie, B. Santra, S. Heun, and H. Ott. *Bistability in a Driven-Dissipative Superfluid.* Phys. Rev. Lett. **116**, 235302 (2016).

[170] F. Letscher, O. Thomas, T. Niederprüm, M. Fleischhauer, and H. Ott. *Bistability Versus Metastability in Driven Dissipative Rydberg Gases.* Phys. Rev. X **7**, 021020 (2017).

[171] M. Fitzpatrick, N. M. Sundaresan, A. C. Y. Li, J. Koch, and A. A. Houck. *Observation of a Dissipative Phase Transition in a One-Dimensional Circuit QED Lattice.* Phys. Rev. X **7**, 011016 (2017).

[172] T. Fink, A. Schade, S. Höfling, C. Schneider, and A. Imamoglu. *Signatures of a dissipative phase transition in photon correlation measurements.* Nature Physics **14**, 365–369 (2018).

[173] T. Tomita, S. Nakajima, I. Danshita, Y. Takasu, and Y. Takahashi. *Observation of the Mott insulator to superfluid crossover of a driven-dissipative Bose-Hubbard system.* Science Advances **3** (2017).

[174] D. N. Basov, R. D. Averitt, and D. Hsieh. *Towards properties on demand in quantum materials.* Nature Materials **16**, 1077–1088 (2017).

[175] T. Byrnes, N. Y. Kim, and Y. Yamamoto. *Exciton–polariton condensates.* Nature Physics **10**, 803–813 (2014).

[176] A. Cavalleri. *Photo-induced superconductivity.* Contemporary Physics **59**, 31–46 (2018).

[177] S. Smolka, W. Wuester, F. Haupt, S. Faelt, W. Wegscheider, and A. Imamoglu. *Cavity quantum electrodynamics with many-body states of a two-dimensional electron gas.* Science **346**, 332–335 (2014).

[178] E. Orgiu, J. George, J. A. Hutchison, E. Devaux, J. F. Dayen, B. Doudin, F. Stellacci, C. Genet, J. Schachenmayer, C. Genes, G. Pupillo, P. Samorì, and T. W. Ebbesen. *Conductivity in organic semiconductors hybridized with the vacuum field.* Nature Materials **14**, 1123–1129 (2015).

[179] G. Mazza and A. Georges. *Superradiant Quantum Materials.* Phys. Rev. Lett. **122**, 017401 (2019).

[180] Y. Ashida, A. Imamoglu, J. Faist, D. Jaksch, A. Cavalleri, and E. Demler. *Quantum Electrodynamic Control of Matter: Cavity-Enhanced Ferroelectric Phase Transition.* Phys. Rev. X **10**, 041027 (2020).

[181] J. B. Curtis, Z. M. Raines, A. A. Allocca, M. Hafezi, and V. M. Galitski. *Cavity Quantum Eliashberg Enhancement of Superconductivity.* Phys. Rev. Lett. **122**, 167002 (2019).

[182] H. Gao, F. Schlawin, M. Buzzi, A. Cavalleri, and D. Jaksch. *Photoinduced Electron Pairing in a Driven Cavity.* Phys. Rev. Lett. **125**, 053602 (2020).

[183] I. Carusotto, A. A. Houck, A. J. Kollár, P. Roushan, D. I. Schuster, and J. Simon. *Photonic materials in circuit quantum electrodynamics.* Nature Physics **16**, 268–279 (2020).

[184] M. Soriente, R. Chitra, and O. Zilberberg. *Distinguishing phases using the dynamical response of driven-dissipative light-matter systems.* Phys. Rev. A **101**, 023823 (2020).

[185] P. Kirton, M. M. Roses, J. Keeling, and E. G. Dalla Torre. *Introduction to the Dicke Model: From Equilibrium to Nonequilibrium, and Vice Versa.* Advanced Quantum Technologies **2**, 1800043 (2019).

[186] K. C. Stitely, A. Giraldo, B. Krauskopf, and S. Parkins. *Nonlinear semiclassical dynamics of the unbalanced, open Dicke model.* Phys. Rev. Research **2**, 033131 (2020).

[187] Y. Shchadilova, M. M. Roses, E. G. Dalla Torre, M. D. Lukin, and E. Demler. *Fermionic formalism for driven-dissipative multilevel systems.* Phys. Rev. A **101**, 013817 (2020).

[188] M. Soriente. *Same but Different. Distinguishing phases of many-body-systems through their in- and out-of-equilibrium spectral functions.* Doctoral thesis, ETH Zurich, Zurich (2021).

[189] M. J. Bhaseen, J. Mayoh, B. D. Simons, and J. Keeling. *Dynamics of nonequilibrium Dicke models.* Phys. Rev. A **85**, 013817 (2012).

[190] V. M. Bastidas, C. Emary, B. Regler, and T. Brandes. *Nonequilibrium Quantum Phase Transitions in the Dicke Model.* Phys. Rev. Lett. **108**, 043003 (2012).

[191] C. Emary and T. Brandes. *Chaos and the quantum phase transition in the Dicke model.* Phys. Rev. E **67**, 066203 (2003).

[192] T. Weber, J. Herbig, M. Mark, H.-C. Nägerl, and R. Grimm. *Three-Body Recombination at Large Scattering Lengths in an Ultracold Atomic Gas.* Physical Review Letters **91**, 123201 (2003).

[193] Z. Zhiqiang, C. H. Lee, R. Kumar, K. J. Arnold, S. J. Masson, A. S. Parkins, and M. D. Barrett. *Nonequilibrium phase transition in a spin-1 Dicke model.* Optica **4**, 424–429 (2017).

[194] Z. Zhang, C. H. Lee, R. Kumar, K. J. Arnold, S. J. Masson, A. L. Grimsmo, A. S. Parkins, and M. D. Barrett. *Dicke-model simulation via cavity-assisted Raman transitions.* Phys. Rev. A **97**, 043858 (2018).

[195] M. Greiner, I. Bloch, O. Mandel, T. W. Hänsch, and T. Esslinger. *Exploring Phase Coherence in a 2D Lattice of Bose-Einstein Condensates.* Phys. Rev. Lett. **87**, 160405 (2001).

[196] K. Jiménez-García, R. L. Compton, Y.-J. Lin, W. D. Phillips, J. V. Porto, and I. B. Spielman. *Phases of a Two-Dimensional Bose Gas in an Optical Lattice.* Phys. Rev. Lett. **105**, 110401 (2010).

[197] J. Stenger, S. Inouye, A. P. Chikkatur, D. M. Stamper-Kurn, D. E. Pritchard, and W. Ketterle. *Bragg Spectroscopy of a Bose-Einstein Condensate.* Phys. Rev. Lett. **82**, 4569–4573 (1999).

[198] D. Clément, N. Fabbri, L. Fallani, C. Fort, and M. Inguscio. *Bragg Spectroscopy of Strongly Correlated Bosons in Optical Lattices.* Journal of Low Temperature Physics **158**, 5–15 (2010).

[199] P. A. Murthy, M. Neidig, R. Klemt, L. Bayha, I. Boettcher, T. Enss, M. Holten, G. Zürn, P. M. Preiss, and S. Jochim. *High-temperature pairing in a strongly interacting two-dimensional Fermi gas.* Science **359**, 452–455 (2018).

[200] D. Petter, A. Patscheider, G. Natale, M. J. Mark, M. A. Baranov, R. van Bijnen, S. M. Roccuzzo, A. Recati, B. Blakie, D. Baillie, L. Chomaz, and F. Ferlaino. *Bragg scattering of an ultracold dipolar gas across the phase transition from Bose-Einstein condensate to supersolid in the free-particle regime.* Phys. Rev. A **104**, L011302 (2021).

[201] J. Léonard, A. Morales, P. Zupancic, T. Donner, and T. Esslinger. *Monitoring and manipulating Higgs and Goldstone modes in a supersolid quantum gas.* Science **358**, 1415–1418 (2017).

[202] D. Nagy, G. Szirmai, and P. Domokos. *Self-organization of a Bose-Einstein condensate in an optical cavity.* Eur. Phys. J. D **48**, 127–137 (2008).

[203] H. Eleuch and I. Rotter. *Width bifurcation and dynamical phase transitions in open quantum systems.* Phys. Rev. E **87**, 052136 (2013).

[204] A. Frölian. *Simulating a topological gauge theory in a Raman-dressed Bose-Einstein condensate.* Phd thesis, Universitat Politècnica de Catalunya (2022).

[205] T. L. Heugel, M. Biondi, O. Zilberberg, and R. Chitra. *Quantum Transducer Using a Parametric Driven-Dissipative Phase Transition.* Phys. Rev. Lett. **123**, 173601 (2019).

[206] K. C. Stitely, S. J. Masson, A. Giraldo, B. Krauskopf, and S. Parkins. *Superradiant switching, quantum hysteresis, and oscillations in a generalized Dicke model.* Phys. Rev. A **102**, 063702 (2020).

[207] Y. Deng, J. Cheng, H. Jing, and S. Yi. *Bose-Einstein Condensates with Cavity-Mediated Spin-Orbit Coupling.* Phys. Rev. Lett. **112**, 143007 (2014).

[208] R. M. Kroeze, Y. Guo, and B. L. Lev. *Dynamical Spin-Orbit Coupling of a Quantum Gas.* Phys. Rev. Lett. **123**, 160404 (2019).

[209] T. E. Lee, F. Reiter, and N. Moiseyev. *Entanglement and Spin Squeezing in Non-Hermitian Phase Transitions.* Phys. Rev. Lett. **113**, 250401 (2014).

[210] J. S. Huber, G. Rastelli, M. J. Seitner, J. Kölbl, W. Belzig, M. I. Dykman, and E. M. Weig. *Spectral Evidence of Squeezing of a Weakly Damped Driven Nanomechanical Mode.* Phys. Rev. X **10**, 021066 (2020).

[211] R. Ramírez, M. Reboiro, and D. Tielas. *Exceptional Points from the Hamiltonian of a hybrid physical system: Squeezing and anti-Squeezing.* The European Physical Journal D **74**, 193 (2020).

[212] U.-J. Wiese. *Ultracold quantum gases and lattice systems: quantum simulation of lattice gauge theories.* Annalen der Physik **525**, 777–796 (2013).

[213] E. Zohar, J. I. Cirac, and B. Reznik. *Quantum simulations of lattice gauge theories using ultracold atoms in optical lattices.* Reports on Progress in Physics **79**, 014401 (2015).

[214] V. Kasper, G. Juzeliūnas, M. Lewenstein, F. Jendrzejewski, and E. Zohar. *From the Jaynes–Cummings model to non-abelian gauge theories: a guided tour for the quantum engineer.* New Journal of Physics **22**, 103027 (2020).

[215] U. Bissbort, D. Cocks, A. Negretti, Z. Idziaszek, T. Calarco, F. Schmidt-Kaler, W. Hofstetter, and R. Gerritsma. *Emulating Solid-State Physics with a Hybrid System of Ultracold Ions and Atoms.* Phys. Rev. Lett. **111**, 080501 (2013).

[216] F. Giustino. *Electron-phonon interactions from first principles.* Rev. Mod. Phys. **89**, 015003 (2017).

[217] M. Eckholt and J. J. García-Ripoll. *Correlated hopping of bosonic atoms induced by optical lattices.* New Journal of Physics **11**, 093028 (2009).

[218] A. Rapp, X. Deng, and L. Santos. *Ultracold Lattice Gases with Periodically Modulated Interactions.* Phys. Rev. Lett. **109**, 203005 (2012).

[219] M. D. Liberto, C. E. Creffield, G. I. Japaridze, and C. M. Smith. *Quantum simulation of correlated-hopping models with fermions in optical lattices.* Phys. Rev. A **89**, 013624 (2014).

[220] H. Zhao, J. Vovrosh, F. Mintert, and J. Knolle. *Quantum Many-Body Scars in Optical Lattices.* Phys. Rev. Lett. **124**, 160604 (2020).

[221] A. Hudomal, I. Vasić, N. Regnault, and Z. Papić. *Quantum scars of bosons with correlated hopping.* Communications Physics **3**, 99 (2020).

[222] R. Ma, M. E. Tai, P. M. Preiss, W. S. Bakr, J. Simon, and M. Greiner. *Photon-Assisted Tunneling in a Biased Strongly Correlated Bose Gas.* Phys. Rev. Lett. **107**, 095301 (2011).

[223] F. Meinert, M. J. Mark, K. Lauber, A. J. Daley, and H.-C. Nägerl. *Floquet Engineering of Correlated Tunneling in the Bose-Hubbard Model with Ultracold Atoms.* Phys. Rev. Lett. **116**, 205301 (2016).

[224] W. Xu, W. Morong, H.-Y. Hui, V. W. Scarola, and B. DeMarco. *Correlated spin-flip tunneling in a Fermi lattice gas.* Phys. Rev. A **98**, 023623 (2018).

[225] L. W. Clark, B. M. Anderson, L. Feng, A. Gaj, K. Levin, and C. Chin. *Observation of Density-Dependent Gauge Fields in a Bose-Einstein Condensate Based on Micromotion Control in a Shaken Two-Dimensional Lattice.* Phys. Rev. Lett. **121**, 030402 (2018).

[226] F. Görg, K. Sandholzer, J. Minguzzi, R. Desbuquois, M. Messer, and T. Esslinger. *Realization of density-dependent Peierls phases to engineer quantized gauge fields coupled to ultracold matter.* Nature Physics **15**, 1161–1167 (2019).

[227] C. Schweizer, F. Grusdt, M. Berngruber, L. Barbiero, E. Demler, N. Goldman, I. Bloch, and M. Aidelsburger. *Floquet approach to $\mathbb{Z}2$ lattice gauge theories with ultracold atoms in optical lattices.* Nature Physics **15**, 1168–1173 (2019).

[228] S. Baier, M. J. Mark, D. Petter, K. Aikawa, L. Chomaz, Z. Cai, M. Baranov, P. Zoller, and F. Ferlaino. *Extended Bose-Hubbard models with ultracold magnetic atoms.* Science **352**, 201–205 (2016).

[229] C. Laflamme, D. Yang, and P. Zoller. *Continuous measurement of an atomic current.* Phys. Rev. A **95**, 043843 (2017).

[230] D. Yang, C. Laflamme, D. V. Vasilyev, M. A. Baranov, and P. Zoller. *Theory of a Quantum Scanning Microscope for Cold Atoms.* Phys. Rev. Lett. **120**, 133601 (2018).

[231] K. T. Geier, J. Reichstetter, and P. Hauke. *Non-invasive measurement of currents in analog quantum simulators.* arXiv preprint arXiv:2106.12599 (2021).

[232] A. Celi, P. Massignan, J. Ruseckas, N. Goldman, I. B. Spielman, G. Juzeliūnas, and M. Lewenstein. *Synthetic Gauge Fields in Synthetic Dimensions.* Phys. Rev. Lett. **112**, 043001 (2014).

[233] B. Gadway. *Atom-optics approach to studying transport phenomena.* Phys. Rev. A **92**, 043606 (2015).

[234] E. J. Meier, F. A. An, and B. Gadway. *Observation of the topological soliton state in the Su–Schrieffer–Heeger model.* Nature Communications **7**, 13986 (2016).

[235] Q. Liang, D. Xie, Z. Dong, H. Li, H. Li, B. Gadway, W. Yi, and B. Yan. *Dynamic Signatures of Non-Hermitian Skin Effect and Topology in Ultracold Atoms.* Phys. Rev. Lett. **129**, 070401 (2022).

[236] E. J. Meier, F. A. An, and B. Gadway. *Atom-optics simulator of lattice transport phenomena.* Phys. Rev. A **93**, 051602 (2016).

[237] D. Schneble, G. K. Campbell, E. W. Streed, M. Boyd, D. E. Pritchard, and W. Ketterle. *Raman amplification of matter waves.* Phys. Rev. A **69**, 041601 (2004).

[238] Y. Yoshikawa, T. Sugiura, Y. Torii, and T. Kuga. *Observation of superradiant Raman scattering in a Bose-Einstein condensate.* Phys. Rev. A **69**, 041603 (2004).

[239] M. M. Cola and N. Piovella. *Theory of collective Raman scattering from a Bose-Einstein condensate.* Phys. Rev. A **70**, 045601 (2004).

[240] T. Wang and S. F. Yelin. *Theory for Raman superradiance in atomic gases.* Phys. Rev. A **72**, 043804 (2005).

[241] E. J. Meier. *Momentum-space lattices for ultracold atoms.* PhD thesis, University of Illinois at Urbana-Champaign (2019).

[242] M. Maik, P. Hauke, O. Dutta, M. Lewenstein, and J. Zakrzewski. *Density-dependent tunneling in the extended Bose–Hubbard model.* New Journal of Physics **15**, 113041 (2013).

[243] F. A. An, E. J. Meier, J. Ang'ong'a, and B. Gadway. *Correlated Dynamics in a Synthetic Lattice of Momentum States.* Phys. Rev. Lett. **120**, 040407 (2018).

[244] F. A. An, B. Sundar, J. Hou, X.-W. Luo, E. J. Meier, C. Zhang, K. R. A. Hazzard, and B. Gadway. *Nonlinear Dynamics in a Synthetic Momentum-State Lattice.* Phys. Rev. Lett. **127**, 130401 (2021).

[245] R. Lin. *Driven-dissipative phenomena in quantum many-body systems.* Doctoral thesis, ETH Zurich, Zurich (2023).

[246] K. Kroeger, N. Dogra, R. Rosa-Medina, M. Paluch, F. Ferri, T. Donner, and T. Esslinger. *Continuous feedback on a quantum gas coupled to an optical cavity.* New Journal of Physics **22**, 033020 (2020).

[247] N. Goldman, G. Juzeliūnas, P. Öhberg, and I. B. Spielman. *Light-induced gauge fields for ultracold atoms.* Reports on Progress in Physics **77**, 126401 (2014).

[248] Z. Gong, Y. Ashida, K. Kawabata, K. Takasan, S. Higashikawa, and M. Ueda. *Topological Phases of Non-Hermitian Systems.* Phys. Rev. X **8**, 031079 (2018).

[249] W. Gou, T. Chen, D. Xie, T. Xiao, T.-S. Deng, B. Gadway, W. Yi, and B. Yan. *Tunable Nonreciprocal Quantum Transport through a Dissipative Aharonov-Bohm Ring in Ultracold Atoms.* Phys. Rev. Lett. **124**, 070402 (2020).

[250] C.-M. Halati, A. Sheikhan, and C. Kollath. *Cavity-induced spin-orbit coupling in an interacting bosonic wire.* Phys. Rev. A **99**, 033604 (2019).

[251] S. Ostermann, H. Ritsch, and F. Mivehvar. *Many-body phases of a planar Bose-Einstein condensate with cavity-induced spin-orbit coupling.* Phys. Rev. A **103**, 023302 (2021).

[252] C.-M. Halati, A. Sheikhan, and C. Kollath. *Cavity-induced artificial gauge field in a Bose-Hubbard ladder.* Phys. Rev. A **96**, 063621 (2017).

[253] T. Chanda, R. Kraus, G. Morigi, and J. Zakrzewski. *Self-organized topological insulator due to cavity-mediated correlated tunneling.* Quantum **5**, 501 (2021).

[254] E. Colella, A. Kosior, F. Mivehvar, and H. Ritsch. *Open Quantum System Simulation of Faraday's Induction Law via Dynamical Instabilities.* Phys. Rev. Lett. **128**, 070603 (2022).

[255] S. W. Hawking. *Black hole explosions?* Nature **248**, 30–31 (1974).

[256] R. Bousso and S. W. Hawking. *Pair creation of black holes during inflation.* Physical Review D **54**, 6312–6322 (1996).

[257] J. M. Kosterlitz and D. J. Thouless. *Ordering, metastability and phase transitions in two-dimensional systems.* Journal of Physics C: Solid State Physics **6**, 1181 (1973).

[258] C. Degen, F. Reinhard, and P. Cappellaro. *Quantum sensing.* Reviews of Modern Physics **89**, 035002 (2017).

[259] . LIGO scientific collaboration. *Enhanced sensitivity of the LIGO gravitational wave detector by using squeezed states of light.* Nature Photonics **7**, 613–619 (2013).

[260] L. McCuller, C. Whittle, D. Ganapathy, K. Komori, M. Tse, A. Fernandez-Galiana, L. Barsotti, P. Fritschel, M. MacInnis, F. Matichard, K. Mason, N. Mavalvala, R. Mittleman, H. Yu, M. E. Zucker, and M. Evans. *Frequency-Dependent Squeezing for Advanced LIGO.* Phys. Rev. Lett. **124**, 171102 (2020).

[261] L. Deng, E. W. Hagley, J. Wen, M. Trippenbach, Y. Band, P. S. Julienne, J. E. Simsarian, K. Helmerson, S. L. Rolston, and W. D. Phillips. *Four-wave mixing with matter waves.* Nature **398**, 218–220 (1999).

[262] J. M. Vogels, K. Xu, and W. Ketterle. *Generation of Macroscopic Pair-Correlated Atomic Beams by Four-Wave Mixing in Bose-Einstein Condensates.* Physical Review Letters **89**, 020401 (2002).

[263] G. K. Campbell, J. Mun, M. Boyd, E. W. Streed, W. Ketterle, and D. E. Pritchard. *Parametric Amplification of Scattered Atom Pairs.* Physical Review Letters **96**, 020406 (2006).

[264] A. Perrin, H. Chang, V. Krachmalnicoff, M. Schellekens, D. Boiron, A. Aspect, and C. I. Westbrook. *Observation of Atom Pairs in Spontaneous Four-Wave Mixing of Two Colliding Bose-Einstein Condensates.* Physical Review Letters **99**, 150405 (2007).

[265] R. G. Dall, L. J. Byron, A. G. Truscott, G. R. Dennis, M. T. Johnsson, and J. J. Hope. *Paired-atom laser beams created via four-wave mixing.* Physical Review A **79**, 011601 (2009).

[266] V. Krachmalnicoff, J.-C. Jaskula, M. Bonneau, V. Leung, G. B. Partridge, D. Boiron, C. I. Westbrook, P. Deuar, P. Ziń, M. Trippenbach, and K. V. Kheruntsyan. *Spontaneous Four-Wave Mixing of de Broglie Waves: Beyond Optics.* Physical Review Letters **104**, 150402 (2010).

[267] D. Pertot, B. Gadway, and D. Schneble. *Collinear Four-Wave Mixing of Two-Component Matter Waves.* Physical Review Letters **104**, 200402 (2010).

[268] R. Bücker, J. Grond, S. Manz, T. Berrada, T. Betz, C. Koller, U. Hohenester, T. Schumm, A. Perrin, and J. Schmiedmayer. *Twin-atom beams.* Nature Physics **7**, 608–611 (2011).

[269] M. Bonneau, J. Ruaudel, R. Lopes, J.-C. Jaskula, A. Aspect, D. Boiron, and C. I. Westbrook. *Tunable source of correlated atom beams.* Physical Review A **87**, 061603 (2013).

[270] S. Hodgman, R. Khakimov, R. Lewis-Swan, A. Truscott, and K. Kheruntsyan. *Solving the Quantum Many-Body Problem via Correlations Measured with a Momentum Microscope.* Physical Review Letters **118**, 240402 (2017).

[271] K. Kim, J. Hur, S. Huh, S. Choi, and J.-y. Choi. *Emission of Spin-Correlated Matter-Wave Jets from Spinor Bose-Einstein Condensates.* Physical Review Letters **127**, 043401 (2021).

[272] M.-S. Chang, Q. Qin, W. Zhang, L. You, and M. S. Chapman. *Coherent spinor dynamics in a spin-1 Bose condensate.* Nature Physics **1**, 111–116 (2005).

[273] B. Lücke, M. Scherer, J. Kruse, L. Pezzé, F. Deuretzbacher, P. Hyllus, O. Topic, J. Peise, W. Ertmer, J. Arlt, L. Santos, A. Smerzi, and C. Klempt. *Twin Matter Waves for Interferometry Beyond the Classical Limit.* Science **334**, 773–776 (2011).

[274] E. M. Bookjans, C. D. Hamley, and M. S. Chapman. *Strong Quantum Spin Correlations Observed in Atomic Spin Mixing.* Physical Review Letters **107**, 210406 (2011).

[275] C. Gross, H. Strobel, E. Nicklas, T. Zibold, N. Bar-Gill, G. Kurizki, and M. K. Oberthaler. *Atomic homodyne detection of continuous-variable entangled twin-atom states.* Nature **480**, 219–223 (2011).

[276] P. Kunkel, M. Prüfer, H. Strobel, D. Linnemann, A. Frölian, T. Gasenzer, M. Gärttner, and M. K. Oberthaler. *Spatially distributed multipartite entanglement enables EPR steering of atomic clouds.* Science **360**, 413–416 (2018).

[277] K. Lange, J. Peise, B. Lücke, I. Kruse, G. Vitagliano, I. Apellaniz, M. Kleinmann, G. Tóth, and C. Klempt. *Entanglement between two spatially separated atomic modes.* Science **360**, 416–418 (2018).

[278] M. Fadel, T. Zibold, B. Décamps, and P. Treutlein. *Spatial entanglement patterns and Einstein-Podolsky-Rosen steering in Bose-Einstein condensates.* Science **360**, 409–413 (2018).

[279] D. Linnemann, H. Strobel, W. Muessel, J. Schulz, R. Lewis-Swan, K. Kheruntsyan, and M. Oberthaler. *Quantum-Enhanced Sensing Based on Time Reversal of Nonlinear Dynamics.* Physical Review Letters **117**, 013001 (2016).

[280] F. Anders, A. Idel, P. Feldmann, D. Bondarenko, S. Loriani, K. Lange, J. Peise, M. Gersemann, B. Meyer-Hoppe, S. Abend, N. Gaaloul, C. Schubert, D. Schlippert, L. Santos, E. Rasel, and C. Klempt. *Momentum Entanglement for Atom Interferometry.* Physical Review Letters **127**, 140402 (2021).

[281] L. Pezzè, A. Smerzi, M. K. Oberthaler, R. Schmied, and P. Treutlein. *Quantum metrology with nonclassical states of atomic ensembles.* Reviews of Modern Physics **90**, 035005 (2018).

[282] S. S. Szigeti, O. Hosten, and S. A. Haine. *Improving cold-atom sensors with quantum entanglement: Prospects and challenges.* Applied Physics Letters **118**, 140501 (2021).

[283] E. Hagley, X. Maître, G. Nogues, C. Wunderlich, M. Brune, J. M. Raimond, and S. Haroche. *Generation of Einstein-Podolsky-Rosen Pairs of Atoms.* Physical Review Letters **79**, 1–5 (1997).

[284] B. Yurke, S. L. McCall, and J. R. Klauder. *SU(2) and SU(1,1) interferometers.* Physical Review A **33**, 4033–4054 (1986).

[285] J. D. Sau, S. R. Leslie, M. L. Cohen, and D. M. Stamper-Kurn. *Spin squeezing of high-spin, spatially extended quantum fields.* New Journal of Physics **12**, 085011 (2010).

[286] G. E. Marti, A. MacRae, R. Olf, S. Lourette, F. Fang, and D. M. Stamper-Kurn. *Coherent Magnon Optics in a Ferromagnetic Spinor Bose-Einstein Condensate.* Phys. Rev. Lett. **113**, 155302 (2014).

[287] B. L. Schumaker and C. M. Caves. *New formalism for two-photon quantum optics. II. Mathematical foundation and compact notation.* Phys. Rev. A **31**, 3093–3111 (1985).

[288] B. Evrard. *Coherent dynamics, relaxation and fragmentation of a spinor Bose-Einstein condensate.* Theses, Université Paris sciences et lettres (2020).

[289] V. Corre, T. Zibold, C. Frapolli, L. Shao, J. Dalibard, and F. Gerbier. *Spin-1 condensates at thermal equilibrium: A SU(3) coherent state approach.* Europhysics Letters **110**, 26001 (2015).

[290] P. B. Blakie, A. S. Bradley, M. J. Davis, R. J. Ballagh, and C. W. Gardiner. *Dynamics and statistical mechanics of ultra-cold Bose gases using c-field techniques.* Adv. Phys. **57**, 363 (2008).

[291] C. D. Mink, A. Pelster, J. Benary, H. Ott, and M. Fleischhauer. *Variational truncated Wigner approximation for weakly interacting Bose fields: Dynamics of coupled condensates.* SciPost Phys. **12**, 051 (2022).

[292] M. Rautenberg and M. Gärttner. *Classical and quantum chaos in a three-mode bosonic system.* Phys. Rev. A **101**, 053604 (2020).

[293] S. L. Rolston and W. D. Phillips. *Nonlinear and quantum atom optics.* Nature **416**, 219–224 (2002).

[294] L. W. Clark, A. Gaj, L. Feng, and C. Chin. *Collective emission of matter-wave jets from driven Bose–Einstein condensates.* Nature **551**, 356–359 (2017).

[295] B. Evrard, A. Qu, J. Dalibard, and F. Gerbier. *From Many-Body Oscillations to Thermalization in an Isolated Spinor Gas.* Phys. Rev. Lett. **126**, 063401 (2021).

[296] F. Paleari, A. Andreoni, G. Zambra, and M. Bondani. *Thermal photon statistics in spontaneous parametric downconversion.* Opt. Express **12**, 2816–2824 (2004).

[297] C. Klempt, O. Topic, G. Gebreyesus, M. Scherer, T. Henninger, P. Hyllus, W. Ertmer, L. Santos, and J. J. Arlt. *Parametric Amplification of Vacuum Fluctuations in a Spinor Condensate.* Physical Review Letters **104**, 195303 (2010).

[298] F. Brennecke, S. Ritter, T. Donner, and T. Esslinger. *Cavity Optomechanics with a Bose-Einstein Condensate.* Science **322**, 235–238 (2008).

[299] S. Fölling, F. Gerbier, A. Widera, O. Mandel, T. Gericke, and I. Bloch. *Spatial quantum noise interferometry in expanding ultracold atom clouds.* Nature **434**, 481–484 (2005).

[300] T. Rom, T. Best, D. van Oosten, U. Schneider, S. Fölling, B. Paredes, and I. Bloch. *Free fermion antibunching in a degenerate atomic Fermi gas released from an optical lattice.* Nature **444**, 733–736 (2006).

[301] T. Schweigler, V. Kasper, S. Erne, I. Mazets, B. Rauer, F. Cataldini, T. Langen, T. Gasenzer, J. Berges, and J. Schmiedmayer. *Experimental characterization of a quantum many-body system via higher-order correlations.* Nature **545**, 323–326 (2017).

[302] M. Prüfer, T. V. Zache, P. Kunkel, S. Lannig, A. Bonnin, H. Strobel, J. Berges, and M. K. Oberthaler. *Experimental extraction of the quantum effective action for a non-equilibrium many-body system.* Nature Physics **16**, 1012–1016 (2020).

[303] R. G. Miller. *The Jackknife–A Review.* Biometrika **61**, 1–15 (1974). Full publication date: Apr., 1974.

[304] S. Colombo, E. Pedrozo-Peñafiel, A. F. Adiyatullin, Z. Li, E. Mendez, C. Shu, and V. Vuletić. *Time-reversal-based quantum metrology with many-body entangled states.* Nature Physics **18**, 925–930 (2022).

[305] L. Salvi, N. Poli, V. Vuletić, and G. M. Tino. *Squeezing on Momentum States for Atom Interferometry.* Physical Review Letters **120**, 033601 (2018).

[306] G. P. Greve, C. Luo, B. Wu, and J. K. Thompson. *Entanglement-enhanced matter-wave interferometry in a high-finesse cavity.* Nature **610**, 472–477 (2022).

[307] R. J. Lewis-Swan and K. V. Kheruntsyan. *Proposal for a motional-state Bell inequality test with ultracold atoms.* Physical Review A **91**, 052114 (2015).

[308] J. Kitzinger, X. Meng, M. Fadel, V. Ivannikov, K. Nemoto, W. J. Munro, and T. Byrnes. *Bell correlations in a split two-mode-squeezed Bose-Einstein condensate.* Physical Review A **104**, 043323 (2021).

[309] A. Qu, B. Evrard, J. Dalibard, and F. Gerbier. *Probing Spin Correlations in a Bose-Einstein Condensate Near the Single-Atom Level.* Physical Review Letters **125**, 033401 (2020).

[310] G. Vitagliano, I. Apellaniz, I. n. L. Egusquiza, and G. Tóth. *Spin squeezing and entanglement for an arbitrary spin.* Phys. Rev. A **89**, 032307 (2014).

[311] J. F. Clauser. *Experimental distinction between the quantum and classical field-theoretic predictions for the photoelectric effect.* Phys. Rev. D **9**, 853–860 (1974).

[312] K. V. Kheruntsyan, J.-C. Jaskula, P. Deuar, M. Bonneau, G. B. Partridge, J. Ruaudel, R. Lopes, D. Boiron, and C. I. Westbrook. *Violation of the Cauchy-Schwarz Inequality with Matter Waves.* Physical Review Letters **108**, 260401 (2012).

[313] M. D. Reid and D. F. Walls. *Violations of classical inequalities in quantum optics.* Phys. Rev. A **34**, 1260–1276 (1986).

[314] T. Wasak, P. Szańkowski, P. Ziń, M. Trippenbach, and J. Chwedeńczuk. *Cauchy-Schwarz inequality and particle entanglement.* Phys. Rev. A **90**, 033616 (2014).

[315] V. Vuletic, A. J. Kerman, C. Chin, and S. Chu. *Observation of low-field feshbach resonances in collisions of cesium atoms.* Physical Review Letters **82**, 1406–1409 (1999).

[316] Y. Li, L. He, and W. Hofstetter. *Lattice-supersolid phase of strongly correlated bosons in an optical cavity.* Phys. Rev. A **87**, 051604 (2013).

[317] M. R. Bakhtiari, A. Hemmerich, H. Ritsch, and M. Thorwart. *Nonequilibrium Phase Transition of Interacting Bosons in an Intra-Cavity Optical Lattice.* Phys. Rev. Lett. **114**, 123601 (2015).

[318] S. F. Caballero-Benitez and I. B. Mekhov. *Quantum Optical Lattices for Emergent Many-Body Phases of Ultracold Atoms.* Phys. Rev. Lett. **115**, 243604 (2015).

[319] N. Dogra, F. Brennecke, S. D. Huber, and T. Donner. *Phase transitions in a Bose-Hubbard model with cavity-mediated global-range interactions.* Phys. Rev. A **94**, 023632 (2016).

[320] Y. Chen, Z. Yu, and H. Zhai. *Quantum phase transitions of the Bose-Hubbard model inside a cavity.* Phys. Rev. A **93**, 041601 (2016).

[321] B. Sundar and E. J. Mueller. *Lattice bosons with infinite-range checkerboard interactions.* Phys. Rev. A **94**, 033631 (2016).

[322] T. Flottat, L. D. F. De Parny, F. Hébert, V. G. Rousseau, G. G. Batrouni, L. de Forges de Parny, F. Hébert, V. G. Rousseau, and G. G. Batrouni. *Phase diagram of bosons in a two-dimensional optical lattice with infinite-range cavity-mediated interactions.* Physical Review B **95**, 1–8 (2017).

[323] R. Liao, H.-J. Chen, D.-C. Zheng, and Z.-G. Huang. *Theoretical exploration of competing phases of lattice Bose gases in a cavity.* Phys. Rev. A **97**, 013624 (2018).

[324] H.-J. Chen, Y.-Q. Yu, D.-C. Zheng, and R. Liao. *Extended Bose-Hubbard Model with Cavity-Mediated Infinite-Range Interactions at Finite Temperatures.* Scientific Reports **10**, 9076 (2020).

[325] X. Guan, J. Fan, X. Zhou, G. Chen, and S. Jia. *Two-component lattice bosons with cavity-mediated long-range interaction.* Phys. Rev. A **100**, 013617 (2019).

[326] K. Lozano-Méndez, A. H. Cásares, and S. F. Caballero-Benítez. *Spin Entanglement and Magnetic Competition via Long-Range Interactions in Spinor Quantum Optical Lattices.* Phys. Rev. Lett. **128**, 080601 (2022).

[327] J. Fan, X. Zhou, W. Zheng, W. Yi, G. Chen, and S. Jia. *Magnetic order in a Fermi gas induced by cavity-field fluctuations.* Physical Review A **98**, 043613 (2018).

[328] A. Camacho-Guardian, R. Paredes, and S. F. Caballero-Benítez. *Quantum simulation of competing orders with fermions in quantum optical lattices.* Physical Review A **96**, 051602 (2017).

[329] L. Carl. *A Bose-Hubbard Model with Cavity-Assisted Spin-Dependent Global-Range Interactions.* PhD thesis, ETH Zürich (2020).

[330] D. Jaksch, C. Bruder, J. I. Cirac, C. W. Gardiner, and P. Zoller. *Cold Bosonic Atoms in Optical Lattices.* Phys. Rev. Lett. **81**, 3108–3111 (1998).

[331] D. S. Rokhsar and B. G. Kotliar. *Gutzwiller projection for bosons.* Physical Review B **44**, 10328–10332 (1991).

[332] E. Altman and A. Auerbach. *Oscillating Superfluidity of Bosons in Optical Lattices.* Phys. Rev. Lett. **89**, 250404 (2002).

[333] S. D. Huber, E. Altman, H. P. Büchler, and G. Blatter. *Dynamical properties of ultracold bosons in an optical lattice.* Phys. Rev. B **75**, 085106 (2007).

[334] X. Chai, L. You, and C. Raman. *Magnetic solitons in an immiscible two-component Bose-Einstein condensate.* Phys. Rev. A **105**, 013313 (2022).

[335] D. van Oosten, P. van der Straten, and H. T. C. Stoof. *Quantum phases in an optical lattice.* Phys. Rev. A **63**, 053601 (2001).

[336] P. M. Chaikin and T. C. Lubensky. *Principles of Condensed Matter Physics*, page 144–212. Cambridge University Press (1995).

[337] A. Dhar, M. Singh, R. V. Pai, and B. P. Das. *Mean-field analysis of quantum phase transitions in a periodic optical superlattice.* Phys. Rev. A **84**, 033631 (2011).

[338] W. Zwerger. *Mott–Hubbard transition of cold atoms in optical lattices.* Journal of Optics B: Quantum and Semiclassical Optics **5**, S9 (2003).

[339] X. Li, D. Dreon, P. Zupancic, A. Baumgärtner, A. Morales, W. Zheng, N. R. Cooper, T. Donner, and T. Esslinger. *First order phase transition between two centro-symmetric superradiant crystals.* Phys. Rev. Res. **3**, L012024 (2021).

[340] A. L. Gaunt, T. F. Schmidutz, I. Gotlibovych, R. P. Smith, and Z. Hadzibabic. *Bose-Einstein Condensation of Atoms in a Uniform Potential.* Phys. Rev. Lett. **110**, 200406 (2013).

[341] E. G. M. van Kempen, S. J. J. M. F. Kokkelmans, D. J. Heinzen, and B. J. Verhaar. *Interisotope Determination of Ultracold Rubidium Interactions from Three High-Precision Experiments.* Phys. Rev. Lett. **88**, 093201 (2002).

[342] E. Altman, W. Hofstetter, E. Demler, and M. D. Lukin. *Phase diagram of two-component bosons on an optical lattice.* New Journal of Physics **5**, 113 (2003).

[343] G.-H. Chen and Y.-S. Wu. *Quantum phase transition in a multicomponent Bose-Einstein condensate in optical lattices.* Phys. Rev. A **67**, 013606 (2003).

[344] A. B. Kuklov and B. V. Svistunov. *Counterflow Superfluidity of Two-Species Ultracold Atoms in a Commensurate Optical Lattice.* Phys. Rev. Lett. **90**, 100401 (2003).

[345] D. S. Hall, M. R. Matthews, J. R. Ensher, C. E. Wieman, and E. A. Cornell. *Dynamics of Component Separation in a Binary Mixture of Bose-Einstein Condensates.* Phys. Rev. Lett. **81**, 1539–1542 (1998).

[346] D.-C. Zhang, S.-P. Feng, and S.-J. Yang. *Quantum phases of two-component bosons in the extended Bose-Hubbard model.* Physics Letters A **427**, 127912 (2022).

[347] G. G. Batrouni and R. T. Scalettar. *Phase Separation in Supersolids.* Physical Review Letters **84**, 1599–1602 (2000).

[348] M. Cheneau, P. Barmettler, D. Poletti, M. Endres, P. Schauß, T. Fukuhara, C. Gross, I. Bloch, C. Kollath, and S. Kuhr. *Light-cone-like spreading of correlations in a quantum many-body system.* Nature **481**, 484–487 (2012).

[349] P. Hauke and L. Tagliacozzo. *Spread of Correlations in Long-Range Interacting Quantum Systems.* Phys. Rev. Lett. **111**, 207202 (2013).

[350] E. I. R. Chiacchio and A. Nunnenkamp. *Dissipation-Induced Instabilities of a Spinor Bose-Einstein Condensate Inside an Optical Cavity.* Phys. Rev. Lett. **122**, 193605 (2019).

[351] B. Buča and D. Jaksch. *Dissipation Induced Nonstationarity in a Quantum Gas.* Phys. Rev. Lett. **123**, 260401 (2019).

[352] K. Roux, V. Helson, H. Konishi, and J. P. Brantut. *Cavity-assisted preparation and detection of a unitary Fermi gas.* New Journal of Physics **23**, 043029 (2021).

[353] J. Zeiher, J. Wolf, J. A. Isaacs, J. Kohler, and D. M. Stamper-Kurn. *Tracking Evaporative Cooling of a Mesoscopic Atomic Quantum Gas in Real Time.* Phys. Rev. X **11**, 041017 (2021).

[354] J. M. Higbie, L. E. Sadler, S. Inouye, A. P. Chikkatur, S. R. Leslie, K. L. Moore, V. Savalli, and D. M. Stamper-Kurn. *Direct Nondestructive Imaging of Magnetization in a Spin-1 Bose-Einstein Gas.* Phys. Rev. Lett. **95**, 050401 (2005).

[355] Y. Liu, S. Jung, S. E. Maxwell, L. D. Turner, E. Tiesinga, and P. D. Lett. *Quantum Phase Transitions and Continuous Observation of Spinor Dynamics in an Antiferromagnetic Condensate.* Phys. Rev. Lett. **102**, 125301 (2009).

[356] S. Sachdev and J. Ye. *Gapless spin-fluid ground state in a random quantum Heisenberg magnet.* Phys. Rev. Lett. **70**, 3339–3342 (1993).

[357] A. Kitaev. *A simple model for quantum holography.* Caltech Lecture Series (2015).

[358] D. Chowdhury, A. Georges, O. Parcollet, and S. Sachdev. *Sachdev-Ye-Kitaev models and beyond: Window into non-Fermi liquids.* Rev. Mod. Phys. **94**, 035004 (2022).

[359] J. Maldacena and D. Stanford. *Remarks on the Sachdev-Ye-Kitaev model.* Phys. Rev. D **94**, 106002 (2016).

[360] J. Maldacena. *The Large-N Limit of Superconformal Field Theories and Supergravity.* International Journal of Theoretical Physics **38**, 1113–1133 (1999).

[361] Z. Luo, Y.-Z. You, J. Li, C.-M. Jian, D. Lu, C. Xu, B. Zeng, and R. Laflamme. *Quantum simulation of the non-fermi-liquid state of Sachdev-Ye-Kitaev model.* npj Quantum Information **5**, 53 (2019).

[362] N. Sauerwein, F. Orsi, P. Uhrich, S. Bandyopadhyay, F. Mattiotti, T. Cantat-Moltrecht, G. Pupillo, P. Hauke, and J.-P. Brantut. *Engineering random spin models with atoms in a high-finesse cavity.* Nature Physics (2023).

[363] D.-W. Wang. *Momentum distribution of noncondensate particles near the superfluid-to-Mott-insulator transition of bosonic atoms in a uniform optical lattice.* Phys. Rev. A **80**, 063620 (2009).

[364] M. Ben Dahan, E. Peik, J. Reichel, Y. Castin, and C. Salomon. *Bloch Oscillations of Atoms in an Optical Potential.* Phys. Rev. Lett. **76**, 4508–4511 (1996).

[365] F. Borgonovi, F. M. Izrailev, and L. F. Santos. *Exponentially fast dynamics of chaotic many-body systems.* Phys. Rev. E **99**, 010101 (2019).

[366] P. Uhrich, S. Bandyopadhyay, N. Sauerwein, J. Sonner, J.-P. Brantut, and P. Hauke. *A cavity quantum electrodynamics implementation of the Sachdev–Ye–Kitaev model.* arXiv preprint arXiv:2303.11343 (2023).

[367] B. Kobrin, Z. Yang, G. D. Kahanamoku-Meyer, C. T. Olund, J. E. Moore, D. Stanford, and N. Y. Yao. *Many-Body Chaos in the Sachdev-Ye-Kitaev Model.* Phys. Rev. Lett. **126**, 030602 (2021).

[368] K. Sandholzer, A.-S. Walter, J. Minguzzi, Z. Zhu, K. Viebahn, and T. Esslinger. *Floquet engineering of individual band gaps in an optical lattice using a two-tone drive.* Phys. Rev. Res. **4**, 013056 (2022).

[369] P. Coleman. *Superconductivity and BCS theory*, page 486–541. Cambridge University Press (2015).

[370] D. J. Young, A. Chu, E. Y. Song, D. Barberena, D. Wellnitz, Z. Niu, V. M. Schäfer, R. J. Lewis-Swan, A. M. Rey, and J. K. Thompson. *Observing Dynamical Phases of a Bardeen-Cooper-Schrieffer Superconductor in a Cavity QED Simulator.* arXiv preprint arXiv:2306.00066 (2023).

[371] A. D. Cronin, J. Schmiedmayer, and D. E. Pritchard. *Optics and interferometry with atoms and molecules.* Rev. Mod. Phys. **81**, 1051–1129 (2009).

[372] D. Linnemann, J. Schulz, W. Muessel, P. Kunkel, M. Prüfer, A. Frölian, H. Strobel, and M. K. Oberthaler. *Active SU(1,1) atom interferometry.* Quantum Science and Technology **2**, 044009 (2017).

[373] T. Chen, D. Xie, B. Gadway, and B. Yan. *A Gross-Pitaevskii-equation description of the momentum-state lattice: roles of the trap and many-body interactions.* arXiv preprint arXiv:2103.14205 (2021).

[374] A. U. J. Lode. *Multiconfigurational time-dependent Hartree method for bosons with internal degrees of freedom: Theory and composite fragmentation of multicomponent Bose-Einstein condensates.* Phys. Rev. A **93**, 063601 (2016).

[375] R. Lin, P. Molignini, L. Papariello, M. C. Tsatsos, C. Lévêque, S. E. Weiner, E. Fasshauer, R. Chitra, and A. U. J. Lode. *MCTDH-X: The multiconfigurational time-dependent Hartree method for indistinguishable particles software.* Quantum Science and Technology **5**, 024004 (2020).

[376] F. Chevy, V. Bretin, P. Rosenbusch, K. W. Madison, and J. Dalibard. *Transverse Breathing Mode of an Elongated Bose-Einstein Condensate.* Phys. Rev. Lett. **88**, 250402 (2002).

Acknowledgments

The past four and a half years at ETH Zurich have been a unique and enriching experience, and I would like to thank the people who have accompanied me during my PhD journey.

First and foremost, I am extremely grateful to my supervisor, Tilman Esslinger, for giving me the opportunity to work in the Quantum Optics (QO) group and pursue my PhD. Tilman has been an exceptional supervisor, granting us enough freedom to develop our own research interests, while always being available, cheerful and supportive. Among many things, I have learned from him that a deep physics intuition can often take us further than brute force calculations.

I want to thank our senior scientist, Tobias Donner, for his active co-supervision, constant support, and guidance in lab and research project matters. I have benefited immensely from Tobi's vast technical expertise—ranging from laser systems to the quirks of AC units—and his sharp scientific writing.

Over the course of my PhD, I had the pleasure of working with different generations of the *Cavity Team*. From the previous generation, I worked with Nishant Dogra and Katrin Kroeger. From Nishant, with his vast theoretical expertise, I learned how to 'mathematically tackle' our experiment and model the most intricate many-body systems. Katrin introduced me to Python data analysis methods and taught me a more systematic approach to lab routines.

My generation is composed by Francesco Ferri and Fabian Finger. Francesco and I started our journey nearly at the same time. From him, I learned how to work as an experimental physicist, and how to tame a cold atoms lab with patience, skill and dedication. His hard work and tireless commitment were contagious, allowing us to transition from fixing 'daily issues' to exploring fascinating many-body physics in the lab. Fabian and I have shared over four years in the lab, office and beyond: I couldn't have asked for a better lab partner. His meticulous approach to lab work and technical skills are invaluable, while his overall calmer and more optimistic attitude have saved us countless times, notably during emergencies like unsticking an ion pump switch using drilling grease. Only together, we managed to push the experiment 'beyond its natural boundaries'.

The (not so) new members of the Cavity Team are Nicola Reiter, Panagiotis (Panos) Christodoulou and Jacob Fricke. Nicola really reinvigorated our team: in the past two years, we have really benefited from her profound understanding of physics and proactive work style; her broad interests are going to shape the future research directions of our lab. Panos has brought immense experimental expertise, keen insights, and a long-term vision for the lab. His critical approach to physics has prompted us to question everything we had taken for granted, greatly deepening our understanding. Our newest member, Jacob, possesses an impressive experimental skill set and a contagious motivation to tackle the most arduous tasks, such as the Rb exchange. With them, the experiment is undoubtedly in excellent hands.

Moreover, I'd like to thank all the members of the QO group for creating such a wonderful work atmosphere. Their selfless help, the numerous stimulating 'Coop discussions' and countless group events have made these years memorable. Every day of my PhD, I eagerly looked forward to going to work, and I am very happy to stay for a while as a wrap-up postdoc.

I also want to express my appreciation to Oded Zilberberg for co-examining my thesis, and for our delightful collaboration at the beginning of my PhD. In addition, I want to thank the theory collaborators with whom I've had the pleasure of working over the years: Rui Lin (with whom I worked side by side, greatly benefiting from his unparalleled simulation skills and deep understanding of our experiment), R.Chitra, Matteo Soriente, Leon Carl (undoubtedly the best master student I've ever supervised), Sebastian D. Huber, Tena Dubcek (with whom we tirelessly 'pushed' our Bose-Hubbard project and crystallized it into a nice paper against all odds), Kevin Stitely, Bernd Krauskopf, and Scott Parkins. Our different collaborations have been truly rewarding. I've learned a multitude of approaches to many-body cavity QED and how to efficiently collaborate beyond a tight-knit team.

Many thanks to Fabian, Nicola, Panos, Jacob, Rui, Tena, Konrad and Tobi for their meticulous proofreading this thesis.

I also want to thank my family and friends for their support over the years. I am extremely thankful to my aunt Chizi and uncle Ernst for their support since I moved to Switzerland, going as far as hosting me during the Covid lockdown and making me feel at home. Moreover, I want to thank my siblings, Valeria and Pepe: I really cherish our close relationship and their ceaseless support. Furthermore, I want to thank my best friend, Humberto, for always being available, and for lifting my spirits with his countless visits, messages and calls.

I am beyond grateful to my girlfriend Leti for her unwavering support, patience and love over the last decade. She has been a pillar for my PhD journey, and I couldn't have succeeded without her.

Last but not least, I want to express my deepest gratitude to my parents, José Luis and Gisela, for their unconditional love and enduring support all these years. It is because of their selflessness and tireless commitment that I am here today.

¡Gracias por tanto!

List of Publications

The main publications discussed in this thesis are:

1. **Spin- and momentum-correlated atom pairs mediated by photon exchange.**
   F. Finger*, R. Rosa-Medina*, N. Reiter, P. Christodoulou, T. Donner, and T. Esslinger. arXiv 2303.11326 (2023).

2. **Phases, instabilities and excitations in a two-component lattice model with photon-mediated interactions.**
   L. Carl, R. Rosa-Medina, S. D. Huber, T. Esslinger, N. Dogra*, and T. Dubcek*. Physical Review Research **5**, L032003 (2023).

3. **Observing Dynamical Currents in a Non-Hermitian Momentum Lattice.**
   R. Rosa-Medina*, F. Ferri*, F. Finger, N. Dogra, K. Kroeger, R. Lin, R. Chitra, T. Donner, and T. Esslinger. Physical Review Letters **128**, 143602 (2022).

4. **Emerging Dissipative Phases in a Superradiant Quantum Gas with Tunable Decay.**
   F. Ferri*, R. Rosa-Medina*, F. Finger, N. Dogra, M. Soriente, O. Zilberberg, T. Donner, and T. Esslinger. Physical Review X **11**, 041046 (2021).

Additional publications produced in the framework of this thesis include:

5. **Quantum Fluctuation Dynamics of Dispersive Superradiant Pulses in a Hybrid Light-Matter System.**
   K. Stitely, F. Finger, R. Rosa-Medina, F. Ferri, T. Donner, T. Esslinger, S. Parkins, and B. Krauskopf. arXiv 2302.08078 (2023).

6. **Dissipation-Engineered Family of Nearly Dark States in Many-Body Cavity-Atom Systems.**
   R. Lin, R. Rosa-Medina, F. Ferri, F. Finger, K. Kroeger, T. Donner, T. Esslinger, and R. Chitra. Physical Review Letters **128**, 153601 (2022).

7. **Continuous feedback on a quantum gas coupled to an optical cavity.**
   K. Kroeger, N. Dogra, R. Rosa-Medina, M. Paluch, F. Ferri, T. Donner, and T. Esslinger. New Journal of Physics **22**, 033020 (2020).

*These authors contributed equally to the corresponding works.

Curriculum Vitae

Personal data

Rodrigo Felipe Rosa-Medina Pimentel
born March 09$^{\text{th}}$, 1994, in Lima, Peru
citizen of Peru and Germany

Address: Flurstrasse 51, 8048 Zürich, Switzerland
Email: rrodrigo@phys.ethz.ch

Education and Research Experience

01/2019 – 09/2023	Ph.D. thesis under the supervision of Prof. Dr. T. Esslinger: *Exploring Dissipative and Coherent Spin Dynamics with Superradiant Quantum Gases* Eidgenössische Technische Hochschule, Zurich, Switzerland
10/2017 – 09/2018	Master thesis under the supervision of Prof. Dr. M. Oberthaler: *Probing Long-Time Spin Dynamics in a ^{87}Rb Bose-Einstein Condensate* Kirchhoff Institute of Physics, Heidelberg, Germany
10/2013 – 09/2016	Graduate studies, University of Heidelberg, Germany
04 – 09/2016	Bachelor thesis under the supervision of Prof. Dr. S. Jochim: *Towards Detection of Noise Correlations in a System of ultracold ^{6}Li* Physikalisches Institut, Heidelberg, Germany
10/2013 – 09/2016	Undergraduate studies, University of Heidelberg, Germany
11/2012	German Abitur, Alexander von Humboldt Schule, Lima, Peru